

Active Pixel Detectors  
for Mass Spectrometry Imaging

Cover: The cover of this thesis shows the total ion image of a transmission electron microscopy (TEM) grid as imaged with the detection system developed within the scope of this dissertation. In particular, a peptide calibration mixture deposited underneath a TEM grid was imaged on a microscope mode mass spectrometer by secondary ion mass spectrometry. The “dots” in this image correspond to the calibration mixture from underneath the TEM grid. The choice for this image is motivated by three factors that are all integral to modern day research. First, this simple image reflects my fascination for the technique and technology that we use in our research. It is fabulous and amazing that we can ablate and ionize microscopic particles off a macroscopic structure and manipulate them through our instrument with electrostatic fields in such a way that the spatial information from the sample surface is retained. Second, samples of the type used to generate this image are prominently used in our lab for ion optical tuning, benchmarking and quality control. Promising “grid images” have paved the way for real life samples and have helped to bring a new detection concept into biological mass spectrometry imaging. Third, this image was taken as part of a collaborative effort. Team work, shared struggle and enthusiasm have made this project and its results possible.

ISBN/EAN: 978-90-77209-64-6

Copyright © 2012 by Julia H. Jungmann.

All rights reserved. No part of this publication may be reproduced, stored in a retrieval system or transmitted in any form or by any means, electronic, mechanical, photocopying, recording, scanning or otherwise, without the permission in writing by the author.

An electronic version of this thesis is available at [www.amolf.nl/publications](http://www.amolf.nl/publications). Paper copies are available from the library of the FOM-Institute AMOLF ([library@amolf.nl](mailto:library@amolf.nl)).

# Active Pixel Detectors for Mass Spectrometry Imaging

ACTIEVE-PIXEL DETECTOREN  
VOOR MASSASPECTROMETRIE IMAGING  
(met een samenvatting in het Nederlands)

## PROEFSCHRIFT

ter verkrijging van de graad van doctor  
aan de Universiteit Utrecht,  
op gezag van de rector magnificus,  
prof. dr. G. J. van der Zwaan,  
ingevolge het besluit van het college voor promoties  
in het openbaar te verdedigen op maandag 19 november 2012  
des middags te 2.30 uur

door

Julia Helga Jungmann

geboren op 2 december 1983  
te Mannheim-Neckarau, Duitsland

Promotor: Prof. dr. R. M. A. Heeren

The work described in this thesis was performed at the FOM-Institute AMOLF, Science Park 104, 1098 XG Amsterdam, The Netherlands.

This work is part of the research programme of the Foundation for Fundamental Research on Matter (FOM), which is part of the Netherlands Organisation for Scientific Research (NWO). Part of this research is supported by the Dutch Technology Foundation STW, which is the applied science division of NWO, and the Technology Programme of the Ministry of Economic Affairs, Project OTP 11956.

*To my family.*



# CONTENTS

<b>1</b>	<b>Introduction</b>	<b>3</b>
1.1	Understanding the World Around Us . . . . .	4
1.2	Mass Spectrometry Imaging . . . . .	5
1.3	The Study of Atoms and Molecules by their Interaction with Light . . . . .	5
1.4	Outline of this Thesis . . . . .	6
<b>2</b>	<b>Emerging Technologies in Mass Spectrometry Imaging</b>	<b>9</b>
2.1	Introduction . . . . .	9
2.2	MSI and its Challenges in a Nutshell . . . . .	10
2.2.1	Sample Preparation . . . . .	12
2.2.2	Mass Analysis and Analyte Localization . . . . .	12
2.2.3	Data Analysis and Interpretation . . . . .	15
2.2.4	Choosing Mass Spectrometry Technology . . . . .	15
2.3	Novel Imaging and Detection Schemes for MSI . . . . .	16
2.3.1	Microprobe Mode MSI . . . . .	16
2.3.2	Microscope Mode MSI . . . . .	18
2.3.3	Throughput . . . . .	18
2.3.4	Detector Technology . . . . .	19
2.3.5	Considerations on the Spatial Resolution . . . . .	21
2.3.6	Pushing Detection Limitations . . . . .	21
2.3.7	Active Pixel Detectors for MSI . . . . .	24
2.4	Identification Strategies . . . . .	26
2.5	Adding a New Dimension: 3D-MSI . . . . .	30
2.6	Ion Mobility: Adding the Shape of a Molecule . . . . .	32
2.7	Summary . . . . .	34
<b>3</b>	<b>Detection and Imaging Systems for Ions, Electrons and Photons</b>	<b>35</b>
3.1	Introduction to Sensors and Detectors . . . . .	35
3.2	Selected Sensor and Detector Technology for Mass Spectrometry . . . . .	36
3.2.1	Array Detectors . . . . .	37
3.2.2	High Mass Detection Systems . . . . .	39
3.2.3	Mass Spectrometry + Imaging . . . . .	41
3.3	State-of-the-Art in Multi-Dimensional Imaging and Detection . . . . .	41
3.3.1	Different Modes of Imaging and Particle Detection . . . . .	41
3.3.2	State-of-the-Art Imaging/Particle Detection Systems . . . . .	45
3.3.3	Performance Criteria for Detector Technology . . . . .	51
3.4	Solid State Pixel Detectors . . . . .	54

3.4.1	Charge-Coupled Device . . . . .	54
3.4.2	Complementary Metal-Oxide-Semiconductor . . . . .	55
3.4.3	The Differences: CCD versus CMOS . . . . .	56
3.4.4	CMOS Imagers Today: Medipix/Timepix versus Other Fast Pixelated Detectors . . . . .	58
3.5	The Medipix/Timepix Detector Family . . . . .	63
3.5.1	Chips of the Medipix/Timepix Detector Family . . . . .	63
3.5.2	Chips with/without a Sensor Layer . . . . .	70
3.5.3	Tiling to Larger Areas . . . . .	71
3.5.4	Readout Hardware & Software for the Medipix/Timepix Detector Family . . . . .	73
3.6	Alternative Imaging Detectors . . . . .	75
3.6.1	IonCCD . . . . .	76
3.6.2	Single Photon Avalanche Photodiode (SPAD) . . . . .	76
3.7	Conclusions . . . . .	76
<b>4</b>	<b>Fast, High Resolution Mass Spectrometry Imaging Using a Medipix Pixelated Detector</b>	<b>79</b>
4.1	Introduction . . . . .	79
4.2	Experimental . . . . .	81
4.2.1	The Medipix Detector Family . . . . .	81
4.2.2	Instrumentation . . . . .	82
4.2.3	Experimental Conditions . . . . .	84
4.2.4	Samples . . . . .	84
4.3	Results and Discussion . . . . .	86
4.3.1	SIMS and LDI Images . . . . .	86
4.3.2	Spatial Resolving Power . . . . .	88
4.3.3	Spatial Resolving Power as a Function of the Threshold Level . . . . .	89
4.4	Conclusion and Outlook . . . . .	89
<b>5</b>	<b>High Dynamic Range Biomolecular Ion Microscopy with the Timepix Detector</b>	<b>93</b>
5.1	Introduction . . . . .	93
5.2	Experimental . . . . .	95
5.2.1	The Medipix/Timepix Detectors . . . . .	95
5.2.2	Timepix Spectra and Images . . . . .	96
5.2.3	Imaging Setup on the Ion Microscope . . . . .	98
5.2.4	Reference Measurement Systems . . . . .	99
5.2.5	Samples . . . . .	99
5.3	Results and Discussion . . . . .	100
5.3.1	3D Timepix Measurements: Imaging and Spectral Information . . . . .	100
5.3.2	Comparison of Spectral Quality between Timepix, ADC and TDC Detection . . . . .	101
5.3.3	Timepix Mass Range . . . . .	108
5.4	Conclusions . . . . .	108

<b>6</b>	<b>Biological Tissue Imaging with a Position and Time Sensitive Pixelated Detector</b>	<b>111</b>
6.1	Introduction . . . . .	111
6.2	Methods . . . . .	114
6.2.1	The Medipix/Timepix Detectors and the Imaging Setup on the Ion Microscope . . . . .	114
6.2.2	Timepix-Generated Spectra . . . . .	115
6.2.3	Timepix-Generated Large-Area Images . . . . .	115
6.2.4	Samples . . . . .	116
6.3	Results and Discussion . . . . .	116
6.3.1	Imaging Capabilities . . . . .	116
6.3.2	Spectral Capabilities on Tissue . . . . .	120
6.3.3	Mass-Selected Imaging on a Biological Sample . . . . .	121
6.3.4	Advantages of Microscope Mode Imaging for High Spatial Resolution . . . . .	124
6.3.5	Large-Area Imaging and Throughput Capabilities . . . . .	124
6.4	Conclusions and Outlook . . . . .	127
<b>7</b>	<b>Implementation of an In-Vacuum, High-Voltage, Pixelated Detection System for Positive and Negative Mode Ion Microscopy</b>	<b>129</b>
7.1	Introduction . . . . .	129
7.2	Experimental . . . . .	131
7.2.1	High Voltage Capabilities: Detector Floating on +12/-8 kV. . . . .	131
7.2.2	High-Vacuum Compatible Chip Carrier and Vacuum Seal . . . . .	134
7.2.3	Active Peltier Cooling System . . . . .	137
7.2.4	Samples . . . . .	138
7.3	Initial Results and Discussion . . . . .	139
7.3.1	Negative Ion Mode . . . . .	139
7.3.2	Positive Ion Mode . . . . .	141
7.4	Conclusions and Outlook . . . . .	142
<b>8</b>	<b>A New Imaging Method for Understanding Chemical Dynamics: Efficient Slice Imaging Using an In-Vacuum Pixel Detector</b>	<b>143</b>
8.1	Introduction . . . . .	143
8.2	Experimental . . . . .	145
8.2.1	The Medipix/Timepix Detector Family . . . . .	145
8.2.2	Setup and Experimental Conditions . . . . .	146
8.3	Results and Discussion . . . . .	150
8.4	Conclusions . . . . .	155
	<b>References</b>	<b>157</b>
	<b>Summary</b>	<b>175</b>
	<b>Samenvatting</b>	<b>179</b>

<b>Acknowledgements</b>	<b>183</b>
<b>List of Publications</b>	<b>187</b>
<b>About the Author</b>	<b>191</b>

# 1

## Introduction

The desire to understand the world around us is intrinsic to human nature. Since the beginning of mankind, humans have investigated our planet, plants, animals, stars, the weather and other physical phenomena. Why does something behave in a certain way? How does it function? How can we find out about this? How can we prove it? We hypothesize about the answers. We design experiments to test our hypotheses. If the experiment tested the right parameters, the experimental results will get us closer to the answer to our questions and/or nourish our scientific curiosity to think and ask more (detailed) questions.

As such, experiments are an integral part of any scientific study. Whether they are Gedanken-experiments in theoretical research, simulations or real physical experiments, they test our hypothesis in a controlled environment. The formulation of a clear, testable hypothesis is a challenge and so is the identification of the parameters that need to be controlled to perform a valid experiment that will return accurate results. Cutting edge, scientific experiments often depend on innovative, unconventional instrumentation. Burning scientific questions lead to technological developments that define and push forward the instrumental state-of-the-art for the sciences, and often the technological standard of our daily life through spun-off user products.

Alfred Nobel realized that scientific discovery and instrumental development are equally important to advance the sciences and mankind. Therefore, in his will from 1895, he establishes the famous Nobel prizes as:

*“... prizes to those who (...) shall have conferred the greatest benefit on mankind. (...) To the person who shall have made the most important discovery or invention within the field of physics. (...) To the person who shall have made the most important chemical discovery or improvement ...”* [1].

Good experimental design is an art. This art has given us valuable instrumentation and numerous techniques that have changed everyday life. Examples [2] include the “development of wireless telegraphy” by Guglielmo Marconi and Karl

Ferdinand Braun (Nobel Prize in Physics, 1909); the “development of laser spectroscopy” by Nicolaas Bloembergen, Arthur Schawlow, Kai Siegbahn (Nobel Prize in Physics, 1981). John Bardeen, William Shockley and Walter Brattain obtained the Nobel Prize in Physics in 1956 “for their researches on semiconductors and their discovery of the transistor effect” on which most of modern electronics are based. Charles Kao, Willard Boyle and George Smith received the Nobel Prize in Physics in 2009 “for groundbreaking achievements concerning the transmission of light in fibers for optical communication” (Kao) and “for the invention of an imaging semiconductor circuit the CCD sensor” (Boyle and Smith), which is applied in countless devices such as portable cameras, mobile phone cameras and laptop computers.

## 1.1 Understanding the World Around Us

The research presented in this thesis represents a contribution to the toolbox available to investigate the world around us. In particular, it adds technology that helps us in understanding the building blocks of nature: atoms, molecules and molecular complexes.

The first part of this thesis investigates the spatial distribution and molecular structure of biologically relevant, complex macromolecular systems. In particular, the relationship between molecular structure and biological or chemical functionality is investigated by mass spectrometry imaging (MSI). In the second part of this thesis, a technique is highlighted which bears the potential to provide fundamental understanding of chemical reactions and reaction dynamics of atoms and small molecules. This technique is applied to molecular spectroscopy and is called velocity map imaging (VMI).

MSI and VMI target similar questions at different levels of complexity. From an instrumental point of view, however, the differences between the two techniques are subtle. Both in MSI and VMI, the analytes of interest are ionized by the interaction of the analyte with an ionization source, the ionized analytes are extracted from the interaction region, sent through a time-of-flight mass spectrometer and projected onto a position-sensitive detector by means of electrostatic fields. As a result, the research questions in both fields call for similar instrumental developments, which are described in this thesis.

The investigation of subcellular detail in MSI, as well as good momentum/energy resolution in VMI are -among other parameters- dependent on the detection system, which must deliver ultra-high spatial resolution. Position- and time-sensitive detection of multiple analytes/fragments in one acquisition cycle is crucial for both techniques. Furthermore, it is necessary to perform these experiments at a high experimental throughput. Large-area biological tissue imaging requires high throughput MSI detection systems due to the depletion of biological sam-

ples. The acquisition of statistically relevant data sets within a reasonable time interval ensures reproducibility and stability of the experimental parameters in VMI.

## 1.2 Mass Spectrometry Imaging

Atoms, molecules and molecular complexes form the basis of life. They are the building blocks of biomolecules like peptides, proteins, lipids and DNA. The investigation of the interaction of these macromolecules reveals insights into the dynamic processes that determine the state of biological systems. It is crucial to understand how biological (mal)function is related to molecular organization. Neurodegenerative diseases, like Alzheimers, and cancer, for instance, change the cellular biochemistry. Therefore, disease studies and diagnosis can benefit from a fundamental understanding of protein identity, distribution and modification. The investigation of this relationship has given rise to several molecular imaging techniques. In particular, the complexity of biological systems both in the healthy and in the diseased state calls for high spatial resolution molecular imaging techniques that can identify a wide range of biological analytes simultaneously. Several imaging techniques, such as atomic force microscopy and scanning electron microscopy, enable high spatial resolution analysis of biological systems but lack chemical identification capabilities. Other techniques distinguish predefined analytes by fluorescent, antibody or radioactive labeling. These techniques require prior knowledge about the sample composition and interfere with the sample integrity. Mass spectrometry imaging [3] is a discovery tool that provides both chemical specificity via the determination of the analyte's mass and analyte localization by the position-correlated detection of the analyte without any prior knowledge of the imaging target.

## 1.3 The Study of Atoms and Molecules by their Interaction with Light

Fundamental physical/chemical processes of atomic or molecular dissociation or ionization are studied in experiments where the system, i.e. the atom or molecule, absorbs one or more photons from a coherent light source. As the photodissociation of a molecule breaks molecular bonds, it can be considered the inverse reaction for the bond formation between the dissociation fragments.

The study of (inverse) chemical reactions and the dynamics thereof has greatly benefitted from the development of ultra-short laser pulses. In particular, the motion of atoms and molecules has directly been probed by femtosecond pulses and the motion of electrons within molecules and atoms by attosecond laser pulses.

The interaction of atoms or molecules with light can be described by the laws of energy and momentum conservation. Therefore, the experimental ion imaging technique has to simultaneously measure the relevant particle velocities and the internal energies of the reaction participants. Velocity map imaging (VMI) [4, 5] is designed to provide these measurements of molecular reaction dynamics. In VMI, molecular dissociation and ionization is investigated for isolated molecules from a beam in the gas phase. After the molecule-light interaction, the electrons and/or ions are guided towards a position-sensitive detector by electric fields. The technique measures the full three-dimensional (3D) velocity distribution of the scattered reaction fragments in one two-dimensional (2D) image. Information on both the kinetic energy and the angular distribution can be extracted from the spatial appearance of the 2D image.

## 1.4 Outline of this Thesis

The research presented in this thesis was carried out in the *Biomolecular Imaging Mass Spectrometry (BIMS) group* at the *FOM-Institute AMOLF* in Amsterdam. The research of the *BIMS group* focuses on the development and application of analytical tools for mass spectrometry based molecular imaging. The development of novel instrumentation and methodology for ultrahigh spatial resolution MSI is prerequisite to enable fundamental and applied research in molecular histology, biochemical and biomedical research. At the same time, the analysis time of readily degrading biological samples must be kept short. In previous years, ultrahigh spatial resolution and high throughput MSI has been enabled with the *AMOLF* mass microscope [6].

*Chapter 2* of this thesis introduces mass spectrometry imaging as an analytical tool for biological and biomedical tissue research. The current state of the technique is evaluated and emerging technologies for high spatial resolution MS imaging and high sample throughput studies are introduced, among other techniques. The evaluation of state-of-the-art MSI technology, in particular for high spatial resolution and high throughput TOF-MSI, reveals that adequate detector technology is the key to successful microscope mode MSI measurements.

The detector technology employed for microscope mode MSI has thusfar not delivered the required performance features. *Chapter 3* of this thesis gives an overview of state-of-the-art ion, electron and photon detection and imaging technology. This chapter evaluates imaging detection systems, which have been used for (microscope mode) MS(I), as well as other techniques. Additionally, active pixel detectors are identified as a promising candidate for high resolution and high throughput imaging experiments.

In the scope of this thesis, this novel imaging approach based on active pixel detectors is evaluated, investigated, implemented and, for the first time, applied

to biological TOF-MSI on an ion microscope and VMI. This involved the transfer of detector technology developed for the fundamental (high energy) physics community to the fields of mass spectrometry (imaging) and fundamental atomic and molecular physics research. Therefore, the project involved close collaboration with the *Medipix collaboration* hosted by the *European Organization for Nuclear Research (CERN)* (Geneva, Switzerland) and the *Detector Research & Development group* of the *National Institute for Subatomic Physics (NIKHEF)* (Amsterdam, The Netherlands). The detection system, active pixel detectors of the Medipix/Timepix chip family, were initially designed and intended for X-ray and  $\gamma$ -ray detection. Hence, the presented project transferred this technology into a different field of application with different experimental requirements.

*Chapter 4* presents the first high spatial resolution MS imaging study with such an in-vacuum pixelated detection system. For these experiments, the Medipix detection system had to be prepared to detect ions/electrons (instead of photons) by the placement of microchannel plates in front of the detection system. An additional challenge was the transfer of an “ambient” environment detection system into a high-vacuum environment. In this first proof-of-concept study, the focus was to test the feasibility of such a detection system for MSI and evaluate the attainable spatial resolution.

Position- and also time-sensitive time-of-flight detection of multiple, simultaneous events is demonstrated in *Chapter 5*. Most importantly, a Timepix chip was implemented for these experiments, which can measure the arrival position of the electrons/ions, i.e. imaging as with the Medipix, but also the arrival time of these events. The Timepix measurements add the time- and hence the mass spectral-dimension to the TOF-measurements. *Chapter 5* evaluates the spectral performance of this new detection system and compares it to established acquisition and detection systems.

*Chapter 6* applies this detection system to the study of biological tissue sections. While the research in *Chapter 4 & 5* mainly used biologically relevant standard mixtures and benchmark samples, *Chapter 6* describes the application of this new technology to biological tissue samples, i.e. mouse testis tissue sections. The experiments presented in this chapter investigate how the new detection system performs on “real world” samples, which contain biological analytes at physiological concentrations, which are difficult to handle and degrade quickly. Additionally, large-area tissue samples require “mosaic” measurements, due to their relatively large size (up to several centimeters-squared). In mosaic measurements, the tissue surface is rastered and analyzed area-by-area and a complete image/data cube ( $x, y, TOF$ ) has to be reconstructed from individual experiments. *Chapter 6* demonstrates that the Timepix detection system possess promising analytical capabilities for biological tissue imaging by evaluating the spatial resolution on tissue, commenting on the spectral performance and by showing that large-area

imaging is feasible.

*Chapter 7* outlines how the analytical capabilities of this detection system can be extended by the application of additional extraction fields. The measurements presented in *Chapter 4* to *Chapter 6* were conducted in positive ion mode. However, it is crucial to extend the system's analytical capabilities to negative ion mode to provide a tool capable of returning complementary data, i.e. positive and negative mode analytes, off biological samples. This is achieved by electrically isolating the detection system from the mass spectrometer and by floating the detection system on up to +12 kV/-8 kV, which results in ion acceleration energies of up to 15 keV/11 keV (compared to 5 keV in the standard setup). Additionally, the high extraction fields provide the capability to analyze large intact proteins.

*Chapter 8* introduces the new detection method to velocity map and slice imaging and was carried out in collaboration with the *Extreme Ultraviolet Physics group* of *AMOLF*. The system's capabilities are used to study the photodissociation of  $\text{NO}_2$ . The experiments establish that the system is very well suited for molecular studies of this type, since it provides high resolution images and hence high energy resolution VMI experiments. Also, the timing capabilities enable convenient "slice images".

The detection system developed within the scope of this thesis represents a valuable analytical tool for highly sensitive, spatially resolved, in-vacuum particle detection. In particular, the microchannel plate/Timepix detection system on an ion microscope delivers the MSI community an extremely powerful instrument for high dynamic range, high mass range and high detector homogeneity studies of lipids, peptides and intact proteins of biomolecular relevance. Ultra-high spatial resolution studies of biological analytes at physiological concentrations directly from tissue demonstrate the power of this system, whose capabilities can be utilized for biological or biomedical MSI studies, fundamental atomic and molecular imaging research or other particle detection-based areas of research.

# 2

## Emerging Technologies in Mass Spectrometry Imaging

*Mass spectrometry imaging (MSI) as an analytical tool for biomolecular and biomedical research targets accurate compound localization and identification. In terms of dedicated instrumentation, this translates into the demand for more detail in the image dimension (spatial resolution) and in the spectral dimension (mass resolution and accuracy), preferably combined in one instrument. At the same time, large-area, biological tissue samples require fast acquisition schemes, instrument automation and a robust data infrastructure. This chapter discusses the analytical capabilities of an “ideal” MSI instrument for biomolecular and biomedical molecular imaging. The analytical attributes of such an ideal system are contrasted with technological and methodological challenges in MSI. In particular, innovative instrumentation for high spatial resolution imaging in combination with high sample throughput is discussed. Detector technology that targets various shortcomings of conventional imaging detector systems is highlighted. The benefits of accurate mass analysis, high mass resolving power, additional separation strategies and multimodal three-dimensional data reconstruction algorithms are discussed to provide the reader with an insight in the current technological advances and the potential of MSI for biomedical research.*

### 2.1 Introduction

Mass spectrometry imaging (MSI) measurements target the visualization of the spatial organization and the identification of molecular masses from biomolecular surfaces [3, 7, 8]. Ideally, a single MSI experiment on one instrument would return an accurate biochemical map of a sample surface. It would identify and localize all compounds with a subcellular lateral resolution, a high mass accuracy and zepto-molar sensitivity. The analysis speed would be so high that large-area

imaging and high sample throughput would be guaranteed. Not solely mass analysis would be performed over a wide mass range but also structural information on sample molecules would be revealed by on-the-fly, data-dependent tandem mass spectrometry. The localization of specific analytes of biomolecular or biomedical samples would be placed in the context of tissue and/or organ functionality using three-dimensional reconstruction algorithms.

Unfortunately, the ideal MSI experiment is far from reality and a single instrument unifying the above capabilities has not been realized to date. A variety of different types of imaging mass spectrometers deliver a range of specific analytical capabilities that can be used in concert. In these spectrometers, a clever piece of instrumentation or artificial intelligence enable measurements that approach one or few of the desirable attributes of the “ideal” MSI experiment. In addition, the field is pushing novel instrumental innovations and the integration of several analytical capabilities into one instrument. Novel multimodal approaches are pursued that analyze one sample with different molecular imaging instruments. Subsequent data correlation analysis is used to combine the generated complementary information and to employ it for revealing more molecular detail. This chapter briefly describes the current state of MSI. It identifies technological and methodological challenges and recent advances in mass spectrometry imaging technology. Emphasis is put on innovative instrumentation for high spatial resolution imaging in conjunction with high sample throughput. Detector technology that targets various shortcomings of conventional imaging detector systems is introduced. Accurate mass identification, enhanced analytical MSI capabilities and multimodal 3D data reconstruction algorithms are described and discussed to provide the reader with an insight in the current technological advances in mass spectrometry imaging.

## 2.2 MSI and its Challenges in a Nutshell

Mass spectrometry identifies compounds based on the atomic composition of the sample molecules and their charge state. Therefore, no detailed prior knowledge of the sample composition is required and analysis becomes feasible. The chemical identification is not limited by analyte preselection as, for instance, in imaging techniques based on fluorescent or radioactive labeling. Hence, the technique itself does not introduce any functional changes on the biomolecules under investigation. The combination of unlabeled identification and analyte localization within a sample provides the possibility to visualize and understand biomolecular modifications and pathways. Depending on the mass analyzer, the detection range of this technique covers single atoms up to macromolecules. In principle, MSI can detect and identify hundreds of compounds with sub-micrometer resolution from complex biological samples surfaces, while maintaining a relatively high

throughput. These features of MSI provide a solid basis to molecular pathology. Currently, MSI is applied to the fields of proteomics [9, 10], lipidomics [11–13] and metabolomics [14–16]. In addition, disease studies like the fundamental understanding of the biochemistry of neurodegenerative diseases [17, 18] or cancer [19], drug distribution studies [16, 20] and forensics [21, 22], among others, benefit from the information revealed by MSI.

Compound localization and identification form the core of MSI as an analytical tool for biomedical research. In terms of MSI instrumentation, these requirements translate into the demand for more detail in the image dimension (spatial resolution) and in the spectral dimension (mass resolution, accuracy and tandem MS capabilities for compound identification) -preferably combined in a single instrument. At the same time, large-area tissue samples call for fast acquisition schemes, instrument automatization and robust data infrastructure, among other desirable features. Figure 2.1 depicts the workflow of a typical MSI experiment. The generic MSI workflow is briefly discussed and challenges are identified. Some advances towards the solutions of these problems are pointed out and will be discussed in more detail further on.

Generally, MSI experiments consist three distinct parts, each of which poses its own challenges but also offers a variety of opportunities for specific sample analysis.

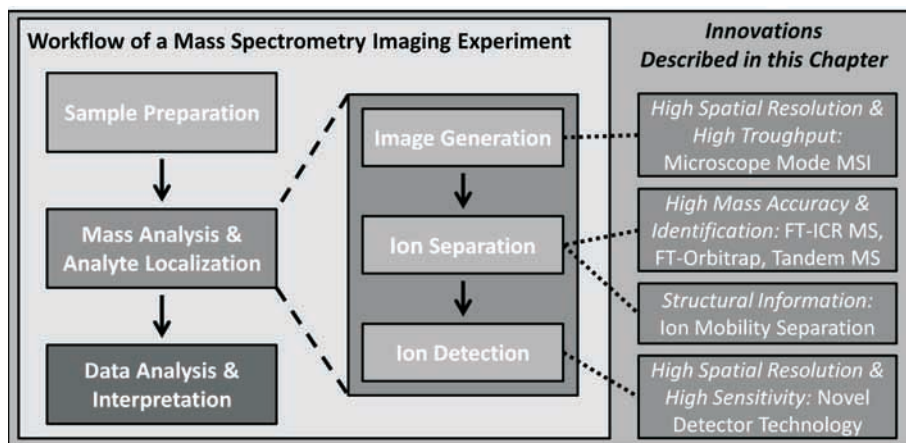


Figure 2.1: General workflow of a mass spectrometry imaging experiment. Technological developments which will be highlighted in this chapter are indicated.

### 2.2.1 Sample Preparation

The first step in an MSI experiment is adequate sample preparation specifically targeted to the envisioned type of study. Sample preparation methods and protocols are an active area of research which merits in depth description and review [23–25] but is beyond the scope of this chapter.

### 2.2.2 Mass Analysis and Analyte Localization

The second step in the MSI workflow represents the mass analysis and the analyte localization, i.e. the actual mass spectrometry and imaging. Generally, MSI requires transferring solid state analytes into the gas phase. Then, the analytes are ionized. The different compounds are separated by their mass-to-charge ratio and eventually detected. In terms of MSI technology, this translates into three distinct areas of instrumentation: image generation, ion separation and ion detection.

#### Image Generation

The image generation comprises the ionization and desorption as well as the formation of an ion optical image. The biomolecules have to be desorbed and ionized such that analytes are transferred from the sample surface into the gas phase. Among others [26–35], this is achieved with photons ((matrix-assisted) laser desorption/ionization, (MA)LDI [26, 27, 36–40]) or primary ions (secondary ion mass spectrometry, SIMS [26, 27, 41–43]) in such a way that the spatial organization of the sample surface is retained. Different ionization methods call for specific sample preparation protocols and target different groups of analytes. The process of ion generation is a crucial part of MSI experiments [27]. The fundamentals of ion/image generation and different ionization sources for MSI are not treated in further detail in this chapter.

The ion/image generation and the obtainable spatial resolution in MSI experiments are intricately related. In microprobe (“sample rastering”) MSI, the spatial resolution is directly determined by the area of ion formation on the sample surface. Hence, most efforts approach the challenge of increasing the spatial resolution by decreasing the spot size of the ionization beam, i.e. the spot size of the laser or primary ion beam.

Alternatively, the spatial resolution can be increased by stepping away from the sample rastering (microprobe mode) approach to microscope mode imaging [6]. This fundamentally different approach decouples the spatial resolution of the system from the desorption/ionization spot by using magnifying ion optics and a position-sensitive detector. Microscope mode MSI is treated in detail in section 2.3.2 of this chapter.

The *analysis speed* and *sample throughput* of a MSI study greatly depend on the (frequency of) ion/image generation. Microscope mode MSI experiments enable high sample throughput MSI studies due to the large desorption/ionization spot as compared to microprobe mode MSI. Sample throughput in microprobe mode MSI experiments has recently been targeted by several groups and will briefly be commented on in section 2.3.3.

By now, impressive technology is available for high throughput microprobe MSI studies on MALDI time-of-flight (TOF) instruments. However, TOF-instruments intrinsically lack the mass resolving power and the mass accuracy that some biomolecular and biomedical imaging studies require. Typically, TOF-MS systems have mass resolving powers below 40,000 and mass accuracies after external calibration larger than 1-5 ppm which is insufficient for accurate compound identification. In the mass range  $m/z < 500$ , accurate compound identification can be possible with TOF-MS. However, chemical noise<sup>1</sup> complicates the compound identification in this mass range. To overcome these limitations, several other MS analyzers are under development to overcome the loss of chemical information due to instrumental mass resolving power and mass accuracy limitations (see ion separation/mass analysis section).

### Ion Separation/Mass Analysis

After desorption and ionization, the analytes are separated on the basis of their mass-to-charge ratio ( $m/z$ ). The choice of mass analyzer depends on the required mass resolving power, mass accuracy, mass range and also availability. Generally, it is desirable and efficient to analyze all ions in one single analysis run.

**Fourier transform ion cyclotron resonance mass spectrometry** (FT-ICR MS) determines the  $m/z$  of an ion from its ion cyclotron resonance frequency in a static magnetic field. Similarly, the  $m/z$  of an ion in a **FT-Orbitrap** mass spectrometer is determined from its oscillation frequency in the electrostatic field of the trap. Since frequencies can be measured with a higher precision than a TOF, these instruments determine the ion mass with a significantly higher accuracy than a TOF-analyzer. Unlike TOF-MS measurements, the mass measurement in FT-MS is independent of the kinetic energy distribution of the ions. This is a clear advantage of FT-MS over TOF-MS where the spread in the kinetic energy distribution of the ions introduces mass inaccuracies. MALDI FT-MS is the most prominent technique in revealing chemically complete and accurate information from a sample. This technique combines a high mass resolving power with a high mass accuracy. It resolves and identifies ions at a single nominal mass that are

---

<sup>1</sup>The term “chemical noise” in (MALDI-) mass spectrometry [44] refers to background ion peaks located at every  $m/z$  value, which can merge with “real analyte” peaks if the signal-to-noise ratio of the measurement is low. Hence, chemical noise can distort analyte identification and represents a practical limit to the sensitivity of MS measurements.

commonly present in MALDI imaging mass spectra [45–47] and provides a highly confident compound identification [48]. The accurate assignment of a molecular formula to a specific mass spectral peak is crucial to MSI studies. Direct molecular identification is only possible if an accurate mass measurement is available from a FT-ICR/FT-Orbitrap MS measurement. Developments in this field will be treated in section 2.4 of this chapter.

***Time-of-flight-MS*** (TOF-MS) is a technique in which all ions are accelerated to a very narrow range of kinetic energies. Then, the ions are separated on the basis of their  $m/z$  in a flight tube. TOF-instruments intrinsically lack the mass resolving power and the mass accuracy that some biomolecular and biomedical imaging studies require. To overcome these limitations, several new techniques are under development to prevent the loss of chemical information due to limited mass resolving power and mass accuracy. If no accurate mass determination is possible, the molecular identity can be determined indirectly.

In particular, confident analyte identification from TOF-MS data can be achieved by tandem MS. Here, a selected parent ion is identified by (repeated) fragmentation and mass spectrometric analysis of the fragments [49]. While tandem MS capabilities are readily available for MALDI-instruments, they are still scarce for SIMS spectrometers where the primary ion beam readily damages the sample surface and ion yields are lower [50–54]. However, in recent years, cluster beam sources have greatly improved the sensitivity, the available mass range and the lateral resolution for biological SIMS [41, 55, 56]. The development of  $C_{60}$ -SIMS TOF-MS instruments with tandem-MS capabilities is a logical consequence [54, 57].

In addition, ***gas phase separation capabilities***, like ion mobility separation, have been incorporated. This technique separates ions of the same mass-to-charge ratio (but that constitute different biomolecules) by their collisional cross section in a collision gas [58–60]. The gas phase separation step is typically conducted prior to the mass analysis in a TOF-spectrometer. Thereby, traveling-wave ion mobility separation reduces the complexity of the sample analysis. It also recovers errors in the spatial image introduced by unresolved peaks. Ion mobility separation will be treated in section 2.6 of this chapter.

## **Ion Detection**

Rubakhin and co-workers describe that the ideal imaging technique for MSI can “simultaneously detect and identify multiple known and unknown compounds present in biological tissues with at least single-cell spatial resolution” [61]. Koppenaal and co-workers outline that the desirable analytical attributes of an ideal MS detector [62] are unit ion-detection efficiency, low or no noise, a high stability, the simultaneous detection of multiple ions, a wide mass range and mass-independent response, a wide dynamic range, a fast response, a short recovery

time and a high saturation level. They add operational attributes as a long life, low maintenance, easy replacement as well as a low replacement cost [62]. The spectrometer design or the envisioned application pose varying requirements to the MS(I) detector technology. For instance, experimental conditions may call for a detection system capable of handling high count rates ( $>10^6$  counts/s) with minimal recovery time [62], detectors with a rapid readout and response (particularly in TOF-MS) [62], single or multiple ion detection [62], low noise (in the detector itself and the readout electronics) for good limits of detection, high sensitivity, accuracy and precision [62]. Biomolecular or biomedical MS applications require detection uniformity in the mass range  $10^2$ - $10^5$   $m/z$  [62]. This poses a challenge to conventional secondary-electron MS detectors (like microchannel plates (MCP) or photomultiplier tubes) for which the mass response levels off for larger ions [62]. This results in a detection disadvantage for macromolecules of biomolecular or biomedical interest as for instance singly-charged, intact macromolecules like proteins studied by MALDI-MS [62]. This detection disadvantage for macromolecules calls for new detector technology. Novel, highly parallel detector technology for MSI is discussed in section 2.3.7.

### 2.2.3 Data Analysis and Interpretation

Finally, step three in the MSI workflow is the analysis and interpretation of the acquired data. MSI experiments return thousands of spectral channels at thousands of positions on the sample surface. Since mass spectra are measured at a raster of positions on the sample surface, the amount of data generated requires specific data treatment techniques. Therefore, software and algorithm development forms an integral part of the MSI field. Data analysis and interpretation are not extensively treated in this chapter as a result of the chosen focus on emerging technologies. It needs little imagination that the bioinformatics aspects of MSI will need a substantial amount of work in the future. An algorithm which reconstructs the localization of specific analytes of biomolecular or biomedical samples in three dimensions and hence places the analyte localization in the context of tissue and/or organ functionality is presented in section 2.5.

### 2.2.4 Choosing Mass Spectrometry Technology

In all of these steps (image generation, ion separation/mass analysis and ion detection), the selected method depends on the information that the experiment aims to reveal. In particular, the available mass spectrometry imaging technology provides different analytical capabilities and has its limitations. Appropriate instrumentation should be chosen to match the anticipated mass range, the mass

resolution, the mass accuracy and the spatial resolution. Furthermore, the instrument's capabilities to perform additional analysis on the ionized sample, as for instance, fragmentation, tandem MS, spectroscopy or ion mobility separation should be considered. Each of the three steps in an MSI experiment has to be carefully planned and performed successfully for the generation of an adequate mass spectrum and corresponding molecular images.

## 2.3 Novel Imaging and Detection Schemes for MSI

### Developments to Improve Sample Throughput, Spatial Image Resolution and Analyte Detection

For many applications, TOF-MS mass analyzers are a good choice for both MALDI- and SIMS-MS. The speed, the obtainable sensitivity, the wide accessible mass range (up to  $m/z=100k$  with MALDI) and the infrastructure for high sample throughput make TOF-MS the mass analyzer of choice for applications where extremely high mass accuracy and mass resolution are not imperative (or tandem MS is available). Microscope mode MSI on a TOF-instrument is discussed as a high throughput, high spatial resolution MSI method.

In MSI, two acquisition modes can be distinguished namely the microprobe and the microscope mode (Figure 2.2).

### 2.3.1 Microprobe Mode MSI

Most commonly, the conventional microprobe mode of acquisition is employed in MSI. In the microprobe mode, the sample is probed with a pulsed desorption/ionization beam (a laser beam in MALDI or a primary ion beam in SIMS), for which either the desorption/ionization beam, the sample or both are moved with respect to one another. At every raster point, a full mass spectrum is generated. An image with a pixel resolution equivalent to the beam size is reconstructed after the experiment provided that the step size/accuracy of the sample or beam movement is not limiting. A disadvantage of small surface probe spots is the small number of ions generated for analysis. Using highly focused primary ion or laser desorption/ionization beams, microprobe mode MSI has delivered high spatial resolution MSI studies. Pulsed primary ion beams [63, 64] and UV/IR lasers in MALDI [65–68] have returned pixel sizes better than  $4\ \mu\text{m}$  and  $7\ \mu\text{m}$ , respectively. Specifically, a MALDI laser spot diameter of less than  $1\ \mu\text{m}$  and an according spatial resolution have been reported by the Spengler group [67].

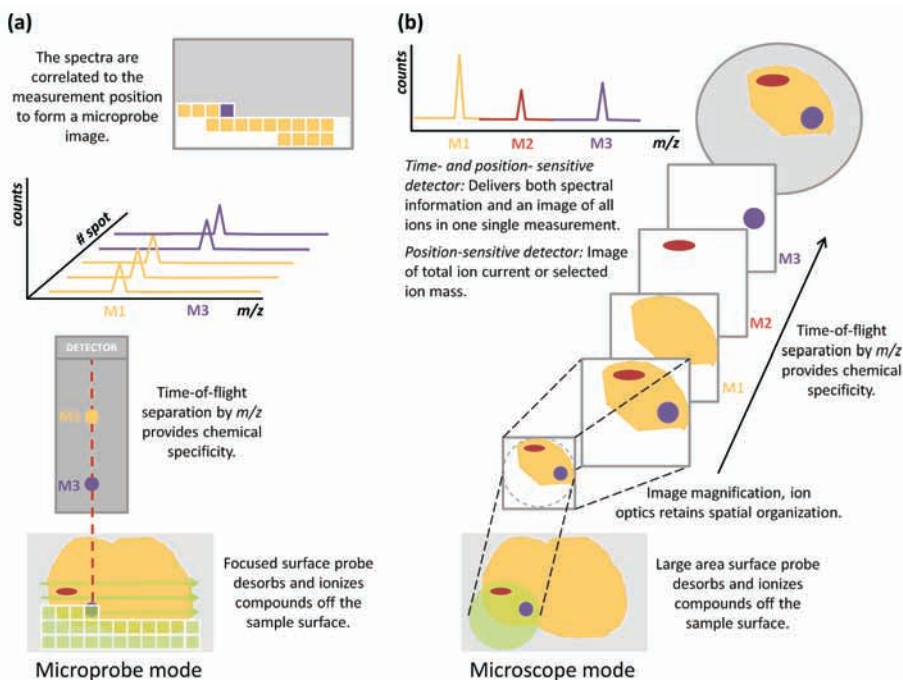


Figure 2.2: A schematic representation of microprobe and microscope mode MSI (adapted from [6]). In microprobe mode MSI (a), the desorption/ionization beam rasters the sample surface. At every raster spot, a mass spectrum is acquired. An image with a pixel resolution equivalent to the beam size is reconstructed after the experiment. In microscope mode MSI (b), a larger area desorption/ionization beam illuminates the sample surface. Ion optics magnifies the molecular images and retains the spatial information. The molecular ion distributions are mapped on a position-sensitive detector.

However, a small surface probe area can bear the disadvantage of long measurement times and the fluence available for surface desorption and ionization may be limiting. Sweedler and co-workers have demonstrated MALDI microprobe MSI at a lateral resolution better than the laser spot size using oversampling [69]. The Vickerman group has pioneered cluster SIMS-MSI, i.e. SIMS imaging with polyatomic primary ions [41, 54, 56]. Polyatomic ions generate less subsurface damage than atomic primary ions and hence enable imaging beyond the static limit (primary ion density results in surface damage of less than 1%).

### 2.3.2 Microscope Mode MSI

Ion microscope mass spectrometers provide an alternative technique to achieve high spatial resolution MSI [6]. Here, surface molecules are illuminated by a large-area desorption/ionization beam. In an ion microscope, the ionized analytes are extracted from the sample surface and imaged onto a position-sensitive detector. Initially all ions are accelerated by an electrical potential with the goal to give every ion the same initial kinetic energy. The instrument's ion optics typically achieves a rather narrow kinetic energy distribution such that negligible errors are introduced to the TOF-measurement and resulting mass assignment. The instrument's ion optics also magnify the initial ion distribution and retain the lateral spatial organization of the surface molecules on their flight path to the detector. Different molecular species are TOF-separated in the instrument's flight tube. The achievable spatial resolving power is on the order of  $4\ \mu\text{m}$  [6]. Importantly, the obtainable spatial resolution in microscope mode MSI is decoupled from the ionization spot size. Rather, the quality and the capabilities of the ion optics in combination with a position- (and time-) sensitive detector determine the lateral resolution (reference [70] shows a schematic representation of such a system). Very large sample surfaces are measured by few individual microscope spots which are then pasted together to form a large microscope MS image [71]. The Heeren group has pioneered microscope mode MSI on a TRIPLE Focusing Time-of-flight (TRIFT) mass spectrometer (Physical Electronics, Inc., Chanhassen, USA) using a detection system based on microchannel plates (MCP) in combination with a charge-coupled device (CCD) camera [6], a delay-line-detector (DLD) [72] and active, pixelated detectors of the Medipix [73]/Timepix [70] detector family.

### 2.3.3 Throughput

In ion microscopes, the desorption/ionization beam size is typically between 200-300  $\mu\text{m}$ , which is about a factor of 100 larger than a typical microprobe mode ionization spot. Comparing the microprobe and the microscope acquisition modes clearly indicates the high throughput capabilities of the latter. As an example, consider a microprobe pixel size (i.e. beam spot) of  $2\times 2\ \mu\text{m}^2$  (4  $\mu\text{m}$  lateral resolution) and a sample area of  $1\times 1\ \text{mm}^2$ . Rastering the sample surface pixel by pixel will result in  $(1,000\times 1,000\ \mu\text{m}^2)/(2\times 2\ \mu\text{m}^2)=250,000$  measurement points. Such a measurement can last several hours. In microscope mode MSI, a field of view of  $200\times 200\ \mu\text{m}^2$  is available. So, for the same sample size of  $1\times 1\ \text{mm}^2$ , only  $(1,000\times 1,000\ \mu\text{m}^2)/(200\times 200\ \mu\text{m}^2)=25$  measurement points are required. A lateral resolution on the order of 4  $\mu\text{m}$  is readily achieved with microscope mode MSI using an appropriate ion optical magnification factor and position-sensitive detector. In microscope mode MSI, the large ionization spot can result in large ion loads on the detection system. Several position-sensitive

detection systems saturate at high ion loads such that the ion generation has to be reduced and the integration time per raster position has to be increased to ensure adequate ion imaging. This can be compensated by a combination of high desorption/ionization beam repetition rates and detector technology that can accommodate high ion loads. Hence, ion microscopes enable fast, automated, high resolution large-area imaging provided that adequate, i.e. fast and position- (and possibly time-) sensitive, detector systems are employed to record high quality molecular images [74].

The improvement of sample throughput in microprobe mode MSI has recently been studied by few groups. McDonnell and co-workers have designed and commissioned an automatic sample loading system for time-efficient, round-the-clock spectrometer operation [19]. An alternative approach to high throughput measurements is an increase in the raster frequency, which results in a decrease in the measurement time without sacrificing analytical information. The Caprioli group has presented such an approach, in which they reduce the measurement time by up to a factor of two by operating a MALDI TOF-MSI system in a continuous scanning mode at a comparatively high laser repetition rate of about 5 kHz [75]. Stoeckli and co-workers generate images of drug distributions in rat sections within less than 15 minutes by using a 1 kHz laser repetition rate and a rastering speed of about 18 mm/s [76]. Sample throughput is a key factor in distinguishing MSI experiments as a robust, analytical technique for biomolecular and biomedical research.

### 2.3.4 Detector Technology

The first microscope mode MSI implementation projected the ions on a position-sensitive detector assembly which consisted of an MCP followed by a phosphor screen and a charge-coupled device (CCD) camera [6]. This detector scheme allowed for the proof-of-principle of the technique. However, the MCP, phosphor screen, CCD camera assembly suffered from the limitation that it cannot link the ion TOF (encoding the  $m/z$ ) and the spatial distribution. During one acquisition, the total ion current can be measured without  $m/z$ -specific localization on the sample. Or alternatively, a particular  $m/z$  species can be selected to pass to the detector by a pair of fast-switching electrodes, called the electrostatic blanker. The combination of several mass-selected images from separate measurements then gives information on the sample composition and according spatial distribution. This detector approach calls for time consuming, highly repetitive measurements on quickly depleting biological samples. A second, more advanced implementation of microscope mode MSI used a delay-line anode for ion detection [72, 77]. A delay-line detector can measure both the ion arrival position and time precisely [78] and thereby lifts the limitations of mass-selected imaging. In addi-

tion, the ion arrival time can be measured precisely by registration of the TOF signal from the MCP detector and correlating this information with the position information from the delay-line anode [79]. A drawback of delay-line detectors is that it can only register a small number of ion events that simultaneously arrive at the detector [80]. This renders it unsuitable for high count rate (MALDI-) MSI experiments. Furthermore, the mass-resolved image reconstruction can be time consuming. Ion optical tuning of the instrument is tedious due to delayed image feedback.

Recently, the implementation of an in-vacuum pixel detector for position- [73, 81] and time-resolved [70, 82, 83] electron and ion imaging was demonstrated and applied to MSI on an ion microscope [70, 73]. This novel detection approach uses a fully integrated, active pixel detector of the Medipix/Timepix detector family [84–86]. Such a detector assembly consists of a chevron MCP followed by four bare Timepix chips (with  $256 \times 256$  pixels of  $55 \times 55 \mu\text{m}^2$  each per chip). Each of the Timepix pixels can return (1) the position of impact of an ion via its pixel address and (2) the ion time-of-flight with respect to an external trigger with a maximum time resolution of 10 ns. The maximum TOF that can be measured per pixel is determined by the counter depth (counter overflows at 11,810). At the maximum time resolution of 10 ns, the counters can measure maximum ion TOFs of about 118  $\mu\text{s}$ . Conveniently, the simultaneous acquisition of the ion TOF and arrival position removes the need for mass-selection using an electrostatic blanker. Hence, mass-resolved images are generated during a single imaging acquisition. Unlike the delay-line detector assembly, this pixelated detector facilitates parallel detection of multiple molecular species and can accommodate significantly more ion hits simultaneously. This bears great potential for both higher count rate and large-area, high resolution molecular imaging experiments. Indeed, peptide and protein mass spectra have been generated over a mass range up to 80 kDa [70] on an ion microscope. An in depth comparison of the quality of the Timepix acquired TOF spectra to established detection techniques such as the recording of mass spectra using a time-to-digital converter (TDC) and an analog-to-digital converter (ADC) was performed [70] (Chapter 5). This novel detector approach outperforms the conventional technology easily in the detector dynamic range, the signal-to-noise ratio, the multiplexed detection on several detector elements, the available mass range, the detection homogeneity, the ability to detect single particles and the detector response to varying MCP gains [70]. Note that the current performance of this detection system is still limited by few technological shortcomings. A future pixelated chip for microscope mode MSI should incorporate multi-stop pixels (i.e. pixels which can accommodate more than one hit per measurements cycles), a larger counter depth (i.e. longer TOFs can be measured) and TDC bins on the order of 100 ps such that the achievable mass resolution becomes comparable to present commercial MSI instrumentation. An ion micro-

scope equipped with such a detector assembly will provide a very powerful MSI instrument for biomolecular or biomedical studies.

### 2.3.5 Considerations on the Spatial Resolution

On an ion microscope, the ultimate spatial resolution is determined by the ion optical design and its ion optical aberrations. Still, ion optical aberrations often do not turn out to be the limiting factor to the spatial resolution of the system. Rather, the accessible spatial resolution is determined by the resolution of the position-sensitive detection system. Both the MCP, phosphor screen, CCD camera assembly [6] and the MCP, delay-line detection system [72, 77] do not deliver spatial resolutions on the order of the ion optical aberrations. For example, the Heeren group ion microscope (used in [6, 70, 72, 73, 77]) delivers a maximum ion optical magnification of  $100\times$ . The spatial resolution of this system is limited by ion optical aberrations beyond 600 nm [87]. This means that at the maximum ion optical magnification, the detector spatial resolution should be no less than  $60\ \mu\text{m}$  ( $=100\times 600\ \text{nm}$ ). In this scenario, the  $60\ \mu\text{m}$  on the imaging detector probe 600 nm on the sample surface. The detection system is not limiting the spatial image resolution. The pixelated Timepix detection system consists of an array of  $55\times 55\ \mu\text{m}^2$  pixels. Hence, the full resolution delivered by the ion microscope can be exploited with this detection system.

### 2.3.6 Pushing Detection Limitations

As mentioned in section 2.2.2, the ideal imaging technique for MSI can “simultaneously detect and identify multiple known and unknown compounds present in biological tissues with at least single-cell spatial resolution” [61]. An evaluation of the three afore mentioned detection systems (Table 2.1) against these criteria indicates that the MCP, phosphor screen, CCD camera system and the MCP, delay-line detection system have difficulties meeting all those criteria. It should be noted that individual characteristics of those systems may be significantly better in detection systems tuned to specific needs of a particular experiment. An example is the extremely high timing resolution of about 18 ps reported for an MCP, delay-line detector system by Vredenburg and co-workers [79]. However, only a very limited number of simultaneous hits can be accommodated by the detection system. To our knowledge, no MCP, phosphor screen, CCD camera system or MCP, delay-line detection system has been reported that combines all of the exceptional performance aspects which could turn those systems into candidates for the “ideal” MSI detection system. The MCP, active pixel detector assembly comes significantly closer to the desirable capabilities of an “ideal” detector assembly for MSI. In particular, biomolecular or biomedical MS applications can benefit from the uniform ion detection in the mass range up to 80 kDa.

Table 2.1: Comparison of three different detection systems used in microscope mode MSI to the “ideal” MSI detection system.

Point of comparison	Ideal MSI detection system	MCP + phosphor screen + CCD camera	MCP + delay-line anode	MCP + active pixel detector (Timepix)
Position- and time-sensitive detection	Yes.	No.	Yes.	Yes.
Single cell spatial resolution ( $\pm 10 \mu\text{m}$ )	Yes.	Yes. <sup>2</sup>	Yes. <sup>2</sup>	Yes. <sup>2</sup>
Unit ion detection efficiency	Yes.	Yes. <sup>3</sup>	Yes. <sup>3</sup>	Yes. <sup>3</sup>
Simultaneous detection of multiple ions	Yes.	Yes. <sup>3</sup>	Yes. <sup>3</sup>	Yes. <sup>3</sup>
High count rates	Yes, $>10^6$ counts/s.	Yes./No. <sup>4</sup>	No. <sup>5</sup>	Yes, $>10^6$ counts/s.
Noise	Low/no noise.	Electronic noise.	Electronic noise.	No electronic noise.
Stability	High.	High.	High.	High.
Mass range <sup>6</sup>	Wide.	MCP high-mass roll-off limited.	MCP high-mass roll-off limited.	$\leq 80 \text{ kDa}$ .

Continued on next page

<sup>2</sup>On an ion microscope imaging mass spectrometer with an appropriate magnification factor.<sup>3</sup>Yes, at sufficiently low count rates. Note, that the active area of a MCP is 70%-80%. Hence, any detection system in combination with a MCP cannot deliver unit quantum efficiency. However, it is advantageous if the second detector stage is capable of registering the MCP electron showers with (near) unit detection efficiency.<sup>4</sup>The phosphor screen can in principle deal with high count rates when operated in signal integration mode, i.e. when no spatial information is collected from the phosphor screen. Under high count rates conditions, the light intensity over-exposes the CCD-camera and all spatial information is lost, making it unsuitable for direct imaging MS experiments under these conditions.<sup>5</sup>Approximately, 10 counts/trigger have been realized at repetition rates of about 2 kHz [72].<sup>6</sup>On ion microscope imaging mass spectrometer.

Table 2.1 – *Continued from previous page*

Point of comparison	Ideal MSI detection system	MCP + phosphor screen + CCD camera	MCP + delay-line anode	MCP + active pixel detector (Timepix)
Mass-independent response	Yes.	No, high mass role-off due to MCP.	No, high mass role-off due to MCP.	Reasonable. <sup>7</sup>
Dynamic range	Wide.	1	1	262,144 elements for parallel detection.
Response	Fast.	Phosphor decay time $\leq 100$ s of $\mu$ s, 138 ps (TDC).	25 ps (TDC)	10 ns (pixel clock)
Recovery time	Short.	Readout time dependent.	Readout time dependent.	Readout time dependent.
Saturation level	High.	1	1	262,144 elements for parallel detection.
Readout/dead time	Rapid./Short.	$\pm 1$ ms	$< 5$ ns	1 ms
High (spectral) sensitivity	High (++).	++	+	++
Timing precision	High.	138 ps (TDC)	25 ps (TDC)	10 ns (pixel clock)
Mass accuracy <sup>8</sup>	High.	Determined by clock stability.	Determined by clock stability.	Determined by clock stability.

*Continued on next page*

<sup>7</sup>Individual Timepix pixels are single-stop TDCs. Ions generated on the same position on the sample surface and hence impinging on the same pixels on the detector cannot be distinguished in a single shot experiment. There is a detection advantage for the lower mass ion. Practically, this effect is not limiting since experiments are typically based on multiple laser shots and the effect is smoothed out by sufficient measurement statistics [70].

<sup>8</sup>The dependence of the mass accuracy on the (stability of the) detection system is evaluated. Note, that generally the mass accuracy is dependent on an instrument function that takes into account the type and the mass accuracy of the mass analyzer itself, the detection system and also the sample surface homogeneity.

Table 2.1 – *Continued from previous page*

Point of comparison	Ideal MSI detection system	MCP + phosphor screen + CCD camera	MCP + delay-line anode	MCP + active pixel detector (Timepix)
Spatial accuracy	High.	Determined by ion optics.	Determined by ion optics.	Determined by ion optics.
Spatial precision <sup>2,9</sup>	High.	4 $\mu\text{m}$	4 $\mu\text{m}$	3-4 $\mu\text{m}$
Life time	Long.	MCP limited.	MCP limited.	MCP limited, but prolonged by sub-saturation operation.
Maintenance	Low.	Low.	Low.	Low.
Replacement	Easy.	Standard assembly, readily exchanged.	Involved, bulky assembly. Major replacement effort.	Compact assembly, readily changed.
Replacement cost	Low (\$).	\$	\$\$\$	\$

### 2.3.7 Active Pixel Detectors for MSI

Considering the high potential of active pixel detectors for MSI, the Medipix/Timepix detector -as a representative of this novel type of detection system- and its outstanding capabilities are outlined in more detail. Very few active pixel detectors with comparable functionality are currently available (Chapter 3). An interesting alternative chip is currently being developed by the *NA62 collaboration* at *CERN* [88–92]. This readout chip achieves a timing resolution of about 100 ps and is designed to accommodate about 73k hits per second per pixel. However, the  $45 \times 40$  (=1800) pixel matrix with a pixel size of  $300 \times 300 \mu\text{m}^2$  compromises the desirable spatial resolution and covers only a rather small area. In addition, the power consumption of the chip is about two orders of

<sup>9</sup>The spatial precision on the sample surface is evaluated in terms of the spatial resolving power, i.e. the sharpness of the sample feature edges. On an ion microscope, the spatial precision depends on the ion optical magnification factor and the element/pixel size on the imaging detector. In microprobe measurements, the spatial precision would be determined by the combination of the ionization spot size and the element size of the detection system.

magnitude higher than for the Timepix chip, which renders practical, in-vacuum implementations on mass spectrometers difficult.

The Medipix/Timepix detector family is developed within the *Medipix collaboration* hosted by *CERN* [93]. The chips of the Medipix detector family in combination with a detection medium -often a semiconductor like silicon bump-bonded on top- belong to the class of hybrid pixel detectors. There are two distinct types of chips within the Medipix detector family: the Medipix single photon counting chips and the Timepix chips, which in addition to the single photon counting capabilities can also be set to measure the time-of-arrival of an event with respect to an external reference signal or to determine the amount of charge deposited per pixel.

Semiconductor materials bump-bonded to Medipix 2 chips are silicon, gallium-arsenide, cadmium telluride, cadmium-zinc-telluride or germanium depending on the application of the detection system. Typically, a 300  $\mu\text{m}$  silicon sensor (lightly n-doped high-resistivity silicon with a p-type implementation in every pixel) is bump-bonded on top of a Medipix chip. On the entrance side, the sensor layer is coated with an aluminum layer of about 150 nm. Through this Ohmic contact, the sensor material is biased by applying a voltage of about 100 V across the sensor.

Depending on the polarity of the applied bias voltage, an electron or a hole current can be collected by the pixels. In silicon, every 3.6 eV of deposited energy creates one electron-hole pair. Hence, the amount of charges generated in the sensor material is directly proportional to the energy deposited by the impinging particle. With such a sensor layer photons and electrons can efficiently be detected provided that the photon or electron kinetic energy exceeds the detection threshold of about 4-5 keV.

When used for X-ray and electron detection, the detection medium converts incident particles into electron-hole pairs, which are collected in the charge-sensitive amplifier of the CMOS (complementary metal-oxide-semiconductor) readout chip. Ions will usually not be accelerated to sufficient energies to penetrate into the sensor layer. However, ions can be detected indirectly by placement of an MCP in front of the detector [73, 94]. The Medipix detector then registers the electron shower produced by each ion impact on the MCP. The particle counting properties consist of the ability to count events that generate a number of electron-hole pairs within a user-defined threshold/energy window.

The threshold energies that are chosen for the discriminator levels lie well above the noise levels of the pixels (on the order of 150 electrons). Therefore, electronics noise free measurements are possible, while background noise of chemical origin or due to (cosmic) radiation can still be picked up. Three additional adjustment bits can be used to equalize the pixel-to-pixel response over the full pixel array. Measurements involving time-of-flight or ultra-high resolution measurements are

performed using Timepix chips. The Timepix chip [86] is derived from the Medipix 2 chip design. The dimensions and geometry of the chip are identical to its predecessor but the functionality on the pixel level is different. Each pixel can be individually selected to operate in one of three modes:

1. The counting mode, in which each pixel counts the number of events.
2. The time-of-flight (TOF) mode, in which the occurrence time of an event is measured with respect to an external trigger/shutter signal.
3. The time-over-threshold (TOT) mode, in which the time is measured during which the charge resulting from the event exceeds the detection threshold level.

The maximum measurement time in TOF and TOT mode is determined by the pixel counter depth in combination with the measurement clock speed. In the implementation on the MSI ion microscope [70], it was chosen to use chips without a sensor layer, so-called bare chips, to improve the response to electron showers through reduced in-sensor electron diffusion. An detailed description of the chips of the Medipix/Timepix detector family is given in Chapter 3.

## 2.4 Identification Strategies

### **Imaging at High Mass Resolving Power and High Mass Accuracy**

One of the key challenges in mass spectrometry imaging is the ability to accurately identify the molecular species imaged. Until recently innovations were predominantly focused on new methods of image generation with time-of-flight MS. TOF-based MS methods are shown to offer high spatial resolution and throughput but lack the mass resolving power and mass accuracy needed for the identification of observed peaks. Unraveling the complexity of molecular profiles at biological surfaces is, however, hampered by the limited mass resolution, sensitivity, dynamic range and spatial resolution of conventional TOF-based mass spectrometric systems. The lack of mass resolving power can result in obscured spatial details when two closely neighboring peaks have different spatial distributions and are not resolved in the mass spectral domain. The availability of high resolution and high mass accuracy mass spectrometers such as FT-ICR MS [95] and FT-Orbitrap MS [96] for imaging MS is providing the needed capabilities for accurate molecular identification.

The Orbitrap mass analyzer [96, 97] is an electrostatic trap wherein tangentially injected ions rotate around a central electrode, being confined by an appropriate voltage between the outer and central electrodes. Mass analysis is based on image current detection of frequencies of axial oscillations. Therefore, its extent

of mass accuracy is limited by the same factors as FT-ICR. The introduction of the Linear Trap Quadrupole (LTQ)-Orbitrap has revolutionized high performance, high throughput mass spectrometry. It is rapidly making its way into high performance MS imaging. The first example that demonstrated the usefulness of high mass resolving power in an MS imaging strategy was provided by Taban and co-workers [46] on an FT-ICR MS. Analyzing endogenous peptide distributions on a rat brain, the authors revealed new spatial detail by separating mass spectral features that were unresolved with comparable lower resolution experiments. Figure 2.3 shows how the increased mass resolving power of an FT-ICR MS system reveals such new spatial detail. Recently, the spatial resolution of FT-Orbitrap-based MSI was improved in an atmospheric pressure scanning microprobe matrix-assisted laser desorption/ionization mass spectrometry (AP-SMALDI MS) experiment using a tightly focused laser beam [98]. Verhaert and co-workers [99] have employed high mass accuracy MSI procedures with an FT-Orbitrap to localize physiologically active peptides in neuronal tissue from American cockroach (*Periplaneta americana*) neurosecretory organs. Their results clearly illustrate that high mass accuracy and high mass resolving power of the Orbitrap analyzer are now routinely achievable in direct tissue analysis and molecular imaging experiments. This high mass resolution MS imaging approach now allows the direct identification and structural analysis of lipids, peptides and proteins from a variety of complex biological surfaces. This detailed information provides new fundamental insight in dynamic biological processes such as cell and tissue differentiation and signaling.

Fourier transform based technologies for imaging bring forward new challenges. The Fourier based technologies provide exquisite molecular detail but are inherently slow. The high mass resolving power requires long transients to be acquired for each pixel. Transients of several seconds per pixel have been reported. This limits the applicability of FT-MS based tissue imaging to compounds that are stable to in-vacuum degradation. Alternatively, ambient pressure high spatial resolution MALDI could be employed [98] to address the in-vacuum degradation issue. New mathematical techniques such as the application of a filtered diagonalization method (FDM) [100] as an alternative for the Fourier transform could be instrumental in improving total acquisition time. The total data volume is a significant limitation on the total analysis time in the generation of high resolution molecular images. This applies for both high spatial resolution as well as high mass resolution approaches. Mass spectrometry imaging at higher resolution therefore also requires developments in data storage, processing and visualization methods. A significant speed up in statistical analysis was recently introduced by the application of graphical processing units (GPUs) for principal component analysis [101]. Parallel preprocessing with cluster approaches demonstrated for high resolution Liquid Chromatography (LC)-MS datasets [102] can now readily

be applied for rapid high resolution MSI. It is clear that on many levels the high mass resolution approaches provide detailed molecular information that complements the MS based molecular imaging technologies. Consequently, more and more researchers are resorting to multimodal imaging approaches in which as much molecular information is gathered from one single piece of tissue.

Proteomics strategies have benefited from the availability of the high mass accuracy methods for a substantial time already. It has resulted in improved throughput and identification capabilities of a wide variety of peptides and proteins and their post-translational modifications [103]. Recently, these methods are established as proteomics-based MS imaging workflows [9]. In the previous section, we argued that increased mass resolving power reveals more spatial and molecular detail. Increased mass accuracy will, similar to the developments in proteomics, enhance the identification capabilities for imaging MS experiments. Imaging small molecules ( $<400m/z$ ) benefits directly as high accuracy allows the direct determination of the elemental composition of a compound. This capability is particularly useful for drug and metabolite imaging [104].

The increased mass accuracy also improves protein identification capabilities in the analysis of tissue section where an on-tissue digestion protocol has been applied. This proteomics imaging strategy employs a similar protein identification workflow as in conventional LC-tandem MS applied to each pixel. The identification is clearly more challenging due to the lack of chromatographic separation techniques after local on-tissue digestion. Here, the combination of high mass resolution (separation power) and high mass accuracy (identification power) is crucial. The high mass accuracy improves the peptide identification scores in conventional protein database searches. Peptide Mass Fingerprinting (PMF) and tandem MS based protocols are commonly used in concert.

Naturally, the combination of both high mass accuracy measurements and very high spatial resolving powers is desirable to meet the demand for detail in the image and in the spectral dimension. Spengler and co-workers used a coaxial objective to generate a laser focus smaller than  $5\ \mu\text{m}$  on several Thermo FT-MS systems (Thermo Scientific GmbH, Bremen, Germany). This approach was employed to generate various high resolution MALDI-based molecular images at the cellular level [105]. Smith and co-workers developed a MSI instrument which combines the high spatial resolution capabilities of a Buckminsterfullerene ( $\text{C}_{60}$ ) cluster ion source (Secondary Ion Mass Spectrometry) with the high mass resolving power and high mass accuracy of FT-ICR MS [106]. This novel instrument features a commercial  $\text{C}_{60}$  primary ion source, a 12 T solariX FT-ICR mass spectrometer and tandem MS capabilities (Bruker Daltonik GmbH, Bremen, Germany). Smith and co-workers demonstrate a microprobe MSI measurement on mouse brain at a  $40\ \mu\text{m}$  pixel size, a mass resolving power better than 100,000 ( $m/\Delta m_{50\%}$ ) and a mass accuracy well below 1 ppm.

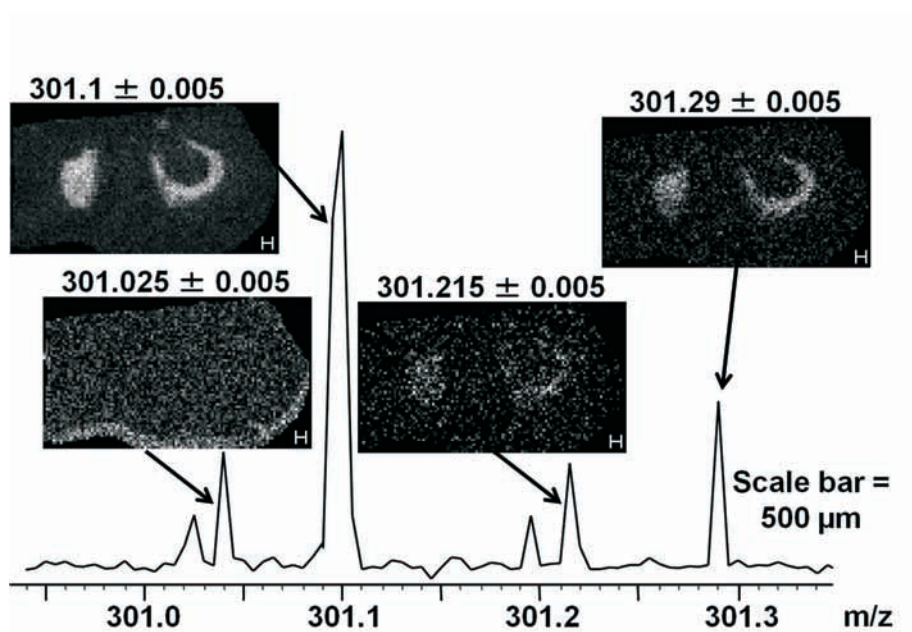


Figure 2.3: High mass resolving power SIMS FT-ICR imaging study of a mouse brain. This figure illustrates how within 0.3 Dalton several molecular peaks can be resolved that all have different spatial distributions. (Previously unpublished result, courtesy of D. F. Smith, R. M. A. Heeren and L. Paša-Tolić).

Extremely high spatial resolution approaches are ultimately limited by the efficiency of the ionization method. How many molecules are available for ionization at the ultimate spatial resolution and how many of those molecules will be ionized, i.e. what is the ionization efficiency? If the ionization efficiency is less than 100%, which holds for most ionization methods, the ionization efficiency will determine a practical achievable resolution. One exception is the microscope mode discussed earlier in this chapter (section 2.3.2).

The previous section has emphasized mass accuracy and mass resolving power as an essential element of MSI identification strategies. One other crucial element in the identification of biomolecules at surfaces in MSI experiments is tandem mass spectrometry. In particular in the absence of sufficient mass accuracy, it is imperative to perform structural analysis by means of selective dissociation to

establish or confirm the identity of the species imaged. The preferred dissociation technique in MS imaging studies is collision induced dissociation (CID) as it is fast, easy to control and the fragment spectra are reasonably well understood or interpretable. A number of tandem MS imaging studies is focused on tryptic peptide identification for proteome imaging studies. These studies can be complicated by overlapping isobaric ions. Ion mobility separation, discussed later in this chapter (section 2.6), prior to tandem MS has proven useful to enhance peptide identification scores from tandem MS studies.

Tandem MS is significantly limited by the signal persistence in most MS imaging experiments. As a result it is not possible to perform tandem MS analysis of each and every peak found in a pixel. Intelligent tandem MS target selection is becoming a prerequisite for focused molecular imaging studies. Target lists based on prior quantitative proteomics analysis from tissue homogenates is a strategy followed by a number of researchers in proteomics. This allows the utilization of a priori knowledge on interesting up- and down-regulated proteins relevant for the experimental condition that is tested. Alternatively, a regular MS imaging experiment can be used to identify interesting spatial molecular structures that can subsequently be utilized for further tandem MS imaging experiments. Targeted tandem MS profiling studies on areas of interests can also be employed to identify the molecules found in those areas.

With the introduction of Multiple Reaction Monitoring (MRM) based imaging strategies [107], it is now also possible to perform quantitative tandem MS studies. Pirman and Yost [108] have used a similar strategy to quantitatively image the distribution of acetyl-L-carnitine in mouse brain tissue sections.

In summary, it is imperative that imaging MS researchers use a smart combination of high mass resolution, high mass accuracy and complementary tandem MS strategies to identify molecular distributions found on biomedical tissue surfaces.

## 2.5 Adding a New Dimension: 3D-MSI

Anatomical atlases based on optical images are widely used for anatomical and physiological reference in the medical profession. These atlases are employed to evaluate healthy and diseased tissue for diagnostic and treatment purposes. Often general disease treatment or management protocols are established solely based on morphological aberrations observed in biopsies. A new method needs to be established that provides a molecular basis for these anatomical atlases. This requires a molecular imaging method that provides a detailed insight in the spatial distribution of a broad range of elements and molecules. These molecular tissue atlases should combine three-dimensional position information with molecular information.

Mass spectrometry imaging is typically a discipline in two spatial dimensions

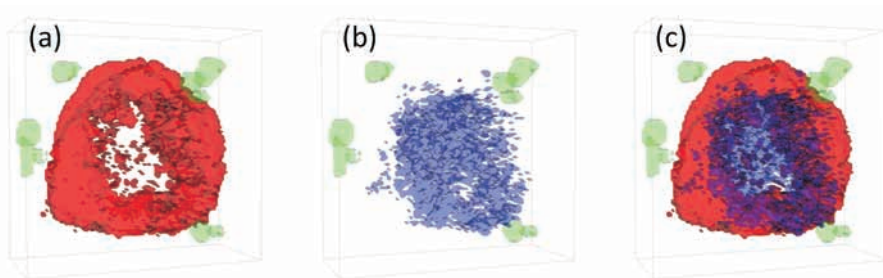


Figure 2.4: Three dimensional molecular reconstruction of a xenografted breast tumor using fiducial marker alignment of individual sections [110]. This reconstruction is generated from molecular ion distributions obtained from the central section of the breast tumor. The fiducial marker ion Chresyl Violet at  $m/z$  262.1 is shown in green in all images. a) Distribution of the molecular ion  $PC(16:0/0:0) [M+H]^+$  at  $m/z$  496.3 is shown in red. b) Distribution of molecular ion  $PC(18:1/18:1) [M+K]^+$  at  $m/z$  824.5 is shown in blue. c) The overlay of (a) and (b). Figure courtesy of K. Chughtai.

(2D). Positioning the laser or the primary ion beam to different locations on the surface results in a comprehensive set of mass spectra. A two-dimensional image of each individual mass spectral peak ( $m/z$ ) can be generated. The 2D spatial information in combination with the  $m/z$  information of the spectra is often referred to as a datacube. The generation of a three-dimensional (3D) dataset requires an additional  $z$ -dimension. In MALDI-MSI this is achieved by successive tissue sectioning with well defined and measured spatial intervals [109, 110]. MSI-data is acquired and subsequently processed to reveal the three-dimensional molecular features. Figure 2.4 shows an example of a 3D MALDI-MSI approach in which lipid volumes in a xenografted tumor are revealed. The processing protocol can include spectral and spatial binning to reduce the total dataset size prior to molecular feature visualization. Different software tools have been developed to visualize these three dimensional reconstructions [111, 112]. Individual mass spectral peaks can be simultaneously displayed using a color scheme in which each color represents a specific molecular feature.

An alternate approach towards the generation of 3D imaging MS datasets at cellular resolution is found in the SIMS domain. The introduction of ion cluster based sputter guns for depth profiling allowed gentle removal of surface layers without the induction of subsurface damage. Sputter sources that employ  $C_{60}$  molecular ions or large argon cluster ions [113, 114] can sputter with a depth resolution of tens of nanometers. This depth resolution enables 3D MSI on a subcellular scale with dynamic SIMS. Chandra and co-workers demonstrated the

generation of 3D elemental images of the mitotic spindle from T98G human glioblastoma tumor cells with dynamic SIMS [115]. Their study demonstrated that 3D SIMS imaging was essential for the analysis of mitotic cells, where specialized regions such as the mitotic spindle were hidden beneath the cell surface. A combination of sputter and analysis cycles with these sources is now employed for SIMS-based molecular 3D imaging. This was demonstrated by Fletcher and co-workers in their visualization of the 3D distribution of phosphocholine and inorganic ions in single cells using a TOF-SIMS approach [116].

In the future, the generation of 3D molecular atlases can be employed to populate comprehensive molecular tissue biobanks, i.e. biological databases, for different tissue types. These atlases can be used to study local molecular changes involved in disease and therapy. Using e-science, grid or cloud technology these immense data volumes can be validated and made available to the biomedical research community for comparative studies. Tissue biobanks should be complemented with patient data, comprehensive proteomics data of tissue homogenates, microarray data and conventional histological images. This approach has the potential to generate new insights in diagnosis, development, treatment and prognosis of disease.

## 2.6 Ion Mobility: Adding the Shape of a Molecule

Alternate methods that are able to unravel the complexity of biochemical surfaces have become available to researchers in mass spectrometry imaging. It has already been established that cells, a tissue section, a tissue extract or a body fluid contain a huge amount of chemical and biological information. A single analytical method is usually insufficient when a better understanding of the function of these different biological systems is targeted. It has been illustrated how high mass resolution techniques can deal with this complexity. An alternate method is to add a gas phase separation technique to the MS imaging workflow. Hyphenated mass spectrometry techniques (e.g. LC-MS, gas chromatography (GC)-MS) are common in the analytical domain and are widely used for increased sensitivity and selectivity for biochemical analysis. Ion mobility spectrometry (IMS) combined with mass spectrometry imaging is one of these approaches that has the potential to provide direct insight in the shape, structure and position of biomolecules. The combination of mass spectrometry with ion mobility spectrometry has already proven an extremely successful technique for determining the structures of ions in gas phase as it allows the separation of different structural isomers [117, 118]. The addition of a molecular imaging component enhances the molecular detail provided [60].

MALDI-ion mobility MS brings an added value to MALDI-MS tissue imaging by the separation of different compound families such as lipids and proteins [59, 119].

The ion mobility cell, positioned between a quadrupole and a time-of-flight analyzer, allows the separation of structural isomers, or compounds with similar  $m/z$ , which cannot be separated by  $m/z$  only (due to TOF-instrument limitations). Different ion conformations have different collisional cross-sections and result in different drift times. This particular property is comparable to liquid chromatography separation and allows the separation and identification of chemical families such as matrix, drugs, lipids and singly or doubly charged peptide ions by their retention time inside the ion mobility cell. Stauber and co-workers [10] demonstrated the ability to separate isobaric ions with ion mobility prior to tandem MS in a MALDI imaging experiment. The fragmentation profiles of different ions enabled a database search with increased specificity by pooling fragments associated to only one parent. The comparison between Mascot scores [120] with and without drift time fragment pooling shows the power of the added IMS separation. Gas phase ion mobility separation is frequently used to separate small matrix ions and their clusters from tryptic peptides and lipids prior to tandem MS. However, signal depletion prohibits extensive tandem MS imaging experiments. This requires an efficient selection of relevant precursor ions that can be realized with ion mobility separation. For example only tryptic peptide ions can be selected for fragmentation when protein identification is targeted in an imaging experiment [121].

The SYNAPT HDMS (Waters Corporation, Milford, USA) is one of the widely implemented ion mobility instruments with MSI capabilities. This instrument has a quadrupole orthogonal acceleration TOF geometry and is equipped with a traveling wave (the so-called T-wave) ion mobility device located between the quadrupole and the TOF analyzer. The ion mobility separator used consists of three consecutive traveling wave regions. The first traveling wave (trap) is used to store ions when IMS is performed, to maximize the duty cycle of the IMS. The next traveling wave section is the actual ion mobility separation device. The final traveling wave device (transfer) is used to transfer ions from the ion mobility separator to the TOF mass analyzer maintaining the ions' separation. Collision induced dissociation (CID) can be achieved in either the trap or transfer T-wave or in both. The instrument is equipped with an interchangeable MALDI source, which can be replaced with atmospheric ionization (AI) sources, such as electrospray ionization (ESI) or atmospheric pressure chemical ionization (APCI). This configuration allows for a variety of atmospheric and in-vacuum MSI experiments. MALDI is performed in an intermediate-pressure environment ( $9 \cdot 10^{-2}$  mbar) using a frequency-tripled Nd:YAG laser (355 nm). Imaging data are obtained in the microprobe mode with a typical resolution of  $80 \mu\text{m}$ . The time per pixel, pertaining to the throughput for MS imaging, is similar to that in conventional TOF-based imaging experiment. The increased dynamic range stems from the fact that per laser shot multiple orthogonal TOF-spectra are acquired following

ion mobility separation.

MALDI-IMS MSI has the ability to improve the imaging of some drugs, metabolites, lipids and peptides by separating such ions from endogenous or matrix-related isobaric ions. It has been applied in variety of studies ranging from whole body imaging of drug dosed rats to imaging signaling proteins in oncological studies [20, 121].

## 2.7 Summary

The ideal or perfect mass spectrometry imaging experiment on tissue can still not be performed as a result of several limitations in spatial resolution, molecular identification capabilities and speed/throughput. In this chapter, we have shown several technological innovations that address these hurdles towards the perfect mass microscope. All of the innovations improve a specific aspect of the MSI workflow described in Figure 2.1. As such, the insight in the molecular organization of molecules on tissue surfaces is drastically improved. Having stated this, it is also clear that it is very difficult to integrate all of the innovations discussed in one single instrument. This implies an intrinsic need for multimodal imaging experiments, in which different molecular detail is brought together. This in turn defines a need for more and improved bioinformatics tools that can integrate and validate this multimodal data. This will, in our opinion, be one of the major areas of innovation for the years to come.

# 3

## Detection and Imaging Systems for Ions, Electrons and Photons

*Instrumental developments for imaging and individual particle detection for biomolecular mass spectrometry (imaging) and fundamental atomic and molecular physics studies are reviewed. Ion counting detectors, array detection systems and high mass detectors for mass spectrometry (imaging) are treated. State-of-the-art detection systems for multidimensional ion, electron and photon detection are highlighted. Their application and performance in three different imaging modes -integrated, selected and spectral image detection- is highlighted. Electro-optical and microchannel plate-based systems are contrasted. The analytical capabilities of solid state pixel detectors -both charge-coupled device (CCD) and complementary metal-oxide-semiconductor (CMOS) chips- are introduced. The Medipix/Timepix detector family is described as an example of a CMOS hybrid active pixel sensor. Alternative imaging methods for particle detection and their potential for future applications are investigated.*

### 3.1 Introduction to Sensors and Detectors

Webster's New World Dictionary defines a sensor as a "device to detect, measure, or record physical phenomena (...)" [122]. However, the definition of what exactly distinguishes a sensor from a detector is often not clear cut and the concepts "sensor", "detector", "sensor system" and "detector system" are used interchangeably in literature. The part of the system that actually "interacts" with the parameter of interest and transforms it into a measurable quantity is generally referred to as a transducer. Hence, transducers are part of a more complex sensor/detector system. The sensor or detector measures the "transduced" parameter and converts it into an electrical signal which can be read by an instrument or user.

Sensor and detector systems form an integral part of our lives on planet Earth.

Every living organism is equipped with thousands of highly complex biological sensors that cover a wide range of functionality. Sound, light, motion, temperature, humidity, toxins, glucose levels and pheromones are only few quantities that sensors in living organisms can be sensitive to. These sensors measure a specific parameter and convert the acquired information into a signal that the organism can process further.

Similarly, humans have developed electronic sensor and detector systems which are designed to measure a specific parameter. Also here, the measurement outcome is converted into a signal which can be recorded for further processing and/or analysis.

Measurement instruments are deeply engrained into our western-world daily lives. Many of us cannot imagine living without fever thermometers, motion-sensors, central heating thermostats, television remote controls, digital photo cameras, medical imaging equipment for X-ray absorption and computed tomography scans, to only name few examples.

Many of those “daily life” sensor and detection systems have originally been developed for scientific research. Only later they were spun-off as user products. Applied and fundamental physics research are active areas of sensor and detector instrumentation development. In these disciplines, dedicated systems are developed for a specific experiment or application field. In this way, the detection system is maximally sensitive to the parameter of interest.

The development of instrumentation for imaging and individual particle detection has progressed tremendously over the past decades. In biomolecular mass spectrometry imaging and fundamental atomic and molecular physics studies, such detection systems register ions, electrons and photons among other particles. The (charged) particle detectors in these fields are mainly instruments which detect, identify or track particles. They measure quantities as the particle energy, the impact position, the particle charge, the intensity of particles etc. The state-of-the-art ion, electron and photon detection and imaging technology, specifically applied in the areas of mass spectrometry (MS), mass spectrometry imaging (MSI) and atomic and molecular physics research, will be introduced in this chapter.

## 3.2 Selected Sensor and Detector Technology for Mass Spectrometry

This section highlights two examples of the most important detection systems which are employed for the detection of charged particles in mass spectrometers: array detectors and high mass detection systems. This section does not attempt to give an in-detail, historic overview of mass spectrometry detectors, rather it

emphasizes few detection systems, which are in frequent use in mass spectrometry today and/or are potential detection systems for mass spectrometry imaging.

### 3.2.1 Array Detectors

Array detectors are traditionally used to record the spatial distribution of a variety of particles, ranging from photons, to subatomic particles, atoms and ions. In mass spectrometry, array detectors are used for the simultaneous detection of multiple ions of different mass-to-charge ratio values. Hence, detector arrays improve the detection limits and measurement precision [123, 124]. They reduce the sample consumption and increase the instrument's duty cycle [123, 124]. Array detectors are a particularly interesting group of detection systems since they are both relevant to MS and MSI research.

#### Microchannel Plate Detectors

A microchannel plate [125] is a thinly sliced plate that consists of several millions of parallel, small diameter, conductive glass tubes which have been fused together. Typical pore diameters are 10-100  $\mu\text{m}$  and channel length-to-diameter ratios are 40-100. The channel axes typically assume a small angle ( $<10^\circ$ ) with respect to the normal to the MCP surface to enhance primary particle detection. A bias voltage is applied across the plate(s). When a primary particle hits the wall of a MCP channel, it liberates secondary electrons. Similar to the working mechanism of a photomultiplier, these electrons free more electrons in turn. Each channel works as an independent secondary electron multiplier. Figure 3.1 shows a schematic representation of a microchannel plate.

A single microchannel plate typically has a gain of  $10^4$ . When higher gains are used, instability and "ion feedback" are observed, i.e. atoms inside the channels are ionized and travel in the opposite direction as the electron avalanche. For higher gains, MCPs are typically arranged in a chevron stack of two plates or a Z-stack of three plates, which translate a single ionizing particle at the frontside of the MCP into a multi-million electron shower (gains  $>10^6$ ) at the backside of the MCP. MCPs have a fill factor, i.e. the ratio of the open pore area to the total MCP area, of about 70-80%. As a result, any detection system in combination with a MCP cannot reach unit detection efficiency. However, it is advantageous if the second detector stage is capable of registering the full particle load exiting the MCP.

Many detection systems for both mass spectrometry and mass spectrometry imaging are based on MCPs. The MCP is used as a conversion/amplification medium [125] which translates a single ion event into a measurable signal. MCPs can be sensitive to electrons, ions, photons (in the ultraviolet (UV) and soft X-rays) and neutrons (possibly in combination with an enhancing coating) etc.

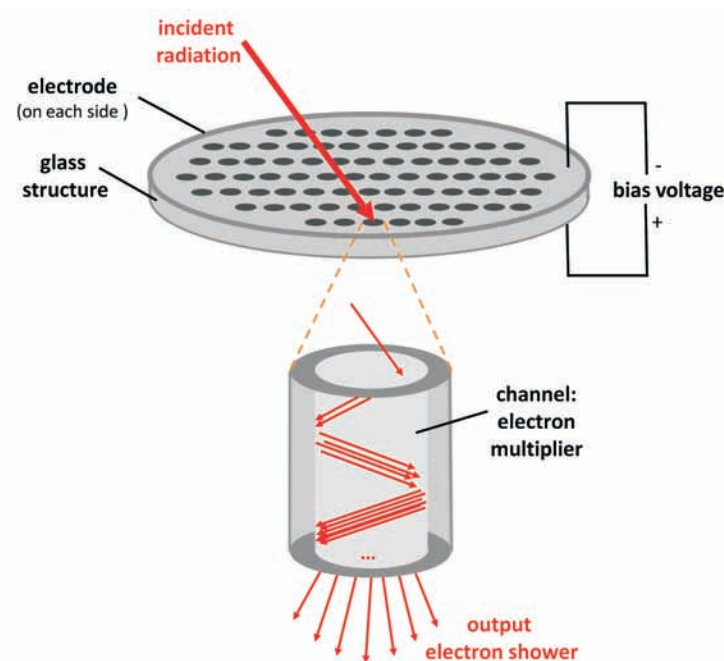


Figure 3.1: Schematic representation of a microchannel plate. A chevron or a Z-stack of MCPs consists of two or three such plates, respectively. The dimensions of the output electron shower depend on the MCP bias voltage (*i.e.* the gain of the plates), the channel diameter and length, the channel bias angle and the distance between the MCP backside and the electron-receiving detection system [126].

Due to their fast response, MCPs can be used for time-of-flight (TOF)-MS measurements in combination with a time-to-digital converter (TDC) where timing resolutions on the order of tens of picoseconds have been realized [79]. In addition, the large MCP area enables the integration of many counts on the detection system. However, MCPs are also often used in combination with a second detector system, both for MS and MSI. Examples include electro-optical imaging detectors and charge-division detectors. These detection systems are also used in MSI and are therefore treated in section 3.3.2. In MS research, MCPs have also been combined with capacitively-coupled detectors and discrete-anode array detectors, which are not covered in this chapter.

As other detection systems which rely on translating particle momentum into a particle count, a limitation of MCPs in MS is the so-called “high-mass roll-off”

of the detector. In a MCP, the ion detection depends on the generation of secondary electrons. The generation of a secondary electron avalanche proportional to the velocity of the incoming particle. As all particles in a TOF-MS are given the same kinetic energy theoretically, high mass ions will impinge on the detector with a relatively low velocity/momentum. Hence, they deposit insufficient energy to create an electron shower. The high mass ions are not detected. The limitations associated with MCPs in imaging experiments are covered in section 3.3.2. Detection systems for high mass ions are described in section 3.2.2.

MCPs are often used as an amplification/conversion stage in the detection process. They are then combined with a second detector stage. Such combinations are mainly used in imaging applications. MCPs are generally well understood and characterized detectors. They are not covered in further detail here. The interested reader is referred to references [123, 124], which cite some 20 publications that document MCP characteristics and performance in several experimental conditions.

### 3.2.2 High Mass Detection Systems

This section highlights selected high mass detection systems for mass spectrometry. In particular, the Covalx HM high mass detection system for macromolecular ions up to 1.2 MDa is described. In addition, cryogenic detectors based on superconducting tunnel junctions, calorimeters/bolometers and recently developed superconducting nanostripline detectors/nanomembrane detectors are introduced.

#### The Covalx HM High Mass Detection System

The Covalx HM high mass detection system (Covalx, Zürich, Switzerland) provides an alternative detection method that circumvents the high-mass roll-off [127, 128]. The Covalx HM uses conversion dynode technology, which enables the detection of macromolecular ions up to 1.2 MDa at nanomolar sensitivity. This ion conversion detector system increases the sensitivity to detect higher mass ions by colliding the ions of interest with a conversion dynode array. The conversion dynode transforms the initial (macromolecular) ions into smaller “secondary” ions, which are accelerated towards a secondary electron multiplier. Due to their higher velocity, the accelerated “secondary” ions are detected with a higher sensitivity than the initial ions would be. Van Remoortere and co-workers have employed the Covalx HM system for MALDI-TOF mass spectrometry imaging and profiling of proteins from tissue up to 70 kDa and 110 kDa, respectively [128]. Seyfried and co-workers employed the Covalx HM detector on a linear MALDI-TOF MS instrument for the analysis of PEGylated (glyco)proteins in the range of 60-600 kDa [129]. They compared the performance of the Covalx to a standard secondary electron multiplier (SEM) detection system. They concluded that the

Covalex HM shows significantly better performance in the mass range above 100 kDa, while the standard SEM outperforms the Covalex HM for protein analysis in the low mass range due to a better signal-to-noise ratio.

### **Cryogenic/Bolometric Detectors for High-Mass Ion Detection**

Cryogenic detectors [62, 130–132] involve a detection mechanism at low, sub-Kelvin, temperatures. Cryodetectors are particularly useful for the detection of high-mass (hundreds of kDa) macromolecular ions which cannot be registered with most other detection systems as, for instance, MCPs due to the detector roll-off at high masses. In a time-of-flight mass spectrometer, all ions are given the same kinetic energy on the order of 5–30 keV. Due to their high mass, macromolecular ions impinge on the detector with a relatively low velocity/momentum. They remain “unseen” by most detection systems since they do not liberate sufficient charge carriers within the detection medium. Cryogenic detection systems have a mass-independent response. They detect slow-moving particles with near unit efficiency. In addition, they cannot only detect the arrival of the ion on the detector but they can also measure the energy deposited by the impinging biomolecule. The kinetic energy of the ion is directly proportional to its charge state  $z$ . Therefore, the energy measurement can be used to identify the charge state of the ion. This is particularly interesting in TOF-MS, where the TOF is proportional to the mass-to-charge ratio  $m/z$  of the ion. Hence, the singly charged monomer, doubly charged dimer and triply charged trimer etc have the same  $m/z$  ratio and cannot be distinguished solely by the TOF.

One type of cryogenic detector are superconducting tunnel junctions. In this system, charge carriers (quasi-particles) are excited across a meV energy gap similar to electron-hole pair generation in a semiconductor material. The current of charge carriers is registered as the arrival signal. The number of created excitations is proportional to absorbed energy. The macromizer (Comet AG, Flamatt, Switzerland) is a commercial cryogenic detection system based on superconducting tunnel junctions. Zenobi and co-workers have demonstrated the analysis of megadalton ions (>500 kDa) on a MALDI TOF-MS using the macromizer [133]. The molecular protein characterization of human plasma lipoproteins using the macromizer was shown by Heller and co-workers [134].

Another type of cryodetectors are calorimeters and bolometer based on superconducting thermometers. In these detection systems the macromolecular ion is received in an absorber material. The particle’s kinetic energy is converted into an increase of temperature which is measured by temperature transducer. Similar to superconducting tunnel junctions, the high-mass ions’ arrival is registered and their kinetic energy is measured.

Recently, high-mass ion detection has been demonstrated with superconducting nanostripline detectors (SSLDs) [135, 136]. These detection systems comprise

a number of narrow (hundreds of nanometers), thin (few nanometers) superconducting Niobium nanowires arranged in a parallel configuration. Zen and co-workers have demonstrated the detection of macromolecular ions up to 132 kDa with such a detection system [135]. Advantages of the SSLDs are the sub-nanosecond response time (as compared to several tens of nanoseconds in superconducting tunnel junctions) and the relatively higher operational temperature of 4.2 K instead of 0.3 K.

Another novel development for high mass ion detection are mechanical nanomembrane detectors for time-of-flight MS [137]. These detection systems consist of a nanomembrane, an extraction electrode, a microchannel plate and an anode. Ion impacts excite mechanical vibrations in the nanomembrane. These oscillations are detected on the MCP/anode by time-dependent field emission of electrons from the vibrating membrane. MALDI TOF-MS on proteins up to 150 kDa has been demonstrated with this system.

### 3.2.3 Mass Spectrometry + Imaging

In mass spectrometry, array detectors [123, 124] have proven the capability to simultaneously detect multiple ions of different mass-to-charge ratio values. This bears the advantages of increasing the detection limits and the measurement precision, and it increases the instrument's duty cycle [123].

Besides these advantages, sample-correlated, position-sensitive detection can introduce another dimension of experimental information to a mass spectrometric measurement. In particular, mass spectrometry imaging merges the benefits of analyte identification by mass spectrometry with the localization information from projecting sample analytes on a position-sensitive detector. In this way, MSI provides the capability to identify analytes of interest and localize them in the "context" of their functionality on a sample surface. Many techniques have been developed for MSI [3, 138] (Chapter 2). Position-sensitive detector technology dedicated to MSI (and related techniques) is treated in section 3.3.

## 3.3 State-of-the-Art in Multi-Dimensional Imaging and Detection

### 3.3.1 Different Modes of Imaging and Particle Detection

This section describes state-of-the-art multi-dimensional ion, electron, photon imaging and detection in mass spectrometry imaging, atomic and molecular physics and related areas. It is important to distinguish between different modes of imaging and particle detection since every application has its distinct requirements on what information is to be extracted from the detection of the ions, elec-

trons, or photons. The information recorded in the different imaging/detection modes differs significantly, even though all modes rely on the detection of individual particle events. Figure 3.2 gives an overview of the different modes of detection.

### **Integrated Image Detection**

Imaging typically involves the (untriggered) accumulation of particle counts on the detector or the integration of particle counts from multiple image acquisitions. The acquired image gives information on the spatial distribution of the particles. The intensity distribution of registered events provides detail on the relative quantity of particles.

Medical X-ray or computed tomography (CT) imaging rely on this type of image acquisition. Also, a “total ion image” in mass spectrometry imaging, i.e. an image of the full ion current, is accumulated in this way. Besides the particle intensity, other quantities as, for instance, the particle velocity, momentum or energy may be extracted from such images in dedicated experiments in which the specific projection method and reconstruction algorithm allow the correlation of image features with these quantities. An example of such a technique is velocity map imaging (VMI) [4, 5] which is employed in fundamental atomic and molecular physics studies. Another example is a laser beam profile measurement where the spatial distribution of the beam intensity is measured with a position-sensitive detector. Hyperspectral imaging is another technique which makes use of integrated image detection. In hyperspectral imaging, objects are investigated by illuminating them with a wide range of optical wavelengths. Depending on its composition, the object under investigation reflects these wavelengths in a characteristic way such that a position-sensitive sensor records a spectroscopic signature of several spectral bands.

### **Selected Image Detection**

A specific, selected part of an event distribution is imaged by gating the detection system or by deflecting particles from reaching the detector, i.e. part of the “spectrum” of information is collected. In this imaging method, the particle selection or detector gating is triggered with respect to the origin of the event creation.

For example, it is desirable to image a selected part of an event distribution in microscope mode MSI [6]. Here, the total ion current can be measured without  $m/z$ -specific localization on the sample during one acquisition (“integrated image detection” as described in the previous section). Or alternatively, a particular  $m/z$ -species can be selected to pass to the detector by a pair of fast-switching electrodes. The combination of several mass-selected images from separate mea-

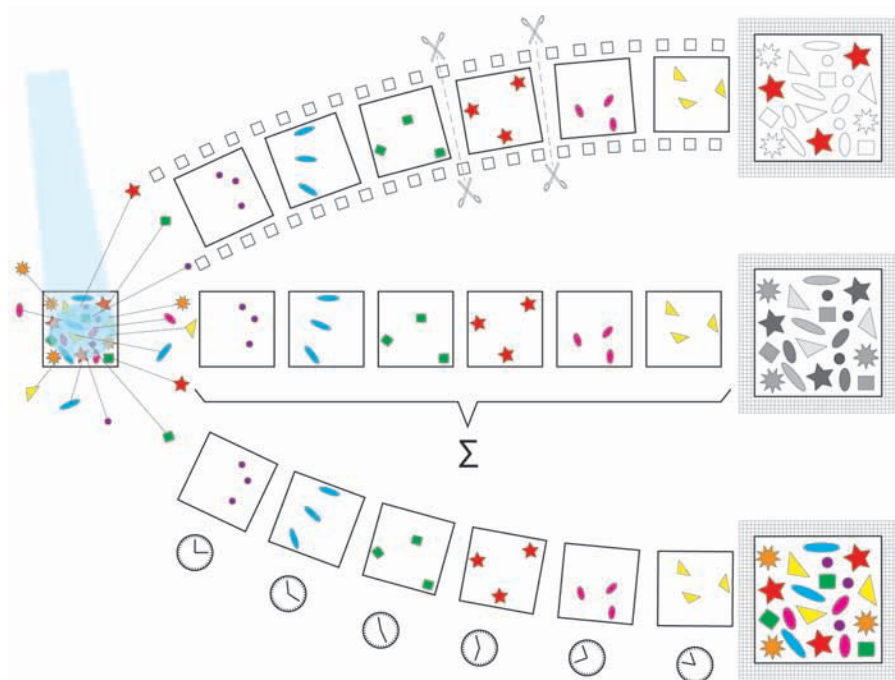


Figure 3.2: Overview of the three different modes of imaging and particle detection: integrated image detection, selected image detection and spectral image detection. The differences between the three imaging modes is illustrated with the example of time-of-flight mass spectrometry imaging. On the left hand side, the sample is ablated with a surface probe. Ions are generated. The ions are sent through a TOF spectrometer, in which they are mass separated. Different mass ions travel behind one another as "molecular images". In integrated image detection (middle), the total ion current is received on the imaging detector. Different masses cannot be distinguished in the image. In selected image detection (top), part of the ion cloud is selected and the localization of this particular mass on the imaging detector is registered. In spectral image detection (bottom), the detection system precisely registers the arrival time and the arrival position of each mass.

measurements then gives information on the sample composition and according spatial distribution. This detection approach allows the successive localization of selected  $m/z$ -species. However, it bears the disadvantage of time-consuming, highly repetitive measurements on quickly depleting (biological) samples.

Another example of gated imaging is “slice imaging” [139–141], a variant of VMI. In slice imaging, the detection is restricted to particles with a specific time-of-flight by rapidly gating the detector. This allows one to exclude all particles from the measurement that have a non-zero velocity component perpendicular to the detector plane, i.e. this method images the “center slice” of the reaction sphere. By measuring the ion distribution of interest directly, slice imaging does not require a mathematical reconstruction of this distribution from the total ion distribution. Therefore, slice imaging is a time-efficient and convenient alternative to VMI.

### Spectral Image Detection

The detection of individual particles typically involves the triggered and precise registration of the particle’s impact position and its arrival time.

Time-of-flight mass spectrometry imaging identifies ions by measuring the individual ion’s time-of-flight with respect to an external trigger and localizes them by registering their position on the detector. The time- and position-sensitive detection of individual ions enables identification and localization of the full ion load in one experiment (contrary to the (gated) imaging) at sufficiently low count rates.

In fundamental atomic and molecular physics research, cold target recoil ion momentum spectroscopy (COLTRIMS) in “reaction microscopes” [142–144] coincidentally measure the vector momenta of several ions and electrons from an induced atomic or molecular reaction. A combination of electric and magnetic fields guides all emitted ions and electrons to opposite time- and position-sensitive detectors. The position of impact, the time-of-flight and the measurement geometry enable the reconstruction of the particles’ trajectories and the reconstruction of their initial momenta, which enables fundamental insight into the nature of these reactions.

The imaging atom probe is the imaging variant of the atom probe field ion microscope [145, 146]. In an imaging atom probe setup, a position- and time-sensitive detector is placed at a distance of several centimeters from the tip. The detection system identifies the sample particles from the tip by time-of-flight mass spectrometry. The imaging ion probe also provides information on the localization of the analytes within the sample by projecting the particles on the position-sensitive detector while retaining the spatial information from the sample surface. Specifically, the imaging atom probe is used to identify different species and their distribution on a crystal surface. Note, that early imaging atom probes were op-

erated in detector gating mode. The identification and localization of individual particles on the atom probe tip provides the possibility of depth profiling and three-dimensional sample reconstruction, i.e. atom-probe tomography.

The choice of detection system and imaging/detection method largely depends on the mode of imaging or particle detection that a particular application requires. Additionally, considerations as the measurement conditions (gas pressure, temperature, chemical environment etc), practicability and system handling may play a significant role in the choice of detection system.

### 3.3.2 State-of-the-Art Imaging/Particle Detection Systems

State-of-the art particle imaging and detection systems currently include electro-optical image detectors, i.e. microchannel plates in combination with a photon detector. In addition, there are charge division detectors such as MCP detectors in combination with a resistive anode, delay-line detector (DLD), a shaped or a cross-strip anode (XSA), or a hybrid active pixel detector (HAPS). Hybrid active pixel detectors are often combined with a semiconductor sensor layer or a gaseous particle conversion medium. Therefore, they do not necessarily require to be combined with a MCP if the particle energy is sufficiently high (section 3.5).

For imaging applications, the spatial resolution obtainable with an MCP is particularly relevant. Here, it should be noted that the spatial resolution in such a detector depends on the spread of the electron cloud exiting the MCP backside, and if applicable the element size of the detection system. The dimensions of this electron cloud depend on the distance between the MCP backside and the secondary detection stage, the potential between these two detection stages, the pore bias angle, and the pores size [126]. The use of a microchannel plate (stack) intrinsically limits the spatial resolution of the detection system due to the dimensions of the pore size. Additionally, the ion-electron shower conversion introduces uncertainty to the impact position information. Most electrons stay within one channel of the MCP. However, the electron shower can spread from one to several MCP pores when the electron avalanche transfers from the first, to the second and possibly third MCP plate. This effect can be partially corrected for using centroiding algorithms. Ultra-high spatial resolution has been realized using MCPs in combination with a segmented second detector by means of centroiding algorithms [94, 147, 148].

#### **Electro-Optical Imaging Detectors: MCP + Photon detector**

Generally, photon detectors convert the MCP electron shower into a photon signal. The electron-to-photon conversion is typically performed in a phosphor

screen or a scintillation crystal. The photons are then collected by a photo-sensitive detector as, for instance, a photo-plate [149], an array of photo-diodes [150–152], a Vidicon camera system [153] or a charge-coupled device (CCD) camera. Electro-optical imaging detectors used for MSI are MCP, phosphor screen, CCD camera systems, which are described below. For details on the other systems, the reader is referred to the references [149–152].

**Phosphor screens & CCD cameras.** A phosphor screen is a thin plate of phosphorus material. Different types of phosphor screens are available, which differ in their emission spectrum and their fluorescence lifetime. In a MCP, phosphor screen, CCD camera combination (Figure 3.3), the electron cloud from the MCP backside is accelerated towards the phosphor screen. The phosphor screen converts the electron signal into photons. The electron-photon conversion factor depends on the phosphor material and the kinetic energy of the electrons. It is typically 20-200 photons per electron. It is possible to coat the backside of the phosphor screen with an aluminum layer to increase the number of photons that are emitted towards the CCD camera [154]. CCD cameras are described in detail in section 3.4.1 on solid state pixel detectors.

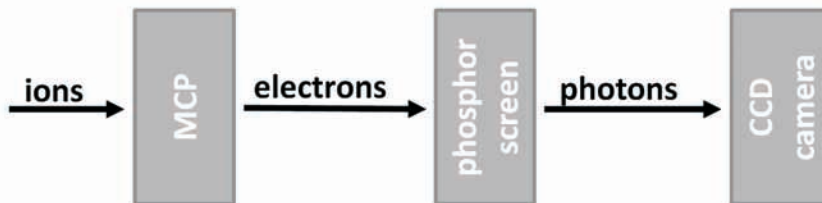


Figure 3.3: Schematic representation of the signal flow in a MCP, phosphor screen, CCD camera detection system.

### MCP in Combination with a Charge Division Detector

In charge division detectors, the electron shower from the MCP is collected by an anode array, which divides the charge among several of its elements. Examples of charge division detectors are resistive anodes, delay-line anodes, shaped-anodes, cross-strip anodes and hybrid active pixel detectors.

**Resistive anode encoders.** A resistive anode encoder detections system [155–157], for secondary ion mass spectrometry, ion microscopy and other applications [156, 157], typically consists of a chevron MCP behind which a resistive anode

is mounted. When an electron cloud from the MCP is hitting the anode plane, a current is delivered to each corner of the anode, typically four corners. The electrodes at the corners of the anode plane are each capacitively coupled to a charge-sensitive preamplifier. The x- and y-position of the event can be computed from the amount of current flowing in each of the four corner electrodes. An advantage of resistive anode encoders is the simplicity of both the detector itself and the electronics. A major disadvantage of resistive anodes is their inability to distinguish simultaneous events. Count rates in excess of 600 kHz are inaccessible.

**Delay-line detectors (DLD).** A delay-line detector is a two-dimensional, position- and time-sensitive detection system. There are two major classes of delay-line systems. A crossed delay-line detectors consists of two orthogonal anodes (Figure 3.4). A hexanode delay-line system [80, 158, 159] comprises three groups of two wires which are setup at a  $120^\circ$  angle with respect to one another. In a delay-line system, the particles which are to be detected impinge on the two-dimensional detector plane. They induce a signal on the delay-line wires, which will travel towards both ends of the wires. The arrival of the two signal pulses at the end of the wire is registered and the difference in arrival time is measured. Since both signal pulses propagate the wire at the same speed, the difference in

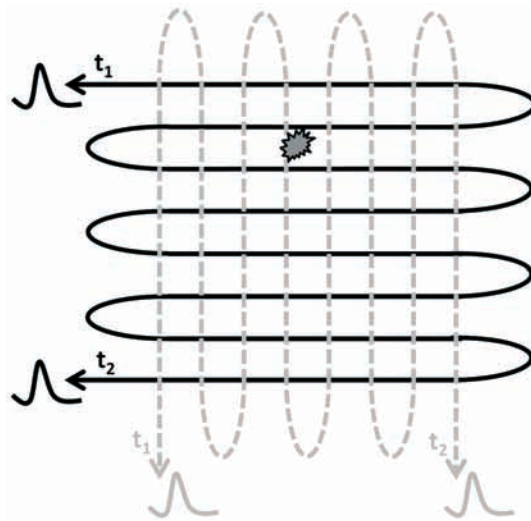


Figure 3.4: Schematic representation of a crossed delay-line detector.

arrival time indicates which distance they have travelled and hence where the particle has impinged on the detector plane. In a crossed delay-line assembly, the position of particle impact is determined from two orthogonal delay-lines. Multiple, (nearly) simultaneous hits cannot unambiguously be reconstructed from a two-wire assembly. A hexanode delay-line system is capable of unambiguously distinguishing few simultaneous events because the three delay-line wires introduce measurement redundancy [80, 158, 159]. The measurement redundancy reduces the “dead area” of the position-sensitive detection system after each event, which originates from the timing electronics’ dead time. Often, each of the three “wires” consists of a pair of wires, hence the name “hexanode”, in a Lecher-line configuration. Such a differential signal line provides almost background free signals by transmitting high frequency signals with low damping and dispersion. The pulses from the delay-lines are typically (pre)amplified, pass a constant-fraction discriminator (CFD) and are then time-stamped by a high timing resolution, on the order of 25 ps, time-to-digital (TDC) converter. Signal reconstruction is necessary. Since the position of impact has to be retrieved from the timing measurements, the reconstruction of integrated images can be computationally involved and time-consuming particularly at high count rates.

***Shaped anodes.*** Shaped-anode detectors smartly provide high spatial resolution detection with a small number of individual, “shaped” detector elements. The original configuration is the so-called wedge- and-strip anode by Anger (Figure 3.5). The y-position is determined by wedge-shaped electrodes, which are obtained by dividing rectangular electrodes diagonally. The x-position is measured by rectangular electrodes, the “strips”, which vary in width across the array. All electrodes measure the deposited charge and the relative amount of charge deposited on the different wedges and strips indicates the central position of the MCP charge cloud. More sophisticated, simplified shaped-anode detectors have been developed [160, 161]. Spatial image resolutions better than 20  $\mu\text{m}$  [162, 163] have been reported. Distinguishing simultaneous events is problematic.

***Cross strip anodes (XSA).*** Two sets of orthogonal (“cross”) strips are deposited on a substrate layer [148, 164, 165]. The two layers of strips, the “x-fingers” and the “y-fingers”, are separated from one another by insulating strips. The area coverage of the detection system is close to unity. The signals from the fingers are typically preamplified, shaped, digitized and time-stamped. When an electron cloud impinges on the fingers of a XSA, the amount of signal detected on the x- and y-fingers enables the reconstruction of the event’s impact position.

***Hybrid active pixel sensors.*** Hybrid active pixel sensors (HAPS) are pixelated image sensors which are typically composed of an application-specific in-

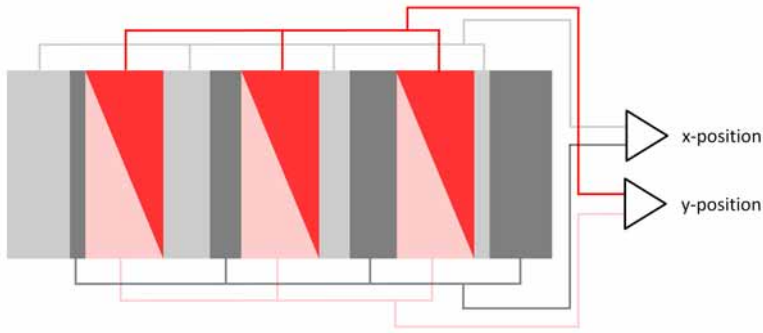


Figure 3.5: Wedge- and-strip anode as proposed by Anger.

tegrated circuit (ASIC) and a semiconductor substrate layer. Each ASIC pixel is connected to a cell of the semiconductor layer. “Active” pixel sensors contain much functionality on the pixel-level. In particular, each pixel has its own charge-to-voltage converter, often a (pre)amplifier, noise correction, discriminators or other digital signal treatment functionality. Hybrid active pixel sensors will be treated in detail in section 3.4.2.

### Areas of Application

Currently, MCPs in combination with crossed delay-line detectors or cross-strip anodes are used for imaging atom probe, COLTRIMS [144], mass spectrometry imaging experiments [72, 77], X-ray photoelectron spectroscopy (XPS) [166] and Auger photoelectron spectroscopy [167] for surface chemistry. The MCP, phosphor screen, CCD camera combination is used for microprobe mode MSI [6] and velocity map imaging experiments [5]. Pixelated detectors with a semiconductor sensor layer are used for velocity map imaging [81]. An MCP in combination with a bare pixelated detector is used for mass spectrometry imaging [70, 82, 83, 168].

### Performance Overview of MCP-Based Detection Systems

Table 3.1 gives an overview on which of the previously described detection systems can be operated in which particle imaging/detection mode. All detection systems are capable of untriggered image acquisition by particle counting and of gated imaging. Only the MCP in combination with the phosphor screen and CCD camera, the resistive anode encoder and the shaped anode cannot register the position and the time-of-flight of individual particles. The state-of-the-art performance of these detection systems and their limitations are discussed below.

Table 3.1: Imaging/particle detection systems versus different imaging modes.

	<b>Integrated Image Detection:</b> $(x, y, intensity)$ , untriggered	<b>Selected Image Detection:</b> $(x, y, intensity)$ , triggered & selective	<b>Spectral Image Detection:</b> $(x, y, tof)$
MCP + phosphor screen + CCD camera	Yes.	Yes.	No.
MCP + resistive anode encoder	Yes.	Yes.	No.
MCP + crossed delay-line detector	Yes.	Yes.	Indirect. <sup>1</sup>
MCP + hexanode delay-line detector	Yes.	Yes.	Indirect. <sup>1</sup>
MCP + shaped anode	Yes.	Yes.	No.
MCP + cross strip anode	Yes.	Yes.	Indirect. <sup>1</sup>
(MCP +) hybrid active pixel sensor	Yes.	Yes.	Direct.

Vallerga, Tremsin, Siegmund and co-workers of the *Space Science Laboratory* of the *University of Berkeley* have developed state-of-the-art detector technology for high spatial, high temporal resolution, high count rate detection of UV photons, electrons, neutrons and small ions. They developed detection systems composed of a MCP stack in combination with a crossed delay-line detector (XDLD) [169–171], a shaped anode [160], a cross strip anode [148], and a Medipix/Timepix ASIC [94, 147, 172, 173]. Table 3.2 compares the performance of these systems to each other and to a MCP in combination with a phosphor screen and a CCD camera [154], a MCP followed by a hexanode delay-line system [80, 158, 159], a MCP combined with a resistive anode encoder [155–157] and a shaped anode detector [160–163].

---

<sup>1</sup>Indirect spectral image detection via event reconstruction.

### 3.3.3 Performance Criteria for Detector Technology

Besides application-specific analytical performance, practical performance criteria play an important role in choosing an appropriate detection system for a particular application. Such criteria are, for instance, the available detector shape and size, the required operating environment (pressure, temperature, chemical requirements), the life time of the detection system, the required maintenance, the ease and cost of replacement. Analytical attributes for both imaging and individual particle detection include the detector noise, the maximum event count rates, the detector's dynamic range, the quantum efficiency, the detector stability and homogeneity, multihit capabilities, the detector response, recovery and readout time.

Most of these performance criteria are relevant to any application. However, depending on the quantities to be measured, some performance criteria are more stringent than others. In the integrated image detection mode and in the selected image detection mode, the (reconstructed) detector element size is one of the most important performance criteria since it is directly related to the lateral image resolution. In the spectral image detection mode ( $x, y, TOF$ ), both the position of impact and the time-of-flight of the particle have to be determined precisely. In terms of detector performance this translates into fine detector segmentation for unambiguous 2D position information, high time resolution measurements and high particle count rates. The performance criteria of three detection systems are compared for microscope mode mass spectrometry imaging in [138] (Chapter 2).

Table 3.2: Performance comparison between a MCP in combination with a phosphor screen and a CCD camera, a resistive anode encoder, a crossed delay-line, a hexanode delay-line, a shaped anode, a cross strip anode, and a hybrid active pixel sensor (HAPS) of the Medipix/Timepix (MPX/TPX) detector family.

Point of comparison	MCP + phosphor screen + CCD camera	MCP + resistive anode encoder	MCP + crossed delay-line detector	MCP + hexanode delay-line	MCP + shaped anode	MCP + cross strip anode	MCP + HAPS (MPX/TPX)
Detector	Phosphor screen, 1,000×1,000 pixels on CCD chip.	4 resistive anodes.	2 orthogonal wires.	3 wires at 120° to one another.	Matched electrodes in the shape of wedges and strips.	2×64 orthogonal wires.	256×256 pixels per chip.
# of MCP used	2	2	3	2	2	2	1 or 2 <sup>2</sup>
Diameter active area [mm]	40-70	25	40	70	25	40	28
Required MCP gain	10 <sup>6</sup>	10 <sup>6</sup>	10 <sup>7</sup>	10 <sup>7</sup>	10 <sup>5</sup> -10 <sup>7</sup>	10 <sup>6</sup>	10 <sup>4</sup> -10 <sup>5</sup>
# Amplifiers	1	4	4	6	≥6	128	65k
Spatial resolution [μm]	50-200	1-2	~17-50 FWHM	13	20	~10 FWHM	55 and 3-5 FWHM <sup>3</sup>

*Continued on next page*

<sup>2</sup>A chevron MCP stack is advantageous to prevent ion feedback through the MCP pores.

<sup>3</sup>The resolution is obtained in the Medipix and Time-over-threshold (TOT) mode, respectively. In TOT mode, the 3-5 μm resolution is achieved using a center-of-gravity centroiding algorithm. The ultimate spatial resolution is limited by the MCP pore size.

Table 3.2 – Continued from previous page

Point of comparison	MCP + phosphor + CCD camera	MCP + resistive anode encoder	MCP + crossed delay-line detector	MCP + hexanode delay-line	MCP + shaped anode	MCP + cross strip anode	MCP + HAPS (MPX/TPX)
Time resolution	1-33 ms <sup>4</sup>	N/A.	~130 ps-25 ns	25 ps	N/A.	~750 ps	10 ns
Maximum count rate	≤1 MHz <sup>5</sup>	600 kHz	1 MHz <sup>6</sup>	2 MHz	50 kHz	5 MHz	GHz in MPX mode, 1 MHz at high resolution <sup>7</sup>
Noise of detector	25 electrons	Electronic noise.	3000 electrons	Electronic noise.	Electronic noise.	1500 electrons	100 electrons
Typical achievable vacuum [mbar]	10 <sup>-9</sup>	10 <sup>-10</sup>	10 <sup>-10</sup>	10 <sup>-10</sup>	10 <sup>-10</sup>	10 <sup>-10</sup>	10 <sup>-7</sup>

<sup>4</sup>The time resolution is determined by the frame rate of the camera: Time resolution=1/frame rate. Typically, frame rates are between 30 frames/second and 1,000 frames/second.

<sup>5</sup>Limited by the decay time of the phosphor screen.

<sup>6</sup>This is an exceptionally high count rate.

<sup>7</sup>A typical cluster from the MCP spans about 5×5 pixels=25 pixels on the pixel detector. Typically, about 10% of the detector's pixels are used per frame, i.e. there are about 250 events per frame (=250 events×25 pixels/event=6,250 pixels used of 65k pixels). For a 2×2 chip assembly, there are 4×250 events=1,000 events per frame. The Berkeley readout runs at 1 kHz. Therefore, 1,000 events/frame×1,000 frames/second=1 million events/second=1 MHz.

## 3.4 Solid State Pixel Detectors

Throughout the last decade, solid state pixel detectors have been introduced to many areas of research and daily life. Solid state chips are widely used in applied and fundamental (physics) research experiments as well as daily life appliances like hand-held digital photo cameras and mobile phones. As the wide areas of application suggest, these chips are practical and cost-efficient detection systems. The following section highlights solid state pixel detectors systems in more detail and explains why they represent an interesting and valuable addition to the detector palette.

The individual detection elements of a solid state pixel detector are patterned as a checkerboard. Each element of the sensor is connected to a matching element of the readout electronics. The two layers are connected by, for instance, solder bumps. In this way, these hybrid detectors combine the sensor and the charge readout in a compact way. Each sensor pixel functions as a small “ionization chamber” [174], in which incident particles are converted into an electron-hole pair current. The pixel size is determined by the dimensions of the readout electronics. The dimensions of the readout electronics scale with the complexity and size of the circuitry on the pixel level. Today, pixel pitches of 10-100  $\mu\text{m}$  are practically accessible. Often, the readout chip extends beyond the semiconductor sensor. This “chip periphery” contains readout and control circuitry, and wire-bonds for external connections. Multiple chips can be tiled together to cover larger detection areas ( $>1 \text{ cm}^2$ ). The periphery of the chips constrain full area coverage of large chip arrays without dead spaces.

Currently, two major classes of pixel detectors are being used as image sensors: charge-coupled device (CCD) sensors and complementary metal-oxide-semiconductor (CMOS) chips [174]. The classic high-resolution pixel array detector is the CCD. CMOS chips are a more recent development. The functionality, working mechanism, requirements and constraints of CCD and CMOS chips are fundamentally different. Hence, the suitability to a specific application of one or the other highly depends on the application’s requirements.

### 3.4.1 Charge-Coupled Device

Since Boyle and Smith’s “Charge couple semiconductor devices” article in 1970 [2], the CCD has not only earned its inventors the Nobelprize (Nobelprize 2009 by the Royal Swedish Academy of Sciences, awarded “for the invention of an imaging semiconductor circuit -the CCD sensor” [175]) but it has also developed into the most widespread wafer-scale silicon detector. CCD imagers consists of a photoactive region (typically an epitaxial layer of silicon) and a transmission region, i.e. a shift register. When a particle impinges on the image sensor, a charge proportional to the energy of the particle is generated within the sensor

pixel. This charge charges a capacitor within the pixel. In a CCD chip, this charge is then transferred by shift registers from pixel-to-pixel along a pixel column, then column by column. The last pixel in the array transfers the charge to an amplifier (typically, one to few amplifiers for the entire pixel array) and a charge-to-voltage converter. Often, an analog buffering step is included. The information collected by the CCD chip is sent off the chip as an analog signal. Sampling and digitization is performed off-chip. A CCD chip is designed and optimized to move electrical charge between capacitive bins (from pixel-to-pixel). Since the charge has to be transferred over thousands of pixels, the charge transfer efficiency must be close to unity as not to lose sensitivity. Today, charge transfer is practically 100% efficient over about  $10^4$  pixels. The sequential pixel-to-pixel, column-to-column readout infers relatively long readout times which scale with the area of the pixel array. CCD readout pixels can be small ( $10 \times 10 \mu\text{m}^2$  pixels). They achieve full area coverage.

### 3.4.2 Complementary Metal-Oxide-Semiconductor

A CMOS chip is manufactured in the so-called CMOS technology for constructing integrated circuits. Among others, microprocessors, microcontrollers, ready-accessible memory (RAM) and many digital logic circuits are constructed in CMOS technology. Also analog circuits, like image sensors in digital cameras, can be CMOS technology based.

CMOS imagers are hybrid active pixel sensors (HAPS) or detectors. In hybrid pixel detectors, the sensor medium and the integrated circuit are processed on different substrates. The chip and the sensor are connected, i.e. hybridized, by fine pitch bump bonding and subsequent flip-chip attachment to a semiconductor sensor medium. Each ASIC (application-specific integrated circuit) readout pixel consists of two distinct parts: an active input region, i.e. the “sensitive input pad”, where an electron or hole current (generated in the semiconductor sensor layer, for instance) is received, and a logical circuitry region where the current signal is (pre)processed. Typically, the ratio of sensitive area to pixel area, i.e. the fill factor, is about 20-30%.

CMOS circuits contain both p-channel and n-channel metal-oxide-semiconductor field-effect transistors (MOSFETs) on the same substrate. In a transistor, the gate (input) is capacitively coupled to the output channel that is connected between the source and the drain electrodes. In a NMOS transistor, a conductive channel is formed when the input electrode is positively biased with respect to the channel. A PMOS transistor functions complementary. Here, a conductive channel is formed when the gate is biased negatively with respect to the source. By connecting the source and the drain of a PMOS and a NMOS transistor, respectively, the signal that switches on one will switch off the other. The combi-

nation of a NMOS and a PMOS transistor forms a complementary MOS (CMOS) circuit. Conveniently, both NMOS and PMOS inverters have a low static power consumption such that CMOS circuits draw no current in the high and the low state of the transistor. Since current only flows when the transistors are switching, CMOS transistors greatly reduce the power consumption in logic circuitry. In a CMOS chip, a lot of functionality can be located on the pixel level. The density of transistors per pixel is high, hence the name “active pixel detectors”. Typically, each pixel contains its own charge-to-voltage converter such that the charge deposited can be locally converted and digitized. Often, the pixel also comprises a (pre)amplifier, noise correction, discriminators or other digital signal treatment functionality. A CMOS chip outputs digital data in a predefined binary format.

### 3.4.3 The Differences: CCD versus CMOS

Figure 3.6 illustrates the difference between the detection of an event by a CCD or a CMOS chip. CCD imagers are typically more sensitive than CMOS imagers since their pixels are constructed for high quality charge transport. CMOS imagers contain more per-pixel-functionality and signal treatment efficiency. More functionality on the pixel level generally translates into more transistors and hence limits the minimum pixel size and sensitive (input pad) area. Unlike a CMOS chip, a CCD chip cannot provide any timing information on the individual particle events. A time stamp may be assigned to a particular image frame (containing multiple events) on the basis of the CCD frame rate of typically 0.01-1 kHz for standard commercial systems.

CMOS imagers can be readout faster than CCD sensors when use is made of their more parallel output structure. Concerning (readout) speed, CMOS sensors have the advantage that all camera functions can be placed on the chip. CMOS technology also enables windowing, i.e. the capability to selectively readout a portion of the image sensor. In CMOS technology, the pixel can in principle be designed to indicate the presence of a hit and to allow the selective readout of struck pixels. This increases the complexity of the pixel logic circuitry but enables higher frame rates for smaller regions of interest.

The responsivity, i.e. the amount of signal that the sensor delivers per unit of input energy, is slightly better in CMOS chips than in CCD chips since it is easier to place gain elements in a CMOS circuit. CCDs have a better image uniformity, i.e. the consistency of response for different pixels under identical illumination conditions, since the CMOS in-pixel amplifiers suffer from offset variation. CCD systems are not treated in further detail. Instead CMOS technology based systems will be focused on since the advantages of these hybrid active pixel detectors, in particular the highly parallel detection and the on-pixel functionality, offer in-

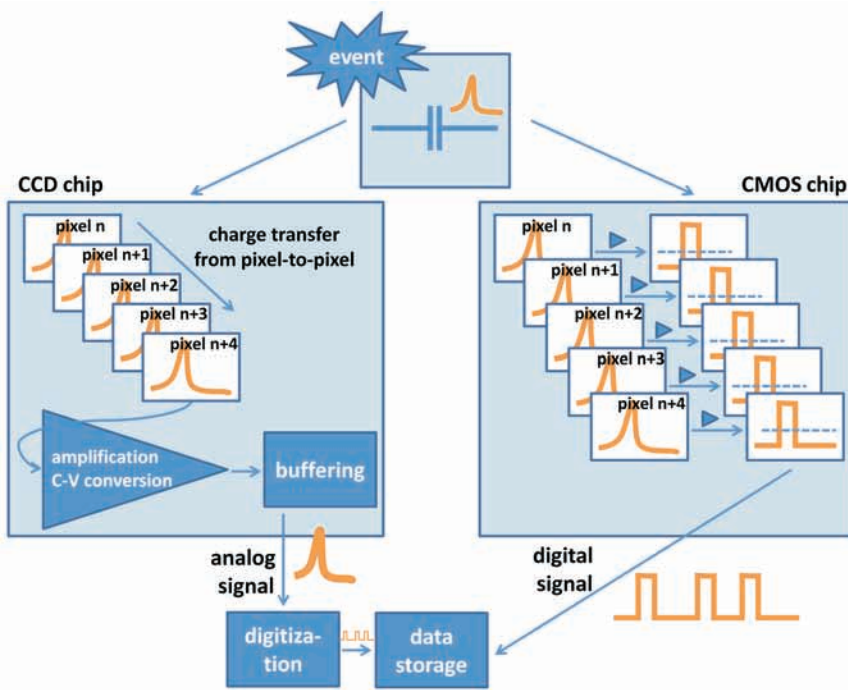


Figure 3.6: Event detection in a CCD chip versus a CMOS chip. For both detection systems, an electrical charge proportional to the particle energy deposited in the sensor is generated within the pixel. The deposited charge charges an in-pixel capacitor. In a CCD chip, the charge is then transferred by shift registers from pixel-to-pixel along a pixel column and an analog signal is sent off the chip. In a CMOS chip, there is significantly more functionality on the pixel level, i.e. the signal (pre)processing takes place in the pixel and a digital signal is sent off the chip.

interesting features for mass spectrometry imaging and fundamental atomic and molecular physics research.

Mass spectrometry imaging and fundamental atomic and molecular physics research has recently used the Medipix/Timepix CMOS detector family [70, 73, 81, 82]. The following section gives a “market overview” of a selected number of presently available and relevant CMOS imagers. These systems are contrasted to each other and to the Medipix/Timepix detector family.

### 3.4.4 CMOS Imagers Today: Medipix/Timepix versus Other Fast Pixelated Detectors

#### Available CMOS Systems

Many (CMOS) pixel imagers have originally been developed for high-energy particle physics applications but are now readily applied to a broader range of imaging applications [176–178]. Typically, detectors for high energy particle physics register individual, charged quanta of radiation with a relatively high spatial and time resolution. On the contrary, many classical imaging applications, like radiology (Medipix [84] and MPEC [179]) or crystallography at synchrotron light sources (XPAD [180–182], PILATUS [183] and EIGER [184]), accumulate untriggered particle events by integration or counting techniques, often with count rates in excess of 1 MHz per pixel (CT applications). The possibility to count individual particles and register extra information, as for instance the particle energy, greatly enhances the image contrast [185].

#### Single Photon Counting Detectors

At the present time, a variety of different CMOS active pixel detectors is available for imaging applications. Most of these detectors are single photon counting chips, which -with some adaptations- can also more generally be used as particle counting devices. A few examples have been selected for comparison to the Medipix 2 photon counting chip. There are other interesting CMOS active pixel detectors available. However, one or more of their specifications, as for instance the pixel size, the pixel matrix geometry, the operation temperature etc, are not suitable for the imaging applications discussed in this thesis and are therefore omitted. Therefore, we compare the Medipix 2 [84, 85, 186] and Medipix 3 [185, 186] chips with the PILATUS II chip [183], the EIGER chip [184], the XPAD3 chip [180–182] and the PImMS chip [168] (Table 3.3).

Table 3.3: Comparison between selected state-of-the-art single photon counting chips.

Feature	Medipix 2	Medipix 3	PILATUS II	EIGER	XPAD3	PImMS
Technology	0.25 $\mu\text{m}$ CMOS	0.13 $\mu\text{m}$ CMOS	0.25 $\mu\text{m}$ UMC <sup>8</sup>	0.25 $\mu\text{m}$ UMC <sup>8</sup>	0.25 $\mu\text{m}$ CMOS	CMOS
Single photon counting	Yes.	Yes. <sup>9</sup>	Yes.	Yes.	Yes.	Yes.
Pixel size [ $\mu\text{m} \times \mu\text{m}$ ]	55 $\times$ 55	55 $\times$ 55	172 $\times$ 172	75 $\times$ 75	130 $\times$ 130	70 $\times$ 70
Pixel array	256 $\times$ 256	256 $\times$ 256	60 $\times$ 97	256 $\times$ 256	80 $\times$ 120	512 $\times$ 512
Pixels/chip	65,536	65,536	5,820	65,536	9,600	262,144
Chip tiling [n=0,1,2,...]	2 $\times$ 2n	2 $\times$ 2n	2 $\times$ 8	2 $\times$ 8 <sup>10</sup>	7 $\times$ n	N/A. <sup>11</sup>
Typical sensor materials	Si, GaAs, CdTe, CdZnTe Ge	Si	Si	Si	Si, CdTe, GaAs, Shottky sensors	N/A.
Sensor sensitive thickness [mm]	0.15-0.3 (Si), 0.5 (GaAs), 1-2 (Cd(Zn)Te)	0.15-0.3 (Si), 0.5 (GaAs), 1-2 (Cd(Zn)Te)	0.32	0.3-0.5	0.5	N/A.
ENC <sup>12</sup> [electrons]	100	60-180 <sup>13</sup>	114	180	100-160	N/A.
Power dissipation per pixel [ $\mu\text{W}$ ]	15	9-15 <sup>14</sup>	10	12	40	30

Continued on next page

<sup>8</sup>UMC=United Microelectronics Corporation, Hsinchu, Taiwan.<sup>9</sup>There are different single photon counting modes: pitch versus spectroscopic mode, single pixel versus charge summing mode, low versus high gain mode.<sup>10</sup>A 2  $\times$  8 chip array forms a so-called module. Groups of  $\leq 4 \times 8$  modules can be tiled.<sup>11</sup>N/A.=During the writing of this thesis, no information on the particular parameter was available (yet) since these systems are still under development.<sup>12</sup>The ENC for chips with/without sensor is different (section 3.5). The numbers stated in the table give an indication of the ENC.<sup>13</sup>The ENC depends on the operation mode of the chip.<sup>14</sup>15  $\mu\text{W}$ /pixel (charge summing mode), 9  $\mu\text{W}$ / pixel (single pixel mode).

Table 3.3 – Continued from previous page

Feature	Medipix 2	Medipix 3	PILATUS II	EIGER	XPAD3	PImMS
Maximum number of frames/second <sup>15</sup>	500	1000	200-416	24k/12k/8k (4/8/12 bit mode)	200-300	20
Dead/readout time	1 ms	0 <sup>16</sup>	2.4 ms	3 $\mu$ s <sup>17</sup>	N/A.	N/A.
Counter depth [bits]	13	Configurable: 1, 4, 12, 24 <sup>18</sup>	20	Configurable: 4, 8, 12, 32 <sup>19</sup>	12 + overflow bit <sup>20</sup>	N/A.
Charge sharing between multiple pixels	Yes.	Limited. <sup>21</sup>	“not an issue”	Yes.	Yes.	N/A.
Online correction mechanisms	Bad pixel map.	Charge summing mode, bad pixel map.	Rate correction <sup>22</sup> , flat field correction, bad pixel map.	N/A.	No.	N/A.

<sup>15</sup>This number corresponds to the frame rate when the entire chip is readout.<sup>16</sup>Depending on the operation mode. In continuous readout mode, there is no dead time.<sup>17</sup>The frames are comparatively short because of the implemented double buffering. The next frame is acquired, while the previous frame is read out.<sup>18</sup>The bit depth is configurable to 1, 4, 12 bits in both the sequential and the continuous acquisition mode, and to 24 bits in sequential mode only.<sup>19</sup>The counter depth of 32 bits is a “virtual” counter depth. This is accessible if several images are summed on the readout control board. This is implemented to reduce the data throughput for long exposure times.<sup>20</sup>Measurements beyond the 12-bit register depth are enabled by the 13th bit, i.e. the overflow bit. The overflow bit registers how many times the register has been filled. Readout of the overflow bit and the measurement register takes place after the acquisition.<sup>21</sup>Here, the charge in every cluster of 4 pixels can be summed and assigned to the pixel with the largest charge on an event-by-event basis.<sup>22</sup>The rate correction depends on the energy and gain settings.

## CMOS Imagers with Timing Capabilities

Single photon counting chips do not have any timing capabilities on the pixel level. A time stamp can only be assigned to an acquired image from the camera's frame rate (typically  $<1$  kHz, time resolution  $\sim 1$  ms), similar to a CCD camera. Up to now, only few CMOS active pixel detectors with timing capabilities on the pixel level have been developed. Table 4 compares the Timepix [86] chip to the NA62 collaboration's timing chip [88–92].

Table 3.4 shows that the Timepix currently is the most obvious and practical choice for many imaging applications in mass spectrometry imaging, atomic and molecular physics research and beyond. The current Timepix chip already delivers a reasonable time resolution and the next generation of chips will improve this point significantly (section 3.5.1). Additionally, the pixel size, the large pixel matrix, the tileability to larger areas and the very high fill factor make the Timepix attractive. The NA62 chip, on the other hand, delivers an outstanding time resolution and measurement range for time-of-flight experiments. However, the large pixel size, the small pixel matrix and the cooling requirements make this chip less attractive for imaging applications.

There are few other ultra-high time resolution CMOS-based developments. Jansson and co-workers have designed an ultra-high time resolution CMOS circuit, which has a time resolution of 12.2 ps and measurement range of 204  $\mu$ s [187]. Another interesting development are the CMOS-based single photon avalanche diodes (SPADs) of Charbon and co-workers [188–190]. These detection devices achieve a time resolution down to 50 ps. However, the maximum measurement time is tens to hundreds of nanoseconds, which is insufficiently long for the time-of-flight mass spectrometry but are used for on-chip fluorescence detection and fluorescence lifetime imaging microscopy [191]. Additionally, the fill-factor of the SPADs is only 2% (up to 14% using microlenses) such that a full event coverage cannot be achieved with the detections system and high spatial resolution imaging is inaccessible.

Table 3.4: Comparison between two selected CMOS imagers with timing capabilities, the Timepix and the NA62 chips.

Feature	Timepix	NA62 chip
Technology	0.25 $\mu\text{m}$ CMOS	0.13 $\mu\text{m}$ CMOS
Counting modes	Event counting, time-of-flight, time-over-threshold.	Time-over-threshold, event counting (by counting TOT events), time-of-flight.
Pixel size [ $\mu\text{m}\times\mu\text{m}$ ]	55 $\times$ 55	300 $\times$ 300
Pixel array	256 $\times$ 256	45 $\times$ 40
Pixels/chip	65,536	1,800
Chip tiling [n=0,1,2,...]	2 $\times$ 2n	2 $\times$ 5
Typical sensor materials	Si	Si
Sensor sensitive thickness	300 $\mu\text{m}$	200 $\mu\text{m}$
ENC <sup>23</sup> [electrons]	100-113	130-185
Power dissipation/pixel	15 $\mu\text{W}$	1.8 mW
Maximum number of frames/second	30-50	$\sim$ 73 khits/s per pixel
Dead time/readout time	300 $\mu\text{s}$ /10 ms <sup>24</sup>	Per 5 pixels: 10 ns
Counter depth	13 bits	Infinite. <sup>25</sup>
ASIC binning time, i.e. time resolution	10 ns	100 ps
Charge sharing between multiple pixels	Yes.	Yes.
Online correction mechanisms	Bad pixel map.	No.
Field of view selection	No.	Yes, by masking a pixel it is taken off the data path and the data bandwidth is increased.

<sup>23</sup>The ENC for chips with/without sensor is different (see 3.5). The numbers stated in the table give an indication of the ENC.

<sup>24</sup>For a 100 MHz readout clock, the chip can be readout serially (all 32 CMOS lines in series) in 10 ms. When reading out the CMOS lines in parallel, the readout takes 300  $\mu\text{s}$ .

<sup>25</sup>The basic time bin is 100 ps. The dynamic range extends to 6.4  $\mu\text{s}$ . However, the chip is certainly readout within these 6.4  $\mu\text{s}$ . The readout electronics board keeps track of how many times 6.4  $\mu\text{s}$  are “filled” by events. In this mode of operation, there is no dead time and the counter depth is infinite.

## 3.5 The Medipix/Timepix Detector Family

### 3.5.1 Chips of the Medipix/Timepix Detector Family

The Medipix detector family is developed within the *Medipix collaboration* hosted by *CERN* [93]. Currently, the *Medipix collaboration* consists of about 20 collaborating institutes from all over the globe that work together on the development of the Medipix chips, readout interfaces and software packages for various applications ranging from high energy particle physics to medical X-ray imaging [186]. The chips of the Medipix detector family in combination with a detection medium -often a semiconductor like silicon bump-bonded on top- belong to a new class of hybrid pixel detectors. There are two distinct types of chips within the Medipix detector family: the Medipix single photon counting chips and the Timepix chips, which in addition to the single photon counting capabilities can also be set to measure the time-of-arrival of an event with respect to an external reference signal or to determine the amount of charge deposited per pixel. Thusfar, three generations of Medipix chips and one generation of the Timepix chip have been developed. Developments of new (variants of the) chips are ongoing. In MSI and atomic and molecular physics research, so far chips of the Medipix 2 [84–86] generation, i.e. the Medipix 2 and the Timepix chips, have been used. Table 3.5 compares all chips of the Medipix/Timepix detector family.

#### Medipix 1

The Medipix chip (or PCC, photon counting chip) [192] was originally designed for counting X-ray photons, without noise or dark current, at high particle fluxes (several gigaphotons/cm<sup>2</sup>/s). The Medipix 1 chip consists of 64×64 pixels with a pixel size of 170×170 μm<sup>2</sup>. Each of the identical pixels has a preamplifier, a discriminator and a 15-bit counter. The chip was bump-bonded to silicon (Si) and gallium-arsenide sensors (GaAs) for direct photon conversion and hence minimum image blurring.

#### Medipix 2

The Medipix 2 [84, 85] detector is the successor of the earlier Medipix 1 chip. The dimensions of a single Medipix chip are 1.4×1.6 cm<sup>2</sup> and the pixel matrix contains 256×256 pixels of 55×55 μm<sup>2</sup> each. The chips are three-side buttable so that chip arrays of 2×2n chips (n=1,2,...) can be tiled without dead space between the chips.

The Medipix 2 chips are typically combined with a semiconductor detection medium bump-bonded on top. Semiconductor materials are silicon, gallium-arsenide, cadmium telluride, cadmium-zinc-telluride or germanium depending on

the application of the detection system (section 3.5.2). Alternatively, a metal grid on insulating pillars can be suspended above the chip [193], a so-called micromegas [194]. The space between the ASIC and the grid is filled with an interaction gas, in which charge amplification occurs due to an electric field bias voltage. These systems are typically used as time-projection-chambers and will not be treated in further detail here.

Typically, a 300  $\mu\text{m}$  silicon sensor (lightly n-doped high-resistivity silicon with a p-type implant in every pixel) is bump-bonded on top of a Medipix chip. On the entrance side, the sensor layer is coated with an aluminum layer of about 150 nm. Through this Ohmic contact, the sensor material is biased by applying a voltage of about 100 V across the sensor. An electron or a hole current can be collected by the pixels. In silicon, every 3.6 eV of deposited energy creates one electron-hole pair. Hence, the amount of charges generated in the sensor material is directly proportional to the energy deposited by the impinging particle. With such a sensor layer, photons and electrons can efficiently be detected provided that the photon or electron kinetic energy exceeds the detection threshold of about 4-5 keV.

When used for X-ray and electron detection, the detection medium converts incident particles into electron-hole pairs, which induce a current in the charge-sensitive amplifier of the CMOS (complementary metal-oxide-semiconductor) readout chip. Ions will usually not be accelerated to sufficient energies to penetrate into the sensor layer. However, ions can be detected indirectly by placement of an MCP in front of the detector [73, 94]. The Medipix detector then registers the electron shower produced by each ion impact on the MCP. The particle counting properties consist of the ability to count events that generate a number of electron-hole pairs within a user-defined threshold/energy window. Each individual pixel comprises an analog and a digital part. The analog input stage consists of a preamplifier and two identical pulse height discriminators. These discriminators generate a digital pulse if the output of the preamplifier falls within a pre-defined energy window. These digital pulses increment a 13-bit pseudo random counter. A pseudo-random counter is a linear feedback shift register. In this type of shift register, each successive register value is generated by a feedback loop from the previous register value. Since all successive register values are predictable and known, these registers can be used as counters. Every register reading encodes a counter value. The shift register values can be converted into ordinary, decimal counter values via a look-up table. Pseudo-random counters are set up such that the combination of binary values in the register is always composed of roughly the same number of ones and zeros. This prevents rapid voltage changes when the counter value is incremented, which is desirable for densely packed electronic circuits like the Timepix chip. Other advantages are that pseudo-random counters are fast counters and that they can be implemented

in hardware.

The threshold energies that are chosen for the discriminator levels lie just above the noise levels of the pixels. Therefore, electronics noise free measurements are possible. Three additional adjustment bits can be used to equalize the pixel-to-pixel response over the full pixel array.

**Equivalent noise charge.** For both Medipix 2 and Timepix chips, the minimum detectable charge per pixel is given by the pixel's noise, i.e. by the "equivalent noise charge (ENC)" [195]. By convention, the minimum charge required to trigger an above-pixel-noise signal is set to  $6 \cdot \text{ENC}$ . The ENC per pixel was determined to be 100 electrons for a bare chip and 113 electrons for a chip bump-bonded to a  $300 \mu\text{m}$  silicon sensor layer. Thus, the minimum detectable charge is approximately 600 electrons for a bare chip pixel and approximately 678 electrons for a chip pixel with a  $300 \mu\text{m}$  silicon sensor layer. The overall chip minimum detectable charge is estimated by adding the pixel-to-pixel mismatch. Typically, a Timepix chip shows a pixel-to-pixel threshold mismatch of about 35 electrons if properly threshold equalized (i.e. if the response of the pixels is homogenized) and a pixel-to-pixel threshold mismatch of about 250 electrons if it is not equalized. Therefore, a bare Timepix chip has a minimum detectable charge of  $6 \cdot \sqrt{(100^2 + 35^2)} = 635$  electrons for an equalized chip and 1,616 electrons for a non-equalized chip, respectively. A Timepix chip with a  $300 \mu\text{m}$  silicon sensor layer has a minimum detectable charge of 710 electrons for an equalized chip and 1,646 electrons for a non-equalized chip, respectively. Importantly, these numbers of electrons can easily be achieved in the electron showers that results from the impact of an ion on a chevron MCP detector (even at sub-saturation MCP gains).

## Timepix

The Timepix chip [86] is derived from the Medipix 2 chip design. Figure 3.9 displays a microscope image of a bare Timepix chip. The dimensions and geometry of the chip are identical to its predecessor but the functionality on the pixel level is different.

Each pixel can be individually selected to operate in one of three modes.

1. *The event counting mode:* Each pixel counts the number of events. This mode is particularly interesting for integrated image detection.
2. *The time-of-flight (TOF) mode:* The occurrence time of an event is measured with respect to an external trigger/shutter signal (Figure 3.7). The chip returns the localization of the event via the pixel address (x- and y-coordinate) and the corresponding TOF. In MSI and VMI, this mode can both be used for selected image detection and spectral image detection.

3. *The time-over-threshold (TOT) mode:* The time is measured during which the charge resulting from the event exceeds the detection threshold level (Figure 3.8). The chip returns the localization of the event via the pixel address (x- and y-coordinate) and the corresponding TOT, i.e. a measure for the charge deposited on the pixel. Ultra-high resolution images can be generated with this mode [94]. If an event covers multiple pixel elements, the TOT information of the event distribution reflects the charge distribution throughout the event. Using this intensity information, the centroid of the event distribution can be computed using a centroiding algorithm.

The maximum measurement time in TOF and TOT mode is determined by the pixel counter depth times the measurement clock speed. The Timepix pixel counter is a 13-bit pseudo-random counter. The maximum counter value of the Timepix chip is 11,810, i.e. 11,810 is the pixel overflow value. This overflow value represents the number of possible pseudo-random counter values for the Timepix chip. Therefore, at the maximum clock speed of 100 MHz (i.e. 10 ns clock cycles), a maximum measurement interval of  $118,10 \cdot 10 \text{ ns} = 118.1 \mu\text{s}$  is available.

Each individual pixel in the chip can be programmed to operate in one of the three modes. Hence, it is possible to use the chip in “checkerboard” mode (or any other desired pattern) where half of the pixels are programmed to operate in the TOF mode and the other half in the TOT mode. If events cover multiple pixels, such an arrangement enables the measurement of the TOF of the event and the high-resolution position determination via a centroid calculation (if the overlap between multiple events on the detector is limited).

In MSI and VMI so far, chips without a sensor layer, so-called bare chips, were used to improve the response to electron showers through reduced in-sensor electron diffusion, i.e. by reducing the charge sharing between neighboring pixels [196–199].

### Medipix 3

The Medipix 3 chip [185] is a single photon counting chip that takes the same geometry as the Medipix 2 chip. However, the inter-pixel architecture is fundamentally changed in order to reduce the effect of charge sharing between multiple detector pixels. Charge summing between groups of  $2 \times 2$  pixels has been introduced. Within such a cluster of pixels, the information obtained by individual pixels is combined to reconstruct the total charge which is then assigned to the pixel with the largest charge. In this way, the  $55 \mu\text{m}$  spatial resolution is maintained, while the spectral distortion due to charge diffusion in the sensor layer is reduced.

The Medipix 3 chip can be operated in several configurations.

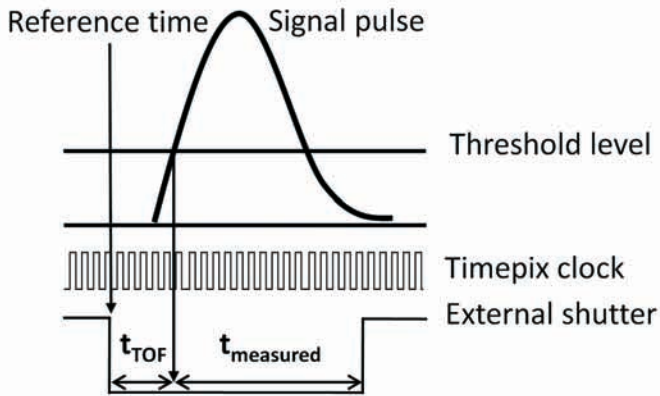


Figure 3.7: Schematic representation of the working mechanism of the TOF mode. The TOF of an event is measured with respect to an external shutter. When an above-threshold signal is induced in the pixel, the pixel counter counts clock cycles until the end of the external shutter interval. The TOF can then be determined from:  $TOF = t_{shutter} - t_{measured}$ .

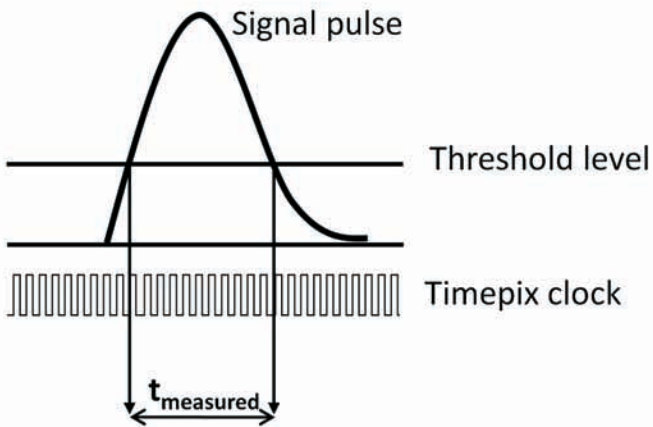


Figure 3.8: Schematic representation of the working mechanism of the TOT mode. The TOT of an event is measured by counting the number of clock cycles during which the pixel is over the threshold.

*Fine pitch mode versus spectroscopic mode:* In the fine pitch mode, every pixel of the chip is connected to a sensor element of the same pitch ( $55\ \mu\text{m}$ ) as typically done for the Medipix 2 chip. In the spectroscopic mode, only one pixel per cluster of  $2\times 2$  pixels is connected to a sensor pixel of  $110\ \mu\text{m}$  pitch. As every  $55\ \mu\text{m}$  pixel has two discriminators and two counters, the resulting  $110\ \mu\text{m}$  pixel can use up to eight thresholds and counters.

*Single pixel or charge summing mode:* As in the current Medipix 2 chip, each pixel works as an individual photon counting element independent of its neighbor pixels in the single pixel mode. Charge summing between groups of  $2\times 2$  pixels has been introduced. Within such a cluster of pixels, the information obtained by individual pixels is combined to reconstruct the total charge which is then assigned to the pixel with the largest charge. In this way, the  $55\ \mu\text{m}$  spatial resolution is maintained, while the spectral distortion due to charge sharing in the sensor layer is eliminated. Charge summing can be used both in the fine pitch and in the spectroscopic mode.

*High gain mode versus low gain mode:* The pixels can be run at high or at low gain.

*Data acquisition and readout sequentially or continuously:* In the sequential acquisition mode, two threshold levels and both of the pixel's 12-bit counters can be used, i.e. a 24-bit counter depth. Readout occurs after each acquisition and results in a dead time. In the continuous acquisition mode, only one threshold level and one 12-bit counter is available for the measurement, while the other one is readout. There is no dead time due to readout in the continuous acquisition mode.

The Medipix 3 is particularly interesting for integrated image detection. In the spectroscopic mode, the eight thresholds and counters will enable colour X-ray imaging, for instance. In addition, the charge summing mode can provide higher resolution images by counter acting the “charge sharing” effect between neighboring pixels.

Table 3.5: Comparison of the Medipix 1, Medipix 2, Medipix 3 and Timepix chips.

Feature	Medipix 1	Medipix 2	Medipix 3	Timepix
Technology	1 $\mu\text{m}$ SACMOS <sup>26</sup>	0.25 $\mu\text{m}$ CMOS	0.13 $\mu\text{m}$ CMOS	0.25 $\mu\text{m}$ CMOS
Acquisition modes	Single photon counting.	Single photon counting.	Single photon counting, fine pitch/spectroscopic, single pixel/charge summing, low/high gain.	Single photon counting, time-of-flight, time-over-threshold.
Pixel size [ $\mu\text{m} \times \mu\text{m}$ ]	170 $\times$ 170	55 $\times$ 55	55 $\times$ 55	55 $\times$ 55
Number of pixels/chip	64 $\times$ 64=4,096	256 $\times$ 256=65,536	256 $\times$ 256=65,536	256 $\times$ 256= 65,536
Sensitive to charge	Positive.	Positive or negative.	Positive or negative.	Positive or negative.
ENC <sup>27</sup> [electrons]	170	100	60-180	100-113
Power dissipated [ $\mu\text{W}$ /pixel]	N/A. <sup>28</sup>	15	9-15 <sup>29</sup>	15
Dead time	384 $\mu\text{s}$ @ 10 MHz	1 ms	None. <sup>30</sup>	300 $\mu\text{s}$ /10 ms <sup>31</sup>
Dynamic range [bits]	15	13	1, 4, 12, 24 <sup>32</sup>	13
Energy range <sup>33</sup>	4-5 keV <sup>34</sup>	4-5 keV <sup>32</sup>	4-5 keV <sup>32</sup>	4-5 keV <sup>32</sup>

<sup>26</sup>SACMOS= self-aligned contact CMOS.<sup>27</sup>The ENC for chips with/without sensor is different (see 3.5). The numbers stated in the table give an indication of the ENC.<sup>28</sup>N/A.=No information available.<sup>29</sup>15  $\mu\text{W}$ /pixel (charge summing mode), 9  $\mu\text{W}$ /pixel (single pixel mode).<sup>30</sup>The chip can be configured to work in the continuous readout mode in which there is no dead time due to readout.<sup>31</sup>For a 100 MHz readout clock, the chip can be readout serially (all 32 CMOS lines in series) in 10 ms. When reading out the CMOS lines in parallel, the readout takes  $\sim 300 \mu\text{s}$ .<sup>32</sup>Programmable to 1-, 4-, 12-bits (in sequential & continuous acquisition mode), 24-bits only in sequential mode<sup>33</sup>The particle energy range that can be detected depends on the sensor material and thickness. This row indicates few typical values.<sup>34</sup>This energy corresponds to the deposition of about 1,500 electrons in a silicon sensor.

## Future Medipix/Timepix Chips

At this point, the collaboration has decided to add two new ASICs to the Medipix detector family, the Timepix 3 and the SmallPix 3 chips. The design specifications for both chips have not been finalized at the point of writing this thesis and may be subject to changes. Planned design features that are particularly interesting to the field of mass spectrometry (imaging) and fundamental atomic and molecular physics research are highlighted.

The Timepix 3 chip will probably have the same dimensions as the Medipix 2/Timepix chip. Major differences between the Timepix and the Timepix 3 chips are that the Timepix 3 chip will acquire both the time-of-arrival and the time-over-threshold in two separate registers in each pixel. In addition, the Timepix 3 will have a so-called “data-push” readout, i.e. pixel readout occurs on an event-by-event basis rather than reading out the entire pixel matrix at the end of the measurement interval. The pixels that are being readout are dead and cannot accommodate any new events during readout. However, the rest of the pixel matrix can still acquire data. Therefore, the data-push readout removes an overall dead time due to reading out the entire pixel matrix at the end of a measurement interval. The time measurements of the Timepix 3 will have a higher timing resolution than the current Timepix chip.

As the name “SmallPix 3” suggests this chip will deviate from the  $55\ \mu\text{m}$  pixel pitch of the Medipix 2/Timepix chips. By designing this ASIC in  $0.60\ \mu\text{m}$  or  $0.130\ \mu\text{m}$  CMOS design, the pixel pitch could be smaller while preserving (or possibly increasing) the on-pixel functionality of the Timepix ASIC. An obvious advantage of a smaller pixel pitch is an increase in spatial resolution. However, through the implementation of super-pixels also applications for which the current  $55\ \mu\text{m}$  pixel pitch suffices benefit from a smaller pixel pitch. Similar to the Medipix 3 design, those super-pixels could share registers. This results in a larger available bit depth (and hence measurement time, for instance, in TOF mode).

### 3.5.2 Chips with/without a Sensor Layer

#### Sensors

The semiconductor layer on top of the ASIC is typically referred to as a “sensor” [200] in the field of ASICs. The chips of the Medipix/Timepix detector family are typically combined with a semiconductor<sup>35</sup> sensor. The pixels of the semiconductor sensor material assume the same pitch as the chip’s pixels. Each sensor pixel is attached to an ASIC pixel by a solder bump (“bump-bonding”). The choice of sensor material largely depends on the application of the chips.

---

<sup>35</sup>Materials are classified as semiconductors if their electrical resistivity is about  $10^3\text{-}10^9\ \Omega\cdot\text{cm}$  and their band gap is a few eV.

Silicon is commonly used as a “multi purpose” sensor for particle detection, for instance, in tracking applications in high energy particle physics. However, its stopping power for photons with energies higher than of 20 keV is low. Since the photon energies in medical radiography can be significantly higher, alternative, high-Z sensor materials are required. Gallium-arsenide, cadmium telluride, and cadmium-zinc-telluride are possible sensor alternatives. These room-temperature semiconductor materials are typically used for high-energy X-ray and  $\gamma$ -ray detection. However, the production of large areas of homogenous, defect-free sensor materials is challenging. Germanium, though requiring cooling to liquid nitrogen temperatures, is used for X-ray experiments at synchrotron light sources [201, 202].

### Sensor Layer or MCP?

When used for X-ray and electron detection, the detection medium converts incident particles into electron-hole pairs, which are collected in the charge-sensitive amplifier of the CMOS readout chip. The charge created in the sensor layer typically spreads out over multiple pixels. This charge sharing effect blurs the image. Ions typically do not have sufficient energy to penetrate into the sensor layer. Ions can be detected indirectly by placing a MCP in front of the detector [73, 94]. The (bare) chip then registers the electron shower produced by each ion impact on the MCP. The introduction of an MCP decreases the detection efficiency due to the 70-80% fill factor of the MCP.

### 3.5.3 Tiling to Larger Areas

For large-area imaging applications, seamless detectors can be desirable. This still poses a challenge. A single chip has an area of about 2 cm<sup>2</sup>. However, many (imaging) applications require larger detector areas. Currently, the 3-side buttable chips can be arranged in rectangular  $2 \times 2n$  ( $n=1, 2, 3, \dots$ ), full-coverage arrays of chips. Larger detector areas can be achieved by tiling multiple  $2 \times 2$  units of detector together as, for instance, suggested by the ReLAXD project [203]. A drawback of tiling larger areas from 4-chip units is the inactive space between detector modules. This dead space is due to the periphery of the chips and the wire-bonds that are located on one side of the ASIC (Figure 3.10).

A step towards the reduction of dead space between chips are through silicon vias (TSV) [204], i.e. vertical electrical connections through the silicon chip, which replace the wire-bonds. The TSVs enable a more compact chip periphery and therefore, reduce the inactive space in large-area, multi-pixel arrays. Unlike wire-bonds, the TSVs do not extend above the chip surface. Therefore, larger semiconductor sensor layers ( $>2 \times 2$  chip array) can be connected to the chip



Figure 3.9: Microscope image of part of a bare Timepix chip.

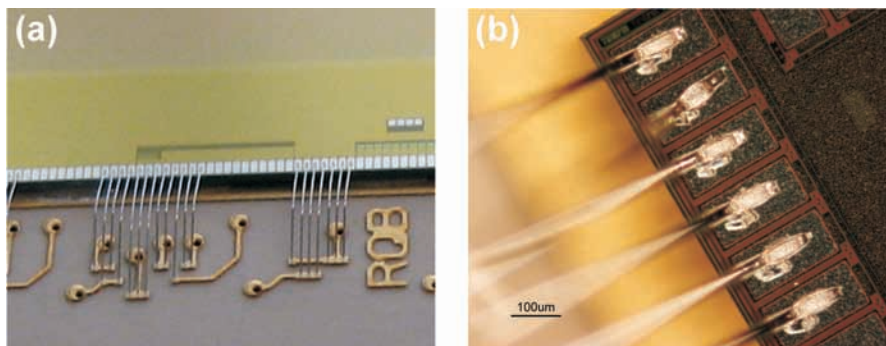


Figure 3.10: (a) Photograph of part of a Timepix chip. The chip periphery, wire-bond pads and wire-bonds are displayed. (b) Microscope image of part of a Timepix chip. The chip periphery, the on-chip wire bond pads and wire-bonds are shown.

array. Still, the sensor size can limit the detector area depending on the semiconductor sensor material. The production of large-area semiconductor sensors is still difficult. Si sensors are routinely produced up to 12 inches in diameter (circular), GaAs up to 6 inches, CdTe up to 3 inches.

### 3.5.4 Readout Hardware & Software for the Medipix/Timepix Detector Family

#### Control and Acquisition Software

Most users within the *Medipix collaboration* control and interact with the chips using the dedicated acquisition software “Pixelman” [205, 206] developed and maintained by the *Pospisil group (IEAP CTU Prague, Czech Republic)*. Pixelman allows to setup measurements, equalize the pixels and test the chips (digital and analog tests, test pulses etc). In addition, the user can extend the functionality of Pixelman via plug-ins. There are few alternative control and readout software packages which have specifically been developed for a particular readout interface.

Among other file formats, the data from the chips can be saved in ASCII (American Standard Code for Information Interchange) format. Typically, the data is saved sparsely, i.e. only pixels that have registered an event are listed in the output data file. The data file is organized in three columns, the x- and y-coordinate of the pixel and the number of events (Medipix mode), time-over-threshold or the time-of-flight. Data processing software depends largely on the specific application in which the ASICs are used.

#### Hardware

**USB.** A number of universal serial bus (USB) readout interfaces have been designed by the *Pospisil group*. In particular, the USB 1.0 readout [207], the USB Lite [208], the USB 2.0 Rapid Universal Interface (RUIN) and the Fast Interface for Timepix Detectors (FITPIX) [209] readouts. Conveniently, these readout boards directly click into the ASIC carrier and the necessary voltages are internally derived from the voltage provided by the USB connection such that no external power supplies are needed. These compact readout interfaces are very well suited for portable measurement setups.

**MUROS2.** The MUROS2 readout [210] represents an interface between the Medipix 2 chip and a general-purpose commercial PCI-based acquisition card (National Instruments, Austin, USA). The on-board FPGA transmits data between the chip(s) and the measurement PC. In addition, the board comprises a number of registers to control the chip operation. Per chip, the CMOS data lines

are readout in series. The MUROS2 is designed to readout chip carriers with a maximum of eight chips. Individual chips are readout in series (Daisy chain).

***ReLAXD readout.*** The ReLAXD readout [203, 211] is a gigabit per second (1 Gbit/s) readout system developed within the framework of the ReLAXD project (high Resolution Large Area X-ray Detector) (Figure 3.11). The ReLAXD module reads out the 4 chips of a  $2 \times 2$  chip array in parallel (CMOS lines in series) and achieves frame rates of up to 120 Hz. The user interacts with the chip via the dedicated acquisition software and graphical user interface Pixelman or the so-called ReLAXD DAQ, dedicated readout and control software for the ReLAXD module. The ReLAXD board needs a supply voltage of about 12 V and provides the Timepix ASICs with the required supply voltages. An on-board FPGA (Lattice LFSC15, Lattice Semiconductor Corporation, Hillsboro, USA) controls the signals to and from the chips. The board communicates with the measurement PC via standard 1 Gbit/s Ethernet such that the hardware requirements are a 1 Gbit/s Ethernet cable (1 Gbit/s, CAT. 5, STP) and a 1 Gbit/s Ethernet card (Intel PRO/1000 PT Server Adapter, Intel Corporation, Santa Clara, USA) in a measurement PC. The ReLAXD readout board and the chip carrier are clicked together in a T-shape configuration. The measurement clock of the Timepix is derived from a 25 MHz local oscillator and can be set between 5 MHz and 100 MHz in steps of 5 MHz. This results in a minimum time resolution of 200 ns and a maximum time resolution of 10 ns. An external trigger (start and stop) can be applied to the chips via the ReLAXD board's external trigger input. Using the Pixelman readout software, the chips can be tested, the adjustment and measurement parameters can be set. A maximum number of 10-30 readout frames per second (frames/s) can be reliably achieved with Pixelman (for acquisition time  $\ll$  readout time). Using the ReLAXD DAQ software, one can readout about 120 frames/s. In Pixelman, the frame rate is limited by the online "de-randomization" of the pixel counter values, while the ReLAXD DAQ reads-out the frames untreated and the de-randomization is carried out offline. So far, the ReLAXD DAQ is a pure readout program with limited features to configure the chips. It is possible to prepare the chips for a measurement in Pixelman and then use the faster ReLAXD DAQ to acquire the data.

***Berkeley quad Timepix parallel readout.*** The Berkeley quad Timepix parallel readout [173] represents a highly parallel readout system dedicated to measurement setups using  $2 \times 2$  Timepix ASICs. The readout system both reads-out all four chips and all 32 CMOS signal lines from the parallel ASIC output at the same time. A frame rate of about 1 kHz can be achieved. The Berkeley readout consists of three subsystems. The first element of this system is the ASIC carrier on which the four Timepix chips are mounted. The CMOS signal

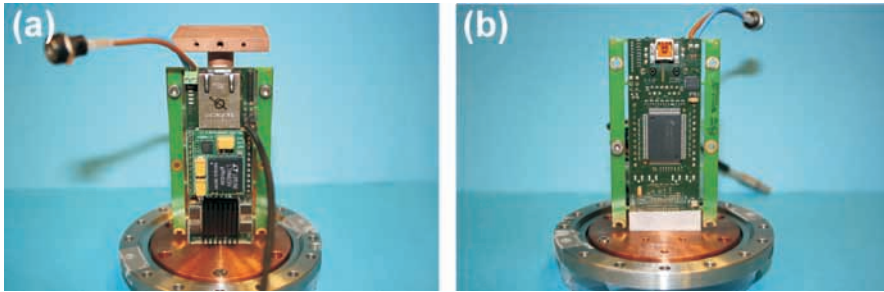


Figure 3.11: ReLAXD readout board top and bottom side.

of two chips is readout from the ASIC carrier by the second subsystem, i.e. two interface boards. On these two interface boards, a field programmable gate array (FPGA) converts the digital data from the ASIC into LVDS (low-voltage differential signaling) logic levels. In this format, the data flows to the third part of the system, in particular to the ROACH (Reconfigurable Open Architecture Computing Hardware) board. The ROACH board is a standalone FPGA-based processing board on which events are extracted from the data stream and passed on to the measurement PC via a 10 Gbit/s Ethernet connection. It should be noted that saving the entire pixel matrix poses a challenge at such high frame rates, which limits the applicability to high count rate experiments.

**More readout systems.** Within the collaboration, several readout interfaces have been developed to target specific applications. Among others, there is the “Parallel Readout Image Acquisition for Medipix” (PRIAM) [212] system for reading out the Medipix 2 chip at kilohertz frame rates. The “Dear-Mama Acquisition System” (DEMAS) [213] reads-out the Medipix 2 chip at 500 Hz and is capable of both data transfer modes, i.e. chip readout via the serial LVDS lines and chip readout via the 32-bit CMOS parallel bus. Another gigabit Ethernet readout system was developed for use in the “Medipix All Resolution System Computed Tomography” (MARS-CT) scanner. A “Speedy PIxel DEtector Readout” (SPIDER) for 1 kHz operation is under development.

## 3.6 Alternative Imaging Detectors

We realize that in the past couple of years, a number of alternative (ion) imaging detectors have been put into operation, few of which are highlighted below.

### 3.6.1 IonCCD

The ionCCD (OI Analytical, Pelham, USA) is a modified CCD array detector for direct charged particle imaging. In particular, the semiconductor part of the CCD (in which the electron-hole pair current is generated upon photon impact) is replaced by a conductive layer of TiN. The conductor collects charge from the impinging ions by charge neutralization. The ionCCD consists of 2,126 pixels. Each pixel has dimensions of  $21 \times 1.5 \mu\text{m}^2$ . There is a  $3 \mu\text{m}$  gap between individual pixels. The fill factor of the ionCCD is 87.5%. Hadjar and co-workers have successfully tested the ionCCD for electrons and (biomolecular) ions [214, 215]. They report that the ionCCD's detection efficiency does not depend on the ion energy, flux and angle of incidence. However, the detection efficiency is directly dependent on the charge state of the incident ion. The quantum efficiency of the chip is about 25-33%. The authors establish the ionCCD as a robust, high potential electron and ion analyzer, which could also be employed as a pixelated readout anode for MCP-based detection systems.

### 3.6.2 Single Photon Avalanche Photodiode (SPAD)

Similar to the work of Charbon [188–190], Wilman and co-workers have implemented a commercial photon-counting silicon detector (Hamamatsu multi-pixel photon counting (MPPC) sensor, Hamamatsu, Japan) in combination with a scintillator for TOF-MS [216]. The ion impinges on the scintillator and causes the photon emission. The photons are registered by the silicon sensor of the SPAD. The active area of this sensor is  $1 \text{ mm}^2$  and the pixel pitch is  $25 \mu\text{m}$ . While the time resolution of the MPPC is on the order of 200-300 ps, the achievable time resolution (and hence mass resolution) is limited by the 40 ns decay time of the scintillator. The authors suggest that an improved version of the scintillator-SPAD detector system could provide a valuable alternative to MCP-based detection systems. Improvements should include a shorter decay time scintillator for more competitive time/mass resolution measurements and larger area detectors (possibly in the form of SPAD arrays).

## 3.7 Conclusions

The detector technology for ions, electrons and photons has greatly advanced over the past decades. Depending on the specific application, several fundamentally different detection mechanisms for ions, electrons and photons have successfully been put into operation. Many novel detector concepts for integrated image detection, selected image detection or spectral image detection have been proposed and are on their way to routine operation. The choice of a specific detection

---

mode and corresponding detector system is largely application-dependent. However, most modern experiments demand high-performance, robust technology, which delivers precise particle detection. The developments of the past years -hybrid active pixel detectors, single photon avalanche photodiodes and the ion-CCD among others- are highly exciting pieces of technology. In particular, the Medipix/Timepix active pixel detector family has a high potential for high resolution, time-resolved imaging applications in MS(I), fundamental atomic and molecular physics research and beyond. These detection systems provide unique analytical capabilities and operational attributes, which conveniently complement the existing particle detection toolbox.



# 4

## Fast, High Resolution Mass Spectrometry Imaging Using a Medipix Pixelated Detector

*In mass spectrometry imaging, spatial resolution is pushed to its limits with the use of ion microscope mass spectrometric imaging systems. An ion microscope magnifies and then projects the original spatial distribution of ions from a sample surface onto a position-sensitive detector, while retaining time-of-flight mass separation capabilities. Here, a new type of position-sensitive detector based on a chevron microchannel plate stack in combination with a 512×512 complementary metal-oxide-semiconductor based pixel detector is coupled to an ion microscope. A spatial resolving power better than 6 μm is demonstrated by secondary ion mass spectrometry and 8-10 μm spatial resolving power is achieved with laser desorption/ionization. A detailed evaluation of key performance criteria such as spatial resolution, acquisition speed and data handling is presented.*

### 4.1 Introduction

Mass spectrometry imaging (MSI) [3, 36, 217] measurements allow the visualization of the spatial structure and identification of the molecular masses from complex surfaces. High spatial resolution is accomplished with ion microscope mass spectrometers, where ions are extracted from the sample surface and projected onto a position-sensitive detector. A spatial resolution better than 4 μm has been reported using UV/IR laser surface probes in matrix-assisted laser desorption/ionization (MALDI) [6, 65–68]. A pulsed primary ion beam as a surface probe can achieve higher spatial resolving powers (1 μm) [63, 64]. The spatial resolution can be further improved by using a more focused primary ion/laser desorption/ionization surface probe. However, fragmentation of the surface molecules and long measurement times are undesired side effects of decreasing the surface probe area. For instance, at a 2×2 μm<sup>2</sup> pixel size (4 μm lateral resolution) and a sample size of 1×1 mm<sup>2</sup>, a typical measurement comprises 250,000 measurement

points and can last several hours.

An alternate approach to increase the spatial resolution is the use of microscope mode MSI. In the microscope mode, surface molecules are desorbed and ionized over a large sample area, typically 200-300  $\mu\text{m}$  in diameter. An ion microscope employs ion optics to project the ionized surface compounds onto a position-sensitive detector while magnifying the image and retaining the spatial information defined by the sample surface. With a field of view of  $200 \times 200 \mu\text{m}^2$  and a sample size of  $1 \times 1 \text{ mm}^2$ , a microscope mode imaging experiment involves 25 measurement points and retains the 4  $\mu\text{m}$  lateral resolution given the corresponding ion optical magnification factor and position-sensitive detection system. The ion optical magnification allows high resolution images to be obtained independent of the ionization source. Microscope mode MSI enables fast, high resolution large-area imaging provided that an adequate, i.e. fast and position-sensitive, detector is used to record high quality molecular images [6].

Position-sensitive detectors most commonly used for microscope mode MSI are combinations of microchannel plates (MCP), a phosphor screen and a charge-coupled device (CCD) camera [6]. In such an approach, an incident ion is converted into an electron shower by the MCP. The phosphor screen converts the electron shower into photons whose spatial distribution is detected by a CCD camera in the form of an electrical signal/digitized image. MCP, phosphor screen, CCD camera detectors are a reliable and well-established imaging technology. However, the luminescence decay time of the phosphor screen (decay of the intensity from 90% to 10%) amounts to typically hundreds of ns to a few ms. This is slow compared to the obtainable MCP time resolution (138 ps in the *AMOLF* setup, time-to-digital converter limited). The time resolution required to resolve different  $m/z$  species on the basis of their time-of-flight towards the detector ( $\sim 15$  ns between  $m/z$  1,000 and 1,001, in the *AMOLF* setup). Therefore, mass-resolved imaging is only possible with an MCP-phosphor screen combination if prior mass-selection in the ion optics has taken place, or if the MCP is gated at a selected arrival time. Both acquisition modes allow only one mass to be recorded at the same time.

Recently, an MCP stack combined with a delay-line detector has been implemented in combination with a  $\text{C}_{60}$  primary ion beam for secondary ion mass spectrometry (SIMS) on an ion microscope for high spatial resolution MSI [72, 77]. The spatial resolving power measured with this setup was 4  $\mu\text{m}$ . However, substantial signal processing is required to convert the timing signal for every hit on the delay-lines into position information. Subsequently, the image has to be reconstructed, which makes the data collection slow. Furthermore, two-layer delay-line detectors cannot support large count rates or and do not have multi-hit capabilities for ions hitting the same spot on the detector. While the development of three-layer delay-line detectors enables the unambiguous detection of two si-

multaneously arriving particles and the detection of particle showers [80], it does not lift above mentioned limitations inherent to this approach.

Complementary metal-oxide-semiconductor (CMOS) pixel detectors can solve a number of the shortcomings of the present-day imaging detectors for ion microscope MSI and can advance this field of research. Pixel detectors contain thousands of individual channels that can be exploited for parallel detection and are capable of fast measurements. Pixel detectors accommodate large count rates and provide multi-hit capabilities, while the recorded image is the real image and no image reconstruction is needed. Pixel detectors have previously been used for the detection of ions in combination with gas electron multipliers [218, 219]. In combination with an MCP stack, pixel detectors are capable of high-resolution, position-sensitive imaging of ions. They represent a compact, robust and cheap alternative to presently used microscope mode MSI detectors.

Possible future advances based on CMOS pixel detectors are the ease of data acquisition and data processing (direct image acquisition), the high spatial resolution (possibly enhanced by centroiding algorithms), the single-particle counting mode (noise-free particle counting as opposed to charge integration in CCD-based detectors) and the capability of some detector generations to take time-resolved images. In perspective of these attractive CMOS detector features, we describe the in-vacuum implementation and capabilities of a novel type of charged-particle detector -a chevron MCP stack in combination with a Medipix 2 imaging read-out chip [84, 85]- for microscope mode MSI. Spatial resolution and data handling are key criteria in distinguishing the new detector from approved technologies. Here, standards on transmission electron microscopy (TEM) grids (low mass ions,  $m/z=358$ ) are imaged by secondary ion mass spectrometry (SIMS) and laser desorption/ionization (LDI) to characterize the MCP/Medipix 2 combination for high spatial resolving power ion microscope MSI.

## 4.2 Experimental

### 4.2.1 The Medipix Detector Family

In this chapter, a detection system based on a Medipix 2 chip [84, 85] is employed. A detailed description of the Medipix/Timepix chips is given in Chapter 3. Attractive features of the Medipix chips for mass spectrometry applications are (1) a mass dependence determined only by the MCP that is placed in front of the detector, (2) digitization of the incident signals by means of integrated counting circuitry and (3) a wide dynamic range (13-bit counter per independent pixel). The Medipix detector provides essentially noise-free measurements, since the energy threshold level can be set well above the noise level of the pixels. Additionally, the response of all pixels can be equalized by three software-controllable

adjustment bits. The Medipix acquisition software, Pixelman (Pixelman software, version 2008/03/30, [205, 206]), controls parameters such as the acquisition time (from fractions of seconds to hours), the acquisition type (individual frames or data accumulation on the chip) and the file type (text, ASCII file, binary file). A data file typically contains a matrix indicating the number of counts registered per individual pixel.

After an acquisition period, the serial chip readout may last from several ms to several seconds depending on the size of the chip array ( $1 \times 1$  or  $2 \times 2n$ ,  $n=1, 2, \dots$ ) and the readout interface. Different readout interfaces are available for accessing the data generated on the chip [203, 207, 210] (see Chapter 3 for a detailed description of the available readout interfaces). Here, a  $2 \times 2$  Medipix 2 detector is combined with a universal serial bus (USB) readout interface [207]. This interface board is compact ( $75 \times 46 \text{ mm}^2$ ) and can directly be coupled to the Medipix printed-circuit board (PCB) without intermediate cabling. The readout speed is 6 Mbit/s, which yields a readout time for the entire chip of hundreds of ms. During chip readout the pixels cannot accommodate new counts, resulting in a dead time equivalent to the readout time of the chips. The effect of this readout/dead time can be minimized by measuring multiple frames, accumulating the images on the chip prior to readout and readout only after a given amount of frames has been measured.

## 4.2.2 Instrumentation

In the implementation on the *AMOLF* ion microscope, the  $2 \times 2$  chip Medipix 2 detector (with a  $300 \text{ }\mu\text{m}$  silicon sensor layer) is suspended 2.5 mm behind a  $\phi=4$  cm chevron micro-channel plate (MCP). The pores of the MCP have a diameter of  $12 \text{ }\mu\text{m}$  on a  $15 \text{ }\mu\text{m}$  center-to-center spacing. The MCP front- and backsides are biased on voltages of -2.1 kV and -0.6 kV, respectively. This corresponds to an MCP gain of  $8 \cdot 10^5$ . These settings result in optimal electron shower sizes on the Medipix 2 detector with the corresponding optimal spatial resolution. The MCP/Medipix 2 detector ensemble -including the USB readout interface- is mounted in a vacuum chamber.

The Medipix detector readout electronics out-gasses and is not designed for high-vacuum compatibility. Therefore, the detector is operated in a differential pumping geometry (Figure 4.1), where the vacuum chamber is constructed in such a way that the MCP represents the conduction limit between the mass spectrometer vacuum system ( $P=1.3 \cdot 10^{-8}$  mbar) and the vacuum chamber that houses the detector and its associated electronics ( $P=1.3 \cdot 10^{-7}$  mbar). A bypass between the mass spectrometer vacuum chamber and the detector vacuum chamber protects the MCP from pressure differences during pumping. The power dissipation of

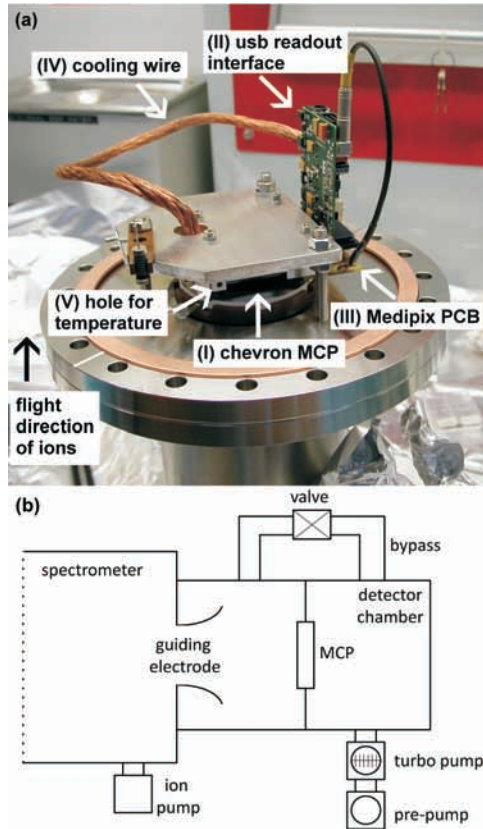


Figure 4.1: (a) Picture of the detector during assembly. The chevron MCP stack (I) is mounted onto the vacuum flange. The Medipix 2 detector is mounted on its aluminum heat sink at a distance of 2.5 mm from the MCP. The Medipix 2 chips face towards the MCP (down in the picture). The USB readout interface (II) is connected to the printed-circuit board (III). The copper strand is part of the active cooling system (IV); it is clamped to the Medipix heat sink and fed out of the vacuum to the active Peltier element cooling system. The hole in the Medipix heat sink (V) enables the installation of a PT-100 temperature probe, which indicates the heat sink temperature close to the point where the Medipix 2 chip is supported. The black arrow indicates the direction of incident ions arriving from the mass spectrometer on the imaging detector. (b) The differential pumping scheme of the setup. The detector chamber contains the detector and its electronics, which out-gas. The MCP separates the spectrometer and detector vacuum. A bypass between the two chambers protects the MCP from critical pressure gradients during pumping.

the detector and readout electronics (estimated 5 W) requires active cooling and temperature monitoring of the chips in the vacuum. For example, without cooling the detector reaches temperatures above 140 °C within 45 minutes of in-vacuum operation, which is fatal to the detection system and indicates the need for an active cooling system. Therefore, the chips' aluminum heat sink is connected to a  $\phi=2$  cm copper wire which is fed to a cooling platform outside the vacuum chamber and cooled by Peltier elements. The temperature of the heat sink is monitored by means of a PT-100 temperature probe. Thus, the chips' heat sink temperature can be maintained between 15 °C and 45 °C.

The MCP/Medipix 2 detector system is mounted on a time-of-flight (TOF) ion microscope mass spectrometer (TRIPLE Focusing Time-of-flight (TRIFT), Physical Electronics, Inc., Chanhassen, USA). The TRIFT mass spectrometer typically delivers an ion optical magnification of a factor of 100 $\times$  (dependent on the ion optics). Thus, a 55 $\times$ 55  $\mu\text{m}^2$  pixel actually probes an area of 550 $\times$ 550  $\text{nm}^2$  on the sample surface. However, spatial resolving powers of this order of magnitude are inaccessible with the current setup due to ion optical aberrations [87]. A schematic representation of the setup elements is displayed in Figure 4.2 and a detailed description of mass spectrometric ion microscopes is covered in detail elsewhere [6].

### 4.2.3 Experimental Conditions

The system was tested with SIMS and LDI. A Cs<sup>+</sup> ion gun with a beam diameter of 270-300  $\mu\text{m}$  was used for SIMS and a Nd:YAG laser (operated at the third harmonic; Bright Solutions, Wedge, Model 355, Cura Carpignano, Italy) at a repetition rate of 187 Hz and a beam diameter of 150-180  $\mu\text{m}$  was used for LDI. The mass range is  $200 \leq m/z \leq 1850$ .

After desorption and ionization from the sample surface, ions traverse the ion-optics and strike the MCP while retaining their original spatial distribution. The time-of-flight of the ion is related to the  $m/z$  value, and thus single masses can be selected (based on their time-of-flight) by the electrostatic blanker in front of the MCP (Figure 4.2). This approach has been described in detail elsewhere [6]. Wincadence software (Version 4.4.0.17, ULVAC-PHI, Inc., 2008) is used for instrument control.

### 4.2.4 Samples

Nickel/copper transmission electron microscope (TEM) grids (Agar Scientific, Stanstead, United Kingdom) were used to characterize the performance of the Medipix 2 detector on the ion microscope. The TEM grids are hexagonal with

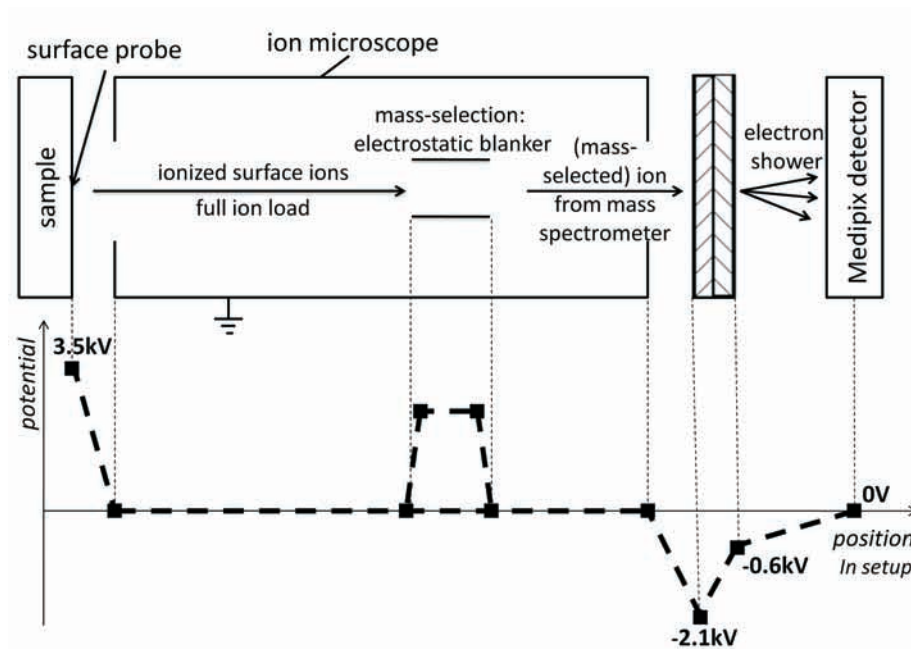


Figure 4.2: (top) Schematic representation of the setup elements such as the sample, surface probe, ion microscope, electrostatic blanker, MCP and Medipix 2 detector. The surface probe desorbs and ionizes the sample surface. The ionized surface particles are electrostatically extracted and guided through the mass spectrometer by the ion optics. Particular  $m/z$  species can be selected from the full-ion load with the electrostatic blanker. The (mass-selected) ion load is detected by the chevron MCP stack and Medipix 2 detector. (bottom) Potential diagram of the experimental setup.

itches of  $37\ \mu\text{m}$  and bar widths of  $8\ \mu\text{m}$ . The grids are glued (silver paint, Agar G302, Agar Scientific, Stanstead, United Kingdom) on top of a layer of green organic dye (green permanent marker, Staedler Lumocolor 318-5, Nürnberg, Germany) deposited on an indium tin oxide (ITO)-coated glass slide. The inset of Figure 4.3a shows an optical image of a hexagonal TEM grid used in the experiments.

## 4.3 Results and Discussion

### 4.3.1 SIMS and LDI Images

Figure 4.3a displays a total ion image of a hexagonal grid sample generated by positive mode SIMS using the  $\text{Cs}^+$  surface ionization probe. The field of view is  $260\ \mu\text{m}$  and the ion optical magnification is  $85\times$ . This image is obtained by on-chip integration of  $\sim 100$  acquisitions of 0.5 s each. The chip measures 100 acquisition frames of 0.5 s each. The data of those frames is meanwhile accumulated on the chip under control of the acquisition software. After 100 frames are acquired, the integrated image is read out. Alternatively, one could measure 100 individual frames of 0.5 s, read out every frame after its acquisition and build the image by offline integration of the frames. However, this results in substantial readout and thus dead time. The online image builder of the acquisition software updates the image after each acquired frame. In these measurements, the hexagonal grid structure is clearly resolved by the detector. The image quality does not improve for longer acquisition periods. Typical intensity values of the integrated images range between 200 and 2,600 counts per pixel such that the bit depth of  $2^{13}$  is not limiting the image acquisition method.

Several characteristic artifacts can be observed in Figure 4.3. The cross indicates where the four individual chips of the detector are connected and consists of three times larger area edge pixels. Therefore, these pixels display higher count intensities and can be observed in the image. This artifact is inherent to the detector geometry and well-defined such that it can be corrected for. There are less signal counts registered in the center of the detector due to a depleted area at the center of the MCP. The image of the grid is slightly distorted due to ion optical distortions which occur especially at a large field of view. An intensity gradient is apparent throughout the image and might be related to sample deterioration. Possibly the intensity gradient is due to a temperature gradient across the chips. The copper cooling wire is attached to one side of the chip heat sink and this side is cooled more efficiently than the opposite side which results in a temperature gradient across the heat sink and chips.

Figure 4.3b shows part ( $140\times 140$  pixels) of an MSI image of the hexagonal grid sample, which was generated by the laser surface probe (LDI). Here, the hexagonal grid was placed over an organic dye deposited on a glass slide. The mass of the organic dye ( $m/z=358$ ) was selected by the electrostatic blanker ( $310\leq m/z\leq 410$ ) and shows a strong signal in the “holes” of the hexagonal grid. The field of view is  $130\ \mu\text{m}$  and the ion optical magnification is  $42\times$ . The hexagonal grid structure only covers about one quadrant of the detector surface. Therefore, part of the full detector image -showing the full field of view- is displayed. The small field of view is most likely due to a non-optimized alignment of the laser beam. The image is generated by on-chip integration of  $\sim 50$  acquisitions of 0.5 s each

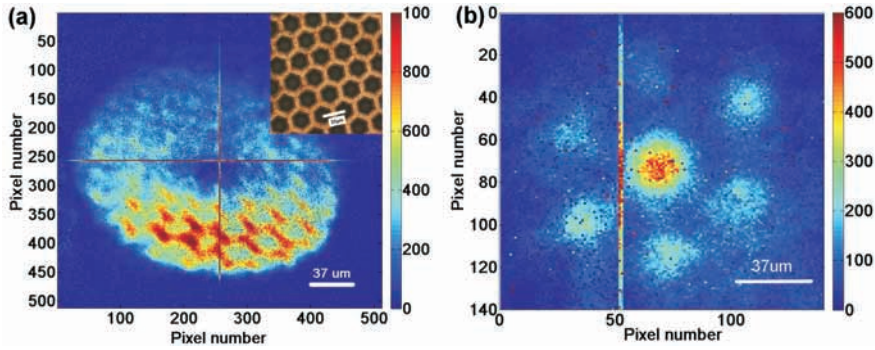


Figure 4.3: Images as generated with the ion microscope (a) in SIMS mode and (b) in LDI mode, acquired at the same Medipix 2 threshold levels. Figure 4.3a displays the full  $m/z$  range (200-1850) obtained by on-chip integration of  $\sim 100$  acquisitions of 0.5 s each. The copper peak is the dominant feature in this experiment. The full  $512 \times 512$ -pixel image is displayed. Figure 4.3b shows the mass-selected organic dye ( $m/z=358$ ) image which displays a strong signal in the “holes” of the grid. The image is obtained by on-chip integration of  $\sim 50$  acquisitions of 0.5 s each. The inset in (a) displays an optical image of a TEM grid.

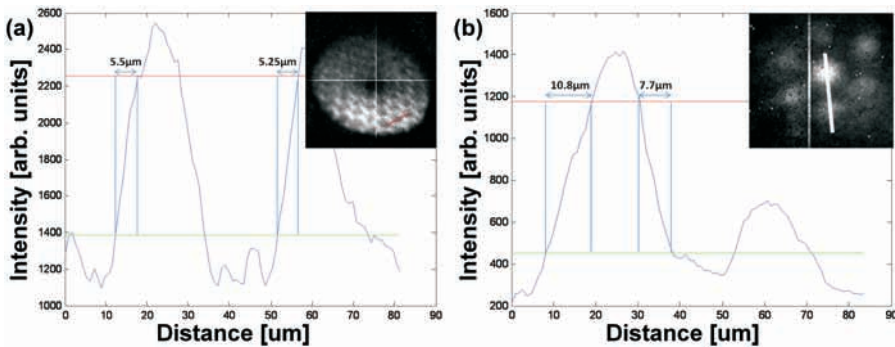


Figure 4.4: (a) Evaluation of the resolving power the MSI image of Figure 4.3a (inset). The red line indicates the data over which the resolving power is evaluated. The graph shows a line scan of the intensity per pixel in arbitrary units as a function of the distance on the grid in microns. The graph reveals a resolving power of about  $5 \mu\text{m}$ . (b) Idem for the LDI image of Figure 4.3b.

(one frame of 0.5 s corresponds to 93 or 94 laser shots since ion generation and detection are not synchronized). The LDI image uses a large surface probe (laser spot size  $\sim 150\text{-}180\ \mu\text{m}$ ) compared to the spatial resolution obtained in the image. The spatial resolving power in this image (see below) is about two orders of magnitude better than the surface probe spot size.

Figure 4.3a and 4.3b demonstrate the ability of “complementary” ion detection with this novel detector approach. The figures show complementary images of the metal grid and the organic dye (“holes”) obtained in positive mode SIMS and LDI surface ionization mode, respectively.

### 4.3.2 Spatial Resolving Power

The spatial resolving power [3, 72], i.e. the sharpness sample feature edges, is typically calculated instead of the resolution in terms of pixel size ( $55\times 55\ \mu\text{m}^2$ ) and ion optical magnification (approximately a factor of  $85\times$  in SIMS and a factor of  $42\times$  in LDI) resulting in one pixel probing  $650\times 650\ \text{nm}^2$  (SIMS) and  $1.31\times 1.31\ \mu\text{m}^2$  (LDI) on the sample surface, respectively. The spatial resolving power has been previously defined as the distance between 80% to 20% intensity of a feature within the image [3, 72]. Testing our images against this criterion of resolving power is realized by making a line scan through the image intensity (Figure 4.4), which yields the pixel-to-pixel intensity properties.

The spatial resolving power of the images shown in Figures 4.3a and 4.3b is evaluated in Figure 4.4a and 4.4b. A line scan (red line in the inset of Figure 4.4a and white line in the inset of Figure 4.4b) is drawn through features of the image (several hexagonal cells of the grid). Figure 4.4a displays the signal intensity throughout the sample features (in arbitrary units) versus the spatial distance on the sample (in  $\mu\text{m}$ ) for the SIMS measurement. The horizontal green and red lines indicate the 20%- and 80%-level of the image features. The spatial resolving power of this measurement is about  $5\ \mu\text{m}$  (for the high intensity part of the image) at an ion optical magnification of a factor of  $85\times$ . A similar analysis of the LDI image (Figure 4.4b) reveals a spatial resolving power of about  $8\text{-}10\ \mu\text{m}$  (for the high intensity part of the image) at an ion optical magnification of a factor of  $42\times$ . The resolution of LDI and SIMS scale with the inverse of the ion optical magnification, thus the spatial resolving power obtained with this detector assembly is independent of the surface ionization probe. Figure 4.4 shows that the detector image matches the physical dimensions of the grid well.

The on-chip integration of hundreds of individual acquisition frames limits the resolution of the detector. Individual ion hits on the MCP are translated into an electron shower which typically spans a circle on several pixels on the Medipix 2 detector (depending among others on the MCP gain, the distance between the detector and MCP, the voltage across this gap and the threshold on the Medipix

detector). Reconstruction of an image of these “smeared” electron signatures blurs the ion image and limits the spatial resolving power. However, these “cluster” event signatures can be exploited for imaging at sub-pixel spatial resolution by means of centroiding [220].

### 4.3.3 Spatial Resolving Power as a Function of the Threshold Level

The dependence of the spatial resolving power on the chip detection threshold level of the chips was studied to determine optimal operation conditions. The total ion image of a hexagonal grid sample generated by positive mode SIMS and the Cs<sup>+</sup> surface ionization probe (bottom inset Figure 4.5) was used to evaluate this relationship. The field of view was 300  $\mu\text{m}$  and the ion optical magnification was 60 $\times$ . The resolving power was evaluated along the red line (procedure analogous to the analysis of Figure 4.4). Figure 4.5 displays the spatial resolving power in microns versus the increasing detection threshold level in arbitrary units for three peaks along the line scan (red, green, blue data points). The lowest threshold level (number 1) was placed just above the chip intrinsic noise edge. At the highest threshold level (number 10), the features in the figure are just not discriminated away. The threshold level was systematically incremented in ten steps between those two levels. The figure indicates that the spatial resolving power improves from about 10  $\mu\text{m}$  to about 5  $\mu\text{m}$  with an increasing detection threshold. The MSI image insets at threshold level 1, 4, 7 and 10 illustrate how the resolving power improves with higher detection threshold levels. Higher threshold levels cut the image’s intensity distribution closer to the top of the distribution, which improves the spatial resolving power as expected. The resulting system resolving power determined here is a convolution of the instrument transmission function and the detector resolving power. As a result, the intrinsic detector resolving power will exceed the values presented in this analysis.

## 4.4 Conclusion and Outlook

We have presented the technical implementation and initial performance of a chevron MCP stack in combination with a Medipix 2 ASIC for direct organic ion imaging using an ion microscope. This detection system has 55 $\times$ 55  $\mu\text{m}^2$  detector pixels and an ion optical magnification of a factor 85 $\times$  (SIMS) and 42 $\times$  (LDI) such that an individual pixel probes an area of 650 $\times$ 650 nm<sup>2</sup> (SIMS) and 1.31 $\times$ 1.31  $\mu\text{m}^2$  (LDI) on the sample surface. The detector is capable of imaging organic material with <6  $\mu\text{m}$  spatial resolving power by positive mode SIMS and with 8-10  $\mu\text{m}$  spatial resolving power using LDI mass spectrometry imaging.

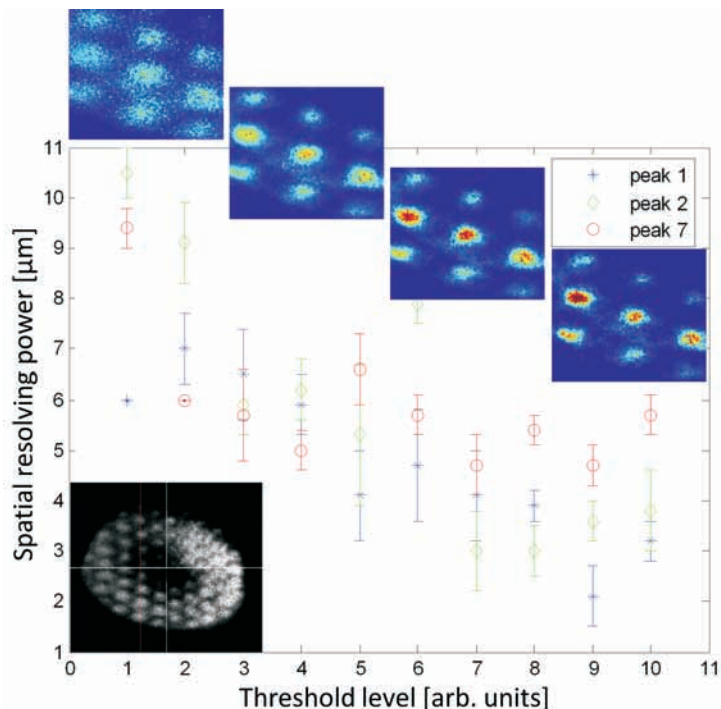


Figure 4.5: Evaluation of the spatial resolving power as a function of the detection threshold level. The spatial resolving power of an MSI image (bottom inset) is evaluated by the line scan method (red line). The spatial resolving power versus the increasing detection threshold level is determined for 3 peaks along the line scan (red, green, blue). The insets at threshold level 1, 4, 7 and 10 illustrate how the MSI image changes by increasing the chips' threshold level of detection.

The Medipix detector family has a large potential for imaging mass spectrometry on biological tissue sections in the near future. Current imaging detectors provide 2D imaging capabilities such that the spatial distribution of a particular ion species, i.e.  $m/z$  value, can only be imaged by selecting the particular ion (based on its time-of-flight) and blanking all other particles. In the presented work, this is achieved with the electrostatic blander. The implementation of an MCP/Timepix detector assembly will alleviate the need for selective ion blanking. The Timepix detector is a variant of the Medipix 2 detector, which -among other features- can measure the time-of-flight of an impinging particle on the pixel level with a time resolution of roughly 10 ns. While the MCP timing will ensure an

accurate mass determination of all incoming ions (accurate mass spectra), the Timepix detector images and measures the time-of-flight of different ion species on the pixel level during the same measurement -thereby eliminating the need for mass-selecting specific ions. The Timepix detector captures time-resolved images of several  $m/z$  species in one measurement, which largely facilitates the data taking and reduces the measurement time.

The current experimental setup is limited in its ability to analyze complex biological samples by limited acceleration voltages. A revision of the setup, including high voltage acceleration capabilities for both ion polarities as well as mass-selection based on a Timepix chip, will allow for the analysis of tissue samples by microscope mode imaging mass spectrometry. The work presented in this chapter represents a step into this direction as it demonstrates the in-vacuum implementation of a Medipix 2 detector in combination with an MCP on an ion microscope. Imaging capabilities and data handling are successfully established. The new detection system combines high spatial resolution imaging with direct imaging capabilities (no image reconstruction/complicated data handling), a mass-independent detector response and a high dynamic range.



# 5

## High Dynamic Range Biomolecular Ion Microscopy with the Timepix Detector

*Highly parallel, active pixel detectors enable novel detection capabilities for large biomolecules in time-of-flight (TOF) based mass spectrometry imaging (MSI). In this work, a 512×512 pixel, bare Timepix assembly combined with chevron microchannel plates (MCP) captures time-resolved images of several m/z species in a single measurement. Mass-resolved ion images from Timepix measurements of peptide and protein standards demonstrate the capability to return both mass-spectral and localization information of biologically relevant analytes from matrix-assisted laser desorption/ionization (MALDI) on a commercial ion microscope. The use of a MCP/Timepix assembly delivers an increased dynamic range of several orders of magnitude. The Timepix returns defined mass spectra already at sub-saturation MCP gains, which prolongs the MCP lifetime and allows the gain to be optimized for image quality. The Timepix peak resolution is only limited by the resolution of the in-pixel measurement clock. Oligomers of the protein ubiquitin were measured up to 78 kDa.*

### 5.1 Introduction

MSI [3, 36, 217, 221] measurements aim at the identification and localization of molecules from complex surfaces [6, 63–68]. High spatial resolution and high throughput studies have been demonstrated with ion microscope mass spectrometers [74].

Microprobe mode MSI has enabled high spatial resolution studies with highly focused primary ion or laser desorption/ionization surface probes, which have returned pixel sizes better than 4  $\mu\text{m}$  and 7  $\mu\text{m}$ , respectively. In particular, UV/IR lasers in MALDI [65–67] and pulsed primary ion beams have delivered spatial resolving powers on this order of magnitude [63]. Decreasing the surface probe area bears the disadvantage of long measurement times.

In microscope mode MSI, surface molecules are desorbed and ionized over a large sample area, typically 200-300  $\mu\text{m}$  in diameter. The large field of view enables fast, large-area image acquisitions [74]. An ion microscope employs ion optics to project the desorbed and ionized surface compounds onto a position-sensitive detector. The initial ion distribution is magnified and the lateral spatial organization of the surface molecules is maintained on their way to the detector. Molecular images are time-of-flight separated, as all ions are accelerated by the same electrical potential and a narrow distribution of ion kinetic energies is achieved by the instrument's ion optics. The ion optical magnification returns images with a high spatial resolving power, on the order of 4  $\mu\text{m}$  [6]. The spatial resolution is not limited by the ionization beam. It is determined by the quality and capabilities of the ion optics and the position-sensitive detector. For a given set of ion optics, the ultimate spatial resolution is limited by ion optical aberrations. However, a spatial resolution on the order of the ion optical aberrations is often inaccessible due to insufficient detector spatial resolution. We show that with a pixelated complementary metal-oxide-semiconductor detector the obtainable spatial resolving power is only limited by the ion optics.

Microscope mode MSI enables fast, high resolution, large-area imaging provided that a fast, two-dimensional, time- and position-sensitive detector is used to record high quality molecular images [6]. In existing implementations, the ions are projected on a position-sensitive detector assembly which consists of an MCP followed by (i) a phosphor screen and a charge-coupled device (CCD) camera or (ii) a resistive/delay-line anode. In the latter case, the ion arrival time is precisely measured as well [78]. Various techniques have been developed where the ion arrival time is measured by decoupling of the TOF signal from the MCP detector [79]. In TOF-MS based MSI, specific molecular masses are distinguished and recorded by simultaneously acquiring the impact position and the TOF of the ion. However, the MCP, phosphor screen, CCD camera assembly cannot link the ion TOF (i.e. the molecular weight) and the spatial distribution. Different molecular masses under observation cannot be measured during one acquisition with this configuration. A pair of fast-switching electrodes, called the electrostatic blanker, are used to select which ions are imaged on the detector. Several mass-selected images from combined separate measurements provide detailed information on the sample composition and according spatial distribution. A delay-line detector combines space- and time-information. However, it can detect only a small number of multiple simultaneous events. A significant amount of time is needed to reconstruct a mass-resolved image, which makes ion optical tuning hard due to the lack of direct image feedback.

In view of the importance that imaging techniques have acquired in biological, biomolecular and biomedical MSI, it is remarkable that the basic technology, i.e. 2D image detection and separate arrival time acquisition, has hardly changed

over the years. Only recently, the use of in-vacuum pixel detectors for position- [73, 81] and time-resolved [82, 83] photoelectron and ion imaging was demonstrated.

In this chapter, the application of such an in-vacuum pixel detector for biomolecular MSI on an ion microscope is demonstrated for the first time. This detector concept comprises a fully-integrated, hybrid solid state pixel detector of the Medipix/Timepix detector family [84–86]. The presented assembly consists of a chevron MCP followed by four Timepix chips, which on the pixel level return (1) the impact position of a particle and (2) the TOF of this particle. The implementation of a Timepix detector for MSI on a TOF microscope mass spectrometer removes the need for mass-selection using an electrostatic blanker as used previously [73]. Mass-resolved images are acquired during a single imaging experiment with this new detector setup (Figure 5.1).

The current project builds on the previous successful implementation of an MCP/Medipix 2 imaging detector assembly for MSI [73] (Chapter 4). This earlier work focused on the imaging capabilities and image quality of this pixelated detector. The present work discusses the additional information that an MCP/Timepix detector assembly offers the MSI community. Timepix-acquired TOF spectra are contrasted with established detection techniques such as the recording of mass spectra using a time-to-digital converter (TDC) and an analog-to-digital converter (ADC). Features of interest are the detector dynamic range, the available mass range, the detection homogeneity, the ability to detect single particles, the ability to resolve isotopes and the detector response to varying MCP gains.

## 5.2 Experimental

### 5.2.1 The Medipix/Timepix Detectors

In this chapter, a MCP/Timepix detection system is used. A detailed description of the Medipix/Timepix detector family is given in Chapter 3. In this experiment, the bare Timepix assembly is read out using a gigabit per second (1 Gbit/s) read-out system [203, 211] developed within the framework of the Relaxd project (high Resolution Large Area X-ray Detector) [203] (Chapter 3). The Relaxd module reads out the 4 chips in parallel and achieves frame rates of 10-30 frames/s. The user interacts with the chip via the dedicated acquisition software and graphical user interface “Pixelman” [205]. Details on the Medipix/Timepix chips, available readout interfaces and various applications are reviewed in reference [186] and Chapter 3.

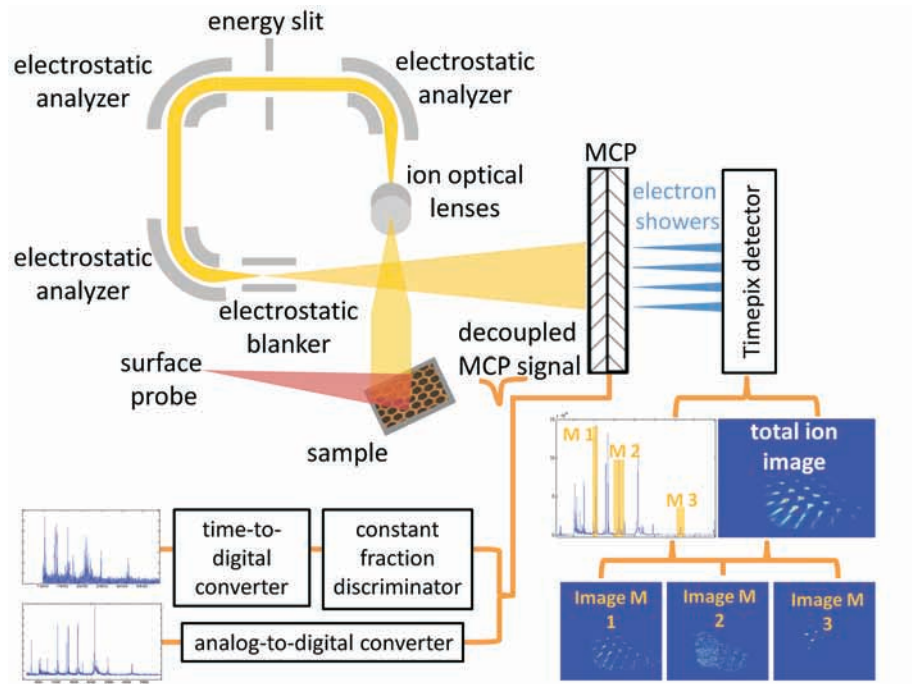


Figure 5.1: A schematic representation of the experimental setup. An MCP/Timepix detector assembly is coupled to an ion microscope. Mass spectra, total and mass-selected ion images are generated from one data set without the need for mass selection and repetitive measurements. The decoupled MCP signal provides a single signal that integrates all events and is acquired by a multi-stop TDC and an ADC.

## 5.2.2 Timepix Spectra and Images

The Timepix detector is run in TOF mode exclusively in this work. The detection system and the MALDI laser are triggered by the master trigger of the ion microscope (Figure 5.2) so that one measurement frame on the detector corresponds to the image and spectral information of one laser shot. During a single measurement frame of typically  $118 \mu\text{s}$ ,  $512 \times 512 = 262,144$  pixels act as individual, parallel detectors. Each Timepix pixel is a single-stop time-to-digital converter (TDC), i.e. each pixel delivers the position (x- and y-pixel coordinate) and the TOF of one event per measurement frame. For every measurement frame, a separate data file is saved, which contains a list of pixel addresses and corresponding TOFs of all pixels that have registered an event. The acquisition of several mea-

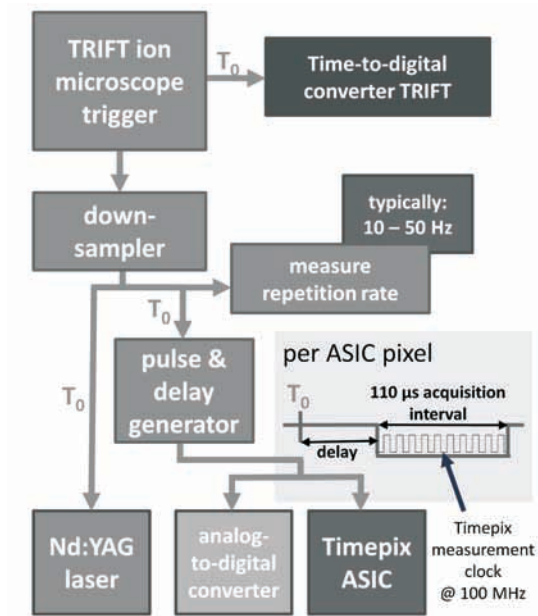


Figure 5.2: The trigger scheme of the experiment ensures that one measurement frame corresponds to one laser shot. The down-sampled trigger of the TRIFT ion microscope is used to trigger the surface probe (Nd:YAG, MALDI laser), the ADC reference measurement system and the Timepix ASIC. On the pixel level, the Timepix ASIC is capable of measuring the TOF of a particle with respect to a reference time ( $T_0$ ). Depending on the expected TOF of the particles of interest, the Timepix measurement interval is delayed with respect to  $T_0$ , i.e. the laser shot. The TDC reference measurement system is directly triggered by the TRIFT master trigger. The Timepix, ADC and TDC measurements can be directly compared to each other.

urement frames is required to obtain a mass spectrum with sufficient statistics as the Timepix pixels are single-stop TDCs and a large fraction of pixels can be covered by the ions generated by a single laser shot. Timepix acquired TOF spectra are then generated by accumulating the measured TOF values of several measurement frames in a histogram. This histogram represents a TOF spectrum of the sample which is subsequently mass calibrated. Typically, 1,000 measurement frames are collected for one spectrum. At a repetition rate of 10 Hz, the accumulation of  $1,000 \times 262,144$  (maximally) individual mass spectra takes about 100 s.

The maximum Timepix measurement interval of  $118 \mu\text{s}$  accommodates part of

a typical ion TOF spectrum. For instance, one Timepix measurement window accommodates the mass range from 0 Da to 1,650 Da. A delay is introduced between the laser shot and the actual measurement interval to allow a molecular weight range of interest to be sampled by the Timepix detector. If required, an extended mass range data set is obtained by measuring the sample for different laser-to-acquisition delays. The spectrum is then stitched together. Total ion images are generated by summing up 1,000 single-frame position measurements. Mass-selected images are generated by extracting the pixel positions corresponding to a particular mass (=TOF) peak from the data set.

### 5.2.3 Imaging Setup on the Ion Microscope

The TOF ion microscope is a TRIPLE Focusing Time-of-flight (TRIFT) mass spectrometer (Physical Electronics, Inc., Chanhassen, USA) [6]. The spatial resolving power of the mass microscope is determined by the homogeneity of the sample surface exposure during desorption and ionization, the ion optical aberrations and magnification, the field of view, and the quality of the imaging detector. Depending on the settings of the ion optics, the TRIFT ion microscope delivers a variable field of view and an ion optical magnification between  $40\times$  and  $100\times$ . Thus, a  $55\times 55\ \mu\text{m}^2$  detector pixel corresponds to, respectively, areas of  $1.38\times 1.38\ \mu\text{m}^2$  and  $550\times 550\ \text{nm}^2$  on the sample surface. The latter value extends beyond the spatial resolving power that is accessible with the current setup due to ion optical aberrations [87].

We have used the third harmonic (355 nm) of a neodymium-doped yttrium aluminum garnet laser (Bright Solutions, Wedge, Model 355, Cura Carpignano, Italy) for the MALDI measurements. It is operated at a repetition rate of 10 Hz, a pulse energy of about 13  $\mu\text{J}$  and a beam diameter of 300-335  $\mu\text{m}$ .

The Timepix assembly is mounted 2 mm behind a  $\phi=4$  cm MCP (12  $\mu\text{m}$  pores, 15  $\mu\text{m}$  pitch). Unless stated otherwise, the MCP is operated at a bias voltage of 2.0 kV (MCP gain= $6.5\cdot 10^6$ ). The bias voltage between the MCP back and the chips was 0.45 kV. The MCP emitted electron cloud spans multiple pixels on the Timepix detector and divides its charge among the individual detector elements. Smaller electron clouds allow for more ion events to be detected. This enables higher count rates and a higher dynamic range. Charge sharing [222] is reduced to a minimum by the use of bare Timepix chips, i.e. the effect of the MCP's charge cloud spreading over multiple pixels and sharing its charge between several detector elements is reduced.

## 5.2.4 Reference Measurement Systems

Reference spectra were simultaneously acquired using established detection techniques, namely a TDC and an ADC, to assess the quality of the Timepix TOF spectra (Figure 5.2). The signal intensity and background noise of the TDC spectra are not influenced by the acquisition of several measurement frames as opposed to one longer measurement. The ADC spectra benefit from this acquisition mode as the noise averages out. The ADC and TDC spectra are recorded from the signal that is decoupled from the high voltage line of the MCP backside (Figure 5.1). The TDC spectrum is generated using the standard spectral acquisition equipment of the TRIFT mass spectrometer. The analog ion signal passes a constant-fraction discriminator (CFD) and is then digitized by a multi-stop TDC with 138 ps time bins. The ADC spectrum is acquired using an 8-bit, high-speed digitizer (Acqiris, DP214, Agilent Technologies, Santa Clara, USA) that was run at 500 MHz resulting in 2 ns bins,  $10^5$  samples and a 200  $\mu$ s measurement interval.

## 5.2.5 Samples

A peptide sample was prepared by positioning a nickel hexagonal thin bar transmission electron microscopy (TEM) grid (700 mesh, G2760N, 3.05 mm diameter, 37  $\mu$ m pitch, 8  $\mu$ m bar width; Agar Scientific Limited, Stansted, UK) on top of a 2  $\mu$ l droplet of 1 mg/ml Bruker Peptide Calibration Standard II (Table 5.1; Bruker GmbH, Bremen, Germany; pepmix in 50% Acetonitrile (ACN), 50% H<sub>2</sub>O, 0.1% trifluoroacetic acid (TFA)) mixed with 10 mg/ml  $\alpha$ -Cyano-4-hydroxycinnamic acid (HCCA in 50% ACN, 50% H<sub>2</sub>O, 0.1% TFA) on an indium-tin-oxide (ITO) coated glass slide. The protein sample is a solution of 1 mg/ml ubiquitin (Sigma-Aldrich, St. Louis, USA; 50% ACN, 50% H<sub>2</sub>O, 0.1% TFA) and 20 mg/ml sinapinic acid (Fluka Analytical, now Sigma-Aldrich, St. Louis, USA; 50% ACN, 50% H<sub>2</sub>O, 0.1% TFA) homogeneously sprayed onto an ITO slide with a Bruker ImagePrep device. Ubiquitin has a  $[M+H]^+$  average mass of 8,565.76 Da.

Table 5.1: Peptides and corresponding mono isotopic and average mass of the Bruker Peptide Calibration Standard II.

Peptide	[M+H] <sup>+</sup> mono isotopic mass [Da]	[M+H] <sup>+</sup> average mass [Da]
Bradykinin 1-7	757.3992	757.86
Angiotensin II	1,046.5418	1,047.19
Angiotensin I	1,296.6848	1,297.49
Substance P	1,347.7354	1,348.64
Bombesin	1,619.8223	1,620.86
Renin Substrate	1,758.9326	1,760.03
ACTH clip 1-17	2,093.0862	2,094.43
ACTH clip 18-39	2,465.1983	2,466.68
Somatostatin 28	3,147.4710	3,149.57

## 5.3 Results and Discussion

### 5.3.1 3D Timepix Measurements: Imaging and Spectral Information

The peptide-TEM grid sample is used to demonstrate the ability to acquire a complete 3D MSI data set in one measurement without the need of mass-selection using an electrostatic blanker. Figure 5.3 displays a data set corresponding to 1,000 laser shots and Timepix frames. The mass spectrum of the peptide standard, the total ion image and the mass-selected images are extracted from the data set. The mass-selected images show different distributions for the analytes on the sample which indicates the ability to localize and identify molecular species from a patterned sample surface. The electrostatic blanker is used to blank ions with  $m/z < 700$  (matrix peaks) to reduce the count rate to the detector and measure the peptide molecular ion peaks over their entire mass range simultaneously. The measurements are performed at an ion optical magnification factor of about  $68\times$  so that a  $55\times 55 \mu\text{m}^2$  pixel on the detector probes an area of  $800\times 800 \text{ nm}^2$  on the sample surface. The spatial resolving power [3, 72], i.e. the sharpness of the sample feature edges, is evaluated by making a line scan through the total ion image. The spatial resolving power of the image features is  $3.4 \mu\text{m}$ . The spatial resolution is not limited by ion optical aberration at this ion optical magnification. Rather, the spatial extent of the MCP electron shower (50-600 pixels depending on the MCP gain) blurs the theoretically accessible  $800\times 800 \text{ nm}^2$  pixel size.

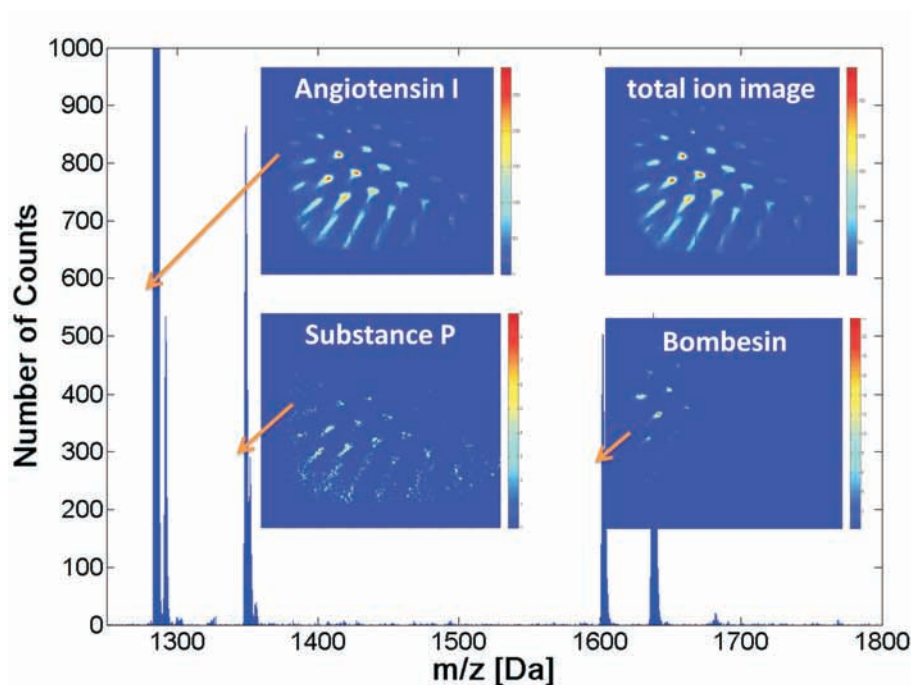


Figure 5.3: A grid on top of a peptide standard solution is imaged by MALDI using the Timepix detector. The full ion spectrum and the corresponding images are acquired in one single measurement. The insets display the mass-selected images corresponding to the respective peptide peaks.

### 5.3.2 Comparison of Spectral Quality between Timepix, ADC and TDC Detection

The effect of the MCP gain, the dynamic range of the spectra, and the peak resolution at the full width at half maximum ( $\Delta m$ )<sub>50%</sub> are used as criteria for comparison of the spectra.

#### Spectra as a Function of the MCP Gain

A MSI experiment is performed on the peptide-TEM grid sample for MCP gain settings between  $4 \cdot 10^5$  (low amplification) and  $6.5 \cdot 10^6$  (saturation). Figure 5.4 displays the total ion spectra of the three measurement systems ( $596 < m/z < 3,596$ ) for different MCP gains. The peptide mass spectra are recorded within one single measurement window by all measurement systems. Table 5.2 summarizes the

differences between the measurement systems relevant to the acquisition of mass spectra.

The Timepix delivers a spectrum containing all spectral features throughout the entire range of MCP gains (Figure 5.4a). Even for low MCP gains ( $4 \cdot 10^5$ ), the Timepix gives a high response and thus high quality spectra. This provides the advantage of not having to run the MCPs in saturation which enhances their lifetime and enables the user to tune the MCP gain for optimum image quality and spatial resolution, which is typically in the low gain range [94]. The high response of the Timepix detector to low gain MCP signals is due to the amplification of one ion hit into an electron shower which impinges on multiple Timepix pixels and results in multiple counts in the mass spectrum. The MCP gain determines the number of pixels covered by an electron shower and hence how many counts are added to the Timepix spectrum for a single ion hit on the MCP. Contrary to a standard TDC, the Timepix detector distinguishes several ions arriving on the MCP at the same time as separate ion events whose counts contribute to the spectrum. The electronics noise-free detection of the Timepix ASIC, i.e. Timepix pixels only fire for real particle events, also adds to the high quality spectra at low MCP gain.

The ADC and the TDC only return spectral info (signal-to-noise  $(S/N) \geq 3$ ) starting from MCP gains of  $4 \cdot 10^6$  because they integrate all events. For these acquisition systems, the spectral features get more distinct the closer the MCP gain approaches saturation. A maximum of one ion count per electron shower is recorded for both the ADC and the TDC.

*Table 5.2: Comparison between Timepix, ADC & TDC spectral acquisition.*

<b>Feature</b>	<b>Timepix</b>	<b>ADC</b>	<b>TDC</b>
MCP gain threshold	$4 \cdot 10^5$	$4 \cdot 10^6$	$4 \cdot 10^6$
Time resolution	10 ns	2 ns	138 ps
TOF range (single experiment)	118 $\mu$ s	200 $\mu$ s	60 ms <sup>1</sup>
Multiplexed detection	Yes.	No.	No.
Detection of ions arriving at the same time	Yes.	Yes.	No.
Multi-stop per detection element	No.	N/A.	Yes. <sup>2</sup>
Electronic noise free	Yes.	No.	No.

<sup>1</sup>In this experiment.

<sup>2</sup>One single element.

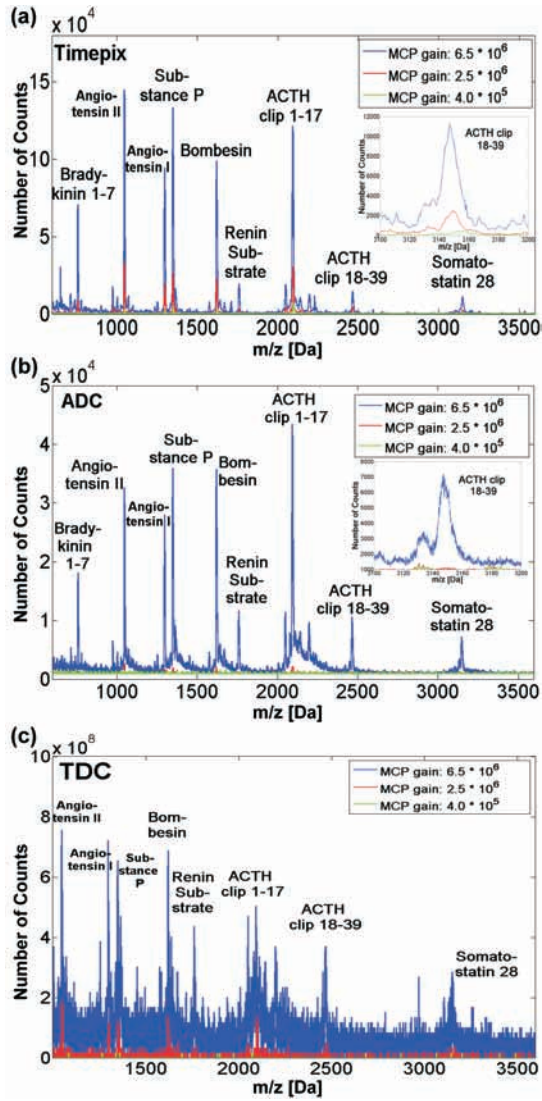


Figure 5.4: Total ion spectrum of the peptide standard sample at MCP gains from  $4 \cdot 10^5$  to  $6.5 \cdot 10^6$  recorded with (a) a Timepix detector, (b) an ADC and (c) a TDC.

The ADC samples the transients of the amplified MCP pick-up signal, i.e. it digitizes the TOF spectra of the individual measurement frames, which are subject to noise. Small pulses are discriminated by a fixed level trigger so that mass spectra cannot be acquired with an ADC in combination with low gain MCP settings (Figure 5.4b). The TDC time-stamps the ion arrival times using the amplified MCP pick-up signal pulses after it has passed through a CFD. At low MCP gains, insufficient signal is provided to the CFD and TDC to return mass spectra of relevant S/N ratio (Figure 5.4c). Contrary to the multiplexed detection with the Timepix, ions arriving at the MCP at different locations at the same time will be counted as one single ion event so that both spatial and intensity information is lost. The CFD/TDC-based detection, results in a significantly lower S/N ratio in the spectra than the Timepix and the ADC detection. The quality of the TDC lies in the capability to assign time stamps with a resolution of 138 ps to the events which allows higher resolution mass measurements. The TRIFT system comprises a multi-stop TDC which prevents depleting the signal at high count rates. The acquisition of mass spectra with a TDC is different from ADC and Timepix measurements and results in a lower S/N. A fair comparison to TDC spectra is impossible. Therefore, the Timepix spectra will be evaluated with respect to ADC spectra.

### **Dynamic Range: Timepix versus ADC**

The detector dynamic range is defined as the ratio between the maximum and the minimum detectable value of a parameter. The Timepix detector assembly has 262,144 pixels, which represents the maximum detectable number of counts within a single measurement frame. However, the MCP translates the molecular ions into MCP clusters, which leave a footprint on multiple pixels of the Timepix detector. For instance, at an MCP gain of  $4 \cdot 10^5$  (low amplification), the average cluster size is 50 pixels and about 5,250 events are distinguished on the detector. Low MCP gains results in smaller clusters, which is favorable for a high dynamic range. Also the voltage difference between the MCP back and the Timepix surface influences the size of the electron showers footprint and hence the dynamic range. The dynamic range of the 8-bit ADC is 256.

The mass spectra displayed in Figure 5.4 are accumulated from 1,000 laser shot acquisitions. The influence of the detector dynamic range on the quality of these built-up mass spectra, i.e. on the detectable range, is assessed. The difference in peak height between the smallest and the highest peak in the total spectrum is a practical measure for the detectable range of the data. These values are extracted for the data sets of Figure 5.4a (Timepix) and 5.4b (ADC). The smallest peak in the total spectrum is defined to have a minimum height of three baseline noise standard deviations above the mean baseline. The Timepix system delivers a

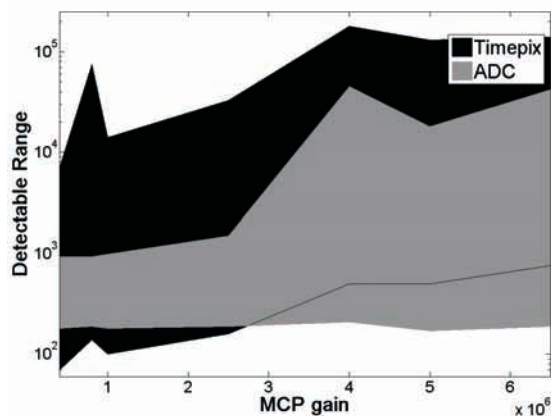


Figure 5.5: Comparison of the detectable range of the Timepix (dark) and the ADC (light) as a function of the applied MCP gain. The Timepix and ADC spectra are each based on 1,000 laser shots. The difference in intensity between the smallest and the highest peaks in the accumulated spectra (of Figure 4a and 4b) is taken as a measure for the detectable range.

considerable spectral dynamic range for all applied MCP gains (Figure 5.5). The difference between the smallest and highest peak is between 7,000 and 75,000 counts for MCP gains from  $4 \cdot 10^5$  to  $2.5 \cdot 10^6$ . For MCP gains above  $4 \cdot 10^6$ , this difference is up to  $1.8 \cdot 10^5$  counts. For the ADC, the difference between the smallest and the highest peak is between 740 and 1,310 counts for MCP gains from  $4 \cdot 10^5$  to  $2.5 \cdot 10^6$ . Above a gain of  $4 \cdot 10^6$ , this difference is up to  $4.4 \cdot 10^4$  counts. The Timepix detectable range outperforms the ADC by one order of magnitude, which is accounted for by the electronic noise-free, multiplexed detection of the amplified ion signal. Note that all electron clouds exiting the back of the MCP are assumed to be related to single ion events on the front surface of the MCP.

#### Peak Resolution at FWHM: $(\Delta m)_{50\%}$

The peak width of Timepix acquired spectra is determined by four factors. First, the 100 MHz pixel clock limits the TOF measurements to a 10 ns time resolution. In the mass range from the peptide bradykinin (757.4 Da  $[M+H]^+$  mono isotopic mass) to the protein bovine serum albumin (66.5 kDa  $[M+H]^+$  average mass), this TOF resolution translates into a mass channel width of about 0.3 Da and 2 Da, respectively, for standard measurement conditions on the TRIFT ion

microscope. Second, there is a clock cycle jitter between the laser shot and the Timepix acquisition window which are currently not synchronized. This results in TOF values that are maximally two clock cycles too short. Third, Timepix peaks are broadened by a time gradient throughout the MCP clusters (Figure 5.6). Not all pixels within one cluster record the same TOF because there is a relationship between the charge deposited on a pixel and the moment it goes over threshold [73, 91]. One ion arrival on the MCP is translated into a spectral peak that spans multiple adjacent time bins ( $\pm 5$  time bins =  $\pm 50$  ns difference in TOF). Fourth, the presence of isotopes broadens the peaks due to a convolved effect of the previous reasons.

The peak resolution at FWHM,  $(\Delta m)_{50\%}$ , was determined for the peptide peaks in the Timepix and ADC spectra. The comparison is based on the highest MCP gain spectra since these are the most favorable conditions for the ADC. Both the Timepix and the ADC have insufficient time resolution (10 ns and 2 ns, respectively) to distinguish isotope patterns. The peptide peaks represent convolutions of the individual isotope peaks centered around the average mass. In the peptide mass range between bradykinin and somatostatin 28 (3,149.57 Da  $[M+H]^+$  average mass), the  $(\Delta m)_{50\%}$  ranges from 4 Da to 15 Da and is comparable for the Timepix and the ADC.

Isotopic resolution is, theoretically, accessible with the Timepix detector if the difference in TOF between the mono isotopic mass and the isotope is longer than 20 ns, i.e. there is more than one clock cycle between the arrival of two adjacent isotopes (1  $m/z$  difference between mass and isotope, standard measurement conditions on the TRIFT ion microscope). Theoretically, resolving isotopes is possible in the mass range up to the peptide somatostatin 28 (3,149.57 Da  $[M+H]^+$  average mass), for which the difference in TOF between the mono isotopic mass and the isotope is 24 ns, i.e. more than 2 Timepix clock cycles. Since the peak width of a single Timepix peak is  $\pm 5$  clock cycles, the detection of isotopes is practically inaccessible with the Timepix detector.

The single-stop TDC nature of the Timepix does not principally exclude isotope detection. Only isotopes impinging on the same pixels of the Timepix detector are not detected in the same acquisition frame. Since a Timepix spectrum is generated from multiple acquisition frames, a range of different particle masses are detected. Generally in MS, single-stop TDCs give a detection advantage to lighter particles.

### Improvement of $(\Delta m)_{50\%}$

Figure 5.6 investigates the broadening of Timepix peaks due to the TOF gradient throughout a single ion cluster. Since the entire cluster corresponds to one ion hit on the MCP, the lowest mass (shortest TOF) within a cluster indicates the

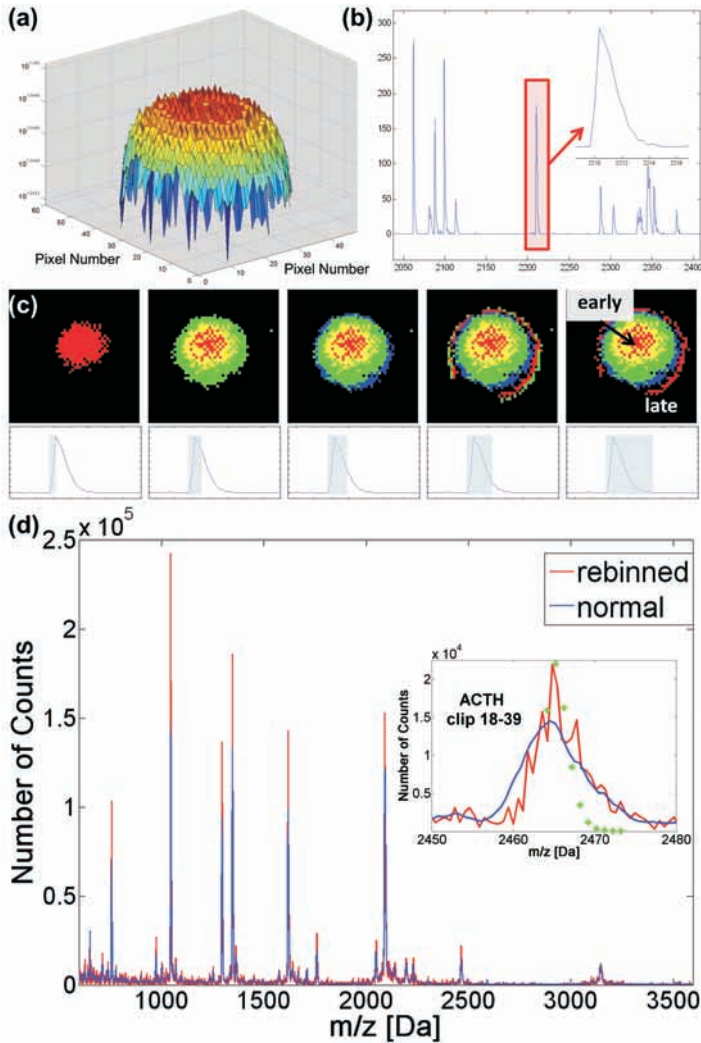


Figure 5.6: (a) The arrival time gradient sketches the 3D spatial evolution of the MCP electron cloud emitted by a single ion arrival. (b) Mass spectrum of a single laser shot on the peptide mix sample. A zoom on the peak ( $m/z=2,211$  Da) shows the broadened mass peak ( $\pm 5$  Da). (c) The MCP cluster evolves on the Timepix detector. (d) “Normal” (blue) and “rebinned” (=deconvoluted) (red) spectrum of the peptide standard. A zoom on ACTH clip 18-39 ( $m/z=2,465.1983$  Da mono isotopic mass) compares the “normal” and “rebinned” peak to the theoretical localization and abundance of the ACTH clip 18-39 isotopes (green).

actual ion mass. To extract this mass information from the Timepix data, the same mass value has to be assigned to all counts within a cluster. This effectively “rebins” the Timepix spectra by accumulating all counts of a broad Timepix peak in the first mass bin. In a single-laser shot spectrum, the width of a peak is then solely limited by the pixel clock. The Timepix data are “rebinned” on the single frame level. The spectrum of a full measurement is generated by adding several “rebinned” measurement frames. Additional peak broadening or a peak shift occurs due to clock cycle jitter between the pixel measurement clock, the external measurement shutter and the laser and is on the order of one to two clock cycles. The Timepix peptide spectrum (Figure 5.4a, highest MCP gain) is “rebinned” (Figure 5.6d). The “rebinning” increases the intensity difference between the smallest and highest peak in the accumulated spectrum from  $1.4 \cdot 10^5$  to  $2.4 \cdot 10^5$ . The  $(\Delta m)_{50\%}$  of the peaks is not significantly changed by the “rebinning”. By building up the total spectrum from several single laser shot spectra, it is statistically possible to record isotope distributions. The individual peptide peaks in the “rebinned” spectrum contain more structure (Figure 5.6d). However, the  $m/z$  bin width in this mass range ( $\pm m/z=2,465$  Da) is about 0.6 Da so that accurate isotope binning is hardly possible at this high mass.

### 5.3.3 Timepix Mass Range

The detectable mass range for our ion microscope combined with the Timepix detector is assessed using the ubiquitin sample. Since the bit depth of the Timepix detector limits the data acquisition to about  $118 \mu\text{s}$ , the ubiquitin spectrum is acquired in seven successive portions (TOF range  $540 \mu\text{s}$ ). These are acquired by introducing an increasing delay between the laser shot and the measurement interval. Due to some overlap in the spectra, it is possible to stitch together the full TOF spectrum. The spectrum (Figure 5.7) shows distinct spectral features up to the nonamer (77.1 kDa) of ubiquitin which demonstrates that a mass range up to 78 kDa is accessible at ion energies of 5 keV with the presented detection system. In conventional mass spectrometers, acceleration voltages well exceeding 5 keV (20 keV or more) are needed to obtain such a high mass sensitivity.

## 5.4 Conclusions

The application of a chevron MCP stack in combination with a bare Timepix chip for direct high dynamic range mass spectrometric imaging of peptides and proteins is demonstrated on an ion microscope. Unlike current commercial MSI detectors, the Timepix detector efficiently captures time-resolved images of a

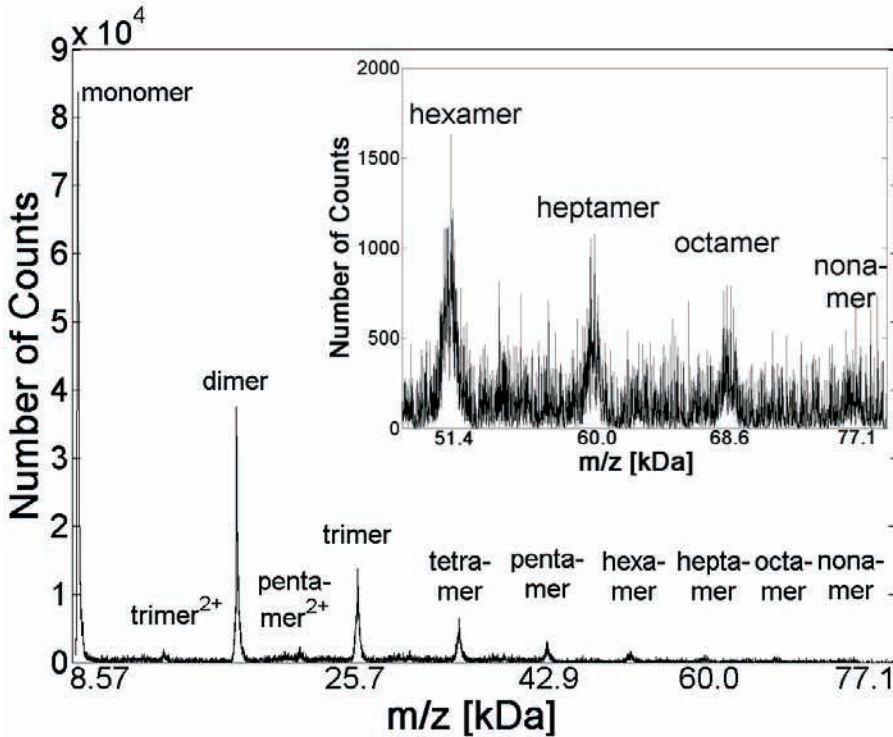


Figure 5.7: Ubiquitin spectrum up to 78 kDa.

wide range of  $m/z$  species in one measurement.

The comparison of Timepix-acquired spectra to “standard” acquisition techniques (TDC and ADC) reveals that the Timepix delivers an order of magnitude greater detectable range than an ADC and returns mass spectra for MCP gains from  $4 \cdot 10^5$ - $6.5 \cdot 10^6$ . The Timepix peak resolution at FWHM  $(\Delta m)_{50\%}$  and the detection of isotope peaks are limited by the 10 ns pixel clock cycle. On the TRIFT ion microscope, the Timepix assembly can detect oligomers of the protein ubiquitin up to 78 kDa.

The performance of the current Timepix detector is limited by the counter depth and the single-stop pixels. As a future perspective, we envisage a successor Timepix chip that incorporates 100 ps TDC bins, a 1 ms total measurement interval and multi- (double-) stop pixels. Standard TOF-MS detection systems are already shown to be outperformed by several unique Timepix system capabili-

ties demonstrated in this chapter. These are the combination of S/N, multiplexed detection, dynamic range and the simultaneous detection of position- and time-information by a single detector system. The combination of this MCP/Timepix detection system and an ion microscope constitutes an extremely powerful MSI instrument for high dynamic range, high mass range and high detector homogeneity studies of intact proteins of biomolecular relevance.

# 6

## Biological Tissue Imaging with a Position and Time Sensitive Pixelated Detector

*We demonstrate the capabilities of a highly parallel, active pixel detector for large-area, mass spectrometric imaging of biological tissue sections. A bare Timepix assembly (512×512 pixels) is combined with chevron microchannel plates on an ion microscope matrix-assisted laser desorption/ionization time-of-flight mass spectrometer (MALDI TOF-MS). The detector assembly registers position- and time-resolved images of multiple  $m/z$  species in every measurement frame. We prove the applicability of the detection system to biomolecular mass spectrometry imaging on biologically relevant samples by mass-resolved images from Timepix measurements of a peptide-grid benchmark sample and mouse testis tissue slices. Mass-spectral and localization information of analytes at physiological concentrations are measured in MALDI TOF-MS imaging experiments. We show a high spatial resolution (pixel size down to  $740 \times 740 \text{ nm}^2$  on the sample surface) and a spatial resolving power of  $6 \mu\text{m}$  with a microscope mode laser field of view of  $100\text{--}335 \mu\text{m}$ . Automated, large-area imaging is demonstrated and the Timepix' potential for fast, large-area image acquisition is highlighted.*

### 6.1 Introduction

Mass spectrometry imaging (MSI) [3, 36, 217, 221] measurements target the identification and localization of molecules from complex surfaces [6, 63–68]. Over the past decade, MSI has developed into a widely used analytical tool for biomolecular and biomedical research. This is achieved as a result of technological developments and improvements in the areas of high spatial resolution, high mass accuracy and high sample throughput [138]. Matrix-assisted laser desorption/ionization (MALDI) time-of-flight (TOF) MSI is commonly used for biomolecular and biomedical studies because of the possibility for high spatial

resolving powers and a wide accessible mass range at high acquisition speeds. There are two major types of MALDI TOF-MSI: Microprobe and microscope mode experiments. At present, commercial MALDI-MSI instruments for high throughput microprobe MSI studies are readily available. In MALDI microprobe MSI, a highly focused pulsed desorption/ionization laser beam probes the sample surface. A full mass spectrum is generated at every raster point. An image is reconstructed after the experiment with a pixel resolution equivalent to the beam size (provided the stepping size/accuracy of the sample/beam movement is not limiting). Highly focused ultra-violet/infra-red laser beams [65–68] have returned pixel sizes below  $7\ \mu\text{m}$ . In particular, the Spengler group has achieved a spatial resolution of less than  $1\ \mu\text{m}$  with a tightly focused ultra-violet laser beam [67]. Disadvantages of small surface probe areas include long measurement times and the loss of sensitivity due to low laser fluence for desorption and ionization. MALDI microprobe MSI at a lateral resolution better than the laser spot size has been demonstrated by over-sampling [69].

Recent studies in microprobe mode MSI have focused on the improvement of sample throughput to obtain more practical large-area or spatial resolution conditions. McDonnell and co-workers use an automatic sample loading system for time-efficient, round-the-clock spectrometer operation [19]. Alternatively, high throughput can be achieved by an increase in the raster/laser frequency. This results in a decrease in the measurement time without sacrificing analytical information. The Caprioli group has reduced the measurement time by up to a factor of two by operating a MALDI TOF-MSI system in a continuous scanning mode at a comparatively high laser repetition rate of about 5 kHz [75]. Stoeckli and co-workers measured images of drug distributions in rat sections within less than 15 minutes with a 1 kHz laser repetition rate and a raster speed of about 18 mm/s [76].

MALDI microscope mode MSI is an alternative approach to microprobe mode imaging [6, 156]. In the microscope mode, a large surface probe desorbs and ionizes surface molecules over a large sample area, typically 200–300  $\mu\text{m}$  in diameter. The large field of view in microscope mode MSI enables fast, large-area image acquisition at high spatial resolution [74]. An ion microscope uses ion optics to project the desorbed/ionized surface compounds onto a position-sensitive detector. Importantly, the initial ion distribution is magnified and the lateral spatial organization of the surface molecules is retained on the flight path to the detector. While the ionization spot size determines the obtainable spatial resolution in microprobe mode, the spatial resolution in microscope mode is decoupled from the ionization spot size. Rather, the spatial resolution is determined by the quality and the capabilities of the ion optics in combination with a position- (and time-) sensitive detector. Spatial resolving powers on the order of  $4\ \mu\text{m}$  have been achieved where a 10  $\mu\text{m}$  charge-coupled device (CCD) camera pixel

probed 1  $\mu\text{m}$  on the sample surface [6].

A large desorption/ionization spot size ensures high throughput in microscope mode MSI. The microscope mode ionization beam size of about 200-300  $\mu\text{m}$  is about one hundred times larger than a typical high spatial resolution microprobe mode desorption/ionization spot size. Hence, analyzing an area of  $200 \times 200 \mu\text{m}^2$  corresponds to one measurement in microscope mode MSI. In microprobe mode, the analysis of the same area corresponds to 40,000 measurements, which would be significantly more time consuming at the same experimental repetition rate. The large ionization spot in microscope mode MSI can result in large ion loads on the detection system, which can lead to detector saturation. As a remedy, the ion generation is reduced (by, for instance, decreasing the laser power) and the integration time is increased to ensure adequate ion imaging. This effect can be counteracted with high desorption/ionization repetition rates and detector technology that can accommodate high ion loads. MALDI-TOF ion microscopes enable fast, automated, high resolution large-area imaging provided that adequate, i.e. position- (possibly time-) sensitive and fast, detector systems are used to record high quality molecular images [70].

Many ion microscope implementations project the ions on a position-sensitive detector assembly, which is traditionally a microchannel plate (MCP) followed by a phosphor screen and a CCD camera system [6] or a resistive/delay-line anode [72, 77]. The MCP, phosphor screen, CCD camera detection system cannot link the ion arrival time (i.e. the molecular weight in TOF-MSI) to the spatial distribution. Typically, different molecular masses cannot all be measured in one acquisition but must be mass-selected for imaging. The information on the sample composition and associated spatial distribution is obtained by combining several mass-selected images from separate measurements. Delay-line detectors deliver space- and time-resolved information. Additionally, they have the advantage of precise ion arrival time measurements [78]. Alternatively, techniques are available for arrival time measurement via a decoupling circuit from the MCP stack [79]. Delay-line detectors still lack sufficient multi-hit capabilities for MALDI-MSI. Also, the reconstruction of the mass-resolved images is time-consuming, which renders ion optical tuning difficult due to the lack of direct image feedback.

Imaging detector technology has acquired an important role in biological, biomolecular and biomedical MSI. In-vacuum pixel detectors, which allow for position- [73, 81] and time-resolved [70, 73, 83] photoelectron and ion imaging, have been increasingly used in the past few years. Brouard and co-workers have implemented an adapted velocity map imaging apparatus in combination with a fast framing CCD camera for microscope mode MSI [168]. In this alternative setup, a detector pixel probes 56  $\mu\text{m}$  on the sample surface and a mass resolution of 5 Da was reported in the mass range from 300-500  $m/z$ .

Recently, we demonstrated the successful implementation of MCP/Medipix 2 [73]

and MCP/Timepix [70] imaging detector assemblies for MSI at a spatial resolving power of few micrometers. In these experiments, a fully-integrated, solid state pixel detector of the Medipix/Timepix [84–86] detector family was combined with a chevron MCP and installed on an ion microscope imaging mass spectrometer. The major characteristics of this application-specific integrated circuit (ASIC) are  $256 \times 256$  pixels of  $55 \times 55 \mu\text{m}^2$  each per chip, no electronics noise and per pixel functionality. On the pixel level, the Timepix detector can be programmed to return both the position of impact of a particle (via the pixel address) and the time-of-flight of this particle (with respect to an external trigger, with a maximum time resolution of 10 ns). Thereby, the Timepix detector alleviates the need of mass-selection and repetitive measurements that were required with systems that could not measure the time-of-flight (i.e. an MCP/phosphor screen assembly). In a single experiment, mass-resolved images were acquired using this new setup [73]. These earlier experiments focused on the imaging capabilities and image quality of the Medipix 2 pixelated detector for MSI [73]. Further, the mass spectral capabilities of the Timepix system were investigated, with respect to the detectable mass range and the sensitivity [70]. It was demonstrated that the pixelated detector unit facilitates the parallel detection of multiple molecular species and significantly reduces the measurement time for large-area, high resolution molecular imaging experiments.

The present work discusses the first results of an MCP/Timepix detector assembly for large-area, high resolution biological tissue imaging on a MALDI-TOF ion microscope mass spectrometer. In particular, the spatial resolution, the image quality and the analytical capabilities of an MCP/Timepix assembly in biological MSI are determined and discussed. The implementation of automated, large-area microscope mode MSI is demonstrated on mouse testis tissue sections. Large-areas of tissue are rastered by the microscope beam and individual images (from each microscope mode position) are stitched together. The Timepix' potential for fast, large-area image acquisition is highlighted.

## 6.2 Methods

### 6.2.1 The Medipix/Timepix Detectors and the Imaging Setup on the Ion Microscope

The ASIC detection system and ion microscope used for the research presented in this chapter is equivalent to the one described in Chapter 5. For the experiments presented in this chapter, the MCPs are biased at a voltage of 1.85 kV (standard sample) and 2.25 kV (tissue sample), which corresponds to an MCP gain of  $10^6$  and  $5 \cdot 10^7$ , respectively. The voltage between the MCP back and the chips was

set to 0.6 kV. Typically the charge of one MCP electron shower is divided among multiple Timepix pixels. This effect and its relation to the dynamic range of the detection system were discussed previously [70] (Chapter 5).

## 6.2.2 Timepix-Generated Spectra

In this work, the Timepix ASIC is operated exclusively in TOF mode. The master trigger of the TRIFT-MS ion microscope triggers both the detection system and the MALDI laser so that one measurement frame of the Timepix detector corresponds to the image and spectral information from one laser shot (the trigger scheme was described previously [70]). The  $512 \times 512$  ( $=262,144$ ) pixels act as individual parallel detectors, which each deliver the position (x- and y- pixel coordinate) and the TOF of an event per measurement frame (i.e. the Timepix pixels are single-stop time-to-digital converters). The data of every measurement frame is saved in a separate sparse data file that contains the pixel address and the corresponding TOF. Timepix-acquired TOF spectra are built by filling the TOF values of several measurement frames into a histogram. This TOF spectrum is mass-calibrated using calibration coefficients calculated from a standard mixture sample. The maximum TOF interval of  $118 \mu\text{s}$ , its relation to the accessible mass range and how wide mass range measurements can be set up by stitching together shorter spectral acquisitions have been discussed in reference [70] (Chapter 5).

## 6.2.3 Timepix-Generated Large-Area Images

Total ion images are generated by summation of multiple single-frame position measurements. Mass-selected images are generated by extracting the pixel positions corresponding to a particular mass peak (i.e. TOF) from the data set. Large-area “mosaic mode” images are generated by probing a macroscopic area on the sample surface with the diffuse ( $\phi=100\text{-}335 \mu\text{m}$ ) laser beam as a surface probe. For example, an area of about  $2 \times 2 \text{ mm}^2$  is analyzed in  $32 \times 32$  “mosaic” tiles. Per mosaic tile, the images/TOF information corresponding to 150-300 laser shots are collected. Then, the stage is moved by  $62.5 \mu\text{m}$  ( $=2 \text{ mm}/32$ ) and the next acquisition is started via the TRIFT II control software (Wincadence, version 4.4.0.17, ULVAC-PHI, Inc., 2008). The MALDI laser spot used here has an elliptical shape, thus the oversampling between the acquisition of tile  $n$  and  $n+1$  ensures that the full sample surface is probed. A home-built software package developed in Matlab (Matlab, Mathworks, Natick, USA; version 7.110.584, R2010b, 32-bits) stitches the mosaic images into a large-area image by partially overlapping the images of the individual tiles. In the “overlap region” pixel intensities are corrected for double-counting by averaging. The program converts the data set into the format of the AMOLF Datacube Explorer [111], which is

used for data analysis. Larger surface areas can be analyzed using larger mosaics or by stitching together a number of smaller-area mosaics.

## 6.2.4 Samples

All samples were prepared on indium-tin-oxide (ITO) coated glass slides. A grid benchmark sample was prepared to assess the spatial resolving power of the system. A nickel hexagonal thin bar transmission electron microscopy (TEM) grid (700 mesh, G2760N, 3.05 mm diameter, 37  $\mu\text{m}$  pitch, 8  $\mu\text{m}$  bar width; Agar Scientific Limited, Stansted, UK) was placed on top of a 2  $\mu\text{l}$  droplet of 1:1 (by volume) mixture of Bruker Peptide Calibration Standard II (Chapter 5, Table 5.1, Bruker GmbH, Bremen, Germany) and 2,5-dihydroxybenzoic acid (DHB; 20 mg/ml in 50% methanol, 50% water, 0.02% TFA).

Mouse testicle (Harlan Laboratories, Boxmeer, The Netherlands; male balb/c mouse) were chosen as biologically relevant benchmark tissue samples. The mouse testis was cryo-sectioned to 20  $\mu\text{m}$  thickness and thaw mounted on an ITO slide. The tissue slices were optically scanned prior to the MS experiments (Mirax Virtual Slide Scanner, Carl Zeiss AG, Oberkochen, Germany). To ensure small matrix crystals, the tissue was coated with a homogeneous layer of DHB matrix (10 mg/ml DHB in 50% methanol, 50% water, 0.02% TFA) with a home-built pneumatic spray device similar to that described by [223] (Figures 6.3-6.5). For large-area MS imaging (Figure 6.6), DHB (20 mg/ml DHB in 50% methanol, 50% water, 0.02% TFA) was applied with the Bruker ImagePrep, which allows fast, large-area matrix coverage at matrix solution droplet sizes of  $\sim 50\text{-}80$   $\mu\text{m}$ .

## 6.3 Results and Discussion

### 6.3.1 Imaging Capabilities

The peptide-TEM grid sample is used to test the large-area imaging capabilities. In particular, the image quality of the stitched mosaic microscope mode image and the spatial resolution is assessed. In this experiment, an automated microscope mode acquisition of  $32 \times 32$  tiles is used. The ion microscope probes an area of  $2.24 \times 2.24$   $\text{mm}^2$  with a raster of 70.1  $\mu\text{m}$  between tiles at a magnification factor of about  $62\times$ . At this magnification factor, each Timepix pixel probes  $880 \times 880$   $\text{nm}^2$  on the sample surface. One hundred individual Timepix acquisition frames corresponding to 100 laser shots are acquired per position and integrated offline. The peptide standard spectrum of this experiment contains the expected peptide peaks in the mass range  $700 < m/z < 3,500$  (data not shown). The spectral quality is in accordance with the time resolution of the Timepix detection system and has been investigated and discussed in detail elsewhere [70]. Figure 6.1 displays

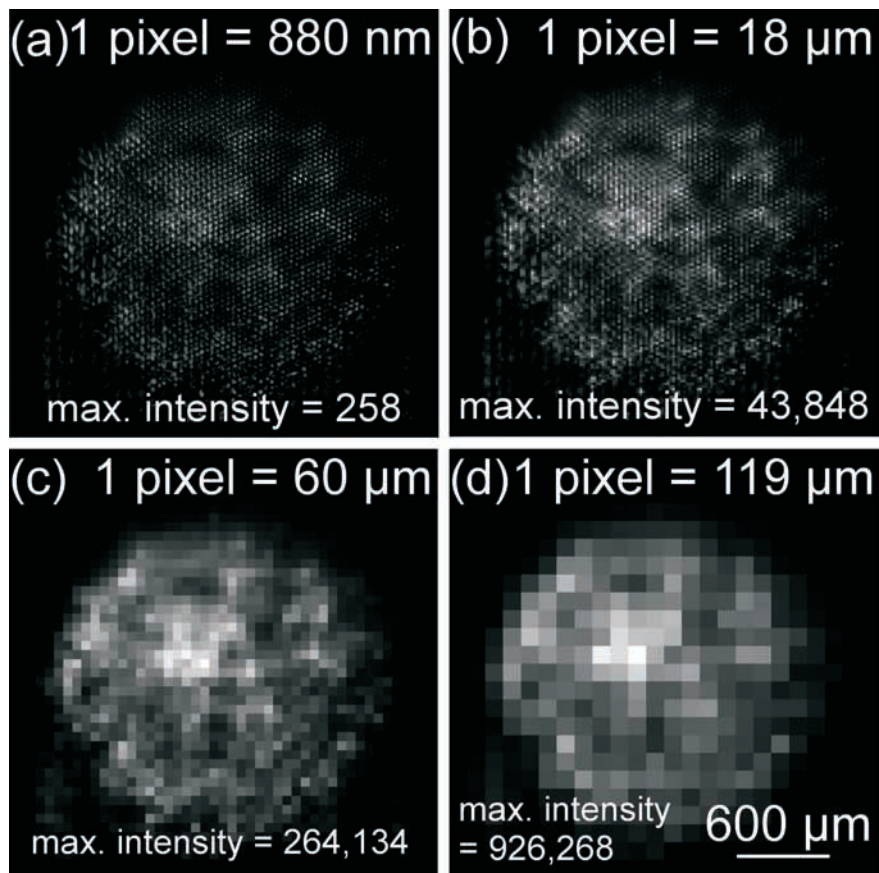


Figure 6.1: Total ion image of the peptide standard-TEM grid sample. The image is composed by stitching together  $32 \times 32$  microscope mode images. (a) Full Timepix resolution, one detector pixel probes  $880 \times 880 \text{ nm}^2$  on the sample surface. (b,c,d) Images at different image resolutions obtained from the same experiment by spatially binning the Timepix data.

the stitched “mosaic” images of a microscope mode MSI experiment on the peptide standard-TEM grid sample at four different pixel sizes. At the full spatial resolution, i.e. when one detector pixel probes  $880 \times 880 \text{ nm}^2$  on the sample surface, the image is composed of  $3,147 \times 3,147$  pixels (Figure 6.1a). This number of pixels is about 7 times higher than the number of pixels on a standard modern computer screen and corresponds to about 28,800 dots per inch. Hence, to fully appreciate the amount of detail revealed by the high spatial resolution, part of the mosaic image can be zoomed into (Figure 6.2). The inhomogeneity of the intensity across the stitched total ion image originates from inhomogeneities in the amount of analytes located in the different areas underneath the TEM grid. The high resolution, large-area microscope mode image obtained at Timepix resolution (Figure 6.1a) is contrasted with images of the sample at lower spatial resolutions. Figure 6.1 displays the stitched mosaic image at resolutions where one pixel probes  $18 \times 18 \mu\text{m}^2$  (Figure 6.1b),  $60 \times 60 \mu\text{m}^2$  (Figure 6.1c) and  $119 \times 119 \mu\text{m}^2$  (Figure 6.1d) on the sample surface. These images are obtained by spatially binning the Timepix-acquired data. In particular, one pixel probes  $18 \times 18 \mu\text{m}^2$  if the counts of  $20 \times 20$  Timepix pixels are binned into a single pixel. Similarly, one pixel probes  $60 \times 60 \mu\text{m}^2$  or  $119 \times 119 \mu\text{m}^2$  on the sample surface if the counts of  $68 \times 68$  and  $135 \times 135$  Timepix pixels are binned into a single pixel. The comparison between the different spatial resolutions demonstrates the increase of spatial detail that is revealed with the increase of the spatial resolution.

The peptide mixture underneath the TEM grid is clearly observed in the image at full Timepix resolution ( $880 \times 880 \text{ nm}^2$ ) and with somewhat less detail at the  $18 \times 18 \mu\text{m}^2$  pixel size. At the pixel sizes of  $60 \times 60 \mu\text{m}^2$  and  $119 \times 119 \mu\text{m}^2$ , the image spatial resolution ranges in regime of standard, commercial MALDI microprobe instruments. At these pixel sizes, the spatial resolution is insufficient to reveal the structure of the TEM grid. The signal intensities displayed in Figure 6.1 represent absolute measurement intensities and are not scaled. As expected, the image contrast is better at larger pixel sizes (maximum intensity= $926,268$ ) than at full resolution (maximum intensity= $258$ ) since the same number of ion counts on the detection system is displayed in less spatial bins.

Note that the intensity values represent relative intensities. No conclusions should be drawn from the absolute intensity values delivered by the Timepix detection system. The Timepix pixels are single-stop time-to-digital converters, i.e. each pixel can accommodate one count per measurement frame and is blind for other ions to arrive later in time-of-flight during the same measurement frame. Operation in a moderate count rate regime minimizes this effect. Figure 6.2 is used to assess the image spatial resolution at full Timepix resolution, i.e. 1 detector pixel probes  $880 \times 880 \text{ nm}^2$  on the sample surface. Figure 6.2a displays a line scan through part of the high resolution image. Figure 6.2b shows a zoom on part of the full resolution Timepix image, where the position of the line scan

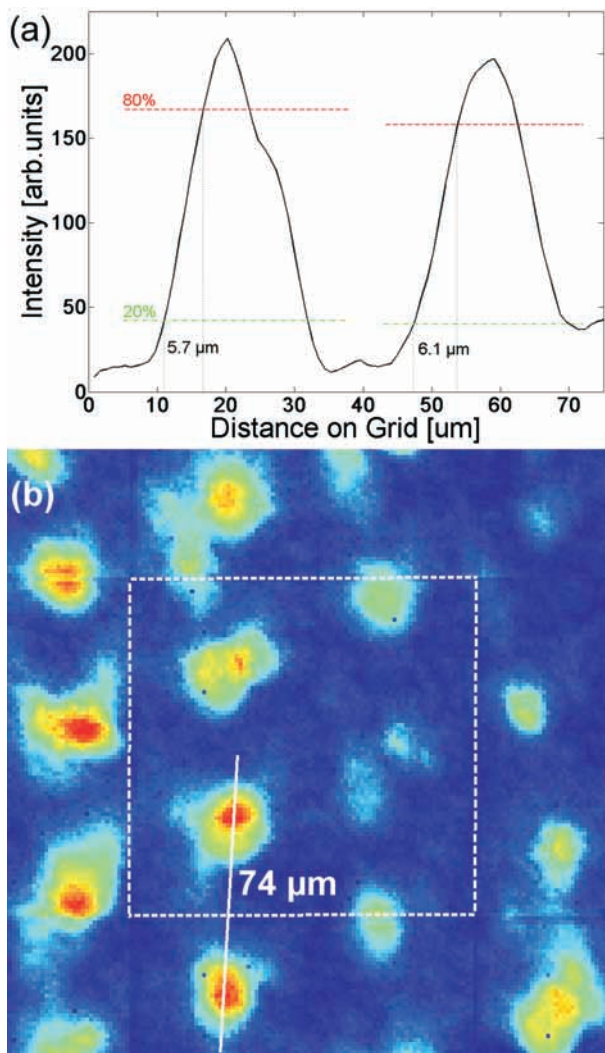


Figure 6.2: (a) Line scan through the image of the peptide mixture-TEM grid sample to assess the spatial resolving power of the imaging setup. The red and green lines indicate 80% and 20% of the maximum peak intensity, respectively. The spatial resolving power is defined as the distance between these two points. (b) Zoom on part of the high resolution image of the peptide standard-TEM grid sample. One pixel in the image corresponds to  $880 \times 880 \text{ nm}^2$  on the sample surface. The line used to generate (a) is shown in white.

is indicated. The line scan spans a distance corresponding to  $74\ \mu\text{m}$  on the TEM grid sample such that two grid cells (pitch  $37\ \mu\text{m}$ ) are included. The spatial resolving power, i.e. sharpness of a feature edge, has previously been defined as the distance between 20% to 80% signal intensity of a feature within an image [3]. With this criterion, a spatial resolving power of  $\sim 6\ \mu\text{m}$  is achieved with the ion microscope in combination with the Timepix detection system. A spatial resolving power on this order of magnitude is expected (i.e. not 880 nm) due to the need for multiple pixels to resolve the feature. Specifically, the MCP electron showers create signal clusters of about 6-10 pixels in diameter on the Timepix detector. Such a cluster corresponds to (cluster diameter·pixel size)/(magnification factor)  $\mu\text{m}$  on the sample surface, i.e.  $(6\cdot 55\ \mu\text{m})/62=5.3\ \mu\text{m}$  to  $(10\cdot 55\ \mu\text{m})/62=8.9\ \mu\text{m}$ . A decreased cluster size would result in a higher spatial resolving power. In addition, large DHB matrix crystals due to the dried droplet sample application can decrease the image resolution. To fully exploit the benefit of the high spatial resolution, significant sample preparation effort is required to ensure that the spatial resolution is not hampered by the sample treatment. This would occur if the matrix crystal size was significantly larger than the achievable pixel size is [223]. The subtle vertical and horizontal lines in Figure 6.2b represent artifacts from the stitching of the mosaic tiles (one tile is emphasized by the broken white lines) and can be removed using smoothing algorithms that have not been applied in these raw images. Note that the borders of these lines define the area of a single measurement tile. Also note that the peptide mixture deposited underneath the metal TEM grid unlike the metal grid itself is readily ionized in this MALDI-MSI experiment, which leads to broadening of this image feature.

### 6.3.2 Spectral Capabilities on Tissue

The spectral capabilities of the detection system on biological tissue samples are investigated with the mouse testicle sample. Figure 6.3 shows a mass spectrum from 93,000 integrated Timepix acquisition frames (i.e. 93,000 laser shots) at a spectral bin size of 1 Da (the interested reader is referred to [70] for a detailed evaluation of the spectral capabilities of the MCP/Timepix detection system). The spectrum is obtained by integrating eight selected-area images that are similar to the two images displayed in Figure 6.4. This number of acquisition frames corresponds to probing about 7% of the testis surface area. The total ion spectrum was baseline subtracted with a linear regression method (window size 5 points, step size 3 points). Ions between 700-900  $m/z$  can be attributed to commonly observed lipid species, which demonstrates that spectral analysis at physiological analyte concentrations on tissue is feasible with this Timepix-based detection system. The inset of Figure 6.3 displays the spectrum at  $1,500 < m/z < 7,130$ . In this  $m/z$  region, distinct peaks are observed which shows that species beyond the

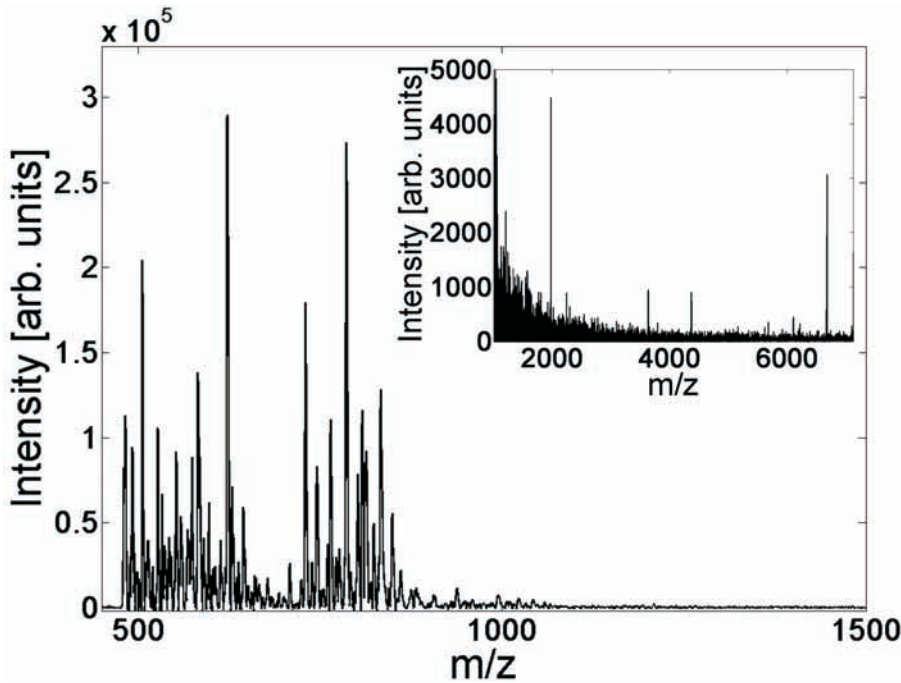


Figure 6.3: Summed, baseline subtracted mass spectrum from 93,000 acquisition frames from mouse testis measured with the Timepix. Many ions are observed in the lipid mass range (700-900  $m/z$ ) and the zoom inset shows higher mass ions.

lipid mass range are accessible with the Timepix-based detection system.

### 6.3.3 Mass-Selected Imaging on a Biological Sample

The imaging capabilities of the detection system are tested on the mouse testis sample. Figure 6.4a displays an optical scan of the tissue slice that is used for the MS imaging experiment. The sample was coated with DHB by a pneumatic sprayer to ensure small matrix crystals of  $\sim 10 \mu\text{m}$  in length. Two large-area acquisitions are carried out at an ion optical magnification factor of  $75\times$ . The experiment shown in Figure 6.4b,c probes an area of  $0.5\times 0.5 \text{ mm}^2$  with  $8\times 8$  microscope mode mosaic tiles. The tile-to-tile raster shift is  $62.5 \mu\text{m}$  and 150 Timepix images (i.e. laser shots) are acquired per tile. The second experiment (Figure 6.4d,e) images an area of  $1\times 1 \text{ mm}^2$  with  $16\times 16$  microscope mode mo-

saic tiles. The tile-to-tile raster is  $56.3\ \mu\text{m}$  and 150 Timepix acquisition frames (i.e. laser shots) are collected. Figure 6.4 displays the total ion image of these experiments (Figure 6.4b,d) and corresponding mass-selected ion images (Figure 6.4c,e).

The images are displayed at the full Timepix resolution and are scaled to 25% of the maximum pixel intensity for increased image contrast. The mass-selected images clearly reveal the distribution of biomolecular analytes at physiological concentrations from the tissue surface. The detection of these analytes at the current acceleration voltage of the ion microscope of 5 keV demonstrates the sensitivity of the detection system.

The total ion image of the  $16\times 16$  mosaic shows image artifacts due to detector saturation. The count rates in this MALDI experiment are high, which results in detector saturation effects that are observed in some tiles as the vertical flares in Figure 6.4d. This detector saturation effect can be eliminated from the data set in two ways. First, the mass-selected images do not contain the saturation effects. The pixels that are in saturation do not return valid TOF/mass spectral information and can be excluded by this criterion. Secondly, the Timepix acquisition frames that contain saturated images contain significantly more pixel counts than the average MALDI frame, in which about 40-70% of the Timepix pixels are triggered. Hence, the corresponding data files are larger in size and can be excluded from further analysis by this criterion. Note that the detector saturation effect prevents the detection of ion events in this area of the detection system and hence distorts the ion optical image and relative image intensity.

Accurate peak assignment remains challenging with the Timepix detection systems in combination with the TOF mass spectrometer. The Timepix clock cycles of 10 ns result in wide mass bins and wide peaks in the spectrum. Thus, the current mass resolution does not enable analyte identification, as outlined in [70] (Chapter 5). Successor chips with a higher time resolution will improve the capabilities for mass assignment significantly. Figure 6.4c shows mass-selected images with  $m/z=491-495$  (blue),  $m/z=595-599$  (green),  $m/z=621-624$  (red) for the  $8\times 8$  mosaic. Figure 6.4e displays mass-selected images with  $m/z=504-507$  (green) and  $m/z=621-624$  (red) for the  $16\times 16$  mosaic. The analyte at  $m/z=621-624$  might be heme, since the optical image in Figure 6.4a displays blood in the area where the analyte is localized in the mass-selected image. The walk “discrepancy” in the mass relates to the above mentioned limitations. The  $m/z=595-599$  analytes might be a di-acyl-glycerol.

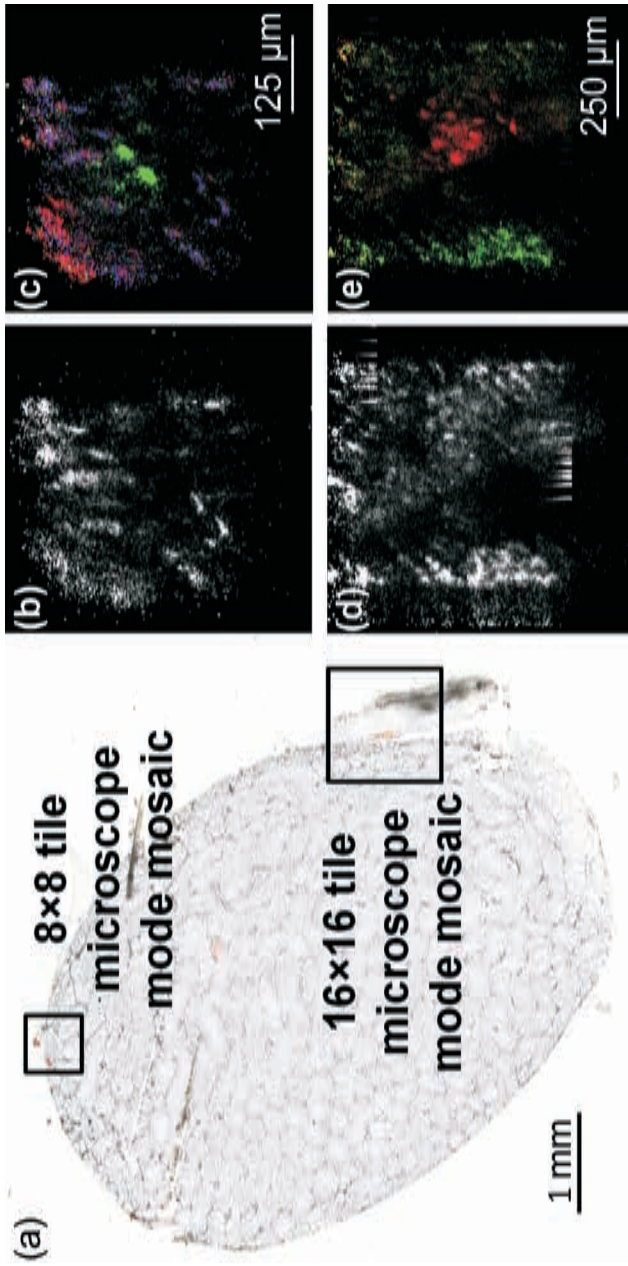


Figure 6.4: (a) Scan of the mouse testis tissue sample. The black squares indicate two areas which have been imaged with the Timepix detection system on the MS ion microscope. (b) Total ion image from the  $8 \times 8$  ( $0.5 \times 0.5 \text{ mm}^2$ ) mosaic, (c) mass-selected images with  $m/z=491-495$  (blue),  $m/z=595-599$  (green),  $m/z=621-624$  (red) for the  $8 \times 8$  mosaic, (d) total ion image from the  $8 \times 8$  ( $1 \times 1 \text{ mm}^2$ ) mosaic and (e) mass-selected images with  $m/z=504-507$  (green) and  $m/z=621-624$  (red) for the  $16 \times 16$  mosaic.

### 6.3.4 Advantages of Microscope Mode Imaging for High Spatial Resolution

The capabilities of high spatial resolution imaging are investigated in closer detail in the  $8\times 8$  microscope mode mosaic on the mouse testis sample (Figure 6.4b,c). Figure 6.5 shows the total ion image and mass-selected ion images of this mosaic at different pixel sizes. At the ion optical magnification factor of about  $75\times$  and at the full Timepix resolution, one Timepix pixel probes  $740\times 740\text{ nm}^2$  on the sample surface (Figure 6.5a, scaled to 25% of the image intensity for increased image contrast). The Timepix acquired data is spatially binned by combining the counts of  $20\times 20$  (pixel size:  $15\times 15\text{ }\mu\text{m}^2$ , Figure 6.5b),  $68\times 68$  (pixel size:  $50\times 50\text{ }\mu\text{m}^2$ , Figure 6.5c), and  $135\times 135$  ( $100\times 100\text{ }\mu\text{m}^2$ , Figure 6.5d) pixels, respectively. The comparison between the different spatial resolution images demonstrates that accurate analyte localization is only ensured at the fine pixel pitches. In particular, the two distinct areas of the analytes at  $m/z=595-599$  (displayed in green) is not resolved by the pixel sizes of  $50\times 50\text{ }\mu\text{m}^2$  and  $100\times 100\text{ }\mu\text{m}^2$ , respectively. The pixel size of  $15\times 15\text{ }\mu\text{m}^2$  and the pixel size of  $740\times 740\text{ nm}^2$  in even greater detail reveals the spatial structure of this analyte.

### 6.3.5 Large-Area Imaging and Throughput Capabilities

Large-area tissue imaging typically targets areas of several square centimeters. Fast, automated MSI technology is required to ensure high throughput experiments. The Timepix detection system in combination with a high frame rate readout system is a potential candidate for high throughput MSI experiments. In the proof-of-principle setup presented here, however, the full potential of the Timepix system cannot be exploited as it could be in a dedicated measurement system, due to data readout limitations.

Figure 6.6 displays mass-selected images from a selected-area imaging experiment on the mouse testis sample. The field of view is  $1.8\times 1.8\text{ mm}^2$ , which corresponds to about 11% of the area of the mouse testis section. This area is imaged in  $32\times 32$  microscope mode mosaic tiles at a raster of  $56.3\text{ }\mu\text{m}$ . The ion optical magnification factor is  $75\times$  such that the pixel resolution corresponds to  $740\times 740\text{ nm}^2$  on the sample surface. Per position, 150 frames corresponding to 150 laser shots are acquired. This typical imaging experiment is based on a total of  $32\times 32\times 150=153,600$  laser shots. At a repetition rate of 10 Hz, this corresponds to a measurement time of 4 hours and 20 minutes. If the experimental repetition rate was 1 kHz, the measurement would only take 2.5 minutes. This means that the entire mouse testicle section ( $5.4\times 5.4\text{ mm}^2$ ) could be measured within a microscope mode MSI experiment of about 23 minutes. For comparison, a microprobe experiment under the same experimental conditions takes significantly longer due to the small ionization probe size. An ionization probe of about

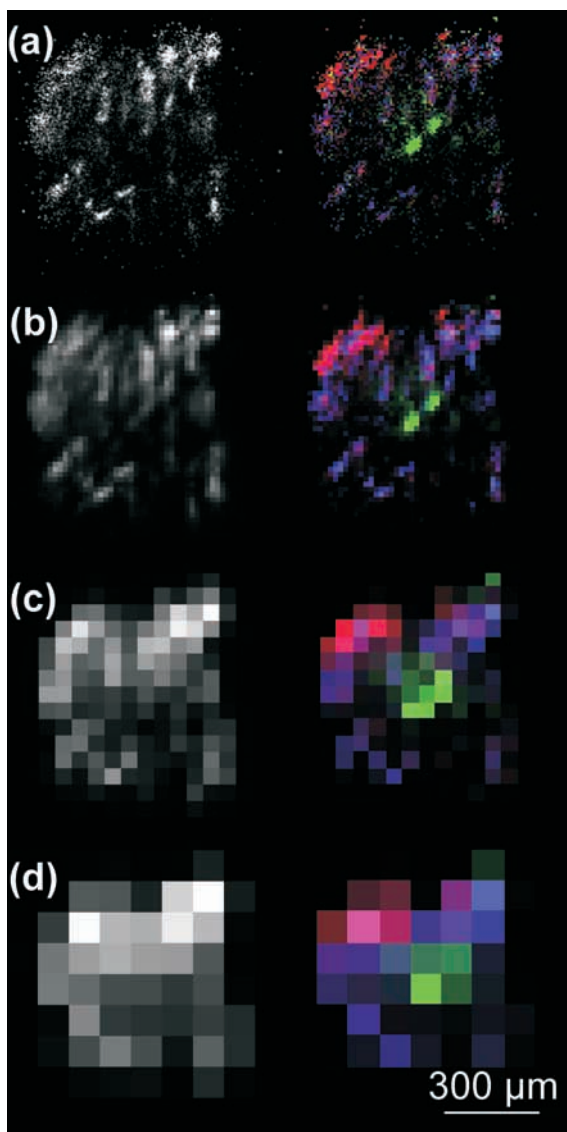


Figure 6.5: Mouse testis selected-area images at different pixel sizes: 1 pixel probes (a)  $740 \times 740 \text{ nm}^2$ , (b)  $15 \times 15 \text{ } \mu\text{m}^2$ , (c)  $50 \times 50 \text{ } \mu\text{m}^2$  and (d)  $100 \times 100 \text{ } \mu\text{m}^2$  on the sample surface. (left) total ion images. (right) mass-selected images with  $m/z=491-495$  (blue),  $m/z=595-599$  (green),  $m/z=624-624$  (red).

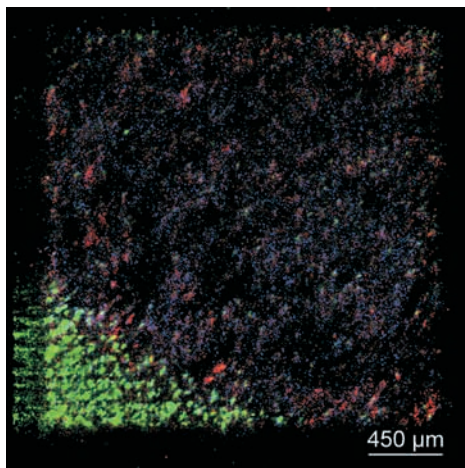


Figure 6.6: Mass-selected mouse testis images at the full Timepix resolution. The field of view is  $1.8 \times 1.8 \text{ mm}^2$  ( $32 \times 32$  microscope mode mosaic tiles,  $2,868 \times 2,868$  pixels) and one pixel probes  $740 \times 740 \text{ nm}^2$  on the sample surface. The selected analyte mass range of  $m/z=320\text{-}322$  (green) appears to be matrix-related since it is observed off-tissue and  $m/z=618\text{-}621$  (red) might correspond to heme. The analyte at  $m/z=726\text{-}729$  (blue) is most likely a lipid. The mass range was blanked below  $m/z$  300. (Note that the color scheme used here is not the same as in Figure 6.4 and 6.5.)

$3 \mu\text{m}$  results in  $(1.8 \text{ mm}/3 \mu\text{m})^2=360,000$  measurement positions. Hence, the experiment requires about  $360,000 \times 150=54,000,000$  laser shots and takes about 350 times longer than a microscope mode experiment.

The main limiting factor to the throughput of the Timepix system is the repetition rate which is determined by the repetition rate of the readout system in combination with the readout software package. Since the chip itself can, in principle, be readout within  $300 \mu\text{s}$  (parallel readout through the 32-bit CMOS lines [86]), repetition rates of 1 kHz are feasible. Within the *Medipix collaboration*, several readout interfaces are under development to specifically target high frame rate applications (see Chapter 3). For the Medipix 2 chip, there are the “Parallel Readout Image Acquisition for Medipix” (PRIAM) and the “Dear-Mama Acquisition System” (DEMAS) systems for reading out frames at kilohertz [212] and 500 Hz [213] frame rates, respectively. Recently, the Berkeley quad Timepix parallel readout [173] was presented. It is a highly parallel readout system dedicated to the readout of  $2 \times 2$  Timepix ASICs at a frame rate of 1 kHz. These readout systems would enable high throughput MSI measurements for the Timepix system described herein. However, the applicability of these kHz readout systems

for MALDI-TOF count rates needs to be investigated.

## 6.4 Conclusions and Outlook

Mass spectrometry imaging (MSI) on biologically relevant samples was shown using a chevron microchannel stack in combination with a bare Timepix application-specific integrated circuit on an ion microscope mass spectrometer. Unlike commercial MSI detection systems based on a MCP, phosphor screen and charge-coupled device camera, this novel detection system provides two-dimensional imaging information, i.e. localization and arrival time measurements ( $m/z$  of the ions) from a single detection system within every single measurement frame. Hence, the Timepix facilitates faster MSI measurements by removing the need for repetitive measurements on different  $m/z$ -species.

The spatial resolution of this detection system on the ion microscope results in pixel sizes of  $740 \times 740$ - $880 \times 880$  nm<sup>2</sup> and a spatial resolving power of about 6  $\mu$ m. The imaging capabilities on biologically relevant samples indicate the system's potential for biomolecular and biomedical MSI, since significantly more structure can be resolved with the Timepix system in microscope mode than at commercially available pixel sizes. Mass-selected images can be generated and the mass spectra show high signal-to-noise ratios. The mass resolution is in accordance with the expectations for a 100 MHz measurement clock.

The throughput of the current Timepix detector in large-area imaging is limited by the low repetition rate of the readout system. Readout systems that perform two orders of magnitude faster repetition rates are feasible and need to be tested at matrix-assisted laser desorption/ionization time-of-flight mass spectrometry (MALDI TOF-MS) count rates. A Timepix successor chip (as sketched in Chapter 3) in combination with a kHz readout system and an ion microscope will result in a state-of-the-art microscope mode MALDI TOF-MSI instrument. Such a system will possess a high dynamic range, a high signal-to-noise ratio, a high mass range, an extremely high spatial resolution and will be capable of the simultaneous measurement of both localization and arrival time of various  $m/z$  ions during one single measurement.

The presented work demonstrates the analytical capabilities of this novel detection system for mass spectrometry imaging on biologically relevant samples. Conveniently, the high degree of flexibility in the design of the MCP/Timepix detector assembly enables the implementation of this detection system on any time-of-flight mass spectrometer. The combination of the system's high spatial resolution capabilities with a high mass resolution, tandem MS or ion mobility mass spectrometer in the future will expand the high end toolbox for MS imaging.



# 7

## Implementation of an In-Vacuum, High-Voltage, Pixelated Detection System for Positive and Negative Mode Ion Microscopy

*The analytical capabilities of our Timepix detection system for mass spectrometry imaging are extended by the application of additional extraction fields. Electrically biasing the detection system at a high potential (+12 kV/-8 kV) delivers effective ion acceleration energies of 15/11 keV, which is comparable to the extraction fields in commercially available ion spectrometers. This high voltage detector upgrade enables measurements on both ion polarities and enables a more sensitive analysis of higher molecular mass ions. The technical implementation of this system and first results are presented.*

### 7.1 Introduction

The analysis of large biomolecular and biomedically relevant macromolecules by mass spectrometry (imaging) is highly challenging and interesting to various areas of application. The reliable and sensitive detection of high-mass ions, in particular large proteins, protein complexes, viruses and bacterial clusters, would provide the life sciences with a powerful, analytical tool, which could also find applications in (bio)medical routine analysis and diagnosis in the future. While technology for efficient ion generation and accurate mass analysis has actively and rapidly developed over the past century, technology for ion detection -particularly of high mass macromolecular complexes- has been lagging behind.

Few examples of high mass detection by electrospray ionization (ESI) in combination with Fourier transform ion cyclotron resonance (FT-ICR) MS or time-of-flight (TOF) MS have been reported. Chen and coworkers have detected coliphage T4 DNA ions of 100 MDa on an FT-ICR MS [224]. Sanglier and co-workers have detected 2.2 MDa native hemocyanins from deep-sea and shore crabs with ESI in combination with a TOF and quadrupole-time-of-flight (Q-TOF) mass analyzer [225]. Similarly, DiFilippo has measured intact viral particles of the tobacco mosaic virus at 40.5 MDa with ESI-TOF [226]. Fuerstenau and co-workers

reported ESI-TOF MS on macromolecules in the MDa range [227]. Electrospray ionization is very efficient for the detection of high mass ions, since it readily produces multiply charged species, which can be detected more easily. However, matrix-assisted laser desorption/ionization, as a “soft” ionization technique, is generally considered a more appropriate choice of ionization source for large intact macromolecules. MALDI is also suitable for mass spectrometry imaging where the lateral organization of the analytes from the sample surface is retained.

Detection systems in MALDI-MS, specifically in MSI, are often based on microchannel plates (MCP, see Chapter 3). A limitation of this secondary-electron multiplier, however, is the so-called “high-mass roll-off” of the detector. In a MCP, the ion detection depends on the generation of secondary electrons. The generation of a secondary electron avalanche proportional to the velocity of the incoming particle. As all particles in a TOF-MS are given the same kinetic energy theoretically, high mass ions will impinge on the detector with a relatively low velocity/momentum. Hence, they deposit insufficient energy to create an electron shower. The high mass ions are not detected as a result.

Alternative detection systems for high-mass measurements with MALDI TOF-MS have been suggested. Park and co-workers presented an inductive detector specifically for MALDI TOF-MS, whose detection efficiency is not ion velocity-dependent and does not saturate at high count rates [228]. Imrie and co-workers reported the detection of above 300 kDa ions with a Faraday cup detector on a MALDI TOF-MS [229]. Spengler and co-workers used a metallic conversion dynode for ion detection/conversion and observed that the detection efficiency of large molecules from MALDI can benefit from optimization for secondary-ion yield rather than secondary-electron detection [230]. This approach is similar to the commercially available Covalex detector (Chapter 3). Cryogenic detectors are another approach to the detection of high mass ions (Chapter 3).

In this chapter, the technical implementation of a Timepix-based detection system for higher mass molecular ions of both polarities is suggested. This system will be both suitable for MS and MSI experiments and will be implemented on the *AMOLF* ion microscope mass spectrometer. In the previous Medipix 2- and Timepix-based setups for MSI [70, 73, 231] (Chapter 4-6), the detector was held at ground potential. Therefore, the imaging system was limited in its ability to analyze high-mass biological samples by limited acceleration voltages. The upgraded detector assembly presented here is operated floating at a voltage of +12 kV/-8 kV. This provides high voltage (HV) acceleration capabilities for both ion polarities. Previously, only positive mode ion imaging of basic and/or salt adduct species was possible with the MCP/Timepix detection system on our ion microscope. The extension to negative mode ion imaging enables the study of acidic species, which enables the analysis of different moieties, i.e. different lipids,

acidic peptides and proteins. Therefore, the capability to study a tissue sample in both positive and negative mode provides complementary information on the biological analytes. In addition, the higher acceleration voltages provide the capability to detect higher mass intact proteins.

Several technical challenges are related to the in-vacuum mounting of the Timepix detector. In earlier work, detectors of the Medipix/Timepix detector family were mounted in-vacuum including substantial parts of the readout electronics in the vacuum chamber [73, 81] (Chapter 4). Here, the implementation of a new, high vacuum compatible chip carrier is presented for the first time. This chip carrier functions as a vacuum seal. As a result, the chips are mounted in-vacuum while the readout electronics is located in-air outside the vacuum chamber. The in-vacuum mounting of the Timepix chips requires active cooling of the in-vacuum components of the system as to prevent overheating. An active cooling system and a temperature monitor with overheating control are presented.

## 7.2 Experimental

The Medipix/Timepix detectors are covered in Chapter 3. The detection system presented in this chapter is similar to the one described in Chapter 5. The ion microscope mass spectrometer has been described in detail in Chapter 5.

### 7.2.1 High Voltage Capabilities: Detector Floating on +12/-8 kV.

The implementation of the Timepix detector on our ion microscope aims at the efficient, position- and time-/mass-resolved analysis of complex biological samples for molecular histology. In earlier Medipix-/Timepix-based imaging systems, the detector was held at ground potential [70, 73, 231]. Therefore, the detection system was limited to acceleration voltages of about 5 kV, i.e. applied by the sample potential of +3 kV and the MCP front bias of -2 kV. In addition, the experiments were limited to the positive ion mode (Chapter 4-6).

To enable the detection of higher mass ions, the entire Timepix detector assembly -including the chips, readout electronics, power supplies, cooling system- presented here is floating at a voltage of about +12 kV (in negative ion mode) and -8 kV (in positive ion mode). This provides high voltage acceleration capabilities for both ion polarities and allows for the analysis of macromolecular ions. Figure 7.1 displays a potential diagram for the operation of the floating Timepix detector assembly in positive and negative ion mode.

Since the Timepix detector assembly is floating at HV, it has to be electrically insulated and shielded from the mass spectrometer and surrounding. Figure 7.2 and 7.3, respectively, illustrate the mechanical and electrical design of the setup,

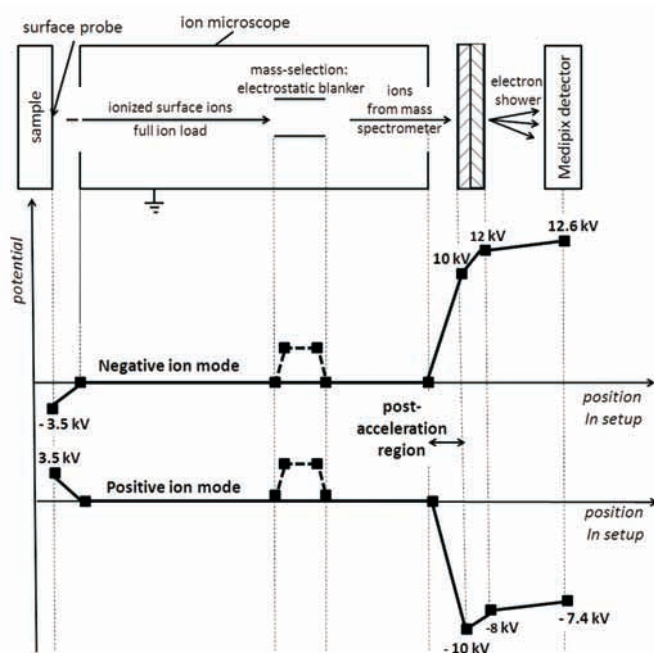
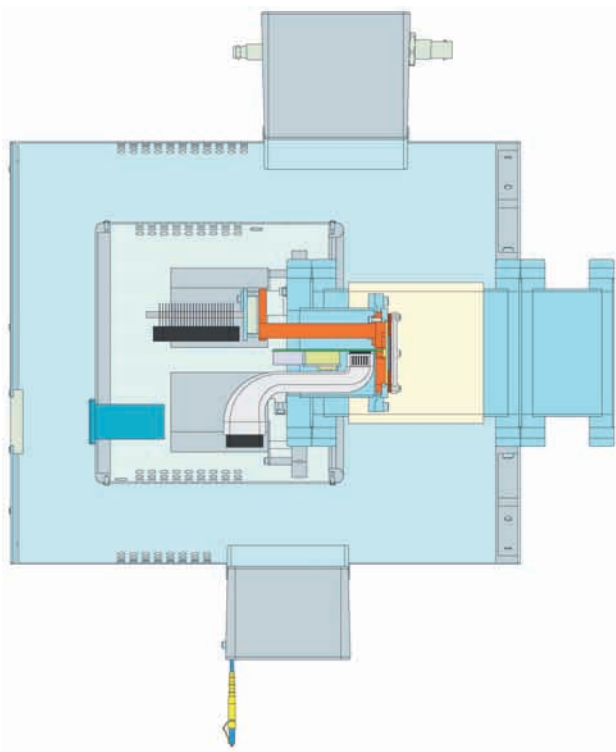


Figure 7.1: Schematic representation of the ion microscope mass spectrometer and potential diagram for the operation of the floating Timepix detector assembly in positive and negative ion mode.

which contains two cylindrical shells: (1) the “inner” setup shell, which is floated at HV and (2) the “outer”, which is held at ground potential. The floating detector assembly is attached to but electrically insulated from the mass spectrometer via a ceramics tube. The MCP/Timepix detector assembly, the ReLAXD readout board (Chapter 3), the cooling system (Peltier elements, temperature controller, fans) and mechanical parts in the inner setup shell are all floated at HV. The floating HV is applied to the inner detector shell from the standard TRIFT II (Physical Electronics, Inc., Chanhassen, USA) power supplies of the ion microscope via a home-made converter situated in the outer/ground potential setup shell. The MCP back- and frontside are powered by the original TRIFT MCP power supplies. A decoupling circuit for the MCP backside signal is in place for signal diagnostics on an oscilloscope or to acquire mass spectra both with the Timepix system and/or an ADC/TDC in parallel (Chapter 5). The ReLAXD board, the Peltier elements, the temperature controller and the fans are powered

by two home-made, switching mode power supplies which are located within the inner detector shell and are also floating at HV. Since the Ethernet signal from the ReLAXD board is at HV, the signal has to be converted to enable the signal transfer into a PC at ground potential. Therefore, the Ethernet signal is translated to an optical fiber protocol via a media converter (Ntron Industrial Ethernet media converter, 1002MC-SX, N-Tron Corporation, Mobile, USA). The non-conducting optical fiber is sent out of the HV setup and the signal is re-converted to the Ethernet protocol via a optical-to-Ethernet media converter (Ntron Industrial Ethernet media converter, 1002MC-SX, N-Tron Corporation, Mobile, USA). Then the signal is coupled to the Ethernet card of the measurement/control personal computer.



*Figure 7.2: Representation of the mechanical design of the HV setup. The inner shell contains the detection system, readout board, temperature control system and signal-converter at high voltage. The outer shell functions as a protective housing.*

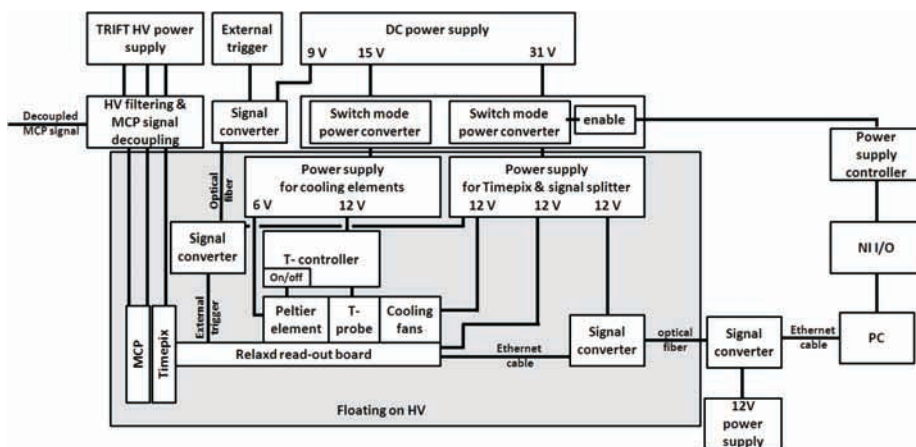


Figure 7.3: Schematic representation of the electrical design of the high voltage setup. The electronics inside the shaded box is floating on HV and is physically contained within the inner shell of the mechanical design (Figure 7.2). The electronics outside the shaded box is at ground potential and is located outside the outer protection shell of the setup.

## 7.2.2 High-Vacuum Compatible Chip Carrier and Vacuum Seal

The Medipix/Timepix detector assemblies and readout electronics are not originally designed for in-vacuum use. The chips are standard mounted on a printed circuit board (PCB) to which another readout PCB is connected. The PCBs are made up of multiple, outgassing FR-4 (fiberglass reinforced epoxy laminates) layers and other non-vacuum compatible electronics components. In earlier proof-of-principle experiments, the Medipix/Timepix detectors and readout electronics were mounted either directly in the spectrometer chamber or a differential pumping stage was used. This resulted in typical pressures of  $P=10^{-7}$  mbar [73, 81]. Despite the high vacuum pressure, the benefits of a new generation of imaging detectors in mass spectrometry imaging and gas-phase atomic and molecular physics research could be established in these experiments.

In this chapter, a new, high-vacuum compatible chip carrier (Figure 7.4) and vacuum seal are presented (Figure 7.5) that increase the performance and implementability of those detectors in ultra-high vacuum applications like MSI.

The carrier acts as a vacuum-tight seal between the vacuum of the mass spectrometer and the in-air components of the system. The chips are mounted in-vacuum while the readout electronics is located in-air outside the vacuum cham-

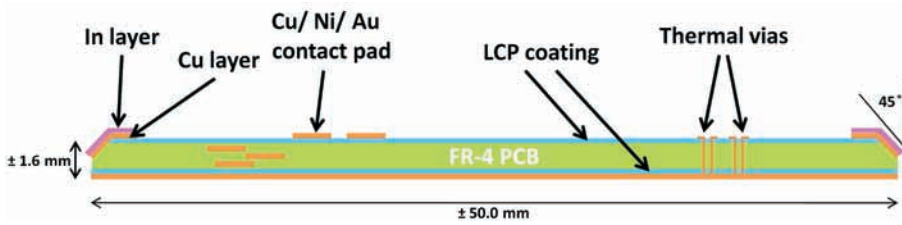


Figure 7.4: Schematic representation of the high-vacuum compatible chip carrier. The chip carrier consists of a standard, multilayer FR-4 PCB to which a layer of liquid crystalline polymer (LCP) is applied on the top and bottom side. The edge of the board is sealed with a layer of copper and indium to prevent outgassing and to provide a metal surface for the vacuum seal between the carrier and the vacuum chamber of the mass spectrometer.

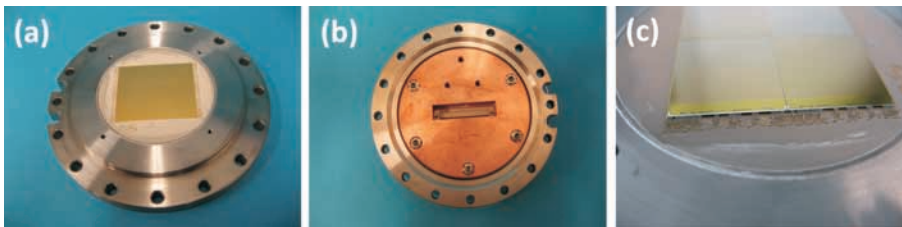


Figure 7.5: Fotos of the high-vacuum compatible chip carrier glued into the stainless steel support. (a) In-vacuum (front) side of the carrier. The four drilled and threaded holes mark the positions on which the MCP support will be attached. (b) In-air (back) side of the chip carrier. The copper block provides mechanical support and functions as a heat sink. The readout interface board can be clicked into the connector located at the center of the chip carrier. (c) Zoom on the bonding pads and wire-bonded chips.

ber. The chip carrier also consists of a standard, multilayer FR-4 PCB. This carrier supports the chips and connects the chips with the readout interface PCB. The FR-4 PCB is coated with Liquid Crystalline Polymer Circuit material (LCP, R/flex 3600 Single Clad Laminate, Rogers Corporation, Advanced Circuit Materials, Chandler, USA) on the top and bottom side which prevents the PCB from outgassing. This material has successfully been applied as a coating for high-vacuum parts in mass spectrometry [232]. The use of standard PCB material bares the advantages of easy, cheap, reliable and well-established electrical design and fabrication. In addition, PCBs can be manufactured in various shapes (rectangular versus circular) and sizes (from few mm up to tens of cm in diame-

ter). In this application, the PCB is circular in shape, has a diameter of about 50 mm and a thickness of about 1.6 mm. The edges of the PCB are (partly) bevelled under an angle of  $45^\circ$  for optimal vacuum sealing in the stainless steel mount. Since the PCB is only coated with LCP on the top and bottom surfaces, the board can outgas via its edges. Therefore, the edges of the board are sealed with a layer of copper (Cu) and indium (In). To ensure the temperature control of the chips, thermal vias are distributed all over the PCB. In addition, a Max6642 (Maxim Integrated Products, Inc., Sunnyvale, USA) temperature sensor is incorporated in the PCB which allows to monitor the temperature of the chips at all times.

The presented chip carrier is mounted in a stainless steel support (Figure 7.5). Since the LCP-coated chip carrier represents a vacuum seal of this system, the connection between the chip carrier and the stainless steel support needs to be vacuum-tight. The support is machined such that the bevelled edge of the chip carrier can be glued (vacuum-compatible, two-component silver epoxy, Hysol TRA-DUCT 2902, Henkel, Düsseldorf, Germany) into the stainless steel support (Figure 7.5a), which is bevelled at the same angle. This vacuum seal was tested on a leak tester (130 l/s high vacuum pump, ASM 180T, Alcatel, Annecy, France). A leak rate of less than  $P=10^{-9}$  mbar·l/s was measured. The leak testing gas, helium at an inlet speed of 4.4 l/s, could not be detected (smallest detectable signal at full pumping speed is  $5.1 \cdot 10^{-12}$  mbar·l/s).

In addition, the chip carrier is mechanically supported by a copper disc (Figure 7.5b), which prevents mechanical stress due to the pressure difference between the vacuum on the chip-side of the carrier and the ambient pressure on the electronics-side of the board. The chip carrier and the copper support disc are connected by an electrically and thermally conducting, two-component silver epoxy glue (EPO-TEK EE129-4, Epoxy Technology, Inc., Billerica, USA). This copper disc also functions as a heat sink and connects the chip carrier to the active, Peltier element-based cooling system. The stainless steel support of the carrier is connected to the mass spectrometer by a  $\phi=1.5$  mm indium thread (Degussa, Hanau, Germany). The combination of the two seals returns the same leak rate, i.e. less than  $P=10^{-9}$  mbar·l/s, and the helium leak testing gas could still not be detected.

The detector system was assembled through the following procedure: (1) glue the chip carrier to the copper cooling disk and into its stainless steel support, (2) probe the Timepix chips, (3) glue them to the chip carrier, (4) wire-bond the chips, (5) mount assembly via indium seal, (6) leak test assembly, (7) install the chip carrier vacuum assembly on the TRIFT ion microscope.

The spectrometer was baked for 48 hours. A spectrometer pressure of  $P=2 \cdot 10^{-9}$  mbar could be established. This represents an improvement of almost two orders of magnitude compared to previous efforts ( $P=10^{-7}$  mbar) which had involved

differential pumping or in-vacuum mounting of the readout electronics.

### 7.2.3 Active Peltier Cooling System

The four Timepix chips dissipate about 4 W in total. Therefore, the in-vacuum mounting of the Timepix chips requires active cooling to prevent overheating. In the presented setup, the chips are cooled actively with two Peltier elements. The Peltier elements and the chips are connected by a series of copper parts. The assembled chip carrier is glued to the copper support/heat sink with thermally conducting glue. The copper heat sink is connected to a copper heat conductor that terminates in a platform on which the two Peltier elements (PE-127-10-13-S, sealed, 37.2 W cooling power at  $\Delta T=0$  and maximum current=3.9 A, maximum  $\Delta T=70$  °C at maximum current=3.9 W and power=0; Global Component Sourcing, Hong Kong) are installed. The Peltier elements are cooled with a heat sink and a fan. The cooling temperature is probed with a PT-100 temperature probe, which is attached to the copper platform next to the Peltier elements. The cooling platform temperature is controlled and held at a given set point, typically 8 °C, with a temperature controller (eTRON M electronic microstat, JUMO GmbH & Co. KG, Fulda, Germany). The temperature of the chips is monitored via the Max6642 temperature sensor, which is located in the chip carrier PCB below the four chips. The FPGA (field-programmable gate array) on the readout board is cooled with a fan (via a cooling tube). The FPGA temperature is also given by the Max6642 which reads a FPGA-internal sensor diode. The chip and the FPGA temperature readings are transferred to the measurement personal computer (PC) via the Ethernet readout connection.

A dedicated temperature monitoring and control software was developed. This software package was incorporated into the Medipix/Timepix readout software Pixelman (Pixelman software, version 2010/03/29, [205, 206]) as a “plug-in”. The temperature monitoring and control software (system overview in Figure 7.6) grabs the chip and FPGA temperature readings from the Ethernet data stream and displays the temperature readings in a graphical user interface (GUI) window. In the GUI, the user can specify an “alarm” and a “switch-off” temperature ( $0 < \text{alarm/switch-off temperature} < 100$  °C) for the chips. If the chip temperature reading is higher than the user-specified alarm temperature for a user-set amount of time ( $0 < \text{alarm time-out} < 100$  s), the GUI goes into alarm status (turns red) and an acoustic alarm sets in. Once the chip temperature exceeds this switch off temperature for a user-set period of time ( $0 < \text{alarm time-out} < 100$  s), the software will shut down the chips’ and readout board’s power supplies to prevent overheating. The switch-off procedure is enabled via a multi-function DAQ unit (NI USB-6008, 12-Bit, 10 kS/s Low-Cost Multifunction DAQ, National Instruments, Austin, USA) and a home-made power supply controller,

which converts the TTL signal from the NI I/O into a “disable” signal for the Timepix and ReLAXD board power supplies.

Typically, the system is operated at an “alarm” temperature of 35 °C and a “switch off” temperature of 45 °C. The software writes the chip and FPGA temperatures as well as the user-set “alarm” and “switch off” temperatures to a log file. This temperature control program enables user-unattended measurements, which is convenient for long and/or over-night experiments.

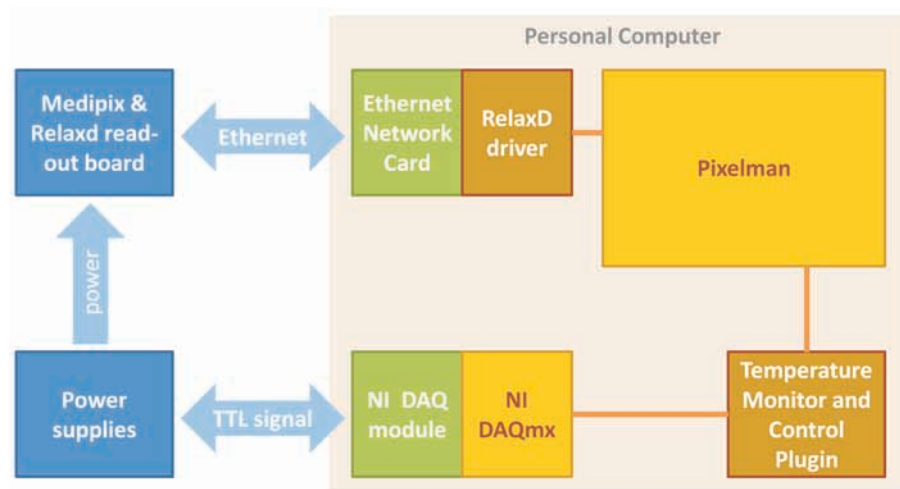


Figure 7.6: Schematic representation of the hardware components and software working mechanism of the temperature monitoring and control implemented for this setup.

## 7.2.4 Samples

A sample of Bruker Protein Calibration Standard I (Bruker Daltonik GmbH, Bremen, Germany, Table 7.1) was prepared on an indium-tin-oxide (ITO) coated glass slide. The protein solution was mixed 1:1 (by volume) with sinapinic acid matrix solution (20 mg/ml in 50% water, 50% acetonitrile) and spots of 1  $\mu$ l were spotted on the ITO slide.

Table 7.1: Proteins and corresponding average masses of the Bruker Protein Calibration Standard I.

Protein	$[M+H]^+$ average $m/z$
Insulin	5,734.51
Ubiquitin I	8,565.76
Cytochrome C	12,360.97
Myoglobin	16,952.30

## 7.3 Initial Results and Discussion

The system described in this chapter has been used for MS in both positive and negative ion mode. The system is operated at a constant MCP gain of  $10^7$  and with a potential difference of 900 V between the MCP backside and the Timepix detector.

### 7.3.1 Negative Ion Mode

Figure 7.7a shows negative ion mode mass spectra of the protein calibration standard in the mass range from 0-15 kDa as a function of the ion acceleration energy from 4-13 keV. The total ion acceleration energy is calculated by the sum of initial kinetic energy given to the ions in the source of the mass spectrometer ( $\sim 3$  keV) plus the post-acceleration voltage at the detector (2-10 keV for singly charged ions, see Figure 7.1). Each spectrum is generated from one mosaic mode acquisition of 5,000 frames, i.e. 5,000 laser shots. The mosaic acquisition rasters a sample area of  $0.9 \times 0.9$  mm<sup>2</sup> with  $16 \times 16$  positions. This method ensures that every measurement covers the same size of sample area. Also, the mosaic mode acquisition averages out hot spots on the sample surface.

In this mass range up to 15 kDa, the calibration standard includes three protein peaks; insulin ( $[M-H]^- = 5,732.51$ ), ubiquitin I ( $[M-H]^- = 8,563.76$ ) and cytochrome C ( $[M-H]^- = 12,358.97$ ). These peaks are clearly observed in the spectra at all ion post-acceleration energies. Figure 7.7a demonstrates that the intensity of the signal (peak and baseline) increases as a function of the ion acceleration voltage. Note that the amount of ions generated in the source region is independent of the acceleration voltage. However, the increase in the signal intensity can be explained by the fact that an increased ion kinetic energy results in an increased ion momentum for a given ion mass. The higher ion momentum upon impact on the MCP increases the probability of creating the first electron needed to start an electron avalanche in the MCP. If the first electron is created, the MCP amplification ( $10^7$ ) is sufficient to ensure detection on the Timepix pixels since only about 650 electrons are required to trigger a pixel.

It is expected that the increase in signal with a higher extraction field levels

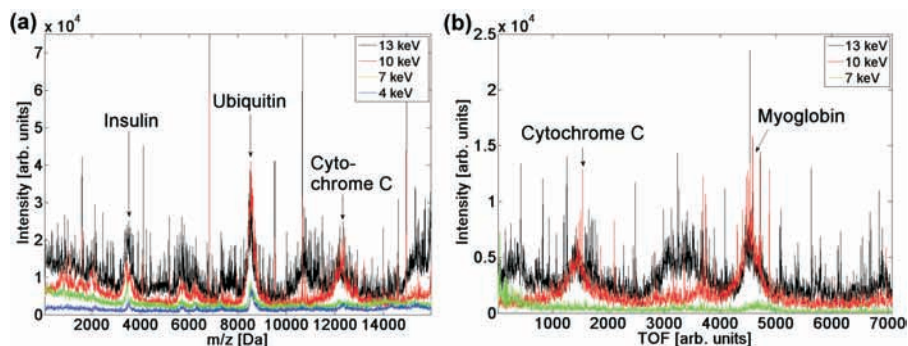


Figure 7.7: (a) Mass spectra of the protein calibration standard in the mass range from 0-15 kDa acquired in negative ion mode at an ion acceleration voltage of 4 keV (blue), 7 keV (green), 10 keV (red) and 13 keV (black). (b) Time-of-flight spectrum of the protein calibration standard in the mass range of about 10-18 kDa acquired in negative ion mode at an ion acceleration voltage of 7 keV (green), 10 keV (red) and 13 keV (black).

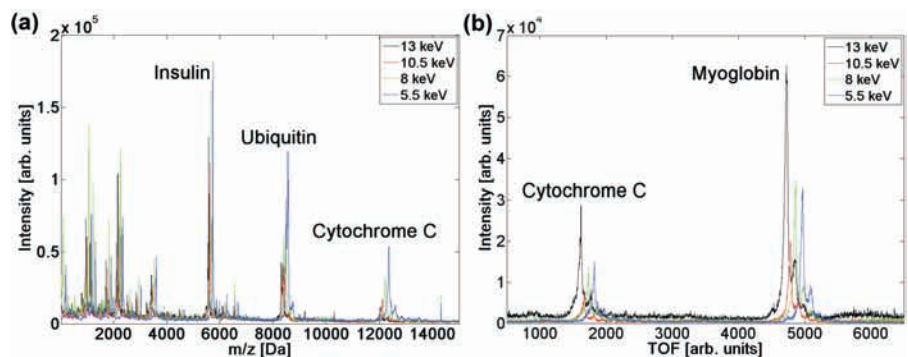


Figure 7.8: (a) Mass spectra of the protein calibration standard in the mass range from 0-14.5 kDa acquired in positive ion mode at an ion acceleration voltage of 5.5 keV (blue), 8 keV (green), 10.5 keV (red), 13 keV (black). (b) Time-of-flight spectrum of the protein calibration standard in the mass range of about 10-18 kDa acquired in positive ion mode at an ion acceleration voltage of 5.5 keV (blue), 8 keV (green), 10.5 keV (red) and 13 keV (black).

off or is not observed at higher count rates and/or higher acceleration voltages, since the number of available pixels is finite. Each pixel is a single-stop TDC,

thus if the count rate is high without additional acceleration voltage, then the extra counts due to the increased acceleration voltage will not be registered if all of the pixels in the field of view have been triggered already.

Figure 7.7b displays the time-of-flight spectrum<sup>1</sup> of the protein calibration standard in the mass range of about 10-18 kDa acquired in negative ion mode at ion acceleration energies of 7-13 keV. In this mass range, the calibration standard includes two protein peaks; cytochrome C and myoglobin ( $[M-H]^- = 16,950.30$ ). Both peaks could be detected in the Timepix-generated spectra at ion acceleration energies exceeding 7 keV. At lower ion acceleration energies no significant peaks (signal-to-noise > 3) could be acquired in this mass range, which proves the benefit of additional post-acceleration fields for the Timepix detection system.

The spectra in Figure 7.7 clearly demonstrate the extension of the previously available analytical capabilities from positive ion mode to negative ion mode. In combination with the instrument presented in this thesis, this enables negative mode ion microscopy, which adds a previously unavailable analytical tool for MSI research.

### 7.3.2 Positive Ion Mode

Figure 7.8a shows positive ion mode mass spectra of the protein calibration standard in the mass range from 0-14.5 kDa as a function of the total ion acceleration energy (5.5-13 keV). The spectra are acquired as outlined in section 7.3.1. As expected, the spectrum shows the peaks of the proteins insulin ( $[M+H]^+ = 5,734.51$ ), ubiquitin ( $[M+H]^+ = 8,565.76$ ) and cytochrome C ( $[M+H]^+ = 12,360.97$ ), as well as lower mass peaks in the mass range  $m/z < 4,000$ . Interestingly, the intensities of the protein peaks (insulin, ubiquitin, cytochrome C) decrease with increasing acceleration voltages on the detector, i.e. with increasing ion acceleration energies. In the lower mass region ( $m/z < 4,000$ ), the inverse is observed, the intensities of the peaks increase with increasing acceleration voltages on the detector. This effect is related to the ion load on the detection system in combination with the single-stop TDCs in the Timepix pixels. The count rates in these positive mode measurements are high, i.e. (nearly) all pixels within the field of view detect an event even at the lowest ion acceleration energy (5.5 keV). With increasing ion acceleration energies, the ion momentum increases and the probability to score a hit (and induce an electron shower) on the MCP increases per ion. Since the Timepix pixels are single-stop TDCs (i.e. once fired the pixels are blind for events arriving later during the same measurement interval), this gives a detection advantage to lower mass (earlier arrival time) ions. In high count rate measurements, higher

<sup>1</sup>Figure 7.7 is displayed as time-of-flight spectrum instead of a mass spectrum due to the peak shifts observed as a function of the ion acceleration energy. This effect is commented on in section 7.3.2.

acceleration voltages result in spectra where the lower mass signal is enhanced (as observed in the mass range  $m/z < 4,000$  of Figure 7.8a) and where the higher mass signal is decreased (as observed for the protein peaks in Figure 7.8a).

Figure 7.8b shows the time-of-flight spectra of the protein calibration standard in the mass range of about 10-18 kDa acquired in positive ion mode at ion acceleration energies of 5.5-13 keV. The cytochrome C and the myoglobin ( $[M+H]^+ = 16,952.30$ ) peaks can be detected in the Timepix-generated spectra. A clear increase of the signal with the increasing ion acceleration energy is observed since the count rates in these measurements are sufficiently low to enable extra counts on previously “unused” pixels.

The higher mass protein spectrum is displayed as a time-of-flight instead of a mass spectrum. In this representation, it becomes apparent that the peaks of the proteins are being shifted to a shorter time-of-flight as a function of the acceleration voltage. This phenomenon can be explained by the increased post-acceleration applied to the ions. As indicated in Figure 7.1, the ion acceleration is composed of two acceleration stages, i.e. the initial acceleration at the sample stage ( $\pm 3$  kV) and the final acceleration behind the mass spectrometer towards the detector (2-10 kV) in the  $\sim 15$ -20 cm long post-acceleration region. The magnitude of the post-acceleration field determines the final time-of-flight of the ions.

## 7.4 Conclusions and Outlook

This chapter describes a high voltage extension of the Timepix detection system for MS(I). This system upgrade can extend the already established advantages of the Timepix, i.e. position- and time-sensitive measurements, measurement of different masses simultaneously, high dynamic range, high throughput and high spatial resolution, among other advantages. In particular, this system will enable positive and negative mode MALDI TOF-MSI in the microscope mode. The high voltage capabilities will enable the analysis of high mass macromolecules. In addition, a detection system with these capabilities is not only suitable for MSI but also more generally for other analytical techniques that depend on time- and position-sensitive measurements.

First experiments were performed with the “high voltage” ion microscope/Timepix system. These experiments establish ion detection capabilities in both positive and negative ion mode, which provides the capability to collect complementary analytical information. The initial experiments indicate that the ion signal is enhanced with an increased post-acceleration voltage in moderate count rate regimes. Future studies should investigate the signal increase as a function of the post-acceleration voltage in different count rate regimes, which will provide systematic experimental guidelines for the optimum application of post-acceleration voltages.

# 8

## A New Imaging Method for Understanding Chemical Dynamics: Efficient Slice Imaging Using an In-Vacuum Pixel Detector

*The implementation of the Timepix CMOS pixel detector in velocity map slice imaging is presented. This new detector approach eliminates the need for gating the imaging detector. In time-of-flight mode, the detector returns the impact position and the time-of-flight of charged particles with 12.5 ns resolution and a dynamic range of about 100  $\mu$ s. The implementation of the Timepix detector in combination with an MCP additionally allows for high spatial resolution information via centre-of-mass centroiding. Here, the detector was applied to study the photodissociation of  $\text{NO}_2$  at 452 nm. The energy resolution observed in the experiment was  $\Delta E/E=0.05$  and is limited by the experimental setup rather than by the detector assembly. All together, this new, compact detector assembly is well-suited for slice imaging and a promising tool for imaging studies in atomic and molecular physics research.*

### 8.1 Introduction

Interest in imaging of reaction products of atomic and molecular collisions, of molecular photodissociation and of photoionization events has triggered the development of several imaging methods and detectors. The detection of the velocity distribution of fragments gives insight into the chemical reaction dynamics. A well-established technique that is used in this context is velocity map imaging (VMI) [4, 5]. In this technique, charged particles -which are either created directly in the reaction or by the application of an ionization laser after the reaction- are extracted from the interaction region and accelerated by an electrostatic field towards a position-sensitive imaging detector (Figure 8.1). The electrostatic optics of a typical VMI spectrometer consist of a repeller plate and a ring extractor plate that together create an electrostatic lens that is constructed such that particles with an identical initial velocity in the detector plane are mapped onto the same

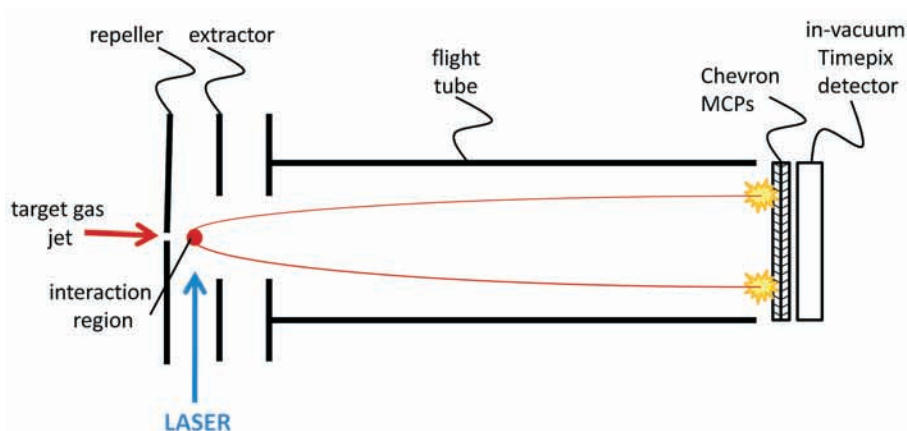


Figure 8.1: Schematic representation of the VMI spectrometer. The molecular beam and the photolysis laser intersect at right angles in between the repeller and extractor electrodes. The potentials applied on the electrodes accelerate the charged particles created in the interaction region towards the detector. At the end of the flight tube, the composite MCP/Timepix detector assembly is mounted in-vacuum.

position on the detector, independent of their starting position in the interaction volume. Therefore, the impact position of a charged particle directly reflects its initial velocity vector in the detector plane.

The position-sensitive detector in a VMI spectrometer usually consists of a set of microchannel plates (MCPs), a phosphor screen and a CCD (charge-coupled device) camera which records the two-dimensional (2D) velocity distribution of the incident ions or electrons. If the detector plane contains an axis of cylindrical symmetry, the 3D velocity distribution can be reconstructed from the 2D image via an inverse Abel transform.

Slice imaging is an imaging method -derived from VMI- that so far has only been applied to ions and that requires no mathematical reconstruction. In slice imaging the detection is restricted to particles with a specific time-of-flight by rapidly switching the MCPs on and off. This allows one to exclude all particles from the measurement that have a non-zero velocity component perpendicular to the detector plane. Slice imaging exploits the dependence of the ion's arrival time on its initial velocity along the detector axis. These time-of-flight differences can be enhanced by using delayed pulsed extraction of the reaction products [139] or by applying very low voltages to the electrodes (DC slicing) [141]. Typically, a time gate of 40 ns is applied to the detector.

Instead of a phosphor screen and a CCD camera, a delay-line detector or a wedge-and-strip anode [81] may be used to record the arrival time and position of electrons and ions. However, this approach necessarily poses limitations on the number of charged particles that can be detected per event/laser shot [233]. The reader is referred to references [81, 234] for an evaluation and comparison of the conventional, established detector approaches.

Here, we propose an alternative imaging detector concept relying on an in-vacuum pixel detector [81]. This hybrid pixelated CMOS detector, a detector of the Medipix/Timepix family [84–86], records (1) the position of impact of a particle and (2) the time-of-flight of this particle with respect to an external trigger with a maximum time resolution of a 12.5 ns and a dynamic range of 13 bits (about 100  $\mu$ s at the optimum time resolution). A typical Timepix detector arrangement consists of 4 chips comprising  $256 \times 256$  pixels of  $55 \times 55 \mu\text{m}^2$  each. Every individual pixel provides the dual functionality of giving the impact position and the time-of-flight information of the impinging particles. In combination with a chevron MCP stack, pixel detectors are capable of high-resolution, position-sensitive imaging of charged particles, where the spatial resolution can be better than the pixel size if an appropriate centroiding algorithm is used [220]. Conveniently, the implementation of a high time resolution, in-vacuum camera removes the need to gate the imaging detector in slice imaging. In this chapter, a proof-of-principle slicing experiment on the photodissociation of  $\text{NO}_2$  is presented. The results obtained demonstrate the utility of pixel detectors like the Medipix/Timepix detector in slice imaging, and furthermore pave the way for the use of this detector in high-repetition rate coincidence imaging experiments.

## 8.2 Experimental

### 8.2.1 The Medipix/Timepix Detector Family

The Medipix detector family has been developed within the *Medipix collaboration* hosted by *CERN* [93] and is described in detail in Chapter 3.

The experiment described in this chapter uses a Timepix chip assembly. The time resolution of these measurements depends on the clock speed applied via the readout interface. For instance, a  $2 \times 2$  Timepix chip array read by a MUROS2 interface [210] can be operated at a maximum clock speed of 80 MHz, resulting in a time resolution of 12.5 ns. Since the data is accumulated in a 13-bits counter per pixel, each pixel has a dynamic range of  $2^{13} \cdot 12.5 \text{ ns} = 102.4 \mu\text{s}$ .

The MUROS2 readout interface is coupled to the Timepix printed-circuit board via an ultra SCSI cable (Ultra 0.8 mm 68 male (VHDCI) to Ultra 0.8 mm 68 male (VHDCI)). The MUROS2 and the PC are interfaced by a National Instru-

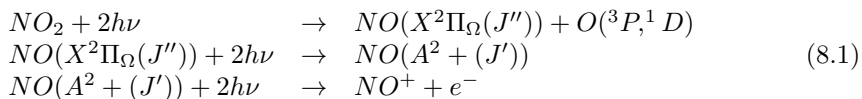
ments DIO-653X card (National Instruments Corporation, Austin, USA). The maximum achievable readout speed for a single chip is 160 Mbit/s, which yields a readout time for the entire chip of about 6 ms [210]. Using a  $2 \times 2$  bare Timepix array, we observe that the readout speed depends on the number of chips in the array and the length of the readout cable. In our experimental configuration, the typical readout time amounts to 80 ms.

The  $2 \times 2$  Timepix detector is read by means of the dedicated Medipix acquisition software, Pixelman (Pixelman software, version 2007/07/24, [205]). Saved data files list the coordinates of pixels that have registered a count in combination with the value registered by the pixels: Either the number of particles counted or the moment it went over threshold (TOF) or the time it remained over threshold (TOT).

The TOF and TOT modes are particularly interesting for sub-pixel spatial resolution imaging provided an event is detected in multiple pixels. Particles can be registered by multiple pixels, for instance, via charge sharing between neighbouring pixels [222]. It also naturally accompanies the use of an MCP in front of the Medipix/Timepix detector, when the detector records an electron shower consisting of thousands of electrons [220]. More details on the advantages of this approach are given below.

## 8.2.2 Setup and Experimental Conditions

In the experiment, a gas sample containing 10%  $\text{NO}_2$  seeded in Ar is expanded into the source chamber via a home-made piezoelectric pulsed valve. The pulsed molecular beam passes through a skimmer into the spectrometer chamber. In this chamber, it is orthogonally crossed with a tuneable 452 nm laser beam, obtained from a Nd:YAG laser (Quanta-Ray DCR-3, Santa Clara, USA) pumped dye laser (Spectra Physics PDL-3, Santa Clara, USA) with Coumarine-47 dye. The repetition rate of the laser is 10 Hz and the pulse duration is 10 ns. The  $\text{NO}_2$  molecules are photodissociated by two 452 nm photons. Subsequently, the NO photofragments are ionized via a (2+2) Resonance Enhanced Multi Photon Ionization (REMPI) scheme.



The dissociation of  $\text{NO}_2$  requires at least 3.11 eV. In this case both the NO- and the O-fragments are left in their ground state. For oxygen, this is the  $^3P_2$  state. Dissociation producing the oxygen  $^3P_1$ ,  $^3P_0$  or  $^1D$  state requires an additional

energy of 0.0196 eV, 0.0281 eV and 1.9673 eV, respectively [235]. The maximum translational energy of the NO fragments (i.e. for ground-state NO) follows from momentum and energy conservation and is 0.81-0.82 eV or 0.14 eV, when the oxygen fragment is left in either one of the  $^3P_J$  states or in the  $^1D$ -state, respectively.

The  $\text{NO}^+$  ions are accelerated through the 10-cm flight tube towards the imaging detector. Voltages on the repeller and extractor were set to -1620 V and -1670 V, respectively. The  $2 \times 2$  bare Timepix detector is mounted approximately 2.5 mm behind a  $\phi=4$  cm chevron MCP-stack. It is desirable to minimize the distance between the MCP backside and the Timepix detector chips in order to minimize the spatial expansion of the MCP electron cloud, which determines the spatial resolution that can be obtained. Currently, the wire-bonds of the chips limit reducing this distance. However, the resulting spatial expansion of the MCP cloud can be counteracted by applying appropriate potentials to the MCP front- and backside. The pores of the MCP have a diameter of 12  $\mu\text{m}$  on a 15  $\mu\text{m}$  centre-to-centre spacing. In typical experiments, the MCP front- and backsides are biased at voltages of -2.1 kV and -0.4 kV, respectively. The latter voltage is used to accelerate the electrons towards the Timepix detector that is at ground potential. Note that the flight-tube is not at ground, but at the same potential as the front of the MCP stack.

In the current slicing experiment, an external shutter signal of 6  $\mu\text{s}$  is applied to the detector (via the MUROS2 interface) at a repetition rate of 10 Hz. The shutter is synchronized to the Q-switch of the Nd:YAG laser. The Timepix chips are operated in time-of-flight (TOF) mode, which means that each pixel records the time  $t$  between the moment it went over threshold and the end of the shutter signal ( $t_{\text{shutter}}$ ). In the remainder of this chapter we will define the time axis by the convention  $t_{\text{shutter}}=0$ . The time-of-flight of the detected particles is denoted by  $\text{tof}$ , where  $\text{tof}=t_{\text{shutter}}-t$ .

Ions impinging on the MCP create an electron shower that shows up as a cluster of several pixels on the Timepix detector. A typical cluster for a single impact is depicted in the inset of Figure 8.2. The colour scale indicates the recorded time. Pixels that went over threshold earlier are coloured white, and the ones that went over threshold later are red, while pixels that did not fire at all are black. There seems to be a relationship between the amount of charge deposited on a pixel and the moment the pixel goes over threshold, i.e. the more charge is deposited on a detector element, the earlier it goes over threshold. Therefore, pixels at the center of the MCP electron cloud footprint go over threshold first, pixels at the rim of the cluster go over threshold last. The typical time difference within a cluster (the difference between red and white pixels in the inset of Figure 8.2) is 20 time bins. One clock cycle is 12.5 ns and thus this corresponds to 250 ns. The cluster is from a single ion impact and the observed temporal spread cannot

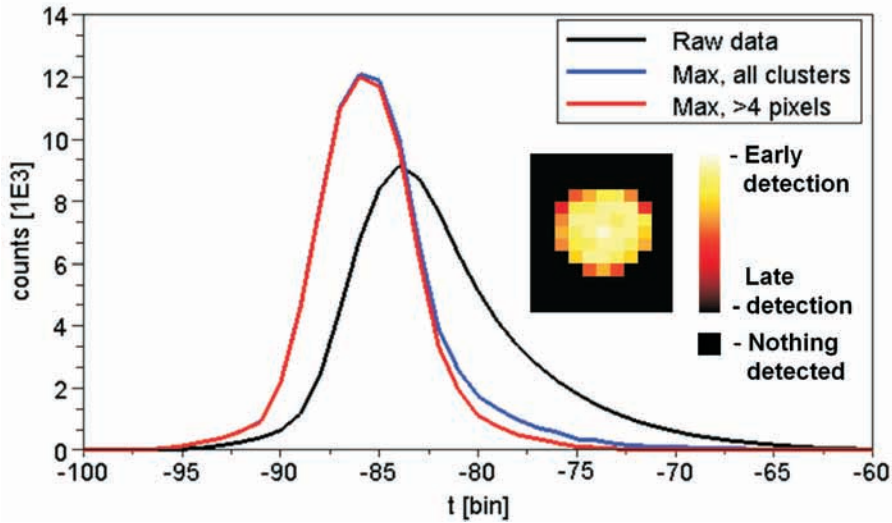


Figure 8.2: Time-of-flight spectrum of  $\text{NO}^+$  fragments after  $\text{NO}_2$  photodissociation and (2+2) REMPI at  $\sim 451.64$  nm (1 bin=12.5 ns). The raw data time-of-flight peak (black) is based on the  $t$  measurements of the Timepix detector. This curve displays an “unphysical” asymmetry caused by the Timepix detector. This is mostly due to charge sharing between pixels and a relationship between the charge deposited per pixel and the moment the pixel goes over threshold. The time resolution, and with that the symmetry of the peak, can be improved by selecting only the minimum-tof pixel for clusters that correspond to the detection of a single particle (blue). There also is a relation between the size of the cluster and the registered arrival time: on average, small clusters show a too late arrival. When omitting clusters comprising four pixels or less, one can correct for the asymmetry in the TOF peak even more (red). Note that the “raw data” curve has been scaled by dividing the amount of pixels that fired by 23, the average cluster size.

be caused by the travel time through the MCP’s and from the MCP’s to the Timepix detector, which is in the order of 1 ns.

The reduced time resolution is caused by charge sharing, i.e. the MCP charge cloud spans multiple pixels on the Timepix detector and divides its charge among those individual detector elements. This effect is reinforced in detectors where a semiconductor sensor layer in direct contact with the readout chip is present. Here, the charge sharing is amplified by the combined effect of the scattering and the diffusion of charge carriers in the silicon sensor [222]. The relative charge sharing between neighbouring pixels depends on the impact particle energy [222] and the drift time in the semiconductor sensor layer, which depends on the ma-

terial characteristics of the sensor layer, the electric field bias and distribution across the sensor and the interaction depth of the incident particle. The average size of a cluster can strongly be influenced by changing the MCP gain and the acceleration potential between the MCP back and the Timepix detector.

Since the time difference between ions that have their initial velocity towards, respectively, away from the detector is only of the order of a few 100 ns, the “raw” temporal resolution, as delivered by the Timepix, is insufficient for slicing experiments. The main plot in Figure 8.2 displays the  $\text{NO}^+$  time-of-flight trace based on the  $t$  measurements of the Timepix. Here, summed over 30,000 laser shots the number of counts (black line) is given as a function of  $t$  in units of Timepix bins (12.5 ns). While the actual ion velocity distribution is symmetric along the time-of-flight axis, the observed time-of-flight peak is strongly asymmetric. This is due to the blurring introduced by charge sharing as described above.

To enhance the spatial resolution in our experiments, we applied a centroiding routine to the raw data. We use only the pixel in the cluster that went over threshold first to estimate the arrival time of the ion, while we use the “centre-of-mass” of the cluster to calculate the position of impact via:

$$C = \frac{\sum t_i \cdot r_i}{\sum t_i}. \quad (8.2)$$

Here,  $r_i$  is the coordinate corresponding to the centre of pixel “ $i$ ”. The weights  $t_i$  are the difference between the arrival time on pixel  $i$  and the first arrival time that is not encountered anymore within cluster  $i$  (thereby giving pixels beyond the cluster boundary zero weight).

To enhance the temporal resolution, we used only used the minimum *tof* pixel for clusters (blue line in Figure 8.2), i.e. the time recorded by the pixel that went over threshold first within a cluster. As expected this peak is sharp and more symmetric than the raw data curve. However, a slight asymmetry can still be observed. This asymmetry can be traced back to a dependence of the measured arrival time of the electron cloud (and thus the ion) on the size of the cluster and can be reduced by omitting clusters consisting of four pixels or less. Such small clusters on average return “later” arrival times than clusters comprising more pixels, possibly due to a dependence of the charge migration time on the total amount of charge deposited. The red line in Figure 8.2 shows the time-of-flight trace when selecting only the minimum *tof* pixel for clusters (as for the blue line) and also omitting clusters comprising less than five pixels. Clearly, the time-of-flight peak is much more symmetric, as it should be. All data shown in the remainder of this work were treated in this way. Note that for each ion impact (and resulting cluster of events on the Timepix detector) we store one arrival time, i.e. the minimum *tof*, and one set of arrival coordinates calculated

via “center-of-mass” centroiding.

In the current experiment 30,000 acquisition frames were recorded. Due to the millisecond readout time of the chips the effective repetition rate of the experiment was 5 Hz and the acquisition lasted about 1.5 hours. In one frame, the detector registered on average 2.6 events. The signal rate was limited to this value in order to keep the probability of double impacts at the same position small.

### 8.3 Results and Discussion

Figure 8.3 displays a series of slices through the NO velocity sphere after photodissociation of NO<sub>2</sub> at 451.64 nm. The numbers in the bottom corner of the images indicate the time-of-flight bins used to generate the images. Recall that each bin is 12.5 ns and that high numbers relate to early events. Bins 85-87 correspond to the centre of the distribution (maximum of the red line in Figure 8.2). The results in Figure 8.3 demonstrate clearly that slices through the NO velocity distribution using the Timepix detector were successfully recorded.

Figure 8.4 displays the velocity distribution of the NO photodissociation fragments in the plane of the detector. The distribution of the centre slice (12.5 ns) is displayed in red, while that of the full (crushed) image, i.e. integration over all time bins, is shown in black. This corresponds to the in-plane velocity distribution observed in a common raw VMI image. The velocity distribution of the centre slice is clearly sharper than the velocity distribution of the full data set. An image of the centre slice (bin 86) is displayed in the right panel of Figure 8.4, along with the integrated image. The kinetic energy distribution, calculated from this slice is compared in Figure 8.5 to that obtained via an iterative inverse Abel transformation of the time-integrated image [236]. The overall shape of the two curves is similar. Still, the quality of the slice image is superior; the noise in the “inversion” (a result of the iterative inversion that recovers the 3D velocity distribution from the 2D projection) exceeds the noise in the slice. Noise in the experimental data is the most likely cause of the difference. A longer integration, and thus reduction of the noise in the experimental image is expected to improve the correspondence between the result from the inversion and from slicing. Note that the centroiding algorithm in principle provides sub-pixel spatial resolution and the slicing result contains more bins than the result from the inverse Abel transform (1,024 instead of 512).

The two peaks that dominate the spectrum (the two dominant rings in the images), correspond to the different states of the oxygen fragment. The peak at 0.8 eV (outer ring in the image) relates to the NO[X<sup>2</sup>Π<sub>Ω</sub>(J’)]+O(<sup>3</sup>P<sub>J</sub>) products, while the peak at 0.1 eV (inner ring) relates to the NO(X<sup>2</sup>Π<sub>Ω</sub>(J’))+O(<sup>1</sup>D) products which necessarily have a lower kinetic energy. Recall that the maximum kinetic energy of the NO fragments (when left in the ground state) is 0.82 eV

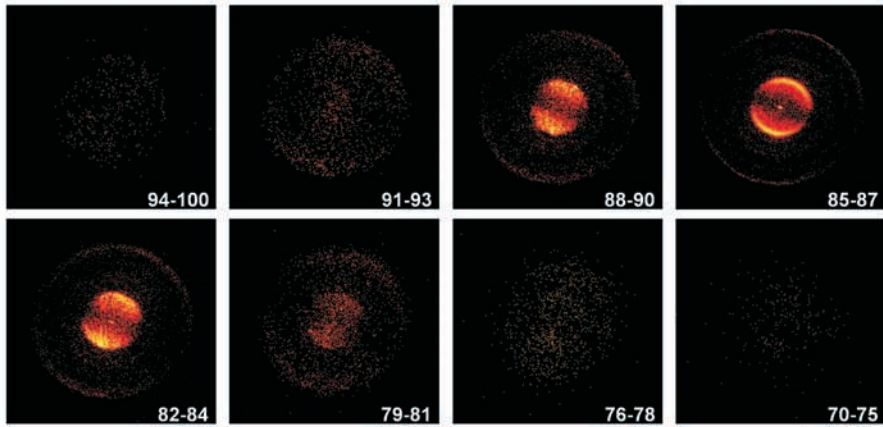


Figure 8.3: Series of slices through the  $\text{NO}^+$  velocity distribution, recorded with a  $2 \times 2$  Timepix detector and represented on a logarithmic colour scale. Each impact position is calculated from the centre-of-mass of the cluster, while the moment of impact is approximated by taking the moment when the first pixel within the cluster went over threshold. Clusters of less than 5 pixels were omitted. The data was binned onto a  $512 \times 512$  matrix.

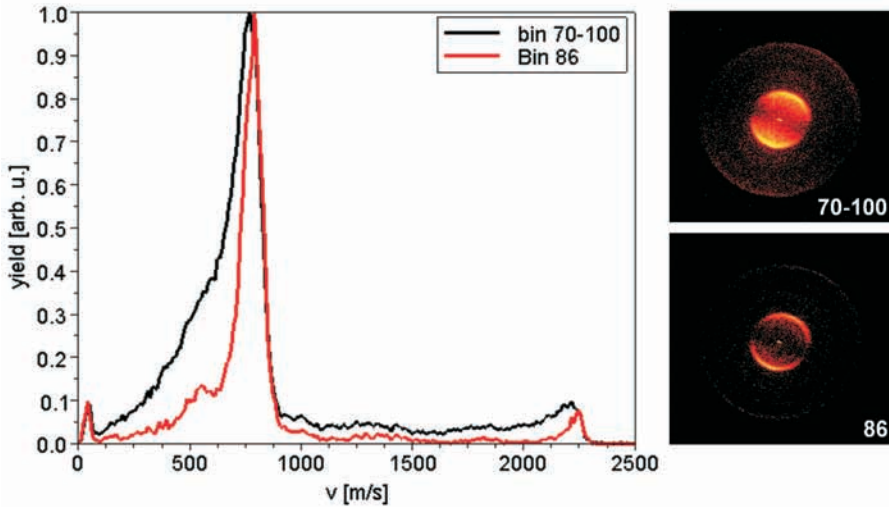


Figure 8.4: The left panel shows the in-plane velocity distribution of the centre slice (red) and the integral over all slices (black). The right panel shows the ion images that correspond to the curves in the left panel.

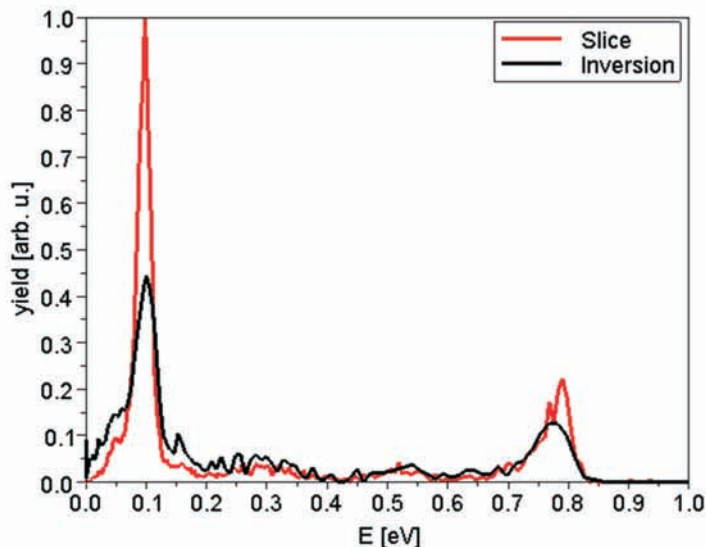


Figure 8.5: Kinetic energy distribution of the center slice (bin 86, red curve) and of the inverted integral image (bin 70-100, black curve). These curves follow from the momentum distributions in Figure 8.4.

when the oxygen fragment is left in one of the  $^3P_J$  states and that it is 0.14 eV when the O fragment is in the  $^1D$  -state. The signal besides the two main peaks is probably due to NO that upon dissociation is left in highly excited states.

The rotational state of the probed NO products can be resolved by tuning the dye laser wavelength. To calibrate the dye laser, the spectrum from a beam of rotationally cold NO was measured, after which a spectrum of NO from  $\text{NO}_2$  dissociation was recorded. Both spectra are plotted in red in Figure 8.6 and compared to simulated spectra [237] represented in black. For reference purposes, the spectrum for NO from dissociation is compared to a two photon  $A \leftarrow X$  spectrum for  $\text{NO}(v=0)$  simulated at 300 K. We assume that in this wavelength range ionization via the  $A \ ^2\Sigma^+$  state dominates the spectrum. However, upon dissociation NO may be left in very highly excited rotational and vibrational states and ionization may occur via different intermediate states than just the A state [238], which means that the actual spectrum is more complex than the simulated one to which it is now compared. Roughly speaking, the right part of the spectrum in the bottom panel of Figure 8.6 corresponds to NO in low rotational levels of the  $^2\Pi_{3/2}$  state which is formed in the  $\text{NO}_2$  dissociation, while the left part corresponds to NO in the  $^2\Pi_{1/2}$  state. Around 452.4 nm, the spectrum

shows the signature of some cold NO that is contained in the NO<sub>2</sub> molecular beam. The current experiments were performed at 451.64 nm, at the top of the peak that is depicted in the top-right panel of Figure 8.6. This peak has a width of approximately 0.03 nm.

Within the peak at 451.64 nm, a few rotational states of NO( $v=0$ ) may be probed. The most likely spectroscopic transitions are provided in Table 8.1 with the recoil-energy of the corresponding NO fragments. The comparison of the experimental spectrum from photodissociation of NO<sub>2</sub> with a simulated 300 K spectrum of NO (Figure 8.6) suggests an important role for NO( $J''=8.5$ ) and NO( $J''=5.5$ ) in the experiment. However, this does not fit with the energy distribution observed in Figure 8.5. The first peak should in that case be at 0.14 eV, and not at 0.10 eV as is the case in the current experiment. The latter number does fit reasonably well to the R<sub>22</sub>+S<sub>12</sub>(17.5) transition which should be found within the same peak (see Table 8.1 and Figure 8.6).

The signal besides the two main peaks in Figure 8.5 is most likely due to NO in highly rotationally and vibrationally excited states. The spectrum is very dense and hence it is difficult to select a single rotational state of NO. Recently Wilkinson and co-workers [238] studied NO<sub>2</sub> dissociation in a slice imaging experiment similar to ours, but using a single photon of 226 nm for dissociation, one for excitation and one for ionization. Although their results are dominated by NO fragments in relatively low rotational levels ( $J'' < 21$ ) of the vibrational ground state that ionize via the A  $^2\Sigma^+$  intermediate state, they also observe signatures of highly rotationally and vibrationally excited states of NO. Ionization of NO molecules in vibrationally excited states ( $v=5$  until  $v=9$ ) at this wavelength proceeds via higher lying intermediate states.

The signal may have been influenced by amplified spontaneous emission (ASE) in our laser beam, which may also cause some of the signal within the two main peaks in Figure 8.5. ASE leads to a slight broadening of peaks in Figure 8.5 towards lower energy, because the experiment was performed close to the short-wavelength edge of the Coumarin 47 wavelength range (444-476 nm when pumped with 355 nm light). If one of the photons in the dissociation process originates from ASE, this leads to a broadening of 0.05 eV towards lower energy or 0.02 eV towards higher energy. In addition, photons from ASE may cause ionization of NO molecules in other than the selected state.

Table 8.1: List of  $A \leftarrow X$  transitions that may be probed around 451.64 nm.

$\Lambda$ [nm]	Transition ( $\Delta N, \Delta J, F'', F', J''$ )	Position [eV]			
		$^1D$	$^3P_2$	$^3P_1$	$^3P_0$
451.627	sS <sub>11</sub> (8.5)+sR <sub>21</sub> (8.5)	0.132	0.817	0.81	0.807
451.634	tS <sub>21</sub> (5.5)	0.136	0.82	0.813	0.81
451.647	rR <sub>22</sub> (17.5)+rS <sub>12</sub> (17.5)	0.109	0.793	0.786	0.783

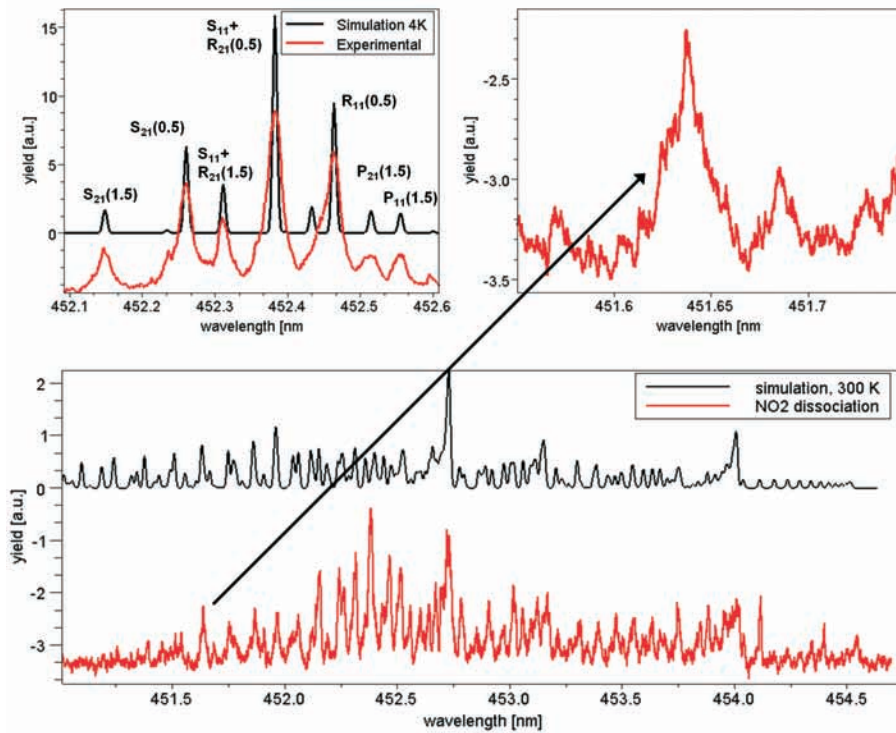


Figure 8.6: Simulated and experimental spectra are depicted in black and red, respectively. The top-left panel shows spectra for cold (4K) NO and is used to calibrate our dye laser. The red line in the bottom panel shows the spectrum for NO from NO<sub>2</sub> dissociation, while the top-right panel zooms in on the peak at which the experiment is performed. As a reference, a simulated 2-photon absorption spectrum for NO at 300 K is provided (black line in the bottom panel).

A better experiment with a higher quality (a narrower laser bandwidth and a lower level of ASE) would be needed to make definitive statements about the interpretation of the measured data and the underlying physics. For an elaborate discussion on the underlying physics, the reader is referred to references [238] and reference cited therein.

The energy resolution in the current experiment is estimated to be  $\Delta E/E=0.05$  from the peak at 0.8 eV, which corresponds to 3 pixels or 165  $\mu\text{m}$  on the detector. This number is most likely governed by (1) the ion optics and applied voltages thereon, (2) the simultaneous presence of several velocity components (see above)

and (3) the fact that oxygen fragments in all three  $^3P_J$  states contribute to this peak (leading to at most 0.01 eV energy difference of the NO atoms).

The experiment was performed at non-optimal VMI conditions. The repeller and extractor electrodes carried relatively high voltages ( $<-1.6$  kV), while the difference between the two electrodes was only 50 V. Recall that the flight tube and front of the detector was also at high voltage ( $-2.1$  kV). As a result, the impact position on the detector may be more sensitive to the initial creation position of the ions than in optimized VMI conditions. Since the ionization volume can be approximated as a cylinder along the laser propagation direction with 1.5 mm length and 100  $\mu\text{m}$  diameter, this effect can significantly contribute to the deterioration of the spatial resolution. This hypothesis is supported by the shape of the centre spot in the bottom right panel in Figure 8.4, which is stretched along the laser propagation axis and approximately measures  $2 \times 5$  pixels ( $110 \times 275 \mu\text{m}^2$ ). This indicates non-ideal VMI conditions and corresponds reasonably well with the observed experimental resolution (3 pixels). The voltages on repeller and extractor were chosen such that the size of the centre spot was as small as possible. It is the combination of the effects described above that leads to the observed resolution, rather than that of the Timepix detector itself.

## 8.4 Conclusions

In conclusion, the use of an MCP/Timepix in-vacuum detector assembly for slice imaging was presented. The combination of high resolution, position-sensitive imaging and time-of-flight measuring on the pixel level makes this detector a well-suited, simple and attractive alternative to conventional ion imaging detector technology.

This new detector approach delivers a timing resolution of 12.5 ns per slice and -so far- an energy resolution of  $\Delta E/E=0.05$ . Recently Vallerga and co-workers [94, 147] demonstrated that the spatial resolution of the Timepix detector in combination with MCPs can be pushed to 8.8  $\mu\text{m}$  when operating the pixels in TOT mode, using a center-of-gravity centroiding algorithm and collecting sufficient statistics. This indicates that the Timepix detector (in combination with the MCP stack) bears outstanding spatial resolution capabilities and that the spatial resolution of the experiment presented here is limited by the experimental setup rather than by the detector approach itself. Still, in the presented experiment, the Timepix detector performs comparable to conventional slice imaging and inversion-algorithm based VMI.

The effective/raw time resolution was found to be worse than 12.5 ns. The measured arrival time within a cluster depends strongly on the position of a pixel in the cluster and also depends somewhat on the cluster size. This is due to charge

sharing of the MCP electron cloud between multiple pixels and to the amount of charge deposited on the individual pixel. This problem has successfully been addressed in this experiment. The relatively long readout time of the detector currently limits the experiment to 5 Hz, but this will be improved in the near future.

The Medipix/Timepix detector family has a large potential for gas-phase research in atomic and molecular physics in the near future. The work presented in [73, 81] and the current work represent first steps towards this. An important next step will be coincident photoelectron and ion detection based on this type of in-vacuum pixel detector, in which the above mentioned difficulties and limitations are less relevant. The combination of the Timepix detector with an MCP and the Timepix's position-sensitive TOF and TOT functionality enable pixel spatial resolution via centroiding algorithms as well as timing information on the tens of ns level. Integrating this functionality and sub-ns timing information from the MCP will enable the coincident detection of photoelectrons and ions in a simple, compact setup.

## REFERENCES

- [1] Nobelprize.org. *Excerpt from the will of Alfred Nobel* (2012).
- [2] Nobelprize.org. *Nobel prizes in physics* (2012).
- [3] L. A. McDonnell and R. M. A. Heeren. *Imaging mass spectrometry*. *Mass Spectrometry Reviews*, **26**, 606–643 (2007).
- [4] D. W. Chandler and P. L. Houston. *Two-dimensional imaging of state-selected photodissociation products detected by multiphoton ionization*. *Journal of Chemical Physics*, **87**, 1445–1447 (1987).
- [5] A. T. J. B. Eppink and D. H. Parker. *Velocity map imaging of ions and electrons using electrostatic lenses: Application in photoelectron and photofragment ion imaging of molecular oxygen*. *Review of Scientific Instruments*, **68**, 3477–3484 (1997).
- [6] S. L. Luxembourg, T. H. Mize, L. A. McDonnell and R. M. A. Heeren. *High-spatial resolution mass spectrometric imaging of peptide and protein distributions on a surface*. *Analytical Chemistry*, **76**, 5339–5344 (2004).
- [7] R. M. Caprioli, T. B. Farmer and J. Gile. *Molecular imaging of biological samples: Localization of peptides and proteins using MALDI-TOF MS*. *Analytical Chemistry*, **69**, 4751–4760 (1997).
- [8] K. Chughtai and R. M. A. Heeren. *Mass spectrometric imaging for biomedical tissue analysis*. *Chemical Reviews*, **110**, 3237–3277 (2010).
- [9] L. MacAleese, J. Stauber and R. M. A. Heeren. *Perspectives for imaging mass spectrometry in the proteomics landscape*. *Proteomics*, **9**, 819–834 (2009).
- [10] J. Stauber, L. MacAleese, J. Franck, E. Claude, M. Snel, B. Kükrer Kaletas, I. M. van der Wiel, M. Wisztorski, I. Fournier and R. M. A. Heeren. *On-tissue protein identification and imaging by MALDI-ion mobility mass spectrometry*. *Journal of the American Society for Mass Spectrometry*, **21**, 338–347 (2010).
- [11] C. Hu, R. van der Heijden, M. Wang, J. van der Greef, T. Hankemeier and G. Xu. *Analytical strategies in lipidomics and applications in disease biomarker discovery*. *Journal of Chromatography B*, **877**, 2836–2846 (2009).
- [12] R. C. Murphy and A. H. J. Merrill. *Lipidomics and imaging mass spectrometry*. *Biochimica et Biophysica Acta*, **1811**, 635–636 (2011).
- [13] N. Goto-Inoue, T. Hayasaka, N. Zaima and M. Setou. *Imaging mass spectrometry for lipidomics*. *Biochimica et Biophysica Acta*, **1811**, 961–969 (2011).
- [14] M. Bedair and L. W. Sumner. *Current and emerging mass-spectrometry technologies for metabolomics*. *Trends in Analytical Chemistry*, **27**, 238–250 (2008).

- [15] D. Y. Lee, B. P. Bowen and T. R. Northen. *Mass spectrometry-based metabolomics, analysis of metabolite-protein interactions, and imaging*. Biotechniques, **49**, 557–565 (2010).
- [16] T. Greer, R. Sturm and L. Li. *Mass spectrometry imaging for drugs and metabolites*. Journal of Proteomics, **74**, 2617–2631 (2011).
- [17] T. C. Rohner, D. Staab and M. Stoeckli. *MALDI mass spectrometric imaging of biological tissue sections*. Mechanisms of Ageing and Development, **126**, 177–185 (2005).
- [18] B. Långström, P. Andrén, O. Lindhe, M. Svedberg and H. Hall. *In vitro imaging techniques in neurodegenerative diseases*. Molecular Imaging and Biology, **9**, 161–175 (2007).
- [19] L. A. McDonnell, G. L. Corthals, S. M. Willems, A. van Remoortere, R. J. M. van Zeijl and A. M. Deelder. *Automated imaging MS: Toward high throughput imaging mass spectrometry*. Journal of Proteomics, **73**, 12791282 (2010).
- [20] P. J. Trim, C. M. Henson, J. L. Avery, A. McEwen, M. F. Snel, E. Claude, P. S. Marshall, A. West, A. P. Princivalle and M. R. Clench. *Matrix-assisted laser desorption/ionization mobility separation-mass spectrometry imaging of vinblastine in whole body tissue sections*. Analytical Chemistry, **80**, 8628–8634 (2008).
- [21] D. R. Ifa, N. E. Manicke, A. L. Dill and R. G. Cooks. *Latent fingerprint chemical imaging by mass spectrometry*. Science, **321**, 805 (2008).
- [22] D. Ifa, A. Jackson, G. Paglia and R. G. Cooks. *Forensic applications of ambient ionization mass spectrometry*. Analytical and Bioanalytical Chemistry, **394**, 1995–2008 (2009).
- [23] B. Kükrer Kaletaş, I. M. van der Wiel, J. Stauber, L. J. Dekker, C. Güzel, J. M. Kros, T. M. Luider and R. M. A. Heeren. *Sample preparation issues for tissue imaging by imaging MS*. Proteomics, **9**, 2622–2633 (2009).
- [24] A. Brunelle and O. Laprévotte. *Recent advances in biological tissue imaging with time-of-flight secondary ion mass spectrometry: Polyatomic ion sources, sample preparation, and applications*. Current Pharmaceutical Design, **13**, 3335–3343 (2007).
- [25] R. L. Caldwell and R. M. Caprioli. *Tissue profiling by mass spectrometry, A review of methodology and applications*. Molecular and Cellular Proteomics, **4**, 394–401 (2005).
- [26] J. C. Vickerman. *Molecular imaging and depth profiling by mass spectrometry-SIMS, MALDI or DESI?* Analyst, **136**, 2199–2217 (2011).
- [27] V. Vidova, M. Volny, K. Lemr and V. Havlicek. *Surface analysis by imaging mass spectrometry*. Collection of Czechoslovak Chemical Communications, **74**, 1101–1116 (2009).
- [28] P. J. Roach, J. Laskin and A. Laskin. *Nanospray desorption electrospray ionization: An ambient method for liquid-extraction surface sampling in mass spectrometry*. Analyst, **135**, 2233–2236 (2010).
- [29] L. Hartmanova, V. Ranc, B. Papouskova, P. Bednar, V. Havlicek and K. Lemr. *Fast profiling of anthocyanins in wine by desorption nano-electrospray ionization mass spectrometry*. Journal of Chromatography A, **1217**, 4223–4228 (2010).
- [30] D. R. Ifa, J. M. Wiseman, Q. Song and R. G. Cooks. *Development of capabilities for imaging mass spectrometry under ambient conditions with desorption electrospray ionization (DESI)*. International Journal of Mass Spectrometry, **259**, 8–15 (2007).

- [31] D. R. Ifa, C. Wu, Z. Ouyang and R. G. Cooks. *Desorption electrospray ionization and other ambient ionization methods: Current progress and preview*. *Analyst*, **135**, 669–681 (2010).
- [32] P. Nemes and A. Vertes. *Laser ablation electrospray ionization for atmospheric pressure, in vivo, and imaging mass spectrometry*. *Analytical Chemistry*, **79**, 8098–8106 (2007).
- [33] P. Nemes, A. S. Woods and A. Vertes. *Simultaneous imaging of small metabolites and lipids in rat brain tissues at atmospheric pressure by laser ablation electrospray ionization mass spectrometry*. *Analytical Chemistry*, **82**, 982–988 (2010).
- [34] S. Trimpin. *A perspective on MALDI alternatives - Total solvent-free analysis and electron transfer dissociation of highly charged ions by laserspray ionization*. *Journal of Mass Spectrometry*, **45**, 471–485 (2010).
- [35] E. D. Inutan, A. L. Richards, J. Wager-Miller, K. Mackie, C. N. McEwen and S. Trimpin. *Laserspray ionization - A new method for protein analysis directly from tissue at atmospheric pressure with ultra-high mass resolution and electron transfer dissociation*. *Molecular and Cellular Proteomics*, **10**, 760–768 (2011).
- [36] P. Chaurand, S. A. Schwartz and R. M. Caprioli. *Imaging mass spectrometry: A new tool to investigate the spatial organization of peptides and proteins in mammalian tissue sections*. *Current Opinion in Chemical Biology*, **6**, 676–681 (2002).
- [37] P. Chaurand, J. Norris, D. Cornett, J. A. Mobley and R. M. Caprioli. *New developments in profiling and imaging of proteins from tissue sections by MALDI mass spectrometry*. *Journal of Proteome Research*, **5**, 2889–2900 (2006).
- [38] D. S. Cornett, M. L. Reyzer, P. Chaurand and R. M. Caprioli. *MALDI imaging mass spectrometry: Molecular snapshots of biochemical systems*. *Nature Methods*, **4**, 828–833 (2007).
- [39] A. Walch, S. Rauser, S. Deininger and H. Höfler. *MALDI imaging mass spectrometry for direct tissue analysis: A new frontier for molecular histology*. *Histochemistry and Cell Biology*, **130**, 421–434 (2008).
- [40] R. J. A. Goodwin, S. R. Pennington and A. R. Pitt. *Protein and peptides in pictures: Imaging with MALDI mass spectrometry*. *Proteomics*, **8**, 3785–3800 (2008).
- [41] J. Fletcher and J. Vickerman. *A new SIMS paradigm for 2D and 3D molecular imaging of bio-systems*. *Analytical and Bioanalytical Chemistry*, **396**, 85–104 (2010).
- [42] J. C. Vickerman. *Molecular SIMS: A journey from single crystal to biological surface studies*. *Surface Science*, **603**, 1926–1936 (2009).
- [43] R. M. A. Heeren, L. A. McDonnell, E. Amstalden, S. L. Luxembourg, A. F. M. Altaear and S. R. Piersma. *Why don't biologists use SIMS?: A critical evaluation of imaging MS*. *Applied Surface Science*, **252**, 6827–6835 (2006).
- [44] A. N. Krutchinsky and B. T. Chait. *On the nature of the chemical noise in MALDI mass spectra*. *Journal of the American Society for Mass Spectrometry*, **13**, 129–134 (2002).
- [45] J. Pól, V. Vidová, G. Kruppa, V. Koblíha, P. Novák, K. Lemr, T. Kotiaho, R. Kostianen, V. Havlcek and M. Volný. *Automated ambient desorption-ionization platform for surface imaging integrated with a commercial Fourier transform ion cyclotron resonance mass spectrometer*. *Analytical Chemistry*, **81**, 8479–8487 (2009).

- [46] I. M. Taban, A. F. M. Altelaar, Y. E. M. van der Burgt, L. A. McDonnell, R. M. A. Heeren, F. J. and G. Baykut. *Imaging of peptides in the rat brain using MALDI-FTICR mass spectrometry*. Journal of the American Society for Mass Spectrometry, **18**, 145–151 (2007).
- [47] E. A. Stemmler, C. R. Cashman, D. Messinger, N. P. Gardner, P. S. Dickinson and A. E. Christie. *High-mass-resolution direct-tissue MALDI-FTMS reveals broad conservation of three neuropeptides (APSGFLGMR amide, GYRKPPFNGSIF amide and pQDLL-HVFLRF amide) across members of seven decapod crustacean infraorders*. Peptides, **28**, 2104–2115 (2007).
- [48] T. K. Sinha, S. Khatib-Shahidi, T. E. Yankeelov, K. Mapara, M. Ehtesham, D. S. Cornett, B. M. Dawant, R. M. Caprioli and J. C. Gore. *Integrating spatially resolved three-dimensional MALDI IMS with in vivo magnetic resonance imaging*. Nature Methods, **5**, 57–59 (2008).
- [49] L. Sleno and D. A. Volmer. *Ion activation methods for tandem mass spectrometry*. Journal of Mass Spectrometry, **39**, 1091–1112 (2004).
- [50] B. J. Garrison, T. Itina, L. V. Zhigilei, A. Delcorte, K. Krantzman, Y. Yingling, C. F. McQuawa, E. Smiley and N. Winograd. *Big molecule ejection - SIMS vs. MALDI*. Applied Surface Science, **203-204**, 69–71 (2003).
- [51] B. J. Garrison. *Atoms, clusters and photons: Energetic probes for mass spectrometry*. Applied Surface Science, **252**, 6409–6412 (2006).
- [52] R. Zenobi and R. Knochenmuss. *Ion formation in MALDI mass spectrometry*. Mass Spectrometry Reviews, **17**, 337–366 (1998).
- [53] P. D. Pichowski, A. J. Carado, M. E. Kurczy, S. G. Ostrowski, M. L. Heien, N. Winograd and A. G. Ewing. *MS/MS methodology to improve subcellular mapping of cholesterol using TOF-SIMS*. Analytical Chemistry, **80**, 8662–8667 (2008).
- [54] J. S. Fletcher, S. Rabbani, A. Henderson, P. Blenkinsopp, S. P. Thompson, N. P. Lockyer and J. C. Vickerman. *A new dynamic in mass spectral imaging of single biological cells*. Analytical Chemistry, **80**, 9058–9064 (2008).
- [55] E. A. Jones, J. S. Fletcher, C. E. Thompson, D. A. Jackson, N. P. Lockyer and J. C. Vickerman. *TOF-SIMS analysis of bio-systems: Are polyatomic primary ions the solution?* Applied Surface Science, **252**, 6844–6854 (2006).
- [56] J. S. Fletcher, N. P. Lockyer and J. C. Vickerman. *Developments in molecular SIMS depth profiling and 3D imaging of biological systems using polyatomic primary ions*. Mass Spectrometry Reviews, **30**, 142–174 (2011).
- [57] A. Carado, M. K. Passarelli, J. Kozole, J. E. Wingate, N. Winograd and A. V. Loboda. *C<sub>60</sub> secondary ion mass spectrometry with a hybrid-quadrupole orthogonal time-of-flight mass spectrometer*. Analytical Chemistry, **80**, 7921–7929 (2008).
- [58] J. A. McLean, W. B. Ridenour and R. M. Caprioli. *Profiling and imaging of tissues by imaging ion mobility-mass spectrometry*. Journal of Mass Spectrometry, **42**, 1099–1105 (2007).

- [59] S. N. Jackson, M. Ugarov, T. Egan, J. D. Post, D. Langlais, J. Albert Schultz and A. S. Woods. *MALDI-ion mobility-TOFMS imaging of lipids in rat brain tissue*. Journal of Mass Spectrometry, **42**, 1093–1098 (2007).
- [60] A. Kiss and R. M. A. Heeren. *Size, weight and position: Ion mobility spectrometry and imaging MS combined*. Analytical and Bioanalytical Chemistry, **399**, 2623–2634 (2011).
- [61] S. S. Rubakhin, J. C. Jurchen, E. B. Monroe and J. V. Sweedler. *Imaging mass spectrometry: Fundamentals and applications to drug discovery*. Drug Discovery Today, **10**, 823–837 (2005).
- [62] D. W. Koppenaal, C. J. Barinaga, M. B. Denton, R. P. Sperline, G. M. Hieftje, G. D. Schilling, F. J. Andrade and J. H. Barnes. *MS detectors*. Analytical Chemistry, **77**, 418 A–427 A (2005).
- [63] I. V. Veryovkin, W. I. Calaway, C. E. Tripa and M. J. Pellin. *Mass spectrometry on the nanoscale with ion sputtering based techniques: What is feasible*. Nuclear Instruments and Methods in Physics Research Section B: Beam Interactions with Materials and Atoms, **261**, 508–511 (2007).
- [64] S. Ghosal, S. J. Fallon, T. J. Leighton, K. E. Wheeler, M. J. Kristo, I. D. Hutcheon and P. K. Weber. *Imaging and 3D elemental characterization of intact bacterial spores by high-resolution secondary ion mass spectrometry*. Analytical Chemistry, **80**, 5986–5992 (2008).
- [65] B. Spengler and M. Hubert. *Scanning microprobe matrix-assisted laser desorption ionization (SMALDI) mass spectrometry: Instrumentation for sub-micrometer resolved LDI and MALDI surface analysis*. Journal of the American Society for Mass Spectrometry, **13**, 735–748 (2002).
- [66] J. A. Bradshaw, O. S. Ovchinnikova, K. A. Meyer and D. E. Goeringer. *Combined chemical and topographic imaging at atmospheric pressure via microprobe laser desorption/ionization mass spectrometry-atomic force microscopy*. Rapid Communications in Mass Spectrometry, **23**, 3781–3786 (2009).
- [67] M. Köstler, D. Kirsch, A. Hester, A. Leisner, S. Guenther and B. Spengler. *A high-resolution scanning microprobe matrix-assisted laser desorption/ionization ion source for imaging analysis on an ion trap/Fourier transform ion cyclotron resonance mass spectrometer*. Rapid Communications in Mass Spectrometry, **22**, 3275–3285 (2008).
- [68] S. L. Luxembourg, L. A. McDonnell, T. H. Mize and R. M. A. Heeren. *Infrared mass spectrometric imaging below the diffraction limit*. Journal of Proteome Research, **4**, 671–673 (2005).
- [69] J. C. Jurchen, S. S. Rubakhin and J. V. Sweedler. *MALDI-MS imaging of features smaller than the size of the laser beam*. Journal of the American Society for Mass Spectrometry, **16**, 1654–1659 (2005).
- [70] J. H. Jungmann, L. MacAleese, J. Visser, M. J. J. Vrakking and R. M. A. Heeren. *High dynamic range bio-molecular ion microscopy with the Timepix detector*. Analytical Chemistry, **83**, 7888–7894 (2011).

- [71] I. Klinkert, L. A. McDonnell, S. L. Luxembourg, A. F. M. Altelaar, E. R. Amstalden, S. R. Piersma and R. M. A. Heeren. *Tools and strategies for visualization of large image data sets in high-resolution imaging mass spectrometry*. Review of Scientific Instruments, **78**, 053716–10 (2007).
- [72] L. A. Klerk, N. P. Lockyer, A. Kharchenko, L. MacAleese, P. Y. W. Dankers, J. C. Vickerman and R. M. A. Heeren.  *$C_{60}^+$  secondary ion microscopy using a delay line detector*. Analytical Chemistry, **82**, 801–807 (2010).
- [73] J. H. Jungmann, L. MacAleese, R. Buijs, F. Giskes, A. de Snaijer, J. Visser, J. Visschers, M. J. J. Vrakking and R. M. A. Heeren. *Fast, high resolution mass spectrometry imaging using a Medipix pixelated detector*. Journal of the American Society for Mass Spectrometry, **21**, 2023–2030 (2010).
- [74] L. A. Klerk, A. F. M. Altelaar, M. Froesch, L. A. McDonnell and R. M. A. Heeren. *Fast and automated large-area imaging MALDI mass spectrometry in microprobe and microscope mode*. International Journal of Mass Spectrometry, **285**, 19–25 (2009).
- [75] J. Spraggins and R. Caprioli. *High-speed MALDI-TOF imaging mass spectrometry: Rapid ion image acquisition and considerations for next generation instrumentation*. Journal of The American Society for Mass Spectrometry, **22**, 1022–1031 (2011).
- [76] G. Hopfgartner, E. Varesio and M. Stoeckli. *Matrix-assisted laser desorption/ionization mass spectrometric imaging of complete rat sections using a triple quadrupole linear ion trap*. Rapid Communications in Mass Spectrometry, **23**, 733–736 (2009).
- [77] M. Frösch, S. L. Luxembourg, D. Verheijde and R. M. A. Heeren. *Mass spectrometry imaging using a delay-line detector*. European Journal of Mass Spectrometry, **16**, 35–45 (2010).
- [78] J. Ullrich, R. Moshhammer, A. Dorn, R. Dörner, L. P. H. Schmidt and H. Schmidt-Böcking. *Recoil-ion and electron momentum spectroscopy: Reaction-microscopes*. Reports on Progress in Physics, **66**, 1463–1545 (2003).
- [79] A. Vredenburg, W. G. Roeterdink and M. H. M. Janssen. *A photoelectron-photoion coincidence imaging apparatus for femtosecond time-resolved molecular dynamics with electron time-of-flight resolution of  $\sigma=18$  ps and energy resolution  $\Delta E/E=3.5\%$* . Review of Scientific Instruments, **79**, 063108–9 (2008).
- [80] O. Jagutzki *et al.* *Multiple hit readout of a microchannel plate detector with a three-layer delay-line anode*. IEEE Transactions on Nuclear Science, **49**, **5**, 2477–2483 (2002).
- [81] G. Gademann, Y. Huismans, A. Gijsbertsen, J. Jungmann, J. Visschers and M. Vrakking. *Velocity map imaging using an in-vacuum pixel detector*. Review of Scientific Instruments, **80**, 103105–7 (2009).
- [82] J. Jungmann, A. Gijsbertsen, J. Visser, J. Visschers, R. M. A. Heeren and M. J. J. Vrakking. *A new imaging method for understanding chemical dynamics: Efficient slice imaging using an in-vacuum pixel detector*. Review of Scientific Instruments, **81**, 103112–7 (2010).
- [83] C. Bamberger, U. Renz and A. Bamberger. *Digital imaging mass spectrometry*. Journal of the American Society for Mass Spectrometry, **22**, 1079–1087 (2011).

- 
- [84] X. Llopart, M. Campbell, R. Dinapoli, D. San Segundo and E. Pernigotti. *Medipix2, a 64k pixel readout chip with 55 micron square elements working in single photon counting mode*. IEEE Transactions on Nuclear Science, **49**, 2279–2283 (2002).
- [85] X. Llopart and M. Campbell. *First test measurements of a 64k pixel readout chip working in single photon counting mode*. Nuclear Instruments and Methods in Physics Research Section A: Accelerators, Spectrometers, Detectors and Associated Equipment, **509**, 157–163 (2003).
- [86] X. Llopart, R. Ballabriga, M. Campbell, L. Tlustos and W. Wong. *Timepix, a 65k programmable pixel readout chip for arrival time, energy and/or photon counting measurements*. Nuclear Instruments and Methods in Physics Research Section A: Accelerators, Spectrometers, Detectors and Associated Equipment, **581**, 485–494 (2007).
- [87] B. Schueler. *Microscope imaging by time-of-flight secondary ion mass spectrometry*. Microscopy Microanalysis Microstructur, **3**, 119–13 (1992).
- [88] G. Mazza *et al.* *The NA62 Gigatracker pixel detector system*. Nuclear Instruments and Methods in Physics Research Section A: Accelerators, Spectrometers, Detectors and Associated Equipment, **617**, 558–559 (2010).
- [89] M. Fiorini *et al.* *The NA62 Gigatracker: Detector properties and pixel read-out architectures*. Nuclear Instruments and Methods in Physics Research Section A: Accelerators, Spectrometers, Detectors and Associated Equipment, **624**, 314–316 (2010).
- [90] M. Fiorini *et al.* *The Gigatracker: An ultra-fast and low-mass silicon pixel detector for the NA62 experiment*. Nuclear Instruments and Methods in Physics Research Section A: Accelerators, Spectrometers, Detectors and Associated Equipment, **628**, 292–295 (2011).
- [91] A. Kluge *et al.* *NA62 Giga Tracker*. In *Proceedings of Science, 19th International Workshop on Vertex Detectors, VERTEX* (2010).
- [92] M. Noy, G. Aglieri Rinella, M. Fiorini, P. Jarron, J. Kaplon, A. Kluge, E. Martin, M. Morel, L. Perktold and P. Riedler. *Characterisation of the NA62 GigaTracker end of column readout ASIC*. Journal of Instrumentation, **6**, C01086 (2011).
- [93] M. Campbell. *Medipix Collaboration (collaboration spokesperson)*.
- [94] J. Vallergera, J. McPhate, A. Tremsin and O. Siegmund. *High-resolution UV, alpha and neutron imaging with the Timepix CMOS readout*. Nuclear Instruments and Methods in Physics Research Section A: Accelerators, Spectrometers, Detectors and Associated Equipment, **591**, 151–154 (2008).
- [95] A. G. Marshall, C. L. Hendrickson and G. S. Jackson. *Fourier transform ion cyclotron resonance mass spectrometry: A primer*. Mass Spectrometry Reviews, **17**, 1–35 (1998).
- [96] A. Makarov. *Electrostatic axially harmonic orbital trapping: A high-performance technique of mass analysis*. Analytical Chemistry, **72**, 1156–1162 (2000).
- [97] A. Makarov, E. Denisov, O. Lange and S. Horning. *Dynamic range of mass accuracy in LTQ orbitrap hybrid mass spectrometer*. Journal of the American Society for Mass Spectrometry, **17**, 977–982 (2006).

- [98] A. Römpp, S. Guenther, Y. Schober, O. Schulz, Z. Takats, W. Kummer and B. Spengler. *Histology by mass spectrometry: Label-free tissue characterization obtained from high-accuracy bioanalytical imaging*. *Angewandte Chemie International Edition*, **49**, 3834–3838 (2010).
- [99] P. D. E. M. Verhaert, M. W. H. Pinkse, K. Strupat and M. C. Prieto Conaway. *Imaging of similar mass neuropeptides in neuronal tissue by enhanced resolution MALDI MS with an ion trap-orbitrap<sup>TM</sup> hybrid instrument*. *Methods in Molecular Biology*, **656**, 433–449 (2010).
- [100] K. Aizikov and P. O'Connor. *Use of the filter diagonalization method in the study of space charge related frequency modulation in Fourier transform ion cyclotron resonance mass spectrometry*. *Journal of The American Society for Mass Spectrometry*, **17**, 836–843 (2006).
- [101] E. A. Jones, R. J. M. van Zeijl, P. Andren, A. M. Deelder, L. Wolters and L. A. McDonnell. *High speed data processing for imaging MS-based molecular histology using graphical processing units*. *Journal of the American Society for Mass Spectrometry*, **23**, 745–752 (2012).
- [102] Y. E. M. van der Burgt, I. Taban, M. Konijnenburg, M. Biskup, M. C. Duursma, R. M. A. Heeren and A. Rompp. *Parallel Processing of Large Datasets from NanoLC-FTICR-MS Measurements*. *Journal of the American Society for Mass Spectrometry*, **18**, 152–161 (2007).
- [103] M. Mann and N. L. Kelleher. *Precision proteomics: The case for high resolution and high mass accuracy*. *Proceedings of the National Academy of Sciences of the United States of America*, **105**, 18132–18138 (2008).
- [104] D. S. Cornett, S. L. Frappier and R. M. Caprioli. *MALDI-FTICR imaging mass spectrometry of drugs and metabolites in tissue*. *Analytical Chemistry*, **80**, 5648–5653 (2008).
- [105] S. Guenther, A. Römpp, W. Kummer and B. Spengler. *AP-MALDI imaging of neuropeptides in mouse pituitary gland with 5  $\mu\text{m}$  spatial resolution and high mass accuracy*. *International Journal of Mass Spectrometry*, **305**, 228–237 (2011).
- [106] D. F. Smith, E. W. Robinson, A. V. Tolmachev, R. M. A. Heeren and L. Paša-Tolić. *C<sub>60</sub> secondary ion fourier transform ion cyclotron resonance mass spectrometry*. *Analytical Chemistry*, **83**, 9552–9556 (2011).
- [107] P. Kovarik, C. Grivet, E. Bourgogne and G. Hopfgartner. *Method development aspects for the quantitation of pharmaceutical compounds in human plasma with a matrix-assisted laser desorption/ionization source in the multiple reaction monitoring mode*. *Rapid Communications in Mass Spectrometry*, **21**, 911–919 (2007).
- [108] D. A. Pirman and R. A. Yost. *Quantitative tandem mass spectrometric imaging of endogenous acetyl-L-carnitine from piglet brain tissue using an internal standard*. *Analytical Chemistry*, **83**, 8575–8581 (2011).
- [109] A. C. Crecelius, D. S. Cornett, R. M. Caprioli, B. Williams, B. M. Dawant and B. Bodenheimer. *Three-dimensional visualization of protein expression in mouse brain structures using imaging mass spectrometry*. *Journal of the American Society for Mass Spectrometry*, **16**, 1093–1099 (2005).

- 
- [110] K. Chughtai, L. Jiang, T. R. Greenwood, I. Klinkert, E. R. Amstalden van Hove, R. M. A. Heeren and K. Glunde. *Fiducial markers for combined 3-dimensional mass spectrometric and optical tissue imaging*. *Analytical Chemistry*, **84**, 1817–1823 (2012).
- [111] I. Klinkert and R. M. A. Heeren. *Methods for full resolution data exploration and visualization for large 2D and 3D mass spectrometry imaging datasets*. In preparation (2012).
- [112] H. Ye, T. Greer and L. Li. *From pixel to voxel: A deeper view of biological tissue by 3D mass spectral imaging*. *Bioanalysis*, **3**, 313–332 (2011).
- [113] A. Kirkpatrick. *Gas cluster ion beam applications and equipment*. *Nuclear Instruments and Methods in Physics Research Section B: Beam Interactions with Materials and Atoms*, **206**, 830–837 (2003).
- [114] I. Yamada. *Investigation of ionized cluster beam bombardment and its applications for materials modification*. *Radiation Effects and Defects in Solids*, **124**, 69–80 (1992).
- [115] S. Chandra. *3D subcellular SIMS imaging in cryogenically prepared single cells*. *Applied Surface Science*, **231–232**, 467–469 (2004).
- [116] J. S. Fletcher, N. P. Lockyer, S. Vaidyanathan and J. C. Vickerman. *TOF-SIMS 3D biomolecular imaging of xenopus laevis oocytes using buckminsterfullerene (C<sub>60</sub>) primary ions*. *Analytical Chemistry*, **79**, 2199–2206 (2007).
- [117] T. Wyttenbach and M. Bowers. *Gas-phase conformations: The ion mobility/ion chromatography method*. In C. Schalley, ed., *Modern Mass Spectrometry*, Springer Berlin/Heidelberg, vol. 225 of *Topics in Current Chemistry*, 207–232 (2003).
- [118] B. C. Bohrer, S. I. Merenbloom, S. L. Koeniger, A. E. Hilderbrand and D. E. Clemmer. *Biomolecule analysis by ion mobility spectrometry*. *Annual Review of Analytical Chemistry*, **1**, 293–327 (2008).
- [119] A. Tempez *et al.* *Matrix implanted laser desorption ionization (MILDI) combined with ion mobility-mass spectrometry for bio-surface analysis*. *Journal of Proteome Research*, **4**, 540–545 (2005).
- [120] D. N. Perkins, D. J. Pappin, D. M. Creasy and J. S. Cottrell. *Probability-based protein identification by searching sequence databases using mass spectrometry data*. *Electrophoresis*, **20**, 3551–3567 (1999).
- [121] M.-C. Djidja, S. Francese, P. M. Loadman, C. W. Sutton, P. Scriven, E. Claude, M. F. Snel, J. Franck, M. Salzert and M. R. Clench. *Detergent addition to tryptic digests and ion mobility separation prior to MS/MS improves peptide yield and protein identification for in situ proteomic investigation of frozen and formalin-fixed paraffin-embedded adenocarcinoma tissue sections*. *Proteomics*, **9**, 2750–2763 (2009).
- [122] *Webster’s New World Dictionary & Thesaurus*. Simon & Schuster Inc. (1996).
- [123] J. H. Barnes and G. M. Hieftje. *Recent advances in detector-array technology for mass spectrometry*. *International Journal of Mass Spectrometry*, **238**, 33–46 (2004).
- [124] A. J. H. Boerboom. *Array detection of mass spectra, a comparison with conventional detection methods*. *Organic Mass Spectrometry*, **26**, 929–935 (1991).

- [125] J. L. Wiza. *Microchannel Plate Detectors*. Nuclear Instruments and Methods in Physics Research Section A: Accelerators, Spectrometers, Detectors and Associated Equipment, **162**, 587–601 (197).
- [126] A. Tremsin and O. H. W. Siegmund. *Spatial distribution of electron cloud footprints from microchannel plates: Measurements and modeling*. Review of Scientific Instrument, **70**, 3282–3288 (1999).
- [127] R. J. Wenzel, S. Kern and R. Zenobi. In *Proceedings of the 54th ASMS Conference on Mass Spectrometry and Allied Topics* (2006).
- [128] A. van Remoortere, R. J. M. van Zeijl, N. van den Oever, J. Franck, R. Longuespée, M. Wisztorski, M. Salzet, A. M. Deelder, I. Fournier and L. A. McDonnell. *MALDI imaging and profiling MS of higher mass proteins from tissue*. Journal of the American Society for Mass Spectrometry, **21**, 1922–1929 (2010).
- [129] B. K. Seyfried, J. Siekmann, O. Belgacem, R. J. Wenzel, P. L. Turecek and G. Allmaier. *MALDI linear TOF mass spectrometry of PEGylated (glyco)proteins*. Journal of Mass Spectrometry, **45**, 612–617 (2010).
- [130] Kraus. *Cryogenic detectors and their application to mass spectrometry*. International Journal of Mass Spectrometry, **215**, 45 – 58 (2002).
- [131] M. Frank, S. E. Labov, G. Westmacott and W. H. Benner. *Energy-sensitive cryogenic detectors for high-mass biomolecule mass spectrometry*. Mass Spectrometry Reviews, **18**, 155–186 (1999).
- [132] M. Frank. *Mass spectrometry with cryogenic detectors*. Nuclear Instruments & Methods in Physics Research Section A: Accelerators Spectrometers Detectors and Associated Equipment, **444**, 375–384 (2000).
- [133] R. J. Wenzel, U. Matter, L. Schultheis and R. Zenobi. *Analysis of megadalton ions using cryodetection MALDI time-of-flight mass spectrometry*. Analytical Chemistry, **77**, 4329–4337 (2005).
- [134] M. Heller, D. Stalder, E. Schlappritzi, G. Hayn, U. Matter and A. Haeberli. *Mass spectrometry-based analytical tools for the molecular protein characterization of human plasma lipoproteins*. Proteomics, **5**, 2619–2630 (2005).
- [135] N. Zen, K. Suzuki, S. Shiki and M. Ohkubo. *Niobium superconducting strip line detectors (SSLD) for time-of-flight mass spectroscopy (TOF-MS)*. Physica C: Superconductivity, **469**, 1684–1687 (2009).
- [136] A. Casaburi, N. Zen, K. Suzuki, M. Ejrnaes, S. Pagano, R. Cristiano and M. Ohkubo. *Subnanosecond time response of large-area superconducting stripline detectors for keV molecular ions*. Applied Physics Letters, **94**, 212502–3 (2009).
- [137] J. Park, H. Qin, M. Scalf, R. T. Hilger, M. S. Westphall, L. M. Smith and R. H. Blick. *A mechanical nanomembrane detector for time-of-flight mass spectrometry*. Nano Letters, **11**, 3681–3684 (2011).
- [138] J. H. Jungmann and R. M. A. Heeren. *Emerging technologies in mass spectrometry imaging*. Journal of Proteomics, **75**, 5077–5092 (2012).

- 
- [139] C. R. Gebhardt, P. Rakitzis, P. C. Samartzis, V. Ladopoulos and T. N. Kitsopoulos. *Slice imaging: A new approach to ion imaging and velocity mapping*. Review of Scientific Instruments, **72**, 3848–3853 (2001).
- [140] V. Papadakis and T. N. Kitsopoulos. *Slice imaging and velocity mapping using a single field*. Review of Scientific Instruments, **77**, 083101–5 (2006).
- [141] D. Townsend, M. P. Minitti and A. G. Suits. *Direct current slice imaging*. Review of Scientific Instruments, **74**, 2530–2539 (2003).
- [142] V. Mergel *et al.* *He<sup>2+</sup> on He: State-selective, scattering-angle-dependent capture cross sections measured by cold target recoil ion momentum spectroscopy (COLTRIMS)*. Nuclear Instruments and Methods in Physics Research Section B: Beam Interactions with Materials and Atoms, **98**, 593–596 (1995).
- [143] J. Ullrich, R. Moshhammer, R. Dörner, O. Jagutzki, V. Mergel, H. Schmidt-Böcking and L. Spielberger. *Recoil-ion momentum spectroscopy*. Journal of Physics B: Atomic, Molecular and Optical Physics, **30**, 2917–2974 (1997).
- [144] R. Dörner, V. Mergel, O. Jagutzki, L. Spielberger, J. Ullrich, R. Moshhammer and H. Schmidt-Böcking. *Cold target recoil ion momentum spectroscopy: A ‘momentum microscope’ to view atomic collision dynamics*. Physics Reports, **330**, 95–192 (2000).
- [145] E. M. Müller, J. A. Panitz and B. S. McLane. *The atom-probe field ion microscope*. Review of Scientific Instruments, **39**, 83–86 (1968).
- [146] M. Leisch. *Atom-probe field ion microscopy*. Microchimica Acta, **107**, 95–104 (1992).
- [147] R. Bellazzini *et al.* *Single photon imaging at ultra-high resolution*. Nuclear Instruments and Methods in Physics Research Section A: Accelerators, Spectrometers, Detectors and Associated Equipment, **591**, 125–128 (2008).
- [148] O. Siegmund, A. Tremsin, J. Vallergera and J. McPhate. *Microchannel plate cross-strip detectors with high spatial and temporal resolution*. Nuclear Instruments and Methods in Physics Research Section A: Accelerators, Spectrometers, Detectors and Associated Equipment, **610**, 118–122 (2009).
- [149] H. G. Boettger, C. E. Giffen and D. D. Norris. *Electro-optical ion detectors in mass spectrometry simultaneous monitoring of all ions over wide mass ranges*. In Y. Talmi, ed., *ACS Symposium Series*. ACS: Washington, D. C (1979), 102, 291318.
- [150] B. Hedfjaell and R. Ryhage. *Electrooptical ion detector for capillary column gas chromatography/negative ion mass spectrometry*. Analytical Chemistry, **51**, 1687–1690 (1979).
- [151] B. Hedfjaell and R. Ryhage. *Electrooptical ion detector for gas chromatography/mass spectrometry*. Analytical Chemistry, **53**, 1641–1644 (1981).
- [152] J. S. Cottrell and S. Evans. *The application of a multichannel electro-optical detection system to the analysis of large molecules by FAB mass spectrometry*. Rapid Communications in Mass Spectrometry, **1**, 1–2 (1987).
- [153] C. E. Giffin, H. G. Boettger and D. D. Norris. *An electro-optical detector for focal plane mass spectrometers*. International Journal of Mass Spectrometry and Ion Physics, **15**, 437–449 (1974).

- [154] J. G. Aase, J. K. Burchill, D. J. Knudsen, J. P. Hackett and B. Moffat. *Spatial resolution and relative brightness of a microchannel plate detector system with P20 and P43 phosphor screens*. Optical Engineering, **50**, 064001 (2011).
- [155] M. Lampton and C. W. Carlson. *Low-distortion resistive anodes for two-dimensional position-sensitive MCP systems*. Review of Scientific Instruments, **50**, 1093–1097 (1979).
- [156] R. W. Odom, B. K. Furman, C. A. Evans, C. E. Bryson, W. A. Petersen, M. A. Kelly and D. H. Wayne. *Quantitative image acquisition system for ion microscopy based on the resistive anode encoder*. Analytical Chemistry, **55**, 574–578 (1983).
- [157] R. H. Brigham, R. J. Bleiler, P. J. McNitt, D. A. Reed and R. H. Fleming. *Characterization of two resistive anode encoder position sensitive detectors for use in ion microscopy*. Review of Scientific Instruments, **64**, 420–10 (1993).
- [158] A. Oelsner, O. Schmidt, M. Schicketanz, M. Klais, G. Schönhense, V. Mergel, O. Jagutzki and H. Schmidt-Böcking. *Microspectroscopy and imaging using a delay line detector in time-of-flight photoemission microscopy*. Review of Scientific Instruments, **72**, 3968–3974 (2001).
- [159] O. Jagutzki, V. Mergel, K. Ullmann-Pfleger, L. Spielberger, Y. Spillmann, R. Dörner and H. Schmidt-Böcking. *A broad-application microchannel-plate detector system for advanced particle or photon detection tasks: large area imaging, precise multi-hit timing information and high detection rate*. Nuclear Instruments and Methods in Physics Research Section A: Accelerators, Spectrometers, Detectors and Associated Equipment, **477**, 244–249 (2002).
- [160] O. H. W. Siegmund, M. Lampton, J. Bixier, S. Chakrabarti, J. Vallerga, S. Bowyer and R. F. Malina. *Wedge and strip image readout systems for photon-counting detectors in space astronomy*. Journal of the Optical Society of America A, **3**, 2139–2145 (1986).
- [161] O. H. W. Siegmund, S. Clothier, J. Thornton, J. Lemen, R. Harper, I. M. Mason and J. L. Culhane. *Application of the wedge and strip anode to position sensing with microchannel plates and proportional counters*. IEEE Transactions on Nuclear Science, **30**, 503–507 (1983).
- [162] J. S. Lapington, A. D. Smith, D. M. Walton and H. E. Schwarz. *Microchannel plate pore size limited imaging with ultra-thin wedge and strip anodes*. IEEE Transactions on Nuclear Science, **34**, 431–433 (1987).
- [163] J. S. Lapington, R. Kessel and D. M. Walton. *Spatial resolution limitations of microchannel plate/conductive charge division readout devices*. Nuclear Instruments and Methods in Physics Research Section A: Accelerators, Spectrometers, Detectors and Associated Equipment, **273**, 663–666 (1988).
- [164] O. H. W. Siegmund, A. Tremsin, J. V. Vallerga and J. Hull. *Cross Strip Anode Imaging Readouts for Microchannel Plate Detectors*. IEEE Transactions on Nuclear Science, **48**, 430–434 (2001).
- [165] O. H. W. Siegmund, A. S. Tremsin, J. V. Vallerga, R. Abiad and J. Hull. *High resolution cross strip anodes for photon counting detectors*. Nuclear Instruments and Methods in Physics Research Section A: Accelerators, Spectrometers, Detectors and Associated Equipment, **504**, 177 – 181 (2003).

- 
- [166] U. Vohrer, C. Blomfield, S. Page and A. Roberts. *Quantitative XPS imaging - new possibilities with the delay-line detector*. Applied Surface Science, **252**, 61–65 (2005).
- [167] G. A. van Riessen and S. M. Thurgate. *Auger photoelectron coincidence spectroscopy: Simplifying complexity*. Surface and Interface Analysis, **38**, 691–698 (2006).
- [168] A. Nomerotski *et al.* *Pixel imaging mass spectrometry with fast silicon detectors*. Nuclear Instruments and Methods in Physics Research Section A: Accelerators, Spectrometers, Detectors and Associated Equipment, **633**, **Supplement 1**, S243–S246 (2011).
- [169] J. V. Vallerga and O. H. W. Siegmund. *2K x 2K resolution element photon counting MCP sensor with > 200 kHz event rate capability*. Nuclear Instruments and Methods in Physics Research Section A: Accelerators, Spectrometers, Detectors and Associated Equipment, **442**, 159–163 (2000).
- [170] O. H. Siegmund, J. V. Vallerga, A. S. Tremsin, J. Mcphate and B. Feller. *High spatial resolution neutron sensing microchannel plate detectors*. Nuclear Instruments and Methods in Physics Research Section A: Accelerators, Spectrometers, Detectors and Associated Equipment, **576**, 178–182 (2007).
- [171] A. S. Tremsin, O. H. W. Siegmund, J. S. Hull, J. V. Vallerga, J. B. McPhate, J. Soderstrom, J.-W. Chiou, J. Guo and Z. Hussain. *High resolution photon counting detection system for advanced inelastic X-ray scattering studies*. IEEE Transactions on Nuclear Science, **54**, 706–709 (2007).
- [172] A. S. Tremsin, J. V. Vallerga, J. B. McPhate, O. H. W. Siegmund, W. B. Feller, L. Crow and R. G. Cooper. *On the possibility to image thermal and cold neutron with sub- $\mu\text{m}$  spatial resolution*. Nuclear Instruments and Methods in Physics Research Section A: Accelerators, Spectrometers, Detectors and Associated Equipment, **592**, 374–384 (2008).
- [173] J. Vallerga, R. Raffanti, A. Tremsin, J. McPhate and O. Siegmund. *MCP detector read out with a bare quad Timepix at kilohertz frame rates*. Journal of Instrumentation, **6**, C01049 (2011).
- [174] H. Spieler. *Semiconductor Detector Systems*. Oxford University Press (2005).
- [175] G. E. Smith. *The invention and early history of the CCD*. Nuclear Instruments and Methods in Physics Research Section A: Accelerators, Spectrometers, Detectors and Associated Equipment, **607**, 1–6 (2009).
- [176] N. Wermes. *Pixel detectors for particle physics and imaging applications*. Nuclear Instruments and Methods in Physics Research Section A: Accelerators, Spectrometers, Detectors and Associated Equipment, **512**, 277–288 (2003).
- [177] N. Wermes. *Pixel detectors for tracking and their spin-off in imaging applications*. Nuclear Instruments and Methods in Physics Research Section A: Accelerators, Spectrometers, Detectors and Associated Equipment, **541**, 150–165 (2005).
- [178] H. Krüger. *2D Detectors for particle physics and for imaging applications*. Nuclear Instruments and Methods in Physics Research Section A: Accelerators, Spectrometers, Detectors and Associated Equipment, **551**, 1–14 (2005).
- [179] M. Locker, P. Fischer, S. Krimmel, H. Kruger, M. Lindner, K. Nakazawa, T. Takahashi and N. Wermes. *Single photon counting X-ray imaging with Si and CdTe single chip pixel detectors and multichip pixel modules*. IEEE Transactions on Nuclear Science, **51**, 1717–1723 (2004).

- [180] P. Pangaud, S. Basolo, N. Boudet, J.-F. Berar, B. Chantepie, P. Delpierre, B. Dinkespiler, S. Hustache, M. Menouni and C. Morel. *XPAD3: A new photon counting chip for X-ray CT-scanner*. Nuclear Instruments and Methods in Physics Research Section A: Accelerators, Spectrometers, Detectors and Associated Equipment, **571**, 321–324 (2007).
- [181] S. Basolo *et al.* *A 20 kpixels CdTe photon-counting imager using XPAD chip*. Nuclear Instruments and Methods in Physics Research Section A: Accelerators, Spectrometers, Detectors and Associated Equipment, **589**, 268–274 (2008).
- [182] N. Boudet *et al.* *XPAD: a hybrid pixel detector for X-ray diffraction and diffusion*. Nuclear Instruments and Methods in Physics Research Section A: Accelerators, Spectrometers, Detectors and Associated Equipment, **510**, 41–44 (2003).
- [183] B. Henrich, A. Bergamaschi, C. Broennimann, R. Dinapoli, E. F. Eikenberry, I. Johnson, M. Kobas, P. Kraft, A. Mozzanica and B. Schmitt. *PILATUS: A single photon counting pixel detector for X-ray applications*. Nuclear Instruments and Methods in Physics Research Section A: Accelerators, Spectrometers, Detectors and Associated Equipment, **607**, 247–249 (2009).
- [184] R. Dinapoli *et al.* *EIGER: Next generation single photon counting detector for X-ray applications*. Nuclear Instruments and Methods in Physics Research Section A: Accelerators, Spectrometers, Detectors and Associated Equipment, **650**, 79–83 (2011).
- [185] R. Ballabriga, M. Campbell, E. Heijne, X. Llopart, L. Tlustos and W. Wong. *Medipix3: A 64k pixel detector readout chip working in single photon counting mode with improved spectrometric performance*. Nuclear Instruments and Methods in Physics Research Section A: Accelerators, Spectrometers, Detectors and Associated Equipment, **633**, **Supplement 1**, S15–S18 (2011).
- [186] M. Campbell. *10 years of the Medipix2 Collaboration*. Nuclear Instruments and Methods in Physics Research Section A: Accelerators, Spectrometers, Detectors and Associated Equipment, **633**, **Supplement 1**, S1–S10 (2011).
- [187] J.-P. Jansson, A. Mantyniemi and J. Kostamovaara. *A CMOS time-to-digital converter with better than 10 ps single-shot precision*. IEEE Journal of Solid-State Circuits, **41**, 1286 – 1296 (2006).
- [188] J. Richardson, R. Walker, L. Grant, D. Stoppa, F. Borghetti, E. Charbon, M. Gersbach and R. K. Henderson. *A 32x32 50ps resolution 10 bit time to digital converter array in 130nm CMOS for time correlated imaging*. In *IEEE 2009 Custom Intergrated Circuits Conference (CICC)* (2009).
- [189] D. Stoppa, F. Borghetti, J. Richardson, R. Walker, R. K. Henderson, M. Gersbach and E. Charbon. *Ultra compact and low-power TDC and TAC architectures for highly-parallel implementation in time-resolved image sensors*. In *2011 International Workshop on ADC Modelling, Testing and Data Converter Analysis and Design and IEEE 2011 ADC Forum* (2011).
- [190] E. Charbon. *Single-photon detection-Evolving CMOS technology for high-erformance*. OPN Optics & Photonics News, 14–15 (2011).
- [191] Y. Maruyama and E. Charbon. *A time-gated 128x128 CMOS SPAD array for on-chip fluorescence detection*. In *Proceedings of the International Image Sensor Workshop (IISW)* (2011).

- 
- [192] M. Campbell, E. H. M. Heijne, G. Meddeler, E. Pernigotti and W. Snoeys. *A readout chip for a  $64 \times 64$  pixel matrix with 15-bit single photon counting*. IEEE Transactions on Nuclear Science, **45**, 751–753 (1998).
- [193] A. A. A. Aarts, H. van der Graaf and S. van der Putten. *New results on a gaseous detector using Medipix2 and Micromegas*. Nuclear Instruments and Methods in Physics Research Section A: Accelerators, Spectrometers, Detectors and Associated Equipment, **563**, 205–208 (2006).
- [194] Y. Giomataris, P. Rebourgeard, J. P. Robert and G. Charpak. *MICROMEAS: A high-granularity position-sensitive gaseous detector for high particle-flux environments*. Nuclear Instruments and Methods in Physics Research Section A: Accelerators, Spectrometers, Detectors and Associated Equipment, **376**, 29–35 (1996).
- [195] X. Llopart Cudie. *Design and characterization of 64k pixels chips working in single photon counting mode*. Ph.D. thesis, Mid Sweden University, Sundsvall, Sweden (2007).
- [196] M. Chmeissani and B. Mikulec. *Performance limits of a single photon counting pixel system*. Nuclear Instruments and Methods in Physics Research Section A: Accelerators, Spectrometers, Detectors and Associated Equipment, **460**, 81–90 (2001).
- [197] M. G. Bisogni *et al.* *Performance of an imaging system based on silicon pixel detectors of different thickness*. IEEE Transactions on Nuclear Science, **52**, 1989–1993 (2005).
- [198] B. Norlin, C. Fröjd, H.-E. Nilsson, H. Graafsma, V. Vonk and C. Ponchut. *Characterisation of the charge sharing in pixellated Si detectors with single-photon processing readout*. Nuclear Instruments and Methods in Physics Research Section A: Accelerators, Spectrometers, Detectors and Associated Equipment, **563**, 133–136 (2006).
- [199] A. Korn, M. Firsching, G. Anton, M. Hoheisel and T. Michel. *Investigation of charge carrier transport and charge sharing in X-ray semiconductor pixel detectors such as Medipix2*. Nuclear Instruments and Methods in Physics Research Section A: Accelerators, Spectrometers, Detectors and Associated Equipment, **576**, 239–242 (2007).
- [200] L. Tlustos. *Performance and limitations of high granularity single photon processing X-ray imaging detectors*. Ph.D. thesis, University of Technology, Vienna, Austria (2005).
- [201] H. Graafsma, T. Thorander, G. W. J. C. Heunen and J. Morse. *Wide dynamic range germanium detector for perturbation crystallography*. Journal of Synchrotron Radiation, **3**, 156–159 (1996).
- [202] D. Pennicard and H. Graafsma. *Simulated performance of high-Z detectors with Medipix3 readout*. Journal of Instrumentation, **6**, P06007 (2011).
- [203] Z. Vykydal, J. Visschers, D. Sabuncuoglu Tezcan, K. De Munck, T. Borgers, W. Ruythooren and P. De Moor. *The RELAXd project: Development of four-side tilable photon-counting imagers*. Nuclear Instruments and Methods in Physics Research Section A: Accelerators, Spectrometers, Detectors and Associated Equipment, **591**, 241–244 (2008).
- [204] S. Spiesshoefer, Z. Rahman, G. Vangara, S. Polamreddy, S. Burkett and L. Schaper. *Process integration for through-silicon vias*. Journal of Vacuum Science & Technology A: Vacuum, Surfaces, and Films, **4**, 824–829 (2005).

- [205] T. Holy, J. Jakubek, S. Pospisil, J. Uher, D. Vavrik and Z. Vykydal. *Data acquisition and processing software package for Medipix2*. Nuclear Instruments and Methods in Physics Research Section A: Accelerators, Spectrometers, Detectors and Associated Equipment, **563**, 254–258 (2006).
- [206] D. Turecek, T. Holy, J. Jakubek, S. Pospisil and Z. Vykydal. *Pixelman: a multi-platform data acquisition and processing software package for Medipix2, Timepix and Medipix3 detectors*. Journal of Instrumentation, **6**, C01046 (2011).
- [207] Z. Vykydal, J. Jakubek and S. Pospisil. *USB interface for Medipix2 pixel device enabling energy and position-sensitive detection of heavy charged particles*. Nuclear Instruments and Methods in Physics Research Section A: Accelerators, Spectrometers, Detectors and Associated Equipment, **563**, 112–115 (2006).
- [208] Z. Vykydal and J. Jakubek. *USB Lite - Miniaturized readout interface for Medipix2 detector*. Nuclear Instruments and Methods in Physics Research Section A: Accelerators, Spectrometers, Detectors and Associated Equipment, **633**, **Supplement 1**, S48–S49 (2011).
- [209] V. Kraus, M. Holik, J. Jakubek, M. Kroupa, P. Soukup and Z. Vykydal. *FITPix - fast interface for Timepix pixel detectors*. Journal of Instrumentation, **6**, C01079 (2011).
- [210] D. San Segundo Bello, M. van Beuzekom, P. Jansweijer, H. Verkooijen and J. Visschers. *An interface board for the control and data acquisition of the Medipix2 chip*. Nuclear Instruments and Methods in Physics Research Section A: Accelerators, Spectrometers, Detectors and Associated Equipment, **509**, 164–170 (2003).
- [211] J. Visser, B. van der Heijden, S. J. A. Weijers, R. de Vries and J. L. Visschers. *A Gigabit per second read-out system for Medipix quads*. Nuclear Instruments and Methods in Physics Research Section A: Accelerators, Spectrometers, Detectors and Associated Equipment, **633**, **Supplement 1**, S22–S25 (2011).
- [212] C. Ponchut, J. Clément, J.-M. Rigal, E. Papillon, J. Vallerga, D. LaMarra and B. Mikulec. *Photon-counting X-ray imaging at kilohertz frame rates*. Nuclear Instruments and Methods in Physics Research Section A: Accelerators, Spectrometers, Detectors and Associated Equipment, **576**, 109–112 (2007).
- [213] M. Maiorino, R. Martinez, G. Pellegrini, G. Blanchot, M. Chmeissani, J. Garcia, M. Lozano, C. Puigdengoles and M. Ullan. *A read-out system for the Medipix2 chip capable of 500 frames per second*. Nuclear Instruments and Methods in Physics Research Section A: Accelerators, Spectrometers, Detectors and Associated Equipment, **563**, 96–99 (2006).
- [214] O. Hadjar, W. K. Fowler, G. Kibelka and W. C. Schnute. *Preliminary demonstration of an IonCCD as an alternative pixelated anode for direct MCP readout in a compact MS-based detector*. Journal of The American Society for Mass Spectrometry, **23**, 418–424 (2012).
- [215] O. Hadjar, G. Johnson, J. Laskin, G. Kibelka, S. Shill, K. Kuhn, C. Cameron and S. Kasan. *IonCCD<sup>TM</sup> for direct position-sensitive charged-particle detection: From electrons and keV ions to hyperthermal biomolecular ions*. Journal of The American Society for Mass Spectrometry, **22**, 612–623 (2011).

- [216] E. S. Wilman, S. H. Gardiner, A. Nomerotski, R. Turchetta, M. Brouard and C. Vallance. *A new detector for mass spectrometry: Direct detection of low energy ions using a multi-pixel photon counter*. Review of Scientific Instruments, **83**, 013304–4 (2012).
- [217] R. M. A. Heeren, D. F. Smith, J. Stauber, B. Kuekrer-Kaletas and L. MacAleese. *Imaging mass spectrometry: Hype or hope?* Journal of the American Society for Mass Spectrometry, **20**, 1006–1014 (2009).
- [218] P. Colas, A. P. Colijn, A. Fornaini, Y. Giomataris, H. van der Graaf, E. H. M. Heijne, X. Llopart, J. Schmitz, J. Timmermans and J. L. Visschers. *The readout of a GEM or micromegas-equipped TPC by means of the Medipix2 CMOS sensor as direct anode*. Nuclear Instruments and Methods in Physics Research Section A: Accelerators, Spectrometers, Detectors and Associated Equipment, **535**, 506–510 (2004).
- [219] A. Bamberger, K. Desch, U. Renz, M. Titov, N. Vlasov, P. Wienemann and A. Zwirger. *Resolution studies on 5 GeV electron tracks observed with triple-GEM and MediPix2/TimePix-readout*. Nuclear Instruments and Methods in Physics Research Section A: Accelerators, Spectrometers, Detectors and Associated Equipment, **581**, 274–278 (2007).
- [220] J. Vallergera, J. McPhate, A. Tremsin, O. Siegmund, V. Mikulec and A. Clark. *Optically sensitive Medipix2 detector for adaptive optics wavefront sensing*. Nuclear Instruments and Methods in Physics Research Section A: Accelerators, Spectrometers, Detectors and Associated Equipment, **546**, 263–269 (2005).
- [221] E. R. Amstalden van Hove, D. F. Smith and R. M. A. Heeren. *A concise review of mass spectrometry imaging*. Journal of Chromatography A, **1217**, 3946–3954 (2010).
- [222] K. Mathieson, M. S. Passmore, P. Seller, M. L. Prydderch, V. O’Shea, R. L. Bates, K. M. Smith and M. Rahman. *Charge sharing in silicon pixel detectors*. Nuclear Instruments and Methods in Physics Research Section A: Accelerators, Spectrometers, Detectors and Associated Equipment, **487**, 113–122 (2002).
- [223] W. Bouschen, O. Schulz, D. Eikel and B. Spengler. *Matrix vapor deposition/recrystallization and dedicated spray preparation for high-resolution scanning microprobe matrix-assisted laser desorption/ionization imaging mass spectrometry (SMALDI-MS) of tissue and single cells*. Rapid Communications in Mass Spectrometry, **24**, 355–364 (2010).
- [224] R. Chen, X. Cheng, D. W. Mitchell, S. A. Hofstadler, Q. Wu, A. L. Rockwood, M. G. Sherman and R. D. Smith. *Trapping, detection, and mass determination of coliphage T4 DNA ions by electrospray ionization Fourier transform ion cyclotron resonance mass spectrometry*. Analytical Chemistry, **67**, 1159–1163 (1995).
- [225] S. Sanglier, E. Leize, A. Van Dorsselaer and F. Zal. *Comparative ESI-MS study of ~2.2 MDa native hemocyanins from deep-sea and shore crabs: from protein oligomeric state to biotope*. Journal of the American Society for Mass Spectrometry, **14**, 419–429 (2003).
- [226] F. DiFilippo, V. Natarajan, M. Bradley, F. Palmer and D. E. Pritchard. *Accurate atomic mass measurements from Penning trap mass comparisons of individual ions*. Physica Scripta, **1995**, 144 (1995).
- [227] S. D. Fuerstenau and W. H. Benner. *Molecular weight determination of megadalton DNA electrospray ions using charge detection time-of-flight mass spectrometry*. Rapid Communications in Mass Spectrometry, **9**, 1528–1538 (1995).

- [228] M. A. Park, J. H. Callahan and A. Vertes. *An inductive detector for time-of-flight mass spectrometry*. Rapid Communications in Mass Spectrometry, **8**, 317–322 (1994).
- [229] D. C. Imrie, J. M. Pentney and J. S. Cottrell. *A Faraday cup detector for high-mass ions in matrix-assisted laser desorption/ionization time-of-flight mass spectrometry*. Rapid Communications in Mass Spectrometry, **9**, 1293–1296 (1995).
- [230] B. Spengler, D. Kirsch, R. Kaufmann, M. Karas, F. Hillenkamp and U. Giessmann. *The detection of large molecules in matrix-assisted UV-laser desorption*. Rapid Communications in Mass Spectrometry, **4**, 301–305 (1990).
- [231] J. H. Jungmann, D. F. Smith, L. MacAleese, I. Klinkert, J. Visser and R. M. A. Heeren. *Biological Tissue Imaging with a Position and Time Sensitive Pixelated Detector*. Journal of the American Society for Mass Spectrometry (2012).
- [232] D. Fries, S. Ivanov, H. Broadbent, R. Willoughby and E. Sheehan. *Micro Ion-Optical Systems Technology [MIST] for Mass Spectrometry Using PCBMEMS*. IEEE International Symposium on Industrial Electronics, ISIE 2007, 3278–3281 (2007).
- [233] K. Ueda and J. H. D. Eland. *Molecular photodissociation studied by VUV and soft x-ray radiation*. Journal of Physics B: Atomic, Molecular and Optical Physics, **38**, S839 (2005).
- [234] J. S. Lapington. *A comparison of readout techniques for high-resolution imaging with microchannel plate detectors*. Nuclear Instruments and Methods in Physics Research Section A: Accelerators, Spectrometers, Detectors and Associated Equipment, **525**, 361–365 (2004).
- [235] C. E. Moore. *Tables of spectra of hydrogen, carbon, nitrogen, and oxygen*. CRC Press, Boca Raton, USA (1993).
- [236] M. J. J. Vrakking. *An iterative procedure for the inversion of two-dimensional ion/photoelectron imaging experiments*. Review of Scientific Instruments, **72**, 4084–4786 (2001).
- [237] *Website of PGOPHER, program for simulating rotational structure of molecules* (2010).
- [238] I. Wilkinson, M. P. de Miranda and B. J. Whitaker. *Photodissociation of NO<sub>2</sub> in the (2) <sup>2</sup>B<sub>2</sub> state: The O(<sup>1</sup>D<sub>2</sub>) dissociation channel*. Journal of Chemical Physics, **131**, 054308–19 (2009).

## SUMMARY

In the framework of this thesis, an in-vacuum, high-voltage electron and ion imaging camera was developed. Among other particles, the system is particularly suitable for the detection of macromolecular ions of either polarity. The new camera is successfully tested on benchmark systems as well as biologically relevant macromolecular tissue samples. Already now, TOF-MSI systems can benefit from several unique system capabilities. These are the combination of high signal-to-noise ratios, the multiplexed detection of events by the highly parallel detection system, the high sensitivity, the dynamic range, the large mass range and the simultaneous detection of position- and time-information by a single detector system.

The first part of this thesis investigates the spatial and molecular structure of biologically relevant, complex macromolecular systems. In particular, the relationship between molecular structure and location, and biological or chemical functionality is investigated by the technique mass spectrometry imaging (MSI). In the second part of this thesis, a technique is highlighted which bears the potential to provide fundamental understanding of chemical reactions and reaction dynamics of atoms and small molecules. This technique is applied to molecular spectroscopy and is called velocity map imaging (VMI).

Mass spectrometry imaging as an analytical tool for biological and biomedical tissue research is introduced in *Chapter 2*. The current state of the technique is evaluated, technological and methodological challenges and recent advances in MSI technology are identified. Emerging technologies for high spatial resolution imaging and high sample throughput studies are introduced. In particular, microscope mode MSI is suggested as a technique for high throughput, high spatial resolution MSI imaging. Among other innovations, detector technology that targets various shortcomings of conventional imaging detector systems is introduced. Challenging experimental conditions in biomolecular MSI require detection systems which can handle high count rates with a minimal recovery time, provide a rapid readout and response, can detect multiple ions simultaneously, have low noise levels, a high sensitivity and detection uniformity. Conventional secondary-electron MS detectors (like microchannel plates (MCP) or photo-multiplier tubes) cannot deliver all these attributes and their mass response levels off for larger mass ions, which results in a detection disadvantage for macromolecules of biomolecular or biomedical interest. The capabilities of various ion, electron and photon

detectors are compared and evaluated against the above-mentioned criteria in *Chapter 3*. A novel, highly parallel class of pixel detectors is introduced and its capabilities for imaging studies are outlined. *Chapter 4 through 8* cover the implementation of such a hybrid active pixel detector for MSI and VMI.

*Chapter 3* gives an overview of state-of-the-art ion, electron and photon detection and imaging technology, specifically applied in the areas of mass spectrometry (MS), mass spectrometry imaging (MSI) and atomic and molecular physics research. Three modes of imaging/particle detection -integrated image detection, selected image detection and spectral image detection- are distinguished and areas of application are identified. Various position- and time-sensitive detection systems are introduced. Most importantly, the Medipix/Timepix detector family is highlighted and its potential for mass spectrometry imaging and fundamental atomic and molecular physics research is outlined.

*Chapter 4* describes a high spatial resolution imaging study with a detection system composed of a chevron microchannel plate stack in combination with a Medipix pixelated detector on an ion microscope. A spatial resolving power better than  $6\ \mu\text{m}$  is demonstrated by secondary ion mass spectrometry (SIMS) and  $8\text{-}10\ \mu\text{m}$  with laser desorption ionization (LDI). The  $55\times 55\ \mu\text{m}^2$  detector pixels in combination with an ion optical magnification factor of  $85\times$  (SIMS) and  $42\times$  (LDI) probe an area of  $650\times 650\ \text{nm}^2$  (SIMS) and  $1.31\times 1.31\ \mu\text{m}^2$  (LDI) on the sample surface. The spatial resolution, the acquisition speed, and the data handling are investigated in detail.

The high spatial resolution MSI experiments with this MCP/Medipix assembly deliver a proof-of-concept for the use of hybrid active pixel detectors in MSI. However, as other current imaging detectors, the MCP/Medipix assembly provides 2D imaging capabilities only. Hence, the spatial distribution of a particular ion species, i.e.  $m/z$  value, can only be imaged by selecting the particular ion (based on its time-of-flight) and blanking all other particles. These measurements are repetitive and time-consuming. The implementation of an MCP/Timepix detector assembly alleviates the need for selective ion blanking. The Timepix detector is a variant of the Medipix 2 detector, which -among other features- can measure the time-of-flight of an impinging particle on the pixel level with a time resolution of 10 ns. *Chapter 5 through 8* demonstrate the implementation and application of a Timepix-based detection system for MSI and VMI.

Novel detection capabilities for large biomolecules in time-of-flight (TOF) based MSI are investigated in *Chapter 5*. In that chapter, a bare Timepix assembly combined with chevron microchannel plates (MCP) captures time-resolved images of several  $m/z$  species in a single measurement. Mass-resolved ion images from Timepix measurements of peptide and protein standards demonstrate the capability to return both mass-spectral and localization information of biologically relevant analytes from matrix-assisted laser desorption ionization (MALDI)

on a commercial ion microscope. Timepix mass spectra deliver an increased dynamic range of over one order of magnitude. The Timepix returns defined mass spectra already at sub-saturation MCP gains, which prolongs the MCP lifetime and allows the gain to be optimized for image quality. The Timepix peak resolution and isotope detection are only limited by the resolution of the in-pixel measurement clock. Oligomers of the protein ubiquitin were measured up to 78 kDa at comparatively low ion energies of 5 keV with the MCP/Timepix detection system. In conventional, commercially available mass spectrometers, acceleration voltages well exceeding 5 keV (20 keV or more) are needed to obtain such a high mass sensitivity.

In *Chapter 6*, we demonstrate the capabilities of a highly parallel, active pixel detector for large-area, mass spectrometric imaging of biological tissue sections. We prove the applicability of the detection system to biomolecular mass spectrometry imaging. The MCP/Timepix system is tested on biologically relevant samples as a peptide-grid benchmark sample and mouse testis tissue slices. Mass-spectral and localization information of analytes at physiological concentrations are measured in MALDI TOF-MS imaging experiments. We show a high spatial resolution (pixel size down to  $740 \times 740 \text{ nm}^2$  on the sample surface) and a spatial resolving power of  $6 \text{ }\mu\text{m}$  with a microscope mode laser field of view of  $100\text{-}335 \text{ }\mu\text{m}$ . Automated, large-area imaging is demonstrated and the Timepix' potential for fast, large-area image acquisition is highlighted.

*Chapter 7* outlines how the analytical capabilities of this detection system can be extended by the application of additional extraction fields. In particular, the detection system is electrically isolated from the spectrometer and can be operated at  $+12 \text{ kV}/-8 \text{ kV}$ , which delivers ion acceleration energies of  $15 \text{ keV}/11 \text{ keV}$ . Hence, this high voltage detector upgrade enables measurements on both ion polarities and enables a more sensitive analysis of higher molecular mass ions. These capabilities prove useful in biological or biomedical studies of lipids, peptides and large intact proteins.

In *Chapter 8*, the implementation of our detection system to velocity map imaging and a variant thereof, slice imaging, is presented. The Timepix detector approach is particularly attractive to slice imaging where only part of the molecular distribution is imaged. The Timepix conveniently eliminates the need for gating the imaging detector. The implementation of the Timepix detector in combination with a microchannel plate additionally enables high spatial resolution information via center-of-mass centroiding. Here, the detector was applied to study the photo-dissociation of  $\text{NO}_2$  at  $452 \text{ nm}$ . The energy resolution observed in the experiment was  $\Delta E/E=0.05$  and is limited by the experimental setup rather than by the detector assembly.

All together, this new, compact detector assembly is well-suited for imaging studies in mass spectrometry imaging, atomic and molecular physics research and

related areas of research. The implementation and the application of this state-of-the art, pixelated, solid state detector has proven highly successful.

## SAMENVATTING

In het kader van dit proefschrift werd een elektronen- en ionen-imaging kamera ontwikkeld die op hoge spanningen in een vacuüm opstelling gebruikt kan worden. Het kamerasysteem is zeer geschikt voor de detectie van macromoleculaire ionen, zowel positief als negatief geladen. Deze nieuwe kamera werd succesvol getest op peptide- en eiwitstandaard-oplossingen en tevens op biologisch relevante macromoleculaire weefselmonsters. In het huidige stadium van onze detectorontwikkelingen kunnen vluchttijd-massaspectrometers nu al profiteren van verschillende unieke aspecten van dit systeem. Het nieuwe detectiesysteem combineert de volgende eigenschappen: Een hoge signaal-ruisverhouding door de gemultiplexde detectie van events met het parallelle detectiesysteem, een hoge gevoeligheid, een groot dynamisch bereik, een groot massabereik en de gelijktijdige detectie van plaats- en tijdsinformatie door een enkel detectiesysteem.

Het eerste deel van dit proefschrift onderzoekt de spatiële en moleculaire structuur van complexe macromoleculaire systemen die biologisch relevant zijn. In het bijzonder wordt de relatie tussen de moleculaire structuur en positie, en de biologische of chemische functionaliteit onderzocht aan de hand van de “massaspectrometrie imaging (MSI)” techniek. In het tweede deel van dit proefschrift wordt de nadruk op de “velocity map imaging (VMI)” techniek gelegd, een techniek die het potentieel heeft om fundamenteel inzicht in chemische reacties en de dynamiek van zulke reacties van atomen en kleine moleculen te geven. Deze techniek werd toegepast in de moleculaire spectroscopie van  $\text{NO}_2$ .

*Hoofdstuk 2* introduceert MSI als een analytische techniek voor biologisch en biomedisch onderzoek aan weefselmonsters. De huidige stand der techniek wordt geëvalueerd, technologische en methodologische uitdagingen en recente technische ontwikkelingen in de MSI worden benoemd. Opkomende technologieën voor hoge spatiële resolutie imaging en hoge verwerkingscapaciteit van monsters worden geïntroduceerd. In het bijzonder wordt microscoop mode MSI als een techniek voor hoge verwerkingscapaciteit van monsters met een hoge spatiële resolutie gepresenteerd. Naast andere innovaties wordt er een detectortechnologie geïntroduceerd die verscheidene tekortkomingen van conventionele imaging detectoren overwint.

Uitdagende experimentele condities in de biomoleculaire MSI vereisen detectiesystemen met de volgende eigenschappen: Het verwerken van hoge count rates met een minimale hersteltijd, een snelle uitlezing en reactietijd, gelijktijdige de-

tectie van meerdere ionen, een laag ruis niveau, een hoge gevoeligheid en een uniforme detectie op het gehele detectorvlak. Conventionele secundaire elektronen detectoren voor massaspectrometrie (zoals “microchannel plates” (MCP’s) of “photomultiplier tubes”) bieden deze eigenschappen niet en tevens neemt hun gevoeligheid af voor hogere ionenmassa’s. Dit is een nadeel voor de detectie van macromoleculen van biomoleculair en biomedische belang. In *Hoofdstuk 3* worden de mogelijkheden van verscheidene ionen-, elektronen- en fotondetectoren vergeleken en op de eerder genoemde criteria gevalueerd. Een nieuwe, in hoge mate parallel opgezette groep van pixeldetectoren wordt geïntroduceerd en de mogelijkheden hiervan voor imaging studies worden beschreven. De *Hoofdstukken 4 tot en met 8* beschrijven de implementatie en evaluatie van een dergelijke hybride, actieve pixeldetector voor MSI en VMI.

*Hoofdstuk 3* geeft ook een overzicht van state-of-the-art ionen-, elektronen- en fotondetectie- en afbeeldingstechnologie, die in het bijzonder wordt toegepast in de vakgebieden van de massaspectrometrie (MS), de massaspectrometrie imaging en de atoom- en molecuulfysica. Drie verschillende modes van imaging-/deeltjesdetectie -namelijk geïntegreerde, geselecteerde en spectrale beelddetectie- worden onderscheiden en toepassingsgebieden van de drie modes worden besproken. Verschillende positie- en tijdgevoelige detectiesystemen worden geïntroduceerd. En meest belangrijk, de Medipix/Timepix detectorfamilie wordt specifiek beschreven en hun potentieel voor MSI en fundamenteel atoom- en fysicaonderzoek wordt geschetst.

*Hoofdstuk 4* beschrijft een imaging experiment bij hoge spatiële resolutie dat gebruik maakt van voornoemde nieuwe detectorsystemen bestaand uit een MCP in combinatie met een Medipix pixeldetector en geïntegreerd met een ionenmicroscop. Met secundaire ionen massaspectrometrie (SIMS) en met laser desorptie ionisatie (LDI) worden oplossende vermogens beter dan  $6\ \mu\text{m}$ , respectievelijk,  $8\text{-}10\ \mu\text{m}$  bereikt. De oppervlakte van  $55\times 55\ \mu\text{m}^2$  van de detectorpixels in combinatie met een ionenoptiek vergrotingsfactor van  $85\times$  (SIMS) en  $42\times$  (LDI) komt met een gebied van  $650\times 650\ \text{nm}^2$  (SIMS) and  $1,31\times 1,31\ \mu\text{m}^2$  (LDI) op het te meten oppervlak overeen. De spatiële resolutie, de acquisitie-snelheid en een optimale gegevensverwerking worden in detail onderzocht.

De hoge spatiële resolutie MSI experimenten met deze MCP/Medipix detector-samenstelling geven een “proof-of-concept” voor het gebruik van hybride, actieve pixel detectoren in de MSI. Echter, zoals andere imaging detectoren die tegenwoordig in gebruik zijn, geeft de MCP/Medipix samenstelling alleen 2D-beelden. Daarom kan de ruimtelijke verdeling van een bepaald ion, dat wil zeggen een bepaalde  $m/z$ -waarde, alleen afgebeeld worden indien dit betreffende ion vooraf geselecteerd wordt (op basis van zijn vluchttijd) en alle andere ionen verwijderd worden. Dit soort metingen vereisen veel bijna identieke metingen en zijn daarom tijdrovend. De implementatie van een MCP/Timepix detector maakt deze ionen-

selectie overbodig. De Timepix is namelijk een variatie van de Medipix2 detector, die -naast andere eigenschappen- per pixel de vluchttijd van een deeltje kan meten met een resolutie van 10 ns. De *Hoofdstukken 5 tot en met 8* laten de implementatie en toepassing van een Timepix-gebaseerd detectiesysteem voor de MSI en de VMI zien.

*Hoofdstuk 5* onderzoekt nieuwe detectiemogelijkheden voor grote biomoleculen in de vluchttijdgebaseerde MSI. Een kale MCP/Timepix samenstelling neemt tijdsopgeloste beelden op van meerdere  $m/z$ -species in één enkele meting. We laten massaopgeloste ionenbeelden van peptide- en proteïne-standaard oplossingen zien. Deze tonen de prestaties van de Timepix, met name de massaspectrale en lokalisatie informatie van biologisch relevante materialen (gegenereerd met MALDI op een commercieel ionen microscoop). Timepix massaspectra geven een vergroot dynamisch bereik van meer dan een orde van grootte vergeleken met huidige detectortechnologie. De Timepix kan massaspectra opnemen, ook als de MCP niet in verzadiging wordt bedreven. Dit verlengt de levensduur van de MCP en geeft de mogelijkheid om de versterkingsfactor aan te passen voor een optimale beeldkwaliteit. Op dit moment zijn de piekresolutie in de massaspectra en de isotoop detectiemogelijkheden van de Timepix alleen gelimiteerd door de tijdsresolutie van de pixel meetklok (10 ns). Het was mogelijk om met dit MCP/Timepix-detectiesysteem oligomeren van de proteïne ubiquitin tot een massa van 78 kDa te detecteren met een verhoudingsgewijze lage ionen-energie van 5 keV. In een conventioneel, commercieel verkrijgbare massaspectrometer wordt een dergelijke hoge massagevoeligheid alleen met een veel hogere versnelspanning in de orde van 20 kV of meer bereikt.

In *Hoofdstuk 6* gebruiken we deze in hoge mate parallelle, actieve pixeldetector om grote oppervlakken van biologische weefselmonsters met MSI te onderzoeken. We tonen hiermee aan dat het detectiesysteem geschikt is voor de biomoleculaire MSI. Het MCP/Timepix-systeem wordt op biologisch relevante monsters zoals een peptide-grid monster en een muistestis weefselmonsters getest. Op het weefseloppervlak zijn biomoleculen in fysiologische concentraties aanwezig. Toch kan massaspectrale- en plaats-informatie van biomoleculen worden verworven in MALDI-vluchttijds-MSI experimenten met dit nieuwe detectiesysteem. In het bijzonder laten we een hoge spatiele resolutie zien (pixels zo klein als  $740 \times 740 \text{ nm}^2$  op het monsteroppervlak) en een oplossend vermogen van  $6 \mu\text{m}$  met een microscopmode laserbundel met een diameter van  $100\text{-}335 \mu\text{m}$ . Verder laten we zien dat grote weefseloppervlakken op een geautomatiseerde manier kunnen worden onderzocht en leggen we de nadruk op het potentieel van de Timepix om snel zulke grote gebieden af te beelden.

*Hoofdstuk 7* geeft aan hoe de analytische vaardigheden van het detectiesysteem kunnen worden uitgebreid door extra elektrostatische versnellingsvelden op de detector aan te leggen. In het bijzonder laten we zien hoe het detectiesysteem

elektrisch geïsoleerd kan worden van de massaspectrometer en op een potentiaal van +12 kV/-8 kV kan worden bedreven. Deze detectorvoltages resulteren in ionenenergieën van respectievelijk 15 keV/11 keV. Deze detectoruitbreiding met hoge voltages maakt metingen van ionen in positieve en negatieve mode mogelijk en geeft de mogelijkheid de gevoeligheid voor ionen met hogere massa's te vergroten. Deze eigenschappen zijn belangrijk voor biologische en biomedische studies van lipides, peptides en zware, intacte eiwitten.

In *Hoofdstuk 8* wordt de implementatie van dit detectiesysteem voor VMI en een variant ervan -namelijk "slice imaging"- getoond. Het tijdsgevoelige Timepix detectiesysteem is bijzonder aantrekkelijk voor "slice imaging" waarin maar een deel van de moleculaire distributie afgebeeld moet worden. Met de Timepix is het namelijk niet nodig om een deel van de deeltjesdistributie weg te halen of de detector selectief aan te zetten om slechts een bepaald gedeelte van de distributie te meten. Verder geeft de implementatie van de Timepix in combinatie met een MCP de mogelijkheid om hoge spatiale resolutie-informatie te winnen via massa-middelpuntbepaling. In dit onderzoek hebben we de detector gebruikt voor een fotodissociatie studie van NO<sub>2</sub> met licht van een golflengte van 452 nm. De energieresolutie die in dit experiment behaald werd was  $\Delta E/E=0.05$  en was niet gelimiteerd door de detector maar ander onderdelen van de experimentele opstelling.

Al met al is deze nieuwe, compacte detectorsamenstelling zeer geschikt voor de massaspectrometrie imaging, atoom- en molecuulfysica en gerelateerde onderzoeksgebieden. De implementatie en toepassing van deze state-of-the-art, gepixelerde, vaste stof detector heeft bewezen zeer succesvol te zijn.

## ACKNOWLEDGEMENTS

*Meisje, kun jij wel wat worden met die twee jongens als begeleiders?*

Poster session, AMO Luntern, 2009

First, I would like to thank my promoter, Ron Heeren, for the opportunity to be part of his multidisciplinary group. Ron, the international visibility of your MS imaging facility is widespread and it is amazing for a young researcher to experience the recognition and impact of your group's work. From the very beginning of my PhD trajectory, it was clear that the goal of this project was threefold: build a mighty machine, do good science and develop into an independent researcher. I highly appreciate the fact that you made yourself available for colorful discussions regarding the direction of the project. You also encourage and support travel to international meetings, so that I could discuss our project with others. We pushed through a tremendous amount of work together. I would like to thank you for your trust in my abilities and your support along the way. Science, communication, politics and the combination thereof: I learned a lot. Thanks a lot for an interesting time.

Every instrument has a soul, a character and sometimes a mind of its own. Some of us understand this, others don't. Along these lines, I first would like to express my respect and gratitude to the instrumentation team. Every one of you has a unique set of amazing skills. I appreciate you sharing your knowledge and experience on mass spectrometry (instrumentation and beyond) with me. We built neat instruments and performed some good experiments. I'm proud of you and us as a team.

First, I would like to thank Marc Duursma for patiently bringing me up to speed in the chemical lab. Marc, thanks to you I can now function self-sufficiently between "the chemists". You always find time to help us and come up with creative solutions to technical challenges. You are teddy-bear and boefje in one, I'm glad that I met you. Also, I would like to thank our group technician, Frans Giskes, for his technical support on the TRIFT mass spectrometer and the neat parts he crafted for the project. Andras Kiss, it was a great pleasure to work with a colleague so (MS) knowledgeable, intelligent, dedicated and funny. We fought a couple of interesting battles together. It was good to have you on my side. Keep up the good work. Your skills and strawberry tiramisu will get you a long way! Piet Kistemaker is our reliable advisor and source of MS knowledge. Piet, I

greatly appreciate your interest in my project and your critical yet constructive comments. Lennaert Klerk, I would like to thank for training me on the TRIFT system and answering lots of questions, even after he left the lab. During the first two years of my PhD, Luke MacAleese was “my postdoc” on the Timepix project. Thank you, Luke, for getting me started, sharing your knowledge, giving good advice and simply being Dr. MacA. Don Smith, I would like to thank for sharing his knowledge of and enthusiasm for (MS) instrumentation. Your analytical mind, insight, patience and “houtje-touwtje” solutions ensure continuity and disaster control in the lab. Thanks for asking good questions and for sticking around during many late-night measurement sessions.

Many thanks also to former and current members of the BIMS group. I thank you for adding to the diverse research environment in the lab. Gert Eijkel, our Matlab wizard, I would like to thank for his efforts for the Timepix project, for good advice on Matlab coding and data analysis. When pragmatic problem-solving and real life data meets simulations, pure mathematical beauty and genius, Andriy Kharchenko, it was interesting to work with you. Many thanks to the rest: Erika Amstalden van Hove (and her wonderful family), Jim Appelmelk, Jaap Boon, Kamila Chughtai, Sana Chughtai, Berta Cillero-Pastor, Lara Fornai, Florian Marty, Nadine Mascini and Stephanie Valarezo.

Our instrumentation development was greatly facilitated by the excellent AMOLF support groups. Many thanks to everyone that helped this project in a solution-oriented way.

The electronics engineering group has made a prominent contribution to the Timepix project. In particular, I would like to thank our group’s electronics engineer, Ronald Buijs, for the many high-quality circuits that he designed for me, for thinking along and excellent “ad hoc”-support. Thanks also to Idsart Attema, Henk Dekker and Duncan Verheijde for their contribution.

For the software engineering, most importantly, I would like to thank Ivo Klinkert, our group’s software engineer. The productive, straight-to-the-point collaboration, the educational pair programming sessions, many valuable thoughts and the corrections to the Dutch summary of this thesis are well appreciated! Thanks also to Sjoerd Wouda for the temperature-control plug-in to Pixelman and to Marco Konijnenburg for software advice.

Many, many thanks to the mechanical design group and the mechanical workshop! In particular, I would like to thank Iliya Cerjak and Dirk-Jan Spaanderman. It was excellent to see how our (crazy) ideas could be translated into feasible, solid mechanical design. As a frequent and demanding customer, I would like to express my appreciation to Wim Brouwer and his team, which has done an incredible amount of spectacular work for the Timepix project: Menno Borsboom, Ricardo Eliazer, Jan van der Linden, Henk Neerings, Wouter van der Weijden and Niels Winkelaar. I would like to thank you all for your skilled work. You

guys made the impossible possible for us. And, you saved our experiments more than once with “emergency surgery” on precious instrument parts.

I would like to thank the manuscript committee of my thesis for their time, comments and perspective on our research and my thesis.

The project presented in this thesis was carried out in collaboration with *NIKHEF*. Many thanks to my *NIKHEF* colleagues for their support and ideas! In particular, I would like to thank Jan Visser and Jan Visschers who run and started up the project from the *NIKHEF* side, respectively. Marten Bosma and I went through our PhD trajectories at the same time. Marten, I’m so glad to have you as a smart, knowledgeable and helpful counterpart at *NIKHEF*. Thanks for probing many Timepix chips for me, sharing your knowledge, giving good advice and many fun trips to conferences/collaboration meetings. Joop Rovekamp was responsible for the assembly and wire-bonding of our chip arrays. Thank you for your efforts! Thanks also to the ReLAXD team, Bas van der Heijden, Vincent van Beveren and Henk Boterenbrood for your efforts in getting us going on the ReLAXD board. Many thanks also to Martin van Beuzekom, Erik Heijne, Jan Koopstra and Enrico Schioppa.

Many thanks to the *Medipix collaboration*. It is inspiring for a young scientist to be exposed to the open, collaborative environment of this unique collaboration. In particular, I would like to thank the *CERN* team: Rafa Ballabriga, Michael Campbell, Xavi Llopart, Lukas Tlustos and Winnie Wong for patiently answering my questions. The Berkeley team has made a great impact on the research presented in this thesis. Thanks to Rick Raffanti, Anton Tremsin and John Vallerga for good discussion and hosting me in their lab.

I would also like to thank the Physical Electronics (Chanhassen, USA) team for their excellent support on the TRIFT system. In particular, I would like to thank Scott Bryan, Sheng Chen, Greg Fisher, John Hammond and Michele Rosati.

During the first two years of my PhD project, I also worked for the *Extreme Ultraviolet Physics group* of Marc Vrakking. I would like to thank Marc for giving me insights into a fascinating field of science and illustrating how instrumentation can, and must be pushed to its limits to squeeze out cutting-edge scientific results. I also would like to thank Marc for the opportunity to be part of extraordinary experiments at world-class facilities such as the *FELICE* facility (Rijnhuizen, NL) and the *BESSY* synchrotron (Berlin, DE). Marc’s team is critical, dedicated, unusually skilled and composed of many special characters. Along these lines, thanks to all of my (former) *AMOLF*- and *MBI-XUV* colleagues: Sascha Birkner, Federico Furch, Georg Gademann, Arjan Gijsbertsen (Thanks for your supervision and advice during the slicing experiment!), Ymkje Huismans (*FELICE* girls!), Axel Hundertmark, Freek Kelkensberg, Rob Kemper, Jesse Klei, Christian Neidel, Truong Nyugen, Arnaud Rouzee, Hinc Schoenmaker, Claus-Peter Schulz, Wing-Kiu Siu, Aneta Stodolna and Chung-Hsin Yang.

I would like to express special thanks to my office mate, amazing colleague and friend, Aneta Stodolna. Working with you was an enormous pleasure. There are not many people that have your skills, efficiency, dedication and persistence. I'm very proud of the work we did together. We've seen ups and downs of our PhD trajectories together. Thanks a lot for support and diversion alike!

On the personal side, I would like to thank my family: Joachim, Helga, Klaus and Donald. Joachim, I never met anyone who can so easily read people's character and predict their behavior. Your opinion is very valuable to me and I'm glad that I can always count on your support. Klaus and Helga, your imperturbable trust in me and my abilities, the fact that you are proud of me, your support, your criticism and love have brought me a long way. Donald, you make me laugh, you understand me and let me be myself. I thank God that I have all of you with me. Thanks for countless good moments. I love you all very much.

*Julia H. Jungmann, Amsterdam, August 2012*

## LIST OF PUBLICATIONS

### **This thesis is based on the following publications:**

J. H. Jungmann, R. M. A. Heeren, *Emerging Technologies in Mass Spectrometry Imaging*, Journal of Proteomics, 75, 16, 5077-5092, 2012 (Chapter 2)

Julia H. Jungmann, Ron M. A. Heeren, *Detection Systems for Mass Spectrometry Imaging: A Perspective on Novel Developments with a Focus on Active Pixel Detectors*, 2012, submitted (Chapter 3)

Julia H. Jungmann, Luke MacAleese, Ronald Buijs, Frans Giskes, Ad de Snaijer, Jan Visser, Jan Visschers, Marc J. J. Vrakking and Ron M. A. Heeren, *Fast, High Resolution Mass Spectrometry Imaging Using a Medipix Pixelated Detector*, Journal of the American Society of Mass Spectrometry, 21, 2023-2030, 2010 (Chapter 4)

Julia H. Jungmann, Luke MacAleese, Jan Visser, Marc J.J. Vrakking, Ron M.A. Heeren, *High Dynamic Range Bio-Molecular Ion Microscopy with the Timepix Detector*, Analytical Chemistry, 83, 20, 7888-7894, 2011 (Chapter 5)

J. H. Jungmann, D. F. Smith, L. MacAleese, I. Klinkert, R. M. A. Heeren, *Biological Tissue Imaging with a Position and Time Sensitive Pixelated Detector*, Journal of the American Society for Mass Spectrometry, accepted, 2012 (Chapter 6)

J. H. Jungmann, A. Gijsbertsen, J. Visser, J. Visschers, R. M. A. Heeren, M. J. J. Vrakking, *A New Imaging Method for Understanding Chemical Dynamics: Efficient Slice Imaging Using an In-Vacuum Pixel Detector*, Review of Scientific Instruments, 81, 2010 (Chapter 8)

### **Other publications:**

A. Kharchenko, J. H. Jungmann, L. MacAleese, R. M. A. Heeren, *Sparse Emission Imaging*, 2012, in preparation

Y. Huismans, A. Rouzée, A. Gijsbertsen, P. S. W. M. Logman, F. Lépine, C. Cauchy, S. Zamith, A. Smolkowska, J. H. Jungmann, J. M. Bakker, G. Berden, B. Redlich, A. F. G. van der Meer, K. J. Schafer, M. J. J. Vrakking, *Photo-Electron Angular Distributions from the Ionization of Xenon Rydberg States by Mid-Infrared Radiation*, 2012, in preparation

A. Kiss, J. H. Jungmann, D. F. Smith, R. M. A. Heeren, *Microscope Mode Secondary Ion Mass Spectrometry Imaging with a Timepix Detector*, 2012, submitted

Arnaud Rouzée, Ymkje Huismans, Freek Kelkensberg, Aneta Smolkowska, Julia Jungmann, Arjan Gijsbertsen, Wing Kiu Siu, Georg Gademann, Axel Hundertmark, Per Johnsson and Marc J.J. Vrakking, *Molecular Movies from Molecular Frame Photoelectron Angular Distribution (MF-PAD) measurements*, *Ultrafast Phenomena in Molecular Sciences*, Springer, edited by Luis Banares, 2012, submitted

Y. Huismans, A. Gijsbertsen, A. S. Smolkowska, J. H. Jungmann, A. Rouzée, P. S. W. M. Logman, F. Lépine, C. Cauchy, S. Zamith, T. Marchenko, J. M. Bakker, G. Berden, B. Redlich, A. F. G. van der Meer, M. Yu. Ivanov, T. Yan, D. Bauer, S. V. Popruzhenko, O. Smirnova and M. J. J. Vrakking, *Scaling Laws for Photoelectron Holography in the Mid-Infrared Wavelength Regime*, *Physical Review Letters*, 109, 1, 013002-5, 2012

Celia Arnaud, *Speeding Up Mass Spec Imaging*, article on our research, *Chemical & Engineering News*, 19 December 2011

Y. Huismans, A. Rouzée, A. Gijsbertsen, J. H. Jungmann, A. S. Smolkowska, P. S. W. M. Logman, F. Lépine, C. Cauchy, S. Zamith, T. Marchenko, J. M. Bakker, G. Berden, B. Redlich, A. F. G. van der Meer, H. G. Muller, W. Vermin, K. J. Schafer, M. Spanner, M. Yu. Ivanov, O. Smirnova, D. Bauer, S. V. Popruzhenko, M. J. J. Vrakking, *Time-Resolved Holography with Electrons*, *Science*, 331, 61-64, 2011

Georg Gademann, Ymkje Huismans, Arjan Gijsbertsen, Julia Jungmann, Jan Visschers, Marc J. J. Vrakking, *Velocity Map Imaging Using an In-Vacuum Pixel Detector*, *Review of Scientific Instruments*, 80, 103105, 2009

Raoul Van Gastel, Sense Jan Van Der Molen, Irakli Sikharulidze, Georg Gademann, Julia Jungmann, Ron M. A. Heeren, Marc Vrakking, *Ruisloos Deeltjes Detekteren*, *Nederlandse Tijdschrift voor Natuurkunde*, 75-11, 2009, 402

## Contributions to Conferences and Seminars:

### Oral Presentations:

Julia H. Jungmann, Donald F. Smith, Luke MacAleese, Jan Visser, Ron M.A. Heeren, *The Timepix Active Pixel Detector for Mass Spectrometry Imaging: Highly Parallel Space- and Time-Resolved Imaging of Biomolecules*, 60th ASMS Conference on Mass Spectrometry and Allied Topics, Vancouver, Canada, 2012

Julia H. Jungmann, Donald F. Smith, Luke MacAleese, Jan Visser, Ron Heeren, *A new molecular imaging approach: Mass Spectrometry Imaging of Bimolecular Ions Using an In-Vacuum Pixel Detector*, NVMS/BSMS International Congress on Mass Spectrometry, Kerkrade, The Netherlands, 2012

Julia H. Jungmann, Luke MacAleese, Jan Visser, Marc Vrakking, Ron Heeren, *Space- and Time-Resolved Imaging of Biomolecules Using an In-Vacuum Pixel Detector*, Physics@FOM Veldhoven, Veldhoven, The Netherlands, 2012

Julia H. Jungmann, Luke MacAleese, Jan Visser, Marc Vrakking, Ron Heeren, *Biomolecular Imaging Mass Spectrometry Using the Timepix Detector*, Medipix Collaboration Meeting, Geneva, Switzerland, 2011

Julia H. Jungmann, Luke MacAleese, Jan Visser, Marc Vrakking, Ron Heeren, *High Dynamic Range Biomolecular Ion Microscopy with the Timepix Detector*, Kleyn Colloquium, FOM-Institute Amolf, Amsterdam, The Netherlands, 2011

Julia H. Jungmann, Luke MacAleese, Jan Visser, Marc Vrakking, Ron Heeren, *A New Molecular Imaging Approach: Space- and Time- Resolved Imaging of Biomolecules Using an in-Vacuum Pixel Detector*, IEEE Medical Imaging Conference, Valencia, Spain, 2011

Julia H. Jungmann, Luke MacAleese, Arjan Gijsbertsen, Jan Visser, Ron Heeren, Marc Vrakking, *Photoelectron & Ion Imaging Using an In-Vacuum Pixel Detector of the Medipix/Timepix Family*, seminar, INCAS<sup>3</sup>, Institute for Sensors and Sensor Systems, Assen, The Netherlands, 2011

Julia H. Jungmann, Luke MacAleese, Arjan Gijsbertsen, Marc Vrakking, Ron Heeren, *Photoelectron & Ion Imaging Using In-Vacuum Pixel Detectors: New detector concepts for Biomolecular Imaging using a Medipix/Timepix Detector*, seminar, PNNL, Richland, United States of America, 2010

Julia H. Jungmann, Arjan Gijsbertsen, Aneta Smolkowska, Ron Heeren, Marc Vrakking, *Photoelectron & Ion Imaging using In-vacuum Pixel Detectors of the Medipix/Timepix Detector Family*, Informal Workshop on Fast Imaging Sensors, Jesus College, Oxford, United Kingdom, 2010

J. H. Jungmann, A. Gijsbertsen, J. Visser, J. Visschers, R. M. A. Heeren, M. J. J. Vrakking, *Photoelectron & Ion Imaging using CMOS Pixel Detectors: Slice Imaging of Molecular Dissociation using the Timepix Detector*, 12th International Workshop on Radiation Imaging Detectors (iWoRID) 2010, Cambridge, United Kingdom, 2010

Julia H. Jungmann, Arjan Gijsbertsen, Luke MacAleese, Ron Heeren, Marc Vrakking, *The Medipix/Timepix Detector Family in Photoelectron & Ion Imaging*, Kleyn Colloquium, FOM-Institute Amolf, Amsterdam, The Netherlands, 2010

Julia H. Jungmann, Arjan Gijsbertsen, Luke MacAleese, Ron Heeren, Marc Vrakking, *Timepix Slicing Experiment*, Medipix Collaboration Meeting, Geneva, Switzerland, 2010

Julia H. Jungmann, Georg Gademann, Luke MacAleese, Ron M. A. Heeren, Marc J. J. Vrakking, *Photoelectron & Ion Imaging Using CMOS Pixel Detectors*, 11th International Workshop on Radiation Imaging Detectors (iWoRiD), Prague, Czech Republic, 2009

## Posters:

J. H. Jungmann, A. Gijsbertsen, J. Visser, J. Visschers, R. M. A. Heeren, M. J. J. Vrakking, *A New Imaging Method for Understanding Chemical Dynamics: Efficient Slice Imaging Using an In-Vacuum Pixel Detector*, Physics@FOM Veldhoven 2011, Veldhoven, The Netherlands, 2011

J. H. Jungmann, L. MacAleese, J. Visser, J. Visschers, M. J. J. Vrakking, R. M. A. Heeren, *A New Molecular Imaging approach: Space- and Time-Resolved Imaging of Biomolecules Using an In-Vacuum Pixel Detector*, Physics@FOM Veldhoven 2011, Veldhoven, The Netherlands, 2011

A. Smolkowska, A. Gijsbertsen, J. Jungmann, M. J. J. Vrakking, *Photoionization Microscopy of He Atoms*, Physics@FOM Veldhoven 2011, Veldhoven, The Netherlands, 2011

Julia H. Jungmann, Luke MacAleese, Andriy Kharchenko, Ronald Buijs, Frans Giskes, Ad de Snaijer, Jan Visser, Jan Visschers, Marc J. J. Vrakking, Ron M. A. Heeren, *Fast, High Resolution Imaging Mass Spectrometry Using a Medipix Pixelated Detector*, 58th ASMS Conference on Mass Spectrometry and Allied Topics Salt Lake City, Utah, United States of America, 2010

J. H. Jungmann, G. Gademann, A. Gijsbertsen, L. MacAleese, R. M. A. Heeren, M. J. J. Vrakking, *Photoelectron & Ion Imaging Using CMOS Pixel Detectors*, Physics@FOM Veldhoven 2010, Veldhoven, The Netherlands, 2010

Leendert A. Klerk, Julia Jungmann, Andriy Kharchenko, Luke MacAleese, Nicholas P. Lockyer, John C. Vickerman, Ron M. A. Heeren, *High Resolution C-60 SIMS and MALDI Mass Microscopy Using Position Sensitive Detectors*, Physics@FOM Veldhoven 2010, Veldhoven, The Netherlands, 2010

Ymkje Huismans, Arnaud Rouzée, A. Gijsbertsen, J. Jungmann, A. Smolkowska, F. Lépine, C. Cauchy, S. Zamith, T. Martchenko, J. Bakker, G. Berden, B. Redlich, L. van der Mer, K. J. Schaefer, M. J. J. Vrakking, *Strong-Field Ionization at Far-Infrared Wavelengths*, Physics@FOM Veldhoven 2010, Veldhoven, The Netherlands, 2010

J.H. Jungmann, G. Gademann, A. Gijsbertsen, L. MacAleese, R. M. A. Heeren, M. J. J. Vrakking, *Photoelectron & Ion Imaging Using CMOS Pixel Detectors*, 33rd Meeting of the section Atomic Molecular and Optical Physics (AMO), Nederlandse Natuurkundige Vereniging, Lunteren, The Netherlands, 2009

Julia H. Jungmann, Luke MacAleese, Ron M. A. Heeren, *Towards High Spatial Resolution in Microscope Mode Imaging Mass Spectrometry Using a Medipix Detector*, 18th International Mass Spectrometry Conference (IMSC), Bremen, Germany, 2009

## ABOUT THE AUTHOR



Julia H. Jungmann was born in Mannheim-Neckarau (Germany) in 1983. After the Jungmann family moved to The Netherlands in 2001, she attended the *Maartens College International School* in Groningen (NL) from which she obtained her International Baccalaureate high school diploma in 2003. From 2003, she studied physics at the *University of Groningen*. In 2006, she obtained her Bachelor of Science in Physics diploma with a minor in Journalism. At the same university, she completed her Masters degree in Experimental Physics “cum laude”. Her Masters project comprised a feasibility study of detecting the amount of gamma-emitting radionuclides suspended in water with advanced algorithms for real-time signal processing. This project was carried out at the *Kernfysisch Versneller Instituut*, Groningen, under the supervision

of Dr. Heinrich Wörtche and in collaboration with *Wetsus*, centre for sustainable water technology, Leeuwarden (NL) and the *Institut Jožef Stefan*, Ljubljana, Slovenia. During her studies, she completed three scientific internships: she worked at the  $\mu$ LAN (*Muon Lifetime Analysis*) precision experiment at the *Paul-Scherrer-Institute* (Villigen, Switzerland) in 2005, the *Physics of Nanodevices* group in the *Zernike Institute for Advanced Materials* at the *University of Groningen* in 2006 and the *European Organization for Nuclear Research (CERN)*, *On-Line Isotope Mass Separator Group* (Geneva, Switzerland) in 2007. From 2009, she has joined the *Biomolecular Imaging Mass Spectrometry* group of Prof. Dr. Ron M. A. Heeren at the *FOM-Institute AMOLF* (Amsterdam, NL). The research was conducted in collaboration with the *AMOLF Extreme-Ultraviolet Physics* group of Prof. Dr. M. J. J. Vrakking (now *Max-Born-Institut*, Berlin, Germany), the *Detector Research & Development* group of Dr. Jan Visser at the *National Institute for Subatomic Physics (NIKHEF)*, Amsterdam, NL) and the *Medipix collaboration* (spokesperson Dr. Michael Campbell). The focus of her dissertation is the implementation and the application of active pixel detectors to mass spectrometry imaging and to fundamental atomic and molecular physics research. The results of this work are presented in this thesis.